ENTROPY, ORDER AND 2D CONFINEMENT OF HARD PARTICLES

MIGUEL GONZÁLEZ PINTO

DISSERTATION TO OBTAIN THE DEGREE OF DOCTOR

SUPERVISORS:
Enrique Velasco Caravaca
Yuri Martínez Ratón

Universidad Autónoma de Madrid
March 2017

Miguel González Pinto: *Entropy, order and 2D confinement of hard particles,* Dissertation to obtain the degree of Doctor, March 2017.

CONTACT:
miguel.gonzalezp@uam.es / miggonpin@gmail.com

AGRADECIMIENTOS

Aunque sea mi nombre el que aparece en la portada, el mérito de este trabajo está lejos de ser únicamente mío. Hay muchas personas que, directa o indirectamente, consciente o inconscientemente, han hecho posible que pueda haber llegado hasta aquí. A todos ellos, y alguno más que se me olvide, les estoy sinceramente agradecido:

A Kike y Yuri, por haberme enseñado tantas cosas, por valorarme en el trabajo (más de lo que merecía) y por poder contar con vuestra amistad. Ha sido un placer trabajar estos años con vosotros.

A mis compañeros de departamento, que han enriquecido sin duda mi experiencia durante el doctorado. En particular a aquellos con los que he convivido más tiempo por haber compartido despacho en algún momento: Ricardo, Javi, David, Blanca, Diego(s). Y también a Carlos por coincidir conmigo más allá de la universidad.

A mi familia, y en particular a mis padres, por guiarme y apoyarme todos estos años.

A mis amigos y hermanos de la 9ª, por compartir tantos momentos estos años, ayudarme a crecer como persona y hacerme sentir en familia a 500 km de casa. A María del Mar por acompañarme, entenderme y aguantarme de cerca durante buena parte de la tesis.

Gracias.

PREFACE

Along these years many people around me –those away from science–, after asking what do I work at, wonder if that is useful. In the same direction are also frequent similar questions when great achievements of fundamental science in the past years appeared in the news. Gravitational waves, (fake) superliminic neutrinos, the Higgs boson... *now that we know this, what can we do? are they going to change our lives?*. Of course they are, but not in the near future as they may think. And probably not in the way we can think of today. That is the great power of fundamental science and the main difference with technology. While the later improves tools and techniques in a foreseeable way, basic science can bring about dramatic changes in the way we see nature and, consequently, unpredictable changes in technology. This also affect to the time scales involved in each field and to the way people out of science see the usefulness of fundamental studies. When a new technological technique is developed it may take some years to reach ordinary people through its applications. On the other hand the time from a discovery in science to its application in any way within the society could take decades. Both basic science and technology are complementary and equally important because they belong to different fields. But as I tried to explain at the beginning technology seems to be the popular daughter of the family whereas science does the work in the shadows. Nevertheless the greater changes are related to the latter. For instance the vast majority of present technology could not exist without foundations of modern physics, mainly quantum mechanics, relativity and condensed matter physics.

Regarding my work, at the beginning I used to answer that kind of questions pointing out the famous applications of my field of study. Of course it was not correct because I do not deal with applications but study how the nature behaves. So I changed the answer and tried to explain this difference between technology and science emphasizing the importance of each one. So the next question I usually have to answer is: *what have you discovered?*. Well, nothing so important that could be explained easily in a few words. As most researchers my work is quite specific and its importance lie in the merge with all the other works in the field. Its presence will go unnoticed for many people but joined together with the rest of the studies makes a solid base to build science. The great and famous discoveries are just the tip of the iceberg.

But I do not think that my only contribution to science is the work summarized in the presetn thesis. In my opinion, as a scientist, it is important to show the spirit of these lines, to explain to people why science is important even when it seems that has nothing to do with us. Lets the scientists satisfy its curiosity.

RESUMEN

This chapter is written in Spanish as required by the University regulations.

La presente tesis expone los principales resultados obtenidos en el desarrollo de mi actividad investigadora bajo la dirección de Enrique Velasco y Yuri Martínez. El trabajo tiene como objetivo comprender la compleja fenomenología presente en sistemas bidimensionales de partículas confinadas y que presentan fases de orden de tipo cristal líquido. La tesis está compuesta en líneas generales de dos partes diferenciadas: un estudio teórico de sistemas de partículas duras y un estudio experimental de partículas granulares sometidas a vibración. El enfoque teórico está basado en la teoría del funcional de la densidad (TFD) para partículas duras en la aproximación de orientaciones restringidas (o aproximación de Zwanzig). La TFD ha demostrado ser una teoría que describe muy bien sistemas de partículas densos y altamente estructurados, y son estas características las que buscamos en un marco teórico para estudiar las fases líquido-cristalinas en las que estamos interesadoos. Para mostrar cuantitativamente cómo funciona la TFD en situaciones de alto confinamiento, hemos incluido una comparación de los resultados obtenidos con dicha teoría con los resultados exactos que se desprenden del método de la matriz de transferencia (MMT) para un sistema de partículas duras cuadradas confinadas en canales estrechos (sólo dos partículas caben en la dirección transversal).

Una vez puesta a prueba la validez de nuestra teoría pasamos a utilizarla en sistemas para los cuales no se pueden obtener resultados exactos. En particular estudiamos las fases líquido-cristalinas que se forman en sistemas de partículas duras rectangulares confinadas en cavidades cuadradas. En función de la relación de aspecto de las partículas, la densidad y el tamaño de la cavidad obtenemos los diagramas de fase del sistema en los que aparecen diferentes estructuras ordenadas de equilibrio: nemático, columnar, esméctico y cristal. Así mismo comparamos las fases obtenidas con las correspondientes de los sistemas de volumen (bulk) para estudiar la influencia del confinamiento. En un segundo estudio utilizamos el mismo marco teórico para un sistema partículas tridimensionales restringidas a una monocapa. Este sistema puede verse como una mezcla de partículas duras en dos dimensiones en el que las fracciones de las diferentes partículas no están fijadas. En este caso nos centramos en el efecto que tiene la biaxialidad de las partículas en la estabilidad de las diferentes fases ordenadas.

Para finalizar la parte teórica de la tesis presentamos un estudio de la dinámica de formación de fases líquido-cristalinas. Para ello hemos hecho uso de la teoría dinámica del funcional de la densidad, una extensión de la TFD que, bajo algunas aproximaciones, es capaz de caracterizar la evolución de los perfiles de

densidad hasta sus estados de equilibrio. En concreto nosotros la hemos aplicado al estudio de formación de estructuras ordenadas en dos situaciones: (i) cuando las fases de volumen son confinadas, y (ii) cuando éstas son perturbadas por la presencia de obstáculos.

La última parte de la tesis está dedicada a un estudio experimental de las propiedades de orden de sistemas granulares de partículas. Para el experimento utilizamos partículas cilíndricas macroscópicas (1mm de diámetro) que están confinadas en un espacio circular cuasi-bidimensional, es decir, el espacio vertical es tal que puede ser formada una única capa de partículas. Este sistema es vibrado verticalmente y como consecuencia las partículas se mueven presentando una dinámica compleja. Nuestro interés por este tipo de sistemas es que bajo ciertas condiciones éstos se ordenan espontáneamente y presentan numerosas similitudes con los sistemas de partículas de equilibrio, aquellos estudiados de forma teórica en la primera parte de la tesis.

CONTENTS

1 INTRODUCTION 1
- 1.1 Liquid crystals 2
  - 1.1.1 Ordered phases 2
- 1.2 How to form a liquid crystal 4
  - 1.2.1 Hard interactions: entropic order 5
- 1.3 Confinement and 2D systems 7
  - 1.3.1 2D systems 8
- 1.4 Theories and models 8
  - 1.4.1 Mesoscopic theories 8
  - 1.4.2 Microscopic theories 9
  - 1.4.3 Simulations 10
- 1.5 Granular media 11
  - 1.5.1 Relation with liquid crystals in equilibrium 12
- 1.6 Thesis outline 13

2 DENSITY FUNCTIONAL THEORY 15
- 2.1 Introduction 15
  - 2.1.1 Splitting the functional 16
- 2.2 Scaled Particle Theory 16
- 2.3 Fundamental Measure Theory 18
- 2.4 Functional for 2D hard rods in Zwanzig approximation 21
  - 2.4.1 Chemical potentials 22
  - 2.4.2 Conjugate gradients method 23
- 2.5 Why DFT? 24

3 PERFORMANCE OF FMT. SQUARES IN NARROW CHANNELS 25
- 3.1 Introduction 25
- 3.2 FMT for parallel hard squares 26
- 3.3 Transfer matrix theory for confined fluids 28
- 3.4 Phase behavior and correlations in bulk 31
- 3.5 Confinement in narrow channels 38
- 3.6 Remarks and comments 44

4 CONFINEMENT OF RODS IN SQUARE CAVITIES 47
- 4.1 Effect of confinement 47
  - 4.1.1 Confinement in a square cavity 47
- 4.2 FMT for the square cavity 50
- 4.3 Bulk phase transitions 53
  - 4.3.1 Isotropic-nematic spinodal 53

4.3.2 Inhomogeneous phases 54
4.4 System properties 55
4.4.1 Local order parameter 56
4.4.2 Pressure 56
4.5 Results 57
4.5.1 $\kappa = 1$ 57
4.5.2 $\kappa = 3$ 60
4.5.3 $\kappa = 6$ 65
4.6 Remarks and comments 70

5 BIAXIAL PARTICLES IN MONOLAYERS 73
5.1 Introduction 73
5.2 Model for board-like particles in a monolayer 75
5.3 FMT for nematic phases 76
5.3.1 Uniform phases and order parameters 77
5.3.2 Bifurcation to biaxial phase 79
5.3.3 Critical end-point of the N-B transition 81
5.4 FMT for nonuniform phases 83
5.5 Results 85
5.5.1 Effect of particle biaxiality 85
5.5.2 Effect of particle aspect ratio κ_1 89
5.6 Remarks and comments 94

6 DYNAMICS OF PATTERN FORMATION 97
6.1 Introduction 97
6.2 DDFT 98
6.3 Systems of study and numerical resolution 99
6.4 Crystallization induced by confinement 100
6.4.1 Magnitudes to quantify the dynamics 100
6.4.2 Dynamic evolution from constant density profiles 103
6.4.3 Dynamic evolution from Col profiles 108
6.4.4 Commensuration transition between Cry structures 111
6.5 Growth of nonuniform phases around obstacles 113
6.5.1 Square and circular obstacles 113
6.5.2 Bar obstacles 115
6.5.3 Other geometries 118
6.6 Remarks and comments 118

7 EXPERIMENTS ON VIBRATED MONOLAYERS OF RODS 121
7.1 Introduction 121
7.2 Setup and image processing 123
7.3 One-component system 124
7.3.1 Order measurements 126
7.3.2 Ordered phases 127
7.3.3 Time evolution of order parameters 128

7.3.4 Dependence with radius of local averaging region 129
7.3.5 Phase diagram of monomers 131
7.3.6 Clustering 132
7.3.7 New point of view: mixture of clusters 136
7.3.8 Beyond the tetratic 138
7.4 Remarks and comments 141

CONCLUSIONES 143

Appendices

A CONJUGATE GRADIENTS 149
A.1 1D minimization 150

B NUMERICAL GRADIENT 151
B.1 Analytical gradient 151
B.2 Numerical gradient 152

C PROOF OF THE MONOTONIC DECREASING OF FREE ENERGY 157

D DDFT: EXPLICIT EXPRESSION OF THE EVOLUTION EQUATION 159

E CONSERVATION OF PARTICLES IN DDFT 163

LIST OF PUBLICATIONS 165

BIBLIOGRAPHY 167

1 INTRODUCTION

We may regard the present state of the universe as the effect of its past and the cause of its future. An intellect which at a certain moment would know all forces that set nature in motion, and all positions of all items of which nature is composed, if this intellect were also vast enough to submit these data to analysis, it would embrace in a single formula the movements of the greatest bodies of the universe and those of the tiniest atom; for such an intellect nothing would be uncertain and the future just like the past would be present before its eyes.

–Pierre-Simon Laplace, *Essai philosophique sur les probabilités*, 1814.

With these words Laplace wrote the first known article on the deterministic view of nature. Since then there have been some arguments against this idea. Especially when quantum mechanics came up with its probabilistic nature and the Heisenberg uncertainty principle. But even with the arrival of modern physics the debate is subtle –see for example the interesting lecture by Stephen Hawking (1)–. Nevertheless, at this point the discussion is more philosophical than scientific because it is not feasible from a practical point of view. As Laplace said, we need an intellect able to process all the data. However, in physics we can only solve analytically systems of two and in some cases three particles.

We could extend Laplace's reasoning to a physical system with many particles –not only to the whole universe–. If we knew all the fundamental interactions between them and its initial conditions in principle we could obtain the state of the system at any time. But, as said before, we are far from being able to do that. In a macroscopic state the number of constituent components is of the order of the Avogadro constant, i.e. $\sim 10^{23}$. Even in much smaller systems the number of interacting particles is too large to make an exact treatment possible. To deal with real situations scientist need to make some simplifications, approximations and carry the system to limits where one can obtain some results. And this is the context where condensed matter physics lives, covering many fields of physics and other sciences like biology, chemistry or material science. It measures system properties and develops mathematical models to understand their physical behaviour.

The problem with condensed matter physics is at the same time responsible of its beauty. In a highly interacting system the whole is not just the sum of its parts and, as a consequence, it usually results in complex and rich behaviours. But this frequently means a lack in physical intuition to face the problems.

1.1 LIQUID CRYSTALS

Liquid crystals are a good example of a condensed matter field of study. A collection of particles interacting individually in a well known way but exhibiting complex behaviours and properties. Although its fundamental interactions may be very simple, there is no possibility to get exact results on the time evolution or stationary state. This is why there are still many active research in the field from different perspectives.

The classical division of states of matter into gas, solid and liquid is not an absolute classification. Many systems do not fit perfectly in one of these phases but present intermediate properties. One example is liquid crystals. As the name suggests, they belong to a state of matter which is neither liquid nor crystal. In other words they present properties of both liquids and crystals at the same time. Liquid crystals are intermediate states and, for this reason, they are also called meshopases or mesomorphic phases –from the greek *meso* which means "between"–. So before characterizing liquid crystals we shall briefly see the differences between crystal and liquid phases.

The main feature of a crystal is the spatially ordered arrangement of its components. Given a basis (or unit cell) we obtain the position of all particles by repeating it periodically in the space. On the other hand, the relative position of molecules in a liquid is not fixed. However, we can obtain the radial distribution function, which gives the probability of finding a particle at a certain distance from another. This function decays with distance and reaches a constant probability, in contrast with the case of crystalline phases, which have long-range order and a radial distribution function which does not decay with distance.

Only with these general characteristics a liquid crystal should be a system with crystal order in some direction(s) but not in the other(s). However, this definition is not complete because we cannot find a partial ordered phase with isotropic components. Anisotropic particles are needed and thus there is another type of ordering which is the orientation of particles. So a liquid crystalline phase can be defined as follows: it is a fluid of anisotropic particles exhibiting orientational order which may also present partial positional –or translational– order.

1.1.1 Ordered phases

For the sake of simplicity we will restrict our attention from now on to systems of rod shaped particles. Rods under different conditions will be the main object of study of this thesis so in this sense examples and explanations will be more clarifying. As a consequence, this introduction is written with no intention to be a general overview of liquid crystals but only to emphasize the characteristics of rod-like liquid crystals. For a general description of liquid crystals see for example (2).

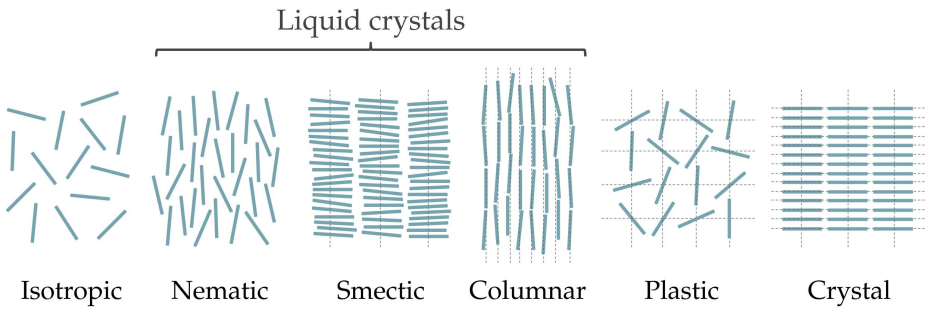

Figure 1.1: Classification of ordered phases in terms of translational and orientational order.

It is possible to classify the different ordered phases by looking at the translational and orientational order of the system:

ISOTROPIC (I) particles have neither positional nor orientational long-range order. It is a fluid-like phase.

NEMATIC (N) the centers of mass of particles are not correlated but particles share a preferential direction of orientation. This direction along which particles are oriented on average is called the director and is present in all phases with orientational order.

SMECTIC (SM) the system presents orientational and partial positional order (in 1D). Particles are arranged in layers (sheets) which are perpendicular to the average orientational vectors of the particles. Particles can flow within their layer but their motion in the perpendicular directions is restricted.

COLUMNAR (COL) as in a smectic phase it has orientational and partial positional order (now in 2D). The difference is that here the average particle orientation is parallel to the layers (columns).

PLASTIC CRYSTAL (P) in this phase particles have full positional order (3D) but no orientational order.

CRYSTAL (CRY) the system is completely ordered.

This classification can also be seen in terms of symmetry. The isotropic phase is invariant under rotations and translations. The nematic is translationally invariant but not completely rotationally invariant because of the presence of a special orientation. The rest of phases are not invariant under rotations and not fully invariant under translations. The difference lies in the degree of invariance, and we can make the discussion in terms of the decreasing order of symmetry. The smectic phase forms layers of particles separated by some typical distance, the smectic wavelength. In figure 1.1 the smectic planes are

perpendicular to the paper and the intersections would be the dashed lines. So this phase is translationally invariant in two dimensions (inside the smectic planes) while in the other dimension it is only invariant under translations by an integer number of the smectic wavelength. The columnar phase is made up by 1D structures, i.e. columns, so it is only invariant under translations along the direction of the columns but not in the other two dimensions. Finally the phases with less symmetry are the crystalline ones. They are invariant only under the set of translations defined by the lattice vectors (3D).

From this general classification the intermediate phases would correspond to liquid crystals: nematic, smectic and columnar. The first clear classification of liquid crystal is attributed to Friedel (3) who defined two main groups: smectic and nematic. He also mentioned a cholesteric phase which nowadays is usually included as a subphase because it is just a twisted nematic. The columnar phase was later discovered in studies of disc-like compounds. This is the reason why it is also known as discotic phase. This name is not appropriate, however, because disc-like particles are not essential to form the aforementioned phase. For instance rods in two dimensions can also organize in columns.

Since this first classification many subphases have been found. For instance different smectic structures have been defined depending on the relative orientation of particles with respect to the layers, and other subphases have been shown to exist when particles inside the layers organize into some particular structure. A complete discussion on the classification of liquid crystal subphases can be found in (4).

1.2 HOW TO FORM A LIQUID CRYSTAL

In order to obtain a liquid crystal structure one could just arrange particles in one of the configurations shown in figure 1.1. A better name for this section should read *how to form a liquid crystal as a stable state*.

Although there are many examples of liquid crystalline structures in our environment, the beginnings of research in this field are related to optical properties of some materials (5, 6). These findings came from the peculiar phenomenology exhibited in their phase transitions. And, as seen before, the reason was the change in the microscopic organization of the material. Scientists found that, in the transitions, the degree of order changed, meaning that the building blocks of liquid crystals were molecules and polymers.

From a scientific point of view it was more an experimental than a theoretical work. Chemists and physicists synthesized and conceived different compounds made of anisotropic molecules in order to obtain materials with the new fascinating properties. But the reason why particles would arrange into those structures was not clear.

One could think that depending on the compound, different attractive molecular forces may be responsible for the order. In fact, attractive interactions must

play a role because they are present at the microscopic scale, but from a fundamental point of view these interactions are not necessary to stabilize a liquid crystal. In 1949 Onsager proved that a system of thin hard rods spontaneously ordered into a nematic phase above a certain density (7). Since then many systems of anisotropic particles interacting through hard forces have been shown to present liquid crystalline textures. Therefore, as an answer to the question posed at the beginning of the section, we can say that it is just the particle anisotropy which is required to form mesophases.

1.2.1 Hard interactions: entropic order

In a system of hard particles (those which cannot overlap) all the allowed configurations have the same internal energy, so the appearance of order can only come from the entropy. This statement may sound a little contradictory from a standard point of view, but it is well understood in the framework of statistical mechanics. We know that the correct interpretation of entropy is just as a measure of the number of configurations accessible to the system, which therefore tends to evolve to states with the maximum volume in phase space, i.e. the maximum number of configurations.

Using an example, let us see how entropy can lead to an ordering transition. Consider a system of hard rods of length L and width d. There are two entropic contributions, the ideal and the interaction (or excess) one, each of them depending both on translational and orientational degrees of freedom of particles

$$S_{total} = S_{id}^{(trans)} + S_{id}^{(orient)} + S_{exc} \tag{1.1}$$

where the excess part cannot be split since the interactions depend on the positions and orientation of rods.

At low densities the ideal part is the only relevant and total entropy is maximized when particle positions and orientations are randomly distributed. However, increasing the density means that interactions are more important and the excess part of the entropy may compete with the ideal one. As a consequence, counter-intuitive behaviour appear in the system in order to increase the total entropy.

The key point of Onsager was to show that the interaction part of the entropy is directly related to the excluded volume –or area in 2D– in the system. The excluded volume is just the forbidden region where the center of mass of a particle cannot be placed, otherwise it would overlap with another. It clearly depends on the relative orientations of particles: in figure 1.2 we show the excluded area for three different cases. The point is that, the smaller the excluded volume of a system, the larger the space available and hence the larger the excess entropy. However, it is straightforward to show that the minimum excluded volume for a pair of rods is reached when they have the same orien-

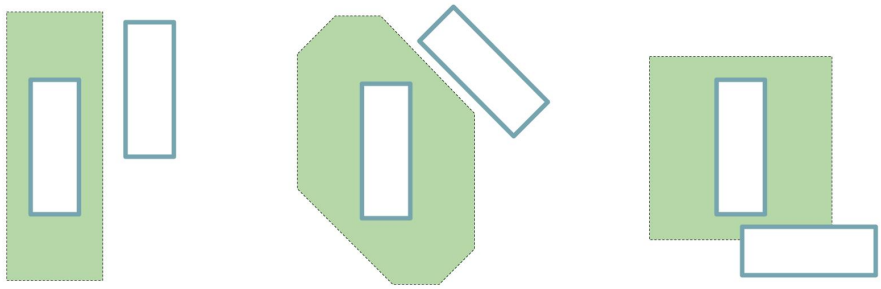

Figure 1.2: Excluded volume (colored area) depending on the relative orientation of particles.

tation, i.e. when the ideal part of entropy is minimum. This is the basis where the competition between entropic contributions comes from.

At low densities there is plenty of free space and the gain in S_{exc} by minimizing the excluded volume is negligible as compared with the decrease in S_{id}. As a consequence, the isotropic phase is stable in the dilute region. Nevertheless, when the density is high enough, a decrease in the ideal entropy can lead to a great increase in the interaction part of entropy and thus the system gets ordered –nematic phase–. Liquid crystal phases with partial positional order (in addition to orientational one) usually takes place at higher densities and the physical arguments of the transitions to these configurations are similar: the minimization of excluded volume due to particle orientation is already established, however, it can be further decreased if particles are ordered spatially because overlapping of excluded volume is optimized and the total free volume increases –smectic, columnar or crystal phases–.

In the previous example we have seen the physical arguments that explain the isotropic-nematic transition as a competition between different entropic contributions. But one should notice that the presence of orientational degrees of freedom are not necessary to get ordered stable configurations in hard systems. For instance hard spheres, which have only translational degrees of freedom, also undergo a first order phase transition between fluid and crystal phases (*8*). The reason for this spontaneous ordering is again the excluded volume: at some density ($\eta_t \sim 0.5$) the maximum in S_{exc} of an ordered configuration compensates the minimum of S_{id} and the total entropy of the crystal structure is maximum. For a more careful discussion one can see section 6.6 of (*9*).

These arguments seem reasonable, and are now well accepted, but this was not always the case. In (*10*) Frenkel mentions an anecdote that brings to light the hard beginnings of these ideas. The first numerical simulations of hard spheres suggesting a freezing at high densities (*11*, *12*) date back from 1957 and provoked much scepticism. That year the topic was discussed at a workshop and a committee of experts, including two Nobel laureates, was asked to vote

whether the result was possible or not. As a result, the committee decided not to believe in the evidence for hard-sphere freezing.

Now we have become used to this kind of arguments with entropy, which are well accepted.

1.3 CONFINEMENT AND 2D SYSTEMS

Bulk liquid crystal properties are interesting by themselves and there are already many open problems to solve. But the presence of external fields brings about more complexity and counter-intuitive behaviours. Particularly interesting, and a main ingredient of this thesis, are the effect of surfaces on the liquid crystal textures. They involve novel phenomena such as wetting, capillarity, anchoring, commensuration effects...

The symmetry of the potential defines also the symmetry of the equilibrium liquid crystal structure. While, under appropriate thermodynamic conditions, bulk systems are translationally invariant, surfaces break this symmetry at least near the interface. In order to properly study surface effects, we must take them into account in the thermodynamic potentials. The grand potential presents a surface term

$$\Omega = U - TS - \mu N + \gamma A$$

with T the temperature, μ the chemical potential, A the surface area and γ its conjugate variable usually known as surface tension.

The rich variety of properties due to confinement comes from the competition between volume –bulk– and area –surface– contributions. The latter will be negligible in large systems and only the region close to surfaces will present an inhomogeneous structure. Here typical phenomena are wetting or surface induced order, also known as anchoring. On the other hand, small systems –such as narrow pores– can show properties very different from bulk because all particles are affected in some way by the walls. In this case additionally to wetting or anchoring we can find frustration and commensuration effects due to the strong confinement. These are the result of the relation between periodicity of the liquid crystal structure and the size of the pore. Depending on the commensuration between them some liquid crystal phases can be frustrated or favoured.

Besides all the interesting phenomenology that emerges from liquid crystal systems in the presence of external fields from a fundamental point of view, this field of study has also attracted a lot of attention because of its important role in technological applications. The vast majority of them are based on ordering properties of liquid crystals and on the fact that particles can be easily oriented using external fields. For example if molecules have an electric dipole they can be aligned using an electric field. Otherwise, order can be induced by confinement.

1.3.1 2D systems

Two-dimensional systems can be viewed as a limit where extreme confinement only allows particles to move on a 2D surface. This will be a fundamental characteristic of the systems studied in the present work. The reasons why these systems are interesting are many.

Firstly they usually have peculiar properties due to its low dimensionality. Furthermore we find a lot of relevant examples of 2D systems in nature such as monolayers, colloids, membranes... Also from a theoretical point of view 2D models are more tractable mathematically and usually it is easier to understand the physics emerging from them.

1.4 THEORIES AND MODELS

As explained in the beginning of the introduction, in practice it is very unusual to know the real interaction between particles and to be able to solve –either analytically or computationally– the exact equations. This is the reason why many different theories exist, each one trying to understand the physics behind these systems from different approaches. However, in most cases we can categorize them in three main groups: mesoscopic or phenomenological theories, microscopic theories and simulations.

1.4.1 Mesoscopic theories

The mesoscopic theories do not deal with interactions between particles but go to a higher level and describe the system in terms of average properties emerging from the particle level. One of the most used is the Ericksen-Leslie continuum theory (*13*–*15*) which is a more general formulation than the first approximation of this kind, the Frank-Oseen theory(*16*). Here the system is seen as a continuum by defining a director field that gives the local orientation of particles. This is the same approach than in fluid mechanics. The contribution of the theory was to provide a free energy function that accounts for the deformations of the director field from its equilibrium position. In other words, how much energy does it cost to deform the orientational field? There are three principal modes of deforming the system locally: splay, twist and bend (see figure 1.3). Taking this into account and realizing some symmetries in the liquid crystal phases, one can obtain an expression in terms of the free energy depending on some parameters that can be fitted experimentally.

The continuum theories work well for confined systems or in the presence of obstacles because they correctly treat the deformation of the liquid crystal near the boundaries. For the same reason, they are usually a good approximation for systems subject to external fields if the deformation of the director is soft enough. However, continuum theories are only used in situations where or-

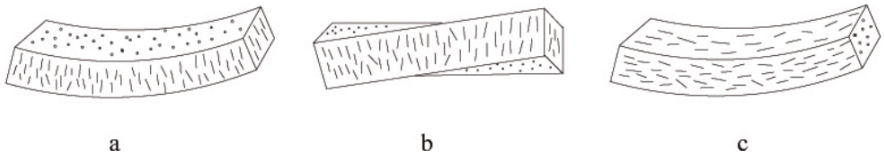

Figure 1.3: Modes of deformation of the orientational field in the continuum theory: (a) splay, (b) twist, (c) bend. Image taken from (*17*).

dered phases are assumed to be stable, for example a well developed nematic, because they are not meant to describe phase transitions.

Another phenomenological theory, and probably the most popular, is that of Landau-de Gennes (*18*). It was developed by Pierre-Gilles de Gennes who generalized the Landau theory for phase transitions. The idea is to identify the order parameter of the system and then express the free energy in terms of proper combinations of the order parameter allowed by symmetry. The number of coefficients in the theory can be reduced by using the symmetries of the system and assuming physical properties of the system, but finally they have to be adjusted by experiments or by other theories.

The Landau-de Gennes approximation has been widely used, but it has some drawbacks, as any other theory. One of them is that, due to the nature of Landau theory, it is only valid near the phase transition and, as a consequence, it only applies to weakly ordered phases. Another disadvantage is the lack of predicting power, at least quantitative, because of the need to adjust the parameters with external results. Also, as any other mesoscopic theory, it looses all information on particle geometry and interactions.

1.4.2 Microscopic theories

This is an intermediate point between phenomenological descriptions and simulations. Microscopic theories capture particle interactions but at some point one must make approximations because of the complicated mathematical framework and the limited operative power –analytic and computational–. For instance, a frequent simplification is to perform a mean field theory for the pair correlation functions. But for most realistic systems it is still too complicated and one must also make approximations at the level of correlations.

The first mean field theory for liquid crystals was the aforementioned work of Onsager (*7*). He studied the isotropic-nematic transition of a system of hard thin rods, for which the intermolecular interaction depends on the position and orientation of particles. The idea of Onsager was to make a virial expansion of the free energy and truncate it to the second order, which leads to an essentially exact theory for infinitely thin rods. Later Zwanzig (*19*) extended the work of Onsager to study the transition of rods with finite aspect ratio. He computed

higher orders of the virial expansion but to do so he had to restrict the possible orientations of particles to a discrete set instead of a continuous.

The importance of Onsager is not just the work itself but the path that he opened. It is the seed of the modern density functional approach that will be explained in more detail in chapter 2.

Another widely used microscopic theory is the Maier-Saupe model (20–22). Here the isotropic to nematic transition is explained via the anisotropic attractive interactions between particles; the packing effects studied by Onsager are completely ignored. The Maier-Suape theory does not take into account the position of particles, but only their orientation. It can be formulated in terms of a self-consistent local potential which depends on particle orientations.

Even though the two theories explained here present different mechanisms responsible for the phase transition, both contain realistic effects. For example in elongated molecular systems van der Waals forces will cooperate with entropic effects in the isotropic-nematic transition. And sometimes one of the mechanisms may be negligible and the system can be well described by one of the approximations. For instance if particles are large enough molecular forces may not play so crucial role and the main contribution to the ordering may be basically entropic.

As mentioned in the previous section all theories and approximations have advantages and drawbacks. Otherwise we would have a theory explaining properly all features and no approximations would be needed. But until that happens it will be necessary to know the positive and negative aspects of theories and consider which of them may be more suitable for our system.

The strong aspect of microscopic theories is that they capture the fundamental physics of the system and all properties emerge naturally, in contrast to phenomenological models. But, as a drawback, the mathematical framework tends to be quite complicated, a number of approximations are needed, and the need to resort to numerical treatment is usually unavoidable.

1.4.3 Simulations

Computer simulations are usually the most fundamental level of resolution when a problem is not exactly solvable. Instead of creating models that approximate or mimic the physics of the system one can take advantage of computational power to solve the fundamental equations. Historically there are two well established methods: molecular dynamics and Monte Carlo simulations.

The idea of molecular dynamics is very simple: to solve the equations of motion for the particles. Once the interaction potential is defined, one can apply Newton's equations and obtain the dynamics of the system. These calculations are usually very expensive from the computational point of view –even for the simpler potential, the hard interaction–. And this effort is proportional to the number of particles in the system and to the time we want to simulate. As a

consequence, one is limited to short times of evolution and small number of particles if we want to obtain the result in a reasonable time.

The Monte Carlo technique (23) is based on the statistical mechanics point of view. Starting from some initial configuration –random in principle– in each step one moves and rotates randomly some particles in order to get another configuration. If the new configuration has a lower free energy than the previous, i.e. $\Delta\mathcal{F} < 0$, then the new configuration is accepted. If $\Delta\mathcal{F} > 0$ it can be accepted with a probability given by a Boltzman distribution $p = e^{-\Delta\mathcal{F}/k_B T}$. This process is repeated as many times as necessary, and configurations will be accepted and rejected step by step. At the end the system will reach equilibrium. The evolution of the system is not real, but the aim of the Monte Carlo method is to obtain canonical averages over equilibrium configurations.

While the Monte Carlo method does not say anything about dynamical properties, molecular dynamics can be used to probe such properties. Both techniques are widely used not only to solve problems that cannot be tackled by with theories but also to test theoretical models. A great advantage of simulations is that we can prepare the systems in conditions that are not feasible experimentally. Their main drawback, as explained above, is the limitation in system size and time because of the high demanding computational power.

1.5 GRANULAR MEDIA

The final part of the thesis –chapter 7– is devoted to the experimental study of vertically vibrated granular rods confined in quasi-2D. The reader may be surprised by the presence in the same work of theoretical studies on liquid crystals and granular matter experiments. However, the reason is to highlight some of the similarities shared by both systems.

Granular matter can be defined as a large ensemble of discrete solid grains in which thermal fluctuations are irrelevant. For this reason they are considered as athermal systems. They spread a wide range of particle sizes. Their minimum size typically lies in the micrometer scale, in which the brownian motion becomes negligible. Because thermal energy does not play a role and because grains are macroscopic, friction and inelastic collisions are present in the interactions between particles. As a consequence, granular systems are very dissipative and they are usually far from equilibrium.

Granular matter is ubiquitous in nature and examples of it appear at all scales: dust, sand, rice, gravel, planetary rings or even the asteroid belt. Granular media cannot be considered as a state of matter, but they frequently share properties with solids and fluids at the same time. For example we can look at sand. It can flow and adapt to the shape of its container like a liquid would do. However, we can stay on it without the risk of sinking. Everybody is used to this dual behaviour since granular materials are all around us. Consequently, scientists and engineers have taken advantage of their properties and now they

play a fundamental role in many disciplines such as manufacturing processes, agriculture, mining, construction...

Historically it is more common that humans first control the engineering of some field and then try to get some understanding from a scientific point of view. For example we learnt how to sail and make boats long before Archimedes set up his principle of buoyancy. Or we dominated the electricity before knowing even what it was. In the same way granular materials have been used in our advantage without being able to explain its behaviour. For instance a recent study (*24*) suggests that engineers in Ancient Egypt would wet sand so as to reduce friction drastically when transporting huge blocks of stone. With no doubt they had to master a lot of tricks with grains in order to build structures like pyramids surrounded by sand.

From the point of view of science the first studies on granular matter are related to great scientists such as Euler, Faraday, Coulomb, Bagnold or Reynolds. But the complexity of granular media and the great interest in research for applied engineering left fundamental studies mostly inactive until the end of the last century. From that point a new interest came associated with the appearance of studies about self-organized systems and pattern formation. Since then the field has become very popular because of the rich phenomena emerging from these complex systems (*25*). Nevertheless, it is still a very challenging topic from the theoretical point of view. One has to deal with a large number of particles far from equilibrium and with complex inelastic interactions. As a consequence, no general theory exists to date but only a collection of different approaches that work relatively well for each situation. There exists no general description such as the Navier-Stokes equations for fluids. On the contrary the different theories and approximations are sometimes based on contradictory concepts.

1.5.1 Relation with liquid crystals in equilibrium

Our interest in granular media comes from the interesting parallelisms they share with equilibrium liquid crystals in some situations (*26*–*30*). Recently several works have pointed in this direction, posing the question of the apparent similarities between two fundamentally different systems.

On the one hand, from a standard view, liquid crystals are microscopic systems complying with thermodynamics and statistical mechanics. Temperature is a relevant variable responsible for agitating particles and allowing the system to explore the phase space and to reach equilibrium at long times.

On the other hand granular materials are athermal systems which, in the absence of any external force, come to rest very rapidly. As a consequence, metastable configurations are very frequent. In order to kick the system out of static configurations one has to introduce an external energy supply. For example let us say that we vibrate the system. Then we need to do it continuously because particles collisions are highly inelastic and energy dissipation

puts the system to rest. Energy injection plays a role similar to temperature in microscopic systems, allowing the system to explore different configurations.

However, this analogy is tricky because the physics behind both systems is very different. In granular media there is a continuous energy dissipation and, consequently, the system is far from equilibrium. Due to this out of equilibrium dynamics the stationary states may not correspond to those of maximum entropy or lower free energy. In fact, a wide variety of non-equilibrium phenomena emerging from granular systems have been reported, such as non-Maxwellian velocity distributions and lack of equipartition (*31*), anomalous diffusion and noise (*32*), nonergodicity (*33*), vortices (*34*) or giant fluctuations (*35*).

But coming back to our initial argument, there exist some conditions (*27*) under which granular media resemble its thermal counterpart. Furthermore these similarities should not be surprising because in many cases exclusion interactions and entropy-driven transformations are the key mechanisms present in both systems. In one case temperature, and in the other external energy input, make the particles explore different configurations which evolve following some kind of minimum steric interaction principle. Granular matter has also been considered to be a testing ground for the study of some aspects of thermal systems that are difficult to see experimentally. In this sense grains can be easily tracked individually and interactions can be considered to be close to hard-like.

1.6 THESIS OUTLINE

The present thesis is composed of two differentiated parts. The first, chapters 2-6, is a theoretical study of bulk and confined systems. We begin in chapter 2 with a description of the density functional theory (DFT) that will be used as our main tool for the study of equilibrium states. Chapter 3 is devoted to test the power of our DFT under strong confinement conditions through the study of hard squares in narrow channels. In order to do so we will compare with exact results system properties such as correlations, density profiles or equations of state. Chapters 4 and 5 present the equilibrium behaviour of hard rectangles confined to square cavities and board particles restricted to a flat surface respectively. In the first one we will compare the phase behaviour at bulk and under confinement and we will study the phase behaviour dependence with the particle aspect ratio and the density. In chapter 5 we study three-dimensional board-like particles with their centers of mass restricted to a monolayer. Here we focus on the dependence of particle biaxiality on the phase behaviour. To complete the first theoretical part of the thesis we dedicate chapter 6 to an introductory study of the dynamics in the framework of our density functional theory. In particular we will analyze the process of pattern formation of two-dimensional particles in confined systems and in presence of obstacles. Finally, chapter 7 is quite different to the previous ones. In it we

present the results of an experimental work on vibrated granular rods. We study in detail the ordering properties of particles in the stationary state and point out some similarities that shares with the equilibrium systems studied in the first part of the thesis.

2 DENSITY FUNCTIONAL THEORY

2.1 INTRODUCTION

The origins of density functional theory (DFT from now on) do not have a unique seminal work (*36*, *37*). In the 1960s several contributions (*38*–*41*) helped to develop the formalism of inhomogeneous classical fluids. This led Percus and Stell to apply functional methods to the theory of classical fluids (*42*).

Parallel to that Hohenberg and Kohn published a paper about the study of an inhomogeneous electron gas (*43*). In this work they found a functional of the density independent of the external potential, $\mathcal{F}[\rho(\mathbf{r})]$, such that the energy functional defined as $E \equiv \int V_{ext}(\mathbf{r})\rho(\mathbf{r})d\mathbf{r} + \mathcal{F}[\rho(\mathbf{r})]$ presents a minimum for the ground-state energy associated with the external potential $V_{ext}(\mathbf{r})$.

Even though this latter work belongs to electronic systems its ideas were applied to classic fluids. Ebner adapted the work of Hohenberg and Kohn to classical fluids (*44*) and combined with the recently born formalism of inhomogeneous fluids, the basis of the modern DFT were set.

The name DFT already gives the basic idea of the theory: here thermodynamic potentials are expressed as functionals of the inhomogeneous one-particle density $\rho(\mathbf{r})$. The key point given by Mermin was that it can be proven –see appendix B of (*9*)– that, given an inter-particle potential, there exists a unique free energy that is a functional solely of the density profile. This functional is intrinsic because it has the same form for all situations and does not depend on any external potential

$$\mathcal{F} : \mathcal{F}[\rho(\mathbf{r})]. \tag{2.1}$$

The second key point of the theory is that given an external potential $V_{ext}(\mathbf{r})$ the equilibrium density profile is unique, and vice versa. Furthermore the equilibrium profile is that which minimizes the grand potential Ω. For fixed temperature T and chemical potential μ one can relate the free energy with the grand potential through a Legendre transformation

$$\Omega[\rho(\mathbf{r})] = \mathcal{F}[\rho(\mathbf{r})] + \int_{\mathcal{V}} d\mathbf{r}\rho(\mathbf{r})(V_{ext}(\mathbf{r}) - \mu) \tag{2.2}$$

and the second result of DFT reads

$$\left.\frac{\delta\Omega[\rho]}{\delta\rho(\mathbf{r})}\right|_{\rho=\rho_{eq}} = 0 \qquad \text{and} \qquad \Omega[\rho] \geqslant \Omega[\rho_{eq}]. \tag{2.3}$$

Strictly Ω and $\mathcal{F}$ are the grand potential and free energy only for $\rho = \rho_{eq}$.

2.1.1 Splitting the functional

In order to find a suitable functional for each system the free energy functional is usually split up into two parts, one corresponding to the ideal gas (non-interacting part) and another part that takes into account the interactions between particles, called the excess part

$$\mathcal{F}[\rho] = \mathcal{F}_{id}[\rho] + \mathcal{F}_{exc}[\rho]. \tag{2.4}$$

The ideal part is the same for all systems and it can be obtained exactly

$$\mathcal{F}_{id}[\rho] = k_B T \int_{\mathcal{V}} d\mathbf{r}\rho(\mathbf{r}) \left[\ln\left(\Lambda^3\rho(\mathbf{r})\right) - 1\right] \tag{2.5}$$

where Λ is the thermal de Broglie wavelength which can be ignored because it shifts the free energy by an additive constant.

The hard part of DFT is of course to find the free energy functional expression. In general it can be obtained exactly only in cases where correlations are very simple. One example is the one-dimensional system of rods whose exact functional was obtained by Percus (*45*). But generally one has to make approximations. These approximations can be justified from a physical point of view thanks to an interesting relation between the excess part of the functional and the direct correlation function

$$c^{(1)}(\mathbf{r}) = -\beta\frac{\delta\mathcal{F}_{exc}[\rho]}{\delta\rho(\mathbf{r})} \tag{2.6}$$

$$c^{(n)}(\mathbf{r}_1, ..., \mathbf{r}_n) = \frac{\delta c^{n-1}(\mathbf{r}_1, ..., \mathbf{r}_{n-1})}{\delta\rho(\mathbf{r}_n)} = -\beta\frac{\delta^n\mathcal{F}_{exc}[\rho]}{\delta\rho(\mathbf{r}_1)\cdots\delta\rho(\mathbf{r}_n)} \tag{2.7}$$

β being the Boltzmann factor and δ the functional derivative.

As a consequence, one can derive an expression for the free energy functional from the direct correlation function of a system of particles, or also from the total correlation function which is related with the latter through the Ornstein-Zernike equation

$$h(\mathbf{r}_1, \mathbf{r}_2) = c^{(2)}(\mathbf{r}_1, \mathbf{r}_2) + \int d\mathbf{r}_3 h(\mathbf{r}_1, \mathbf{r}_3)\rho(\mathbf{r}_3)c^{(2)}(\mathbf{r}_3, \mathbf{r}_2). \tag{2.8}$$

In the next sections we will derive the free energy functional used in this thesis. In order to understand the physical approximations we will start by presenting the scaled particle theory for hard rods and then we will extend it to the fundamental measure theory in which our model is based.

2.2 SCALED PARTICLE THEORY

Imagine we have a one-dimensional system of N_i polydisperse hard rods of length L_i. We want to know the work required to insert a particle of length

l. From thermodynamic fluctuation theory the probability of finding a hole of size l is given by

$$\lambda = e^{-\beta W(l)} \tag{2.9}$$

$W(l)$ being the work required to create such a hole. On the other hand, if the total space of the system is L, the free space available will be $L - \sum_i N_i(L_i + l)$. And in the limit of low density, or small sizes (i.e. $l << L_i$), the probability of finding a free space for the test particle is

$$\lambda = 1 - \sum_i \frac{N_i}{L} L_i = 1 - \sum_i \rho_i L_i = 1 - \eta \tag{2.10}$$

with ρ_i the density of the 'i' species and η the packing fraction. Comparing equations 2.9 and 2.10 we get for $l << 1$

$$\beta W = -\ln(1-\eta). \tag{2.11}$$

In the limit of large scaled particle length, $l >> L_i$, the other particles are much smaller and they behave like a gas and, consequently, the work required to insert that particle is obtained in thermodynamics as

$$\beta W = pl \tag{2.12}$$

p being the pressure of the gas.

For general cases scaled particle theory (*46*) assumes that the work to insert a particle of arbitrary length is an interpolation of both limits (expanding equation 2.9 in Taylor series). And if we substitute l by L_i this work is equal to the excess part of the chemical potential of species 'i'

$$\beta \mu_{exc}^{(i)} = -\ln(1-\eta) + \beta p L_i. \tag{2.13}$$

From here we can obtain an expression for the free energy density Φ using some thermodynamic relations. From

$$\frac{\partial \Phi_{exc}}{\partial \rho_i} = \beta \mu_{exc}^{(i)} = -\ln(1-\eta) + \beta p L_i \tag{2.14}$$

we obtain

$$\sum_i \rho_i \frac{\partial \Phi_{exc}}{\partial \rho_i} = -\rho \ln(1-\eta) + \beta p \eta. \tag{2.15}$$

The second thermodynamic relation is

$$\beta p = \sum_i \rho_i \frac{\partial \Phi}{\partial \rho_i} - \Phi \tag{2.16}$$

with $\Phi = \Phi_{id} + \Phi_{exc}$ the total free energy density, the ideal part being

$$\Phi_{id} = \sum_i \rho_i \left[\ln(\rho_i \mathcal{V}_i) - 1\right] \tag{2.17}$$

from which the ideal contribution to the pressure reads

$$\beta p_{id} = \sum_i \rho_i \frac{\partial \Phi_{id}}{\partial \rho_i} - \Phi_{id} = \rho. \tag{2.18}$$

Then equation 2.16 becomes

$$\beta p(1-\eta) = \rho - \rho \ln(1-\eta) - \Phi_{exc}. \tag{2.19}$$

This is a differential equation in Φ_{exc} and when solved with the appropriate conditions ($\rho_i \to 0 \Rightarrow \Phi_{exc} \to 0$) one gets

$$\Phi_{exc} = -\rho \ln(1-\eta). \tag{2.20}$$

2.3 FUNDAMENTAL MEASURE THEORY

The free energy density obtained in the previous section has been derived for uniform systems. But, what happens when dealing with inhomogeneous density profiles? In this situation $\rho_i = \rho_i(x)$ and the probability of finding a particle at a certain location depends on its neighbouring particles. There are several recipes to take into account local correlations between particles, see for example (*36*). The local density approximation (LDA) is the simpler generalization to non-uniform fluids and it only works well when inhomogeneities are weak and smooth. In a higher level of complexity we find the weighted density approximation (WDA) which contains a coarse-grained local density (*47*). Correlations are taken into account through a weighted function that averages the density profile in the local area. In this approximation sharp profiles such as fluids near walls and under confinement are successfully captured.

However, Rosenfeld (*48*) went a step further developing the fundamental measure theory (FMT). It was a big step and has been successfully used because it describes reasonably well profiles and correlations of hard particles under strong confinement and in highly inhomogeneous situations. An important feature of FMT is the existence of several weighted densities containing information about particle geometry. This is the theory that we will use in most of the thesis and it is obtained for hard rods below.

For inhomogeneous fluids correlations are important so we cannot just replace ρ by $\rho(x)$ in equation 2.20. In order to take this into account we can substitute density and packing fraction by functions that average them in a local environment

$$\Phi_{exc}(x) = -n_0(x) \ln\left[1 - n_1(x)\right] \tag{2.21}$$

with

$$n_\alpha = \sum_i \int_{\mathcal{L}} dx' \rho_i(x') \omega_i^{(\alpha)}(x - x') = \sum_i \left[\rho_i * \omega_i^{(\alpha)}\right](x). \tag{2.22}$$

The weighted functions $\omega_i^{(\alpha)}$ and the interval where we average are still to be defined. Notice that imposing $\rho \neq \rho(x)$ we must recover $n_0 = \rho$ and $n_1 = \eta$.

In order to get $\omega_i^{(\alpha)}$ we will compare the free energy functional in the low density limit with a virial expansion in density. Taking the power series up to the first term we have

$$\beta \mathcal{F}_{\text{exc}}[\{\rho_i\}] = -\frac{1}{2} \sum_{ij} \int_{-\infty}^{+\infty} dx \int_{-\infty}^{+\infty} dx' \rho_i(x) \rho_j(x') f_{ij}(x - x') \tag{2.23}$$

where f_{ij} is the Mayer function. For hard particles the interacting potential between them $V_{ij}(x)$ is infinite when they overlap and zero otherwise, so the Mayer function can be written as

$$f_{ij}(x) = e^{-\beta V_{ij}(x)} - 1 = -\Theta\left(\frac{L_i + L_j}{2} - |x|\right) \tag{2.24}$$

$\Theta(x)$ being the Heavyside function. The virial expansion then reads

$$\beta \mathcal{F}_{\text{exc}}[\{\rho_i\}] = -\frac{1}{2} \sum_{ij} \int_{-\infty}^{+\infty} dx \int_{x - \frac{L_i + L_j}{2}}^{x + \frac{L_i + L_j}{2}} dx' \rho_i(x) \rho_j(x'). \tag{2.25}$$

On the other hand, equation 2.21 in the limit of low density becomes

$$\Phi_{\text{exc}}(x) = -n_0(x) \ln[1 - n_1(x)] \approx n_0(x) n_1(x). \tag{2.26}$$

Then

$$\beta \mathcal{F}_{\text{exc}}[\{\rho_i\}] = \int_{-\infty}^{+\infty} dx n_0(x) n_1(x). \tag{2.27}$$

Comparing equations 2.25 and 2.27 we obtain the form of the weighted functions $\omega_i^{(\alpha)}$. To do so let us apply a functional derivative to the free energy in both equations

$$-c_{ij}(x - x') \equiv \frac{\delta^2 \beta \mathcal{F}_{\text{exc}}[\{\rho_i\}]}{\delta \rho_i(x) \delta \rho_j(x')} = -f_{ij}(x - x') \tag{2.28}$$

and the second functional derivative of equation 2.27, after some calculation, is given by

$$\begin{aligned} -c_{ij}(x - x') &\equiv \frac{\delta^2 \beta \mathcal{F}_{\text{exc}}[\{\rho_i\}]}{\delta \rho_i(x) \delta \rho_j(x')} = \\ &= \int dx'' \left\{ \omega_j^{(1)}(x' - x'') \omega_i^{(0)}(x - x'') + \omega_j^{(0)}(x' - x'') \omega_i^{(1)}(x - x'') \right\} \end{aligned} \tag{2.29}$$

In order to compare both results it is easier to perform a Fourier transform. From equation 2.28

$$\hat{c}_{ij}(q) = \int_{-\infty}^{\infty} dx e^{iqx} \Theta\left(\frac{L_i + L_j}{2} - |x|\right) = \frac{2}{q} \sin\left(q\frac{L_i + L_j}{2}\right) = \\ = \frac{2}{q}\left(\sin\frac{qL_i}{2}\cos\frac{qL_j}{2} + \sin\frac{qL_j}{2}\cos\frac{qL_i}{2}\right) \quad (2.30)$$

and the Fourier transform of equation 2.29

$$\hat{c}_{ij}(q) = \hat{\omega}_j^{(1)}(q)\hat{\omega}_i^{(0)}(q) + \hat{\omega}_j^{(0)}(q)\hat{\omega}_i^{(1)}(q) \quad (2.31)$$

where we have used the property that the Fourier transform of a convolution is equal to the product of the Fourier transform of the functions. Therefore we can identify

$$\hat{\omega}_i^{(0)}(q) = \cos\frac{qL_i}{2} \quad (2.32)$$

$$\hat{\omega}_i^{(1)}(q) = \frac{2}{q}\sin\frac{qL_i}{2}. \quad (2.33)$$

At this point we have already obtained the weighted functions in Fourier space. Applying an inverse Fourier transform we get them in real space

$$\omega_i^{(0)}(x) = \frac{1}{2}\delta\left(\frac{L_i}{2} - |x|\right) \quad (2.34)$$

$$\omega_i^{(1)}(x) = \Theta\left(\frac{L_i}{2} - |x|\right) \quad (2.35)$$

with δ the Dirac delta function.

These weighted functions lead to the exact functional of Percus for hard rods in 1D. However, no exact functionals can be found at higher dimensions. Several approximations and functionals exist for each system. An interesting method to obtain functionals is to start from the exact functional in 1D –or 0D in other systems– and add to the excess free-energy density additional terms which depends on new weighted densities. These in turn are calculated through convolutions between the density profiles and one-particle weights which integrals give the rest of fundamental measures in higher dimensions. This method, combined with the dimensional crossover criterion, allows us to fix the final functional form of the free-energy density functional. The dimensional crossover guarantees that functionals of $D-1$ dimensions emerge from the functionals of D dimensions when confining the density profile $\rho(\{x_1, ..., x_D\}) \to \rho(\{x_1, ..., x_{D-1}\})\delta(x_D)$. The important point is that functionals fulfilling this crossover criterion describe strongly inhomogeneous systems much better.

2.4 FUNCTIONAL FOR 2D HARD RODS IN ZWANZIG APPROXIMATION

In this thesis we mainly study systems of confined hard rods in 2D and at high densities. As mentioned in the previous section, no exact functional exists for this kind of system so some approximations have to be made. Our choice has been a functional in the Zwanzig approximation: rods can only be oriented in two perpendicular directions, for example along x and y axes. This may seem a strong simplification but we should notice that ordered phases at intermediate and high densities are mainly composed of particles pointing in the same direction –nematic, smectic, columnar, crystal– or two perpendicular directions –tetratic–. Furthermore the main advantage of the Zwanzig approximation is that the Mayer function can be decomposed in a finite set of weighted functions with the free energy functional fulfilling dimensional crossover (*49*, *50*).

Within this approximation a system of hard rods with length L and width σ has the following Mayer function

$$f_{ij}(\mathbf{r}) = -\Theta\left(\frac{\sigma_x^i + \sigma_x^j}{2} - |x|\right)\Theta\left(\frac{\sigma_y^i + \sigma_y^j}{2} - |y|\right) \tag{2.36}$$

where we have defined $\sigma_k^i \equiv \sigma + (L-\sigma)\delta_{ik}$ as the size of species $i = \{x, y\}$ (with its main axis pointing to x or y) along the k-axis, with δ_{ik} the Kronecker delta.

The system of rods in the Zwanzig approximation is equivalent to a mixture of two species, rods with its long axis L pointing in the x direction and rods with its long axis along the y direction. In this way we define two local densities $\rho_\nu(\mathbf{r})$ with $\nu = \{x, y\}$ respectively. In two dimensions rectangles have as the fundamental measures their edge-lengths and area, and the excess part of the free energy density comes as (*49*)

$$\Phi_{\text{exc}}(\mathbf{r}) = -n_0(\mathbf{r})\ln\left[1 - n_2(\mathbf{r})\right] + \frac{n_{1x}(\mathbf{r})n_{1y}(\mathbf{r})}{1 - n_2(\mathbf{r})} \tag{2.37}$$

with the weighted densities defined as

$$n_\alpha(\mathbf{r}) = \sum_{\nu=\{x,y\}} \left[\rho_\nu * \omega_\nu^{(\alpha)}\right](\mathbf{r}). \tag{2.38}$$

Then, proceeding in the same way as in the previous section, it is easy to obtain the weighted functions

$$\omega_\nu^{(0)}(\mathbf{r}) = \frac{1}{4}\delta\left(\frac{\sigma_x^\nu}{2} - |x|\right)\delta\left(\frac{\sigma_y^\nu}{2} - |y|\right) \tag{2.39}$$

$$\omega_\nu^{(1x)}(\mathbf{r}) = \frac{1}{2}\Theta\left(\frac{\sigma_x^\nu}{2} - |x|\right)\delta\left(\frac{\sigma_y^\nu}{2} - |y|\right) \tag{2.40}$$

$$\omega_\nu^{(1y)}(\mathbf{r}) = \frac{1}{2}\delta\left(\frac{\sigma_x^\nu}{2} - |x|\right)\Theta\left(\frac{\sigma_y^\nu}{2} - |y|\right) \tag{2.41}$$

$$\omega_\nu^{(2)}(\mathbf{r}) = \Theta\left(\frac{\sigma_x^\nu}{2} - |x|\right)\Theta\left(\frac{\sigma_y^\nu}{2} - |y|\right). \tag{2.42}$$

2.4.1 Chemical potentials

In the grand canonical ensemble the chemical potential of the species are determined by the reservoir. Together with volume and temperature they form the three independent and constant thermodynamic variables. We look for a solution of the problem at fixed values of these two parameters. In order to do so we put the system in contact with an infinite reservoir that can interchange particles with our system. If this thermodynamic bath corresponds to a uniform fluid we have that the total density $\rho = \rho_x + \rho_y$, and the packing fraction $\eta = \rho L\sigma$ does not depend on spatial variables. The fraction of particles of each species can be defined through an orientational order parameter $Q \in [0, 1]$

$$\rho_x = \frac{\rho}{2}(1+Q), \quad \rho_y = \frac{\rho}{2}(1-Q). \tag{2.43}$$

If $Q \neq 0$ the reservoir will be in a nematic phase. Using the expression for the total free energy density

$$\Phi = \sum_\nu \rho_\nu [\ln \rho_\nu - 1] - n_0 \ln(1-n_2) + \frac{n_{1x}n_{1y}}{1-n_2} \tag{2.44}$$

where the weighted functions for uniform fluids are

$$n_0 = \rho_x + \rho_y = \rho \tag{2.45}$$

$$n_{1x} = \frac{\rho}{2}[L + \sigma + (L-\sigma)Q] \tag{2.46}$$

$$n_{1y} = \frac{\rho}{2}[L + \sigma - (L-\sigma)Q] \tag{2.47}$$

$$n_2 = \eta = \rho L\sigma. \tag{2.48}$$

We arrive at the following expression for the total free energy density $\Phi = \Phi_{id} + \Phi_{exc}$

$$\Phi = \rho\left(\ln\rho - 1 + \frac{1}{2}\left[(1+Q)\ln\left(\frac{1+Q}{2}\right) + (1-Q)\ln\left(\frac{1-Q}{2}\right)\right] - \ln(1-\eta) + \frac{\eta}{4(1-\eta)}\left[(\kappa+\kappa^{-1}+2) - (\kappa+\kappa^{-1}-2)Q^2\right]\right). \quad (2.49)$$

The minimization of Φ with respect to Q gives the following equation, which should be solved to find the equilibrium value of Q

$$Q = \frac{1 - e^{-y(\kappa+\kappa^{-1}-2)Q}}{1 + e^{-y(\kappa+\kappa^{-1}-2)Q}}. \quad (2.50)$$

In this expression we have defined $y \equiv \eta/(1-\eta)$. Then the chemical potentials $\beta\mu_\nu = \partial\Phi/\partial\rho_\nu$ can be calculated from

$$\beta\mu_x = \beta\mu^{(0)} + \ln[1+Q] - \frac{\eta}{2(1-\eta)}\left(\kappa+\kappa^{-1}-2\right)\left[\frac{\eta Q}{2(1-\eta)} + 1\right]Q \quad (2.51)$$

$$\beta\mu_y = \beta\mu^{(0)} + \ln[1-Q] - \frac{\eta}{2(1-\eta)}\left(\kappa+\kappa^{-1}-2\right)\left[\frac{\eta Q}{2(1-\eta)} - 1\right]Q \quad (2.52)$$

with

$$\beta\mu^{(0)} = \ln\left[\frac{\rho}{2(1-\eta)}\right] + \frac{\eta}{1-\eta} + \frac{\eta(2-\eta)}{4(1-\eta)^2}(\kappa+\kappa^{-1}+2). \quad (2.53)$$

However, it can be shown that both expressions are equal at equilibrium and $\mu_x = \mu_y$ in all different phases.

2.4.2 Conjugate gradients method

Let us recover the grand potential

$$\Omega[\{\rho_\nu\}] = \mathcal{F}[\{\rho_\nu\}] + \sum_\nu \int_{\mathcal{A}} d\mathbf{r}\rho_\nu(\mathbf{r})\left[V^\nu_{ext}(\mathbf{r}) - \mu_\nu\right] \quad (2.54)$$

where the free energy functional is composed of an excess part, given by equation 2.37, and the ideal part

$$\Phi_{id}(\mathbf{r}) = \sum_\nu \rho_\nu(\mathbf{r})\left[\ln\rho_\nu(\mathbf{r}) - 1\right]. \quad (2.55)$$

As explained before, DFT guarantees that the equilibrium density profiles are those which minimize the grand potential. In our case the functional derivatives take the explicit form

$$\beta\frac{\delta\Omega[\{\rho_\nu\}]}{\delta\rho_\nu(\mathbf{r})} = \ln\rho_\nu(\mathbf{r}) + \sum_\alpha \phi^\nu_\alpha(\mathbf{r}) + \beta\left[V^\nu_{ext}(\mathbf{r}) - \mu_\nu\right] \quad (2.56)$$

with $\alpha = \{0, 1x, 1y, 2\}$ and where we have defined

$$\phi_\alpha^\nu(\mathbf{r}) \equiv \left[\frac{\partial\Phi}{\partial n_\alpha} * \omega_\nu^{(\alpha)}\right](\mathbf{r}). \tag{2.57}$$

Imposing $\delta\Omega/\delta\rho_\nu = 0$ we get an integral equation for $\rho(\mathbf{r})$ which cannot be solved analytically

$$\rho_\nu(\mathbf{r}) = \exp\left[\sum_\alpha \phi_\alpha^\nu(\mathbf{r}) + \beta\left(V_{ext}^\nu(\mathbf{r}) - \mu_\nu\right)\right]. \tag{2.58}$$

We need to solve it numerically. Several methods can be applied, such as fixed point iteration. But taking into account that the free energy functional may present some local minima, a good choice is the conjugate gradients method which is explained in appendix A.

2.5 WHY DFT?

There are several reasons why we use DFT and in particular the FMT version developed here. Since we study systems of large number of particles the number of available microstates is enormous and the calculations of the partition function is impracticable. For the same reason simulations are of limited practical value because it would take too long to reach equilibrium and obtain accurate averages.

Among the different theories for liquid crystals, DFT provides a very appropriate framework to study inhomogeneous fluids. In this sense it is well known that DFT deals accurately with fluids under confinement and in the presence of walls (*9*, *36*), situations that are analysed in the present thesis. In particular FMT is an ideal approximation to construct functionals for hard rods because it is based on the geometrical properties of particles.

However, one should also keep in mind some aspects. For example the theorem that the grand potential exhibits a minimum for the equilibrium density profile –equation 2.3– is only valid for the exact free energy functional. When the functional is approximate the accuracy of the results will depend on how the functional is constructed.

Another aspect is the treatment of phase transitions. Depending on the approximation used to build the functional one may obtain different results. But when using mean field functionals it is frequent to overestimate the strength of phase transitions. Because mean field theories do not account for fluctuations sometimes these functionals predict transitions that may vanish when fluctuations are introduced.

The next chapter is a continuation of this section. We will study in detail the performance of FMT in confined systems from a rigorous point of view. By comparison with exact results and simulations we will show how FMT performs at different levels, from equations of state to particle correlations.

3 PERFORMANCE OF FMT. SQUARES IN NARROW CHANNELS

3.1 INTRODUCTION

The aim of the present chapter is twofold. First, the study of two-dimensional hard particles under high confinement is interesting by itself since confinement is known to affect the usual –bulk– behaviour of a system of particles. In particular, the system of study will be hard squares in a channel, and we mentioned high confinement because in the channel we assume that only two particles can fit in the transverse direction at most. The second aim of the chapter –and the main one in the present thesis– is to study the performance of FMT at bulk and under confinement conditions for square particles. It has been proved before that functionals of hard spheres and disks fulfilling the dimensional crossover property are very accurate in high confinement (*51*–*55*) and that they accurately predict the properties of hard-sphere crystals (*56*) and fluid-crystal interfaces (*57*, *58*). However, there is no evidences for such accuracies in the case of other anisotropic particles. Consequently, in this chapter we will test our FMT to understand its strengths and weak points, and this will serve as a guide to interpret results in future chapters, to know what is trustable and what we should be careful with.

To test the performance of our FMT we study the thermodynamics (equations of state), structure (density profiles) and correlation (pair correlation functions) of the confined fluid and check these results against the (exact) transfer matrix method (TMM) solution and Monte Carlo (MC) simulations. While FMT results have been obtained by the author of the present thesis, TMM and MC have been carried out by collaborators and, consequently, these methods will only be described in a general way.

The system of study is depicted in figure 3.1. Hard-square particles of side σ are confined in a narrow channel with parallel hard walls of section H. The Zwanzig approximation is used, meaning that particles are always in the same orientation because of the symmetry of squares. Two different channels, corresponding to two different symmetries of the external potential representing the walls, will be studied. A channel with walls parallel to one of the sides of the particles –panel (a)–, and a channel with walls at an angle of 45° with respect to the particle sides. Note that this latter case is equivalent to that of confined rhombuses, as depicted in panel (b). The possible channel sizes are those for which no more than two particles can fit in the transverse direction of the chan-

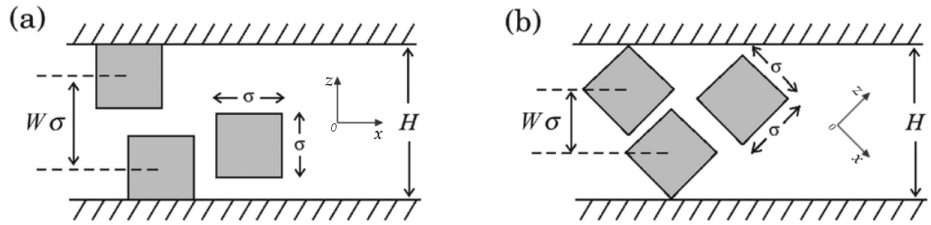

Figure 3.1: Schematic of the two channels studied. (a) Channel with walls parallel to one of the sides of the squares. (b) Channel with walls at an angle of 45° with respect to the particle sides. σ is the side-length of the squares, H the channel thickness and W is the length available to the centres of mass of the squares in the transverse direction. The frames of reference are also represented for each case.

nel. This means $2\sigma \leqslant H < 3\sigma$ for the parallel case and $\sqrt{2}\sigma \leqslant H < 3\sqrt{2}\sigma$ for the oblique one.

One could expect that, as the channel thickness becomes larger and the bulk limit is approached, the results will become progressively worse. For the purpose of evaluating the predictive power of the present functional in the description of bulk systems, a minimization using a Gaussian parametrization was performed and the resulting equations of state were checked against Molecular Dynamics simulations (59). Alternatively, the equation of state from the Percus-Yevick (PY) approximation, both from virial and compressibility routes, were also obtained and compared with simulations. Finally, pair correlations functions were calculated from (i) the same PY approximation, (ii) the Ornstein-Zernike relation together with the direct correlation function obtained from the FMT functional, and (iii) the test-particle route (which involves functional minimization with a particle fixed at the origin).

3.2 FMT FOR PARALLEL HARD SQUARES

In the present system the theory is presented simpler than the one developed in section 2.4 because squares have only one length (side σ) and there is only one component in the Zwanzig approximation. The weighted functions are

$$\omega^{(0)}(\mathbf{r}) = \frac{1}{4}\delta\left(\frac{\sigma}{2} - |x|\right)\delta\left(\frac{\sigma}{2} - |y|\right) \tag{3.1}$$

$$\omega^{(1x)}(\mathbf{r}) = \frac{1}{2}\Theta\left(\frac{\sigma}{2} - |x|\right)\delta\left(\frac{\sigma}{2} - |y|\right) \tag{3.2}$$

$$\omega^{(1y)}(\mathbf{r}) = \frac{1}{2}\delta\left(\frac{\sigma}{2} - |x|\right)\Theta\left(\frac{\sigma}{2} - |y|\right) \tag{3.3}$$

$$\omega^{(2)}(\mathbf{r}) = \Theta\left(\frac{\sigma}{2} - |x|\right)\Theta\left(\frac{\sigma}{2} - |y|\right) \tag{3.4}$$

the weighted densities having the following explicit form

$$n_0(\mathbf{r}) = \frac{1}{4}\left[\rho\left(x-\frac{\sigma}{2},y-\frac{\sigma}{2}\right)+\rho\left(x-\frac{\sigma}{2},y+\frac{\sigma}{2}\right) +\rho\left(x+\frac{\sigma}{2},y-\frac{\sigma}{2}\right)+\rho\left(x+\frac{\sigma}{2},y+\frac{\sigma}{2}\right)\right] \tag{3.5}$$

$$n_{1x}(\mathbf{r}) = \frac{1}{2}\left\{\int_{x-\sigma/2}^{x+\sigma/2} dx'\left[\rho\left(x',y-\frac{\sigma}{2}\right)+\rho\left(x',y+\frac{\sigma}{2}\right)\right]\right\} \tag{3.6}$$

$$n_{1y}(\mathbf{r}) = \frac{1}{2}\left\{\int_{y-\sigma/2}^{y+\sigma/2} dy'\left[\rho\left(x-\frac{\sigma}{2},y'\right)+\rho\left(x+\frac{\sigma}{2},y'\right)\right]\right\} \tag{3.7}$$

$$n_2(\mathbf{r}) = \int_{x-\sigma/2}^{x+\sigma/2} dx' \int_{y-\sigma/2}^{y+\sigma/2} dy' \rho(x',y'). \tag{3.8}$$

The excess part of the free energy density can be expressed as

$$\Phi_{\text{exc}}(\mathbf{r}) = -n_0(\mathbf{r})\ln\left[1-n_2(\mathbf{r})\right] + \frac{n_{1x}n_{1y}(\mathbf{r})}{1-n_2(\mathbf{r})} \tag{3.9}$$

and the ideal part reads

$$\Phi_{\text{id}}(\mathbf{r}) = \rho(\mathbf{r})\left[\ln\rho(\mathbf{r})-1\right]. \tag{3.10}$$

The grand potential takes the form

$$\Omega[\{\rho\}] = \mathcal{F}[\{\rho\}] + \int_{\mathcal{A}} d\mathbf{r}\rho(\mathbf{r})\left[V_{\text{ext}}(\mathbf{r})-\mu\right] \tag{3.11}$$

with the external potential being defined by the channel. Depending on the situation we have two possibilities. If the channel walls are parallel to one of the square sides –figure 3.1(a)– the external potential will be

$$\beta V_{\text{ext}}(\mathbf{r}) = \begin{cases} 0, & \text{if } |z| \leqslant \dfrac{H-\sigma}{2}, \\ \infty, & \text{otherwise.} \end{cases} \tag{3.12}$$

But in the case where the channel walls are at an angle of 45° with respect to the particle sides –figure 3.1(b)– the potential takes the form

$$\beta V_{\text{ext}}(\mathbf{r}) = \begin{cases} 0, & \text{if } |z-x| \leqslant \dfrac{H}{\sqrt{2}}-\sigma, \\ \infty, & \text{otherwise.} \end{cases}. \tag{3.13}$$

Note that the frame of reference is always related to the squares –see figure 3.1– and located at the center of the channel. For this reason the potential in the oblique channel depends on both coordinates (x,z).

Because the external potential is hard, one can just ignore V_{ext} in the equations and impose $\rho(\mathbf{r}) = 0$ outside the channel, i.e. in the regions where the potential is ∞.

The derivative of the excess part of the free energy with respect to the weighted densities –equation 2.57– takes the explicit form

$$\phi_0(\mathbf{r}) = -\frac{1}{4}\ln\left\{\left[1-n_2\left(x-\frac{\sigma}{2},y-\frac{\sigma}{2}\right)\right]\times\left[1-n_2\left(x-\frac{\sigma}{2},y+\frac{\sigma}{2}\right)\right] \times\left[1-n_2\left(x+\frac{\sigma}{2},y-\frac{\sigma}{2}\right)\right]\times\left[1-n_2\left(x+\frac{\sigma}{2},y+\frac{\sigma}{2}\right)\right]\right\} \tag{3.14}$$

$$\phi_{1x}(\mathbf{r}) = \frac{1}{2}\int_{x-\sigma/2}^{x+\sigma/2} dx'\left[\frac{n_{1y}(x',y-\sigma/2)}{1-n_2(x',y-\sigma/2)}+\frac{n_{1y}(x',y+\sigma/2)}{1-n_2(x',y+\sigma/2)}\right] \tag{3.15}$$

$$\phi_{1y}(\mathbf{r}) = \frac{1}{2}\int_{y-\sigma/2}^{y+\sigma/2} dy'\left[\frac{n_{1x}(x',y-\sigma/2)}{1-n_2(x',y-\sigma/2)}+\frac{n_{1x}(x',y+\sigma/2)}{1-n_2(x',y+\sigma/2)}\right] \tag{3.16}$$

$$\phi_2(\mathbf{r}) = \int_{x-\sigma/2}^{x+\sigma/2} dx'\int_{y-\sigma/2}^{y+\sigma/2} dy'\left[\frac{n_0(x',y')}{1-n_2(x',y')}+\frac{n_{1x}n_{1y}(x',y')}{[1-n_2(x',y')]^2}\right]. \tag{3.17}$$

To finish this section, we also calculate the longitudinal pressure of the confined fluid as

$$\beta p = A^{-1}\left[\int_{\mathcal{A}} d\mathbf{r}\rho(\mathbf{r})\frac{\delta\beta\mathcal{F}[\rho]}{\delta\rho(\mathbf{r})}-\beta\mathcal{F}[\rho]\right] = A^{-1}\int_{\mathcal{A}} d\mathbf{r}\left[\frac{n_0(\mathbf{r})}{1-n_2(\mathbf{r})}+\frac{n_{1x}n_{1y}(\mathbf{r})}{(1-n_2(\mathbf{r}))^2}\right]. \tag{3.18}$$

3.3 TRANSFER MATRIX THEORY FOR CONFINED FLUIDS

As mentioned in the introduction we have focused our interest on channels that can hold two particles at most in the transverse direction, mainly because for these small systems the TMM can produce exact results. It is still a great challenge to extend the list of exactly solvable models in the direction of confined fluids starting from the one-dimensional Tonks gas (*60*), where the particles interact with only a few neighbours. The problem arises from the appearance of additional positional freedoms, which gives rise to increasing number of interactions. Therefore the successful one-dimensional methods must be extended for pair interactions with a finite number of neighbours. Along this line the transfer matrix method has proved to be very successful to get exact results for very narrow pores (*61*).

Although the formalism of the transfer matrix method is transparent, the equations for the eigenfunctions and eigenvalues (from which we can obtain the thermodynamical and structural properties of the fluid) can be obtained in analytic form only for a few model systems such as the classical spin models on one- and two-dimensional lattices (*62*, *63*), one-dimensional gases of

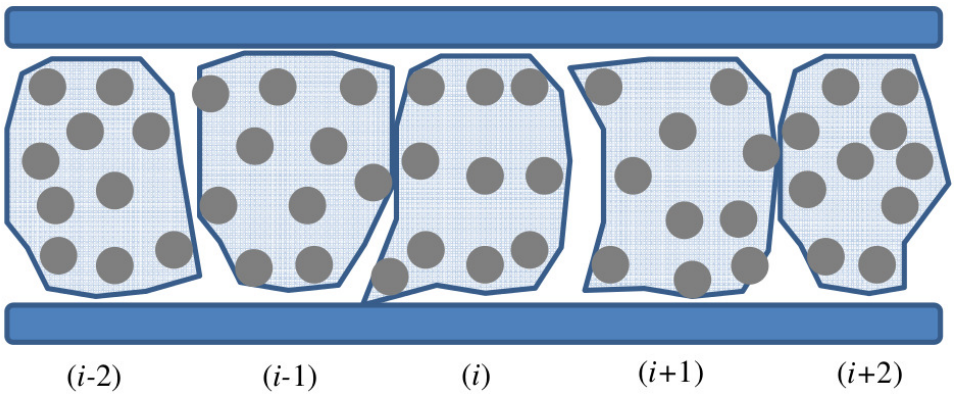

Figure 3.2: The smallest separable clusters (m-mer) of the confined fluids.

some rotors (*64*, *65*) and the quasi-one-dimensional fluid of hard rhombuses in very narrow pores (*66*). However, the equation for the eigenfunctions has been solved numerically for several continuum models in the past, where only nearest neighbour interactions are present. The most important examples are the system of hard disks confined between two parallel walls (*61*, *66*–*69*) and that of hard spheres in a cylindrical channel (*61*, *70*, *71*). The application of the transfer matrix method has proved to be a formidable task for those systems, where the particles can interact with $m > 1$ neighbours. The first numerical transfer matrix solution for parallel hard squares confined between soft walls – periodic boundary walls–, where both first- and second-neighbour interactions are present, is due to Percus and Zhang (*72*). Recently the method has been applied successfully in the presence of hard walls for both hard disks (*73*) and parallel hard squares (*74*).

The basic idea of TMM is to find the configurational part of the partition function as a trace of the matrix products of low dimensional matrices. In the case of 2D confinement, where particles are confined between two parallel walls –see figure 3.2–, it is useful to change from the canonical to the isobaric ensemble, where the longitudinal pressure p is chosen to be the independent variable. In this new ensemble, one can perform changes of variables in particle positions and find the size of the minimal cluster (m) to simplify the isobaric partition function as much as possible.

Without going into details, one can show that the configurational part of the partition function can be written as

$$Z_{NpT} = \int d\chi_1 \cdots \int d\chi_{N/m} K(\chi_1, \chi_2) \cdots K(\chi_{N/m}, \chi_1) = \mathrm{Tr}(K^{N/m}) \qquad (3.19)$$

where the kernel function is defined as

$$K(\chi_i, \chi_{i+1}) = \int_0^\infty e^{-\beta[U(\chi_i, \chi_{i+1}, X_{i,i+1}) + pHX_{i,i+1}]} dX_{i,i+1}. \qquad (3.20)$$

Here χ_i is a short notation for all the internal positional variables of the i-*th* cluster, i.e. the m pieces of transverse coordinates and $m-1$ pieces of relative longitudinal coordinates of the m particles in the i-*th* cluster. Furthermore, $X_{i,i+1}$ is the difference between the longitudinal coordinates of the centres of the neighbouring (i-*th* and $i+1$-*th*) clusters, and $U(\chi_i, \chi_{i+1}, X_{i,i+1})$ is the potential energy of particles from the i-*th* and $i+1$-*th* clusters, which is infinity if any two particles overlap and zero otherwise. We also mention that the matrix product is defined as $K^2(\chi_{i-1}, \chi_{i+1}) = \int d\chi_i K(\chi_{i-1}, \chi_i) K(\chi_i, \chi_{i+1})$.

In the derivation of equation 3.19 we emphasize that the size of the minimal cluster is equal to the number of possible interactions of a chosen particle with the other ones if the positional order of the particles are kept fixed along the longitudinal direction ($x_1 < x_2 \cdots < x_N$). This is equivalent to the statement that all particles can interact with $2m$ neighbours only (m neighbours in forward and m neighbours in backward directions along the pore). In addition to this, the χ_1 and $\chi_{N/m+1}$ coordinates are the same as in equation 3.19. The size of the minimal cluster depends on the particle-particle interaction and the width of the channel. Figure 3.2 represents a case where a system can be divided into clusters of ten particles. Since the result of the trace operation in equation 3.19 does not depend on the basis used, it is worth determining the eigenvalues and the eigenfunctions of the kernel function K to obtain the partition function, as follows

$$Z_{NpT} = \mathrm{Tr}\left(K^{N/m}\right) = \sum_n \lambda_n^{N/m} \tag{3.21}$$

where λ_n and Ψ_n are the n*th* eigenvalue and eigenfunction of the following integral equation

$$\int d\chi_{i+1} K(\chi_i, \chi_{i+1}) \Psi_n(\chi_{i+1}) = \lambda_n \Psi_n(\chi_i). \tag{3.22}$$

As can be seen from equation 3.20, the kernel function is not symmetric for wider channels because a cluster formed by more than one particle is generally not symmetric under reflection, and if we interchange the i-*th* and $i+1$-*th* clusters the opposite sides of the clusters will interact with each other. Therefore we can get a second eigenvalue equation in the following form

$$\int d\chi_i K(\chi_i, \chi_{i+1}) \overline{\Psi}_n(\chi_i) = \overline{\lambda}_n \overline{\Psi}_n(\chi_{i+1}). \tag{3.23}$$

It can be proved that $\overline{\Psi}_n(\chi_i)$ can be expressed from $\Psi_n(\chi_i)$ with some coordinate changes and $\overline{\lambda}_n = \lambda_n$. One can see from equation 3.23 that only the largest eigenvalue λ_0 contributes to the partition function in the thermodynamic limit ($N \to \infty$), i.e. the Gibbs free energy can be written as

$$\frac{\beta G}{N} = -\frac{1}{m} \log \lambda_0. \tag{3.24}$$

The equation of state of the system can be obtained from the relation between the longitudinal dimension of the channel L and the longitudinal pressure, which is given by $p = -\frac{1}{H}\frac{\partial F}{\partial L}$, which corresponds to the following equation in the (N, p, T) ensemble:

$$\rho^{-1} = \frac{\partial G/N}{\partial p} \tag{3.25}$$

where ρ is the density ($\rho^{-1} = HL/N$).

We can also gain some information about the positional distribution of the particles from the eigenfunction of the largest eigenvalue, because $f(\chi) = \Psi_0(\chi)\overline{\Psi}_0(\chi)$ represents the normalized probability distribution function of the cluster with m particles ($\int d\chi f(\chi) = 1$).

The eigenvalue equation 3.23 simplifies substantially for parallel hard squares –see (*74*)–. For channel-widths H between σ and 2σ equation 3.23 reduces to the Tonks equation for one-dimensional hard rods (*60*). In the case of wider channels ($H > 2\sigma$), the number of independent positional variables of the eigenfunctions is $2m-1$ for a cluster of m particles, because m coordinates give the positions of m particles along the transverse direction, while $m-1$ relative distances are needed for giving the relative positions of the particles along the pore. This means that dimers form the clusters and Ψ_0 depends on two transverse coordinates (z_1, z_2) and one longitudinal distance x for $2\sigma < H < 3\sigma$. In general the size of the minimal cluster is equal to the number of interacting neighbours of a given particle, which means that $m = 1$ for first neighbour interactions, $m = 2$ for first and second neighbour interactions, and so on. In general one can conclude that the minimal size of the cluster is equal to i and $\Psi_0(z_1, \ldots, z_i; x_1, \ldots, x_{i-1})$ for $i\sigma < H < (i+1)\sigma$, where i is an integer number. At this point it is important to note that the present transfer matrix method cannot be extended for bulk systems, because the number of neighbours of a given particle and the size of the minimal cluster diverge with increasing channel width.

3.4 PHASE BEHAVIOR AND CORRELATIONS IN BULK

In this section the bulk behaviour of our FMT functional is studied. However, the results presented here have not been obtained by the author of the present thesis but by coauthors in the context of our collaborative work (*75*). However, I believe these results should be mentioned here in order to complete the study of the functional performance in the bulk part and, consequently, to let us discuss results of future chapters regarding bulk conditions.

The study of parallel hard squares at bulk was based on a Gaussian parametrization of the density profile

$$\rho(\mathbf{r}) = \nu \prod_{n=1}^{D} \left[\sqrt{\frac{\alpha}{\pi}} \sum_{k=-\infty}^{\infty} e^{-\alpha(x_n - kd)^2} \right] \tag{3.26}$$

where $(x_1, x_2) \equiv (x, z)$, $D = 1, 2$ is the dimensionality of the inhomogeneities ($D = 1$ for columnar and $D = 2$ for crystal phases), d is the lattice period, i.e. the distance between layers –in the columnar phase (Col)– or the simple square lattice parameter –in the crystal phase (Cry)–. The prefactor ν represents the occupancy probability –one minus the fraction of vacancies– for Cry, while it is equal to $\rho_0 d$ for the Col phase, where ρ_0 is the mean density per unit cell. The free energy density $\beta\mathcal{F}[\rho]/A$ is minimized with respect to the Gaussian parameter α and the period d for a fixed mean density ρ_0. Note that, in the crystal, the mean packing fraction and the occupancy probability are related through $\eta_0 = \rho_0\sigma^2 = \nu\sigma^2/d^2$.

The use of a Gaussian instead of a free parametrization could seem a bit simplistic. However, we should note that the present parametrization was recently tested in (*76*) where it was compared with the results obtained from the free-minimization of the present functional. The authors showed that, apart form minor deviations –small underestimation of the fraction of vacancies and small deviations for the predicted Col-Cry coexistence densities–, the present approximation works remarkable well. Later in this section the results obtained from the minimization will be compared with the simulation results of (*59*).

The second aim of the present section is the study of bulk correlations through the pair correlation function $g(\mathbf{r})$ –with $\mathbf{r} = (x, z)$–. We use the FMT functional and follow two different routes. First, we use the Ornstein-Zernike (OZ) relation, with the direct correlation function obtained from the second functional derivative of the FMT functional as an input, and predict the function $g_{fmt-oz}(\mathbf{r})$. Second, we use the test-particle route (TP): a hard square is fixed at position $(0, 0)$ which acts as an external potential on the rest of the particles. The FMT functional is then minimized to obtain $g_{fmt-tp}(\mathbf{r})$. As a third and last step, we have used the Percus-Yevick (PY) approximation which, along with the OZ relation, gives an integral equation for the cavity function $y(\mathbf{r}) = g(\mathbf{r})e^{\beta v(\mathbf{r})}$ (with $v(\mathbf{r})$ the hard-core pair potential)

$$y(\mathbf{r}) = 1 + \rho \iint_{\mathcal{A}_0} y(\mathbf{r}')\,d\mathbf{r}' - \rho \iint_{\mathcal{A}_\mathbf{r} \cap (\mathcal{A} \setminus \mathcal{A}_0)} y(\mathbf{r}')y(\mathbf{r} - \mathbf{r}')\,d\mathbf{r}' \tag{3.27}$$

where ρ is the number density, A is the total area of the system, A_0 is the area of a square of dimensions $\sigma \times \sigma$ located at the origin, and $A_\mathbf{r}$ is the area of a square of the same size located at $\mathbf{r}$. Then we can compare the FMT results with those from the PY approximation, $g_{py}(\mathbf{r})$. As we will see, the FMT for hard squares (and also for hard cubes) gives pair correlations different from the PY result. This scenario is different for hard spheres, where the direct correlation function obtained from FMT is the same as that from the PY approximation.

Note that the cavity function satisfies the relation

$$y(\mathbf{r}) = \begin{cases} -c(\mathbf{r}), & \mathbf{r} \in \mathcal{A}_0 \\ g(\mathbf{r}), & \mathbf{r} \in \mathcal{A} \setminus \mathcal{A}_0 \end{cases} \tag{3.28}$$

where $c(\mathbf{r})$ is the direct correlation function. Equation 3.27 was solved numerically for different values of packing fractions $\eta = \rho\sigma^2$, using the fixed-point algorithm. With the function $y(\mathbf{r})$, the inverse structure factor can be obtained by calculating the integral inside the core of $y(\mathbf{r})$, weighted with cosines functions:

$$S^{-1}(q_x, q_z) = 1 - 4\eta \int_0^1 dx \int_0^1 dz \cos(q_x x) \cos(q_z z) y(x, z). \tag{3.29}$$

The inverse structure factor will be used to look for instabilities of the fluid phase with respect to density modulations with crystalline symmetry.

From $g_{py}(\mathbf{r})$ one can calculate the equation of state using the virial route

$$\beta p_v = \rho + \frac{\rho^2}{4} \int_{\mathcal{P}} \Delta g(x, z) dl \tag{3.30}$$

where the line integral is taken over the perimeter $\mathcal{P}$ of a square centered at $(0, 0)$, while the integrand is the jump of the pair correlation function at the perimeter –which, according to the PY approximation, is zero inside the core–. Also, the equation of state can be calculated from the compressibility route:

$$\frac{\partial \beta p_c}{\partial \rho} = 1 - \rho \hat{c}(0, 0) \tag{3.31}$$

where $\hat{c}(0, 0) = \int_{\mathcal{A}_0} c(x, y) dx dy$ is the Fourier transform of the direct correlation function at zero wave-vector.

Note that $\Delta g(\mathbf{r}) = -c(\mathbf{r})$ when $\mathbf{r} \in \mathcal{P}$, which follows from the continuity of the cavity function $y(\mathbf{r}) = g(\mathbf{r}) - c(\mathbf{r})$ along the perimeter. Substituting this equation in equation 3.30, together with the FMT expression for the direct correlation function

$$-\eta c_{fmt}(x, z) = \left[\xi + \xi^2(2 - x - z) + \xi^2(1 + 2\xi)(1 - x)(1 - z)\right] \times \\ \times \Theta(1 - x)\Theta(1 - z) \tag{3.32}$$

(with $\xi \equiv \eta/(1 - \eta)$ and where x and z are in units of σ), one can obtain the analytical result

$$\beta p_v = \frac{\rho}{(1 - \eta)^2} \tag{3.33}$$

which coincides with the pressure obtained from the compressibility route of equation 3.31. This result demonstrates that the FMT is consistent with respect to the route used.

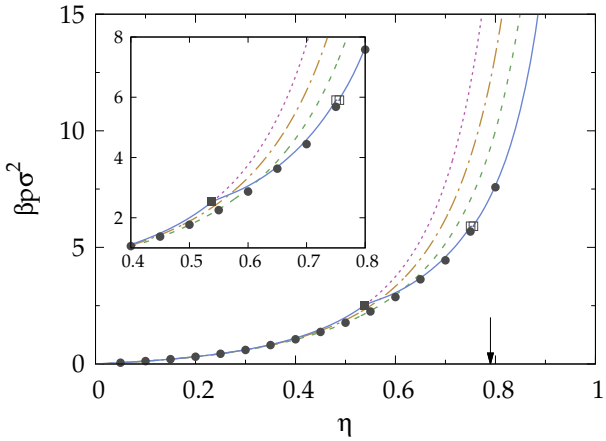

Figure 3.3: Equation of state of parallel hard squares as obtained from the PY virial route (green dashed curve), compressibility route (brown dot-dashed curve), and FMT approach (blue solid curve). The purple dotted curve shows the equation of state of the metastable fluid according to FMT (which coincides with the SPT). Filled circles represent MD results from (*59*), which predict a fluid-to-crystal transition at a value of packing fraction shown with an arrow. The filled square represents the fluid-to-columnar second-order transition, while open squares represent the coexistence densities at the first-order columnar-to-crystal transition, both predicted by FMT. The inset is a detail of the main figure.

Figure 3.3 presents all the equations of state obtained from FMT, PY virial route (PYV), PY compressibility route (PYC) and MD simulations from (*59*). The FMT (blue solid line) predicts a bifurcation from the fluid to the Col and Cry phases at the same packing fraction ($\eta = 0.538$), with the Col phase more stable than the Cry phase up to $\eta \sim 0.75$, at which the Cry and Col free-energy branches cross. The Col-Cry transition is of first order but weak, with coexisting densities $\eta_{\mathrm{Col}} = 0.726$ and $\eta_{\mathrm{Cry}} = 0.730$ obtained from a free minimization –see (*76*)–, while the corresponding values from a Gaussian parametrization are 0.750 and 0.756, respectively. An interesting behaviour of parallel hard squares and cubes is the relatively large fraction of vacancies –about 15% for squares– that the system can accept at the bifurcation point. Recent MC and MD studies show that this is indeed the case; in fact, these anisotropic particles (with frozen or free orientations) crystallise with such a large fraction of vacancies (as compared with HS) that it has been proposed that the Cry phase is stabilised by vacancies (*77*, *78*). By contrast, the FMT does not predict correctly the stability of the Cry phase with respect to the Col phase in the range $0.538 < \eta < 0.750$ –the Col phase should be unstable due to long-wavelength density fluctuations not taken into account in density-functional theory–. Also, the precise location of the bifurcation point to the Cry phase is not correct: simulations predict a

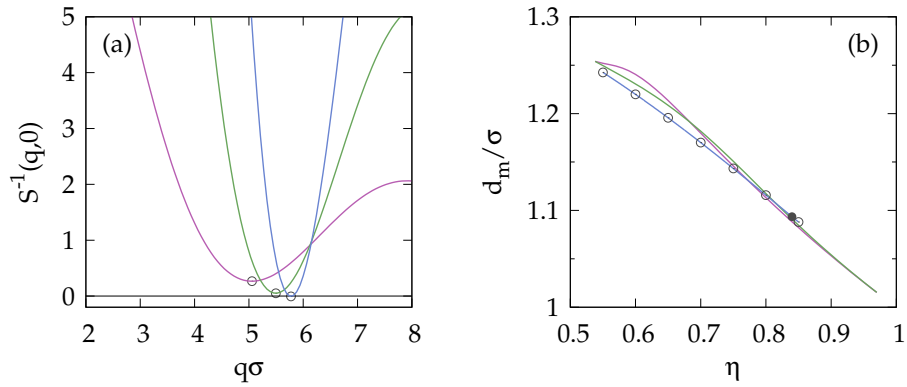

Figure 3.4: (a) PY inverse structure factor evaluated in the neighbourhood its absolute minimum as a function of the wavenumber $q\sigma$ for $\eta = 0.55$ (purple curve), 0.75 (green curve) and 0.85 (blue curve). (b) Lattice parameters d_m/σ (with open circles joined by blue lines) corresponding to the absolute minima of $S^{-1}(q,0)$ as a function of η. Filled circle corresponds to the estimated fluid-to-crystal transition using the PY approximation. Green and purple curves correspond to the periods of columnar and crystal phases, respectively, as obtained from the FMT approach.

value of about 0.79, while FMT gives a value of 0.538. However, if we identify the Col phase as a fluid with lower spatial symmetry, its equation of state compares fairly well with that given by MD simulation for $\eta > 0.6$. Also, the transition to the Cry phase given by the theory ($\simeq 0.75$) and simulations ($\simeq 0.79$) are similar. The major differences are restricted to the interval $0.5 < \eta < 0.6$ about the bifurcation point. For $\eta > 0.75$, above the Col-Cry transition predicted by FMT, the agreement is perfect. This is due to the fact that the FMT recovers cell theory, which is known to describe the high-density crystalline phase remarkably well. The PYV equation of state (green dashed curve) is very close to that obtained from MD simulation (solid circles) up to $\eta \approx 0.65$, beyond which the pressure is overestimated. Also, it exhibits better performance than FMT in the interval $0.5 < \eta < 0.6$ about the bifurcation –see figure 3.3–. Finally the equation of state from PYC (brown dot-dashed line) is always above that obtained from PYV. Then we can conclude that the PYC equation of state is worse than that from PYV compared with MD results.

Also the fluid phase instability with respect to Cry-phase fluctuations was studied using PYC by calculating the divergence of the inverse structure factor calculated from equation 3.29. Figure 3.4(a) shows a zoom of $S^{-1}(q,0)$ close to the value q^* where it becomes zero for three different packing fractions. The PY approach predicts an instability at $\eta \approx 0.84$, above that predicted by MD, with a value of lattice parameter at bifurcation of $d/\sigma \sim 1.09$. However, this result should be taken with some care because at these high values of η the function $g(\mathbf{r})$ becomes negative at some points –around some minima of $g(\mathbf{r})$–. Figure

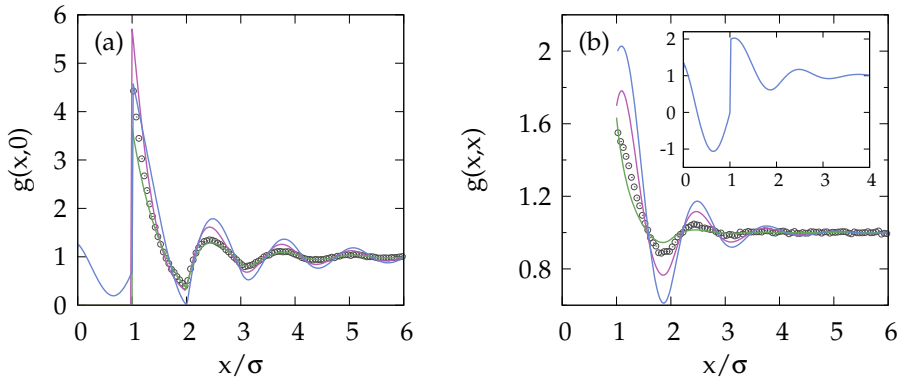

Figure 3.5: (a) Pair correlation functions $g_{fmt-oz}(x,0)$ (blue curves), $g_{py}(x,0)$ (green curves), and $g_{fmt-tp}(x,0)$ (purple curves) for $\eta = 0.5$ along the normal direction. Symbols show MC simulation results. (b) Pair correlation functions $g_{\alpha}(x,x)$ along the diagonal direction for the same value of η, as obtained from the same theories and with meaning of lines and symbols as in panel (a). Inset: function $g_{fmt-oz}(x,x)$ including also its value inside the core.

3.4(b) shows the lattice parameters obtained from FMT –for the Col (green curve) and Cry (purple curve) phases– and the value of $d_m \equiv 2\pi/q_m$ (open circles), where q_m is the wavenumber corresponding to the absolute minima of $S^{-1}(q,0)$ with respect to q. We see that the results from both theories are similar in the neighbourhood of the fluid-to-crystal transition predicted by PY (solid circle).

Now we test pair correlation functions. As a reference, standard MC simulations were conducted on systems of $1-2\times10^3$ squares, with equilibration and averaging number of MC steps of order 10^6. The pair correlation function $g_{fmt-oz}(\mathbf{r})$ was calculated from FMT using the equation 3.32 and the OZ relation. As an example, figure 3.5 shows the case $\eta = 0.5$ (blue curves) just before the fluid-to-columnar bifurcation point. Also, the test-particle route and the PY approximation from equation 3.27 were used to calculate $g_{fmt-tp}(\mathbf{r})$ (purple curves) and $g_{py}(\mathbf{r})$ (green curves), respectively. MC simulations results are also shown with symbols. We should note that the MC results of pair correlations at contact were calculated by extrapolating to contact. Panels (a) and (b) show the functions $g(x,0)$ and $g(x,x)$, respectively along the normal direction from the centre of the square and along the diagonal direction. As can be seen from the figure, the FMT-OZ approximation overestimates bulk correlations, since the damped oscillations have a larger amplitude and decay more slowly. Similarly, the FMT test-particle route overestimates correlations, but to a lesser extent. It is interesting to note that although the FMT-OZ approach gives a contact value $g_{fmt-oz}(\sigma,0)$ similar to that of simulations, the corner value $g_{fmt-oz}(\sigma,\sigma)$ is overestimated. By contrast, the test-particle route gives a value $g_{fmt-tp}(\sigma,0)$

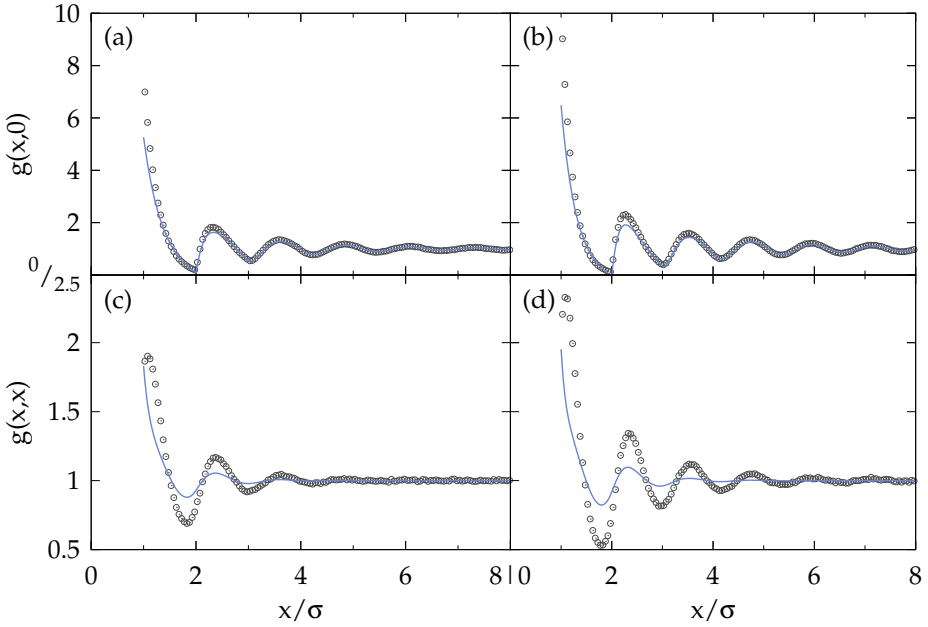

Figure 3.6: Pair correlation functions $g_{py}(x,0)$ [(a) and (b)], and $g_{py}(x,x)$ [(c) and (d)] for $\eta = 0.6$ [(a) and (c)], and $\eta = 0.65$ [(b) and (d)]. Symbols are the corresponding MC results.

which overestimates that of simulations, while $g_{fmt-tp}(\sigma,\sigma)$ is very similar to simulations. The function $g_{fmt-oz}(\mathbf{r})$ is different from zero inside the core, which shows that the FMT direct correlation function is different from that obtained from the PY approximation, a result confirmed from $g_{py}(\mathbf{r})$ –see green curves–. We can see that the PY approximation gives remarkably good results for the pair correlation function, except for the value at $(\sigma,0)$, which is underestimated, while $g_{py}(\sigma,\sigma)$ is similar to that of simulations. Note that the amplitude and decay of the other peaks are very well described by this approximation, at least for this value of packing fraction. We have confirmed that $c_{py}(\mathbf{r})$ and $c_{fmt-oz}(\mathbf{r})$ are different, the former being a non-polynomic function of two variables except for some particular directions where becomes a linear or a parabolic function of a single variable –note that $c_{fmt}(\mathbf{r})$ is a second order polynomial with respect to the variables x and z–. This behaviour is remarkably different from that of hard spheres, where the FMT direct correlation function coincides with the PY result.

To finish this section, figure 3.6 compares results from the PY approximation (solid lines) and MC simulations (symbols) for $g(x,0)$ and $g(x,x)$ and for packing fractions $\eta = 0.6$ and $\eta = 0.65$ (above the Col-Cry bifurcation predicted from FMT; note that the results from FMT are absent in this figure because the Ornstein-Zernike closure cannot be used to calculate pair correlations for non-

uniform phases). At high densities the function $g_{py}(x,0)$ is reasonably close to that from MC –except for the contact value–. However, $g_{py}(x,x)$ strongly underestimates correlations –see figure 3.6–. To summarize, we can say that the PY approximation, as applied to the calculation of $g(\mathbf{r})$ for parallel hard squares and possibly also for hard cubes, although performing better than FMT, does not have the same degree of accuracy as for hard spheres. The fact that it seems to predict a fluid-to-crystal transition at densities close to $\eta = 0.79$ –in contrast to FMT, which predicts a bifurcation at 0.54– can be used to include it as a main ingredient to construct a modified version of FMT. The bad description (with respect to the hard-sphere case) of correlations featured by the PY theory is a general trend in many models of anisotropic particles. A modification of FMT to include PY correlations will certainly spoil the accurate description of the present density functional for highly confined systems of parallel hard squares –an issue studied in the next section–. The 2D $\rightarrow$ 1D dimensional cross-over property is not fulfilled any more when the structure of the functional is modified to include PY correlations.

3.5 CONFINEMENT IN NARROW CHANNELS

Next we consider study the performance of FMT in high confinement. First we study the case of a channel parallel to one of the square sides, and later we will discuss the case of the oblique channel. For the parallel channel we compare density profiles, equations of state and correlation functions of our functional with the exact TMM results and MC simulations for different channels of sections $H = (W+1)\sigma = 2.08$, 2.5 and 2.92. Here W is defined as the space available to the particle centers of mass –in units of σ–. This definition makes more sense when the parallel and oblique channels are studied together (note that for the oblique case $H = (W+\sqrt{2})\sigma$).

Results from FMT have been obtained by discretizing the density profile and minimizing the resulting grand potential. For the study of equations of state and density profiles we have used the one-dimensional density $\rho(z)$, which is uniform in the longitudinal direction of the channel. This is justified since minimization of $\Omega[\{\rho(x,z)\}]$ results in equilibrium profiles that only depend on the z component for the conditions studied. As a consequence, we have been able to achieve a finer mesh corresponding to $\sigma = 10^4$ points. However, in order to obtain the correlation functions, it is necessary to minimize the grand potential with a two-dimensional density profile because it is inhomogeneous in both directions –later it will be explained how we get correlation functions–. In this case the discretization of the system correspond to $\sigma = 10^2$ points.

The comparison of density profiles and equations of state are shown in figure 3.7 for the three selected channels. Panels (a)-(c) show the normalized density profiles $\rho^*(z) = \rho(z)/\int_{-H/2}^{H/2}\rho(z)dz$. In each panel profiles corresponding to dif-

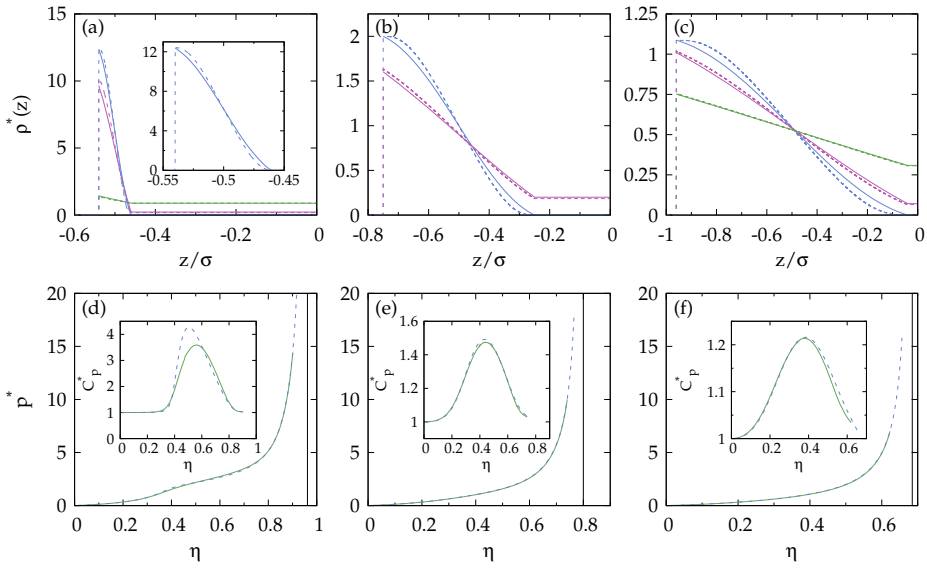

Figure 3.7: (a)-(c) Normalized density profiles $\rho^*(z)$ in the channel as obtained from FMT (dashed) and TMM (solid). Only half of the density profiles are shown since $\rho(z) = \rho(-z)$, with the channel centered at $z = 0$. (a) $W = 1.08$ and packing fractions $\eta = 0.3$ (green), 0.6 (purple) and 0.8 (blue). Inset: zoom of curves corresponding to $\eta = 0.8$. (b) $W = 1.5$ and $\eta = 0.4$ (purple) and $\eta = 0.7$ (blue). (c) $W = 1.92$ and $\eta = 0.2$ (green), $\eta = 0.4$ (purple) and $\eta = 0.6$ (blue). Panels (d)-(f) correspond to the equations of state resulting from FMT (dashed) and TMM (solid) for the cases $W = 1.08$ (d), $W = 1.5$ (e) and $W = 1.92$ (f). Vertical lines show the close-packing value. Inset: heat capacity as a function of η from FMT (blue dashed) and TMM (green solid).

ferent packing fractions, $\eta = \sigma^2 H^{-1} \int_{-H/2}^{H/2} \rho(z)dz$, are represented. In panels (d)-(f) the longitudinal pressure in dimensionless units, $p^* \equiv \beta p \sigma^2$, is depicted with an additional inset showing the scaled heat capacity at constant pressure –without the kinetic term– $C_p^* \equiv C_p/Nk_B - 1 = (p^*/\eta)^2/(\partial p^*/\partial \eta)$. In the equations of state we have also represented the close-packing value of the packing fraction, which is –assuming the maximum number of particles that fit in the transverse direction is two– $\eta_{cp} = 2\sigma/H$.

For $W = 1.08$ the density profiles resulting from FMT (dashed lines) as applied to confined parallel hard squares are very similar to the exact ones (solid curves) –panel (a)–. Only small differences in shape are seen for high packing fractions: while the FMT predicts Gaussian-type density profiles –better seen in the inset–, with a small plateau near the contact and a Gaussian-like decay, the exact results show density profiles with approximately linear shape except in a very small neighbourhood of the wall. Note that, apart from these differences, intervals in which the density profiles are not negligible are exactly the same, leading to a huge adsorption of both layers at the walls. The equation

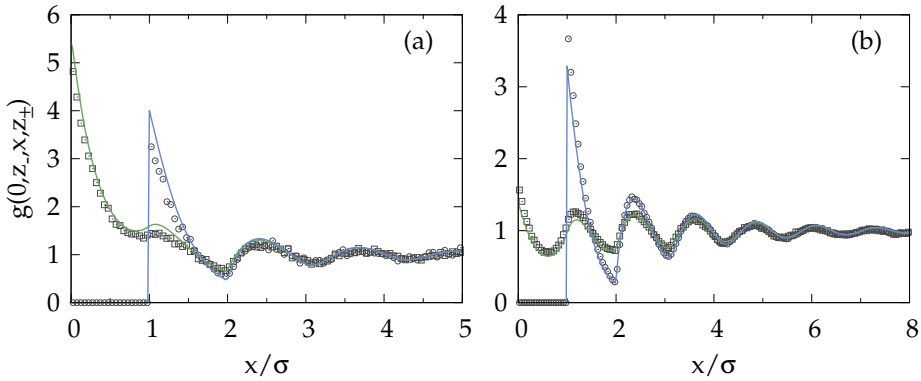

Figure 3.8: Pair correlation functions $g(0, z_-, x, z_-)$ (blue lines and circles) and $g(0, z_-, x, z_+)$ (green lines and squares) for channels with $W = 1.08$ and packing fractions $\eta = 0.4$ (a) and 0.6 (b). Symbols represent MC results.

of state predicted from FMT is almost identical to the exact result –panel (d)–. It is interesting to note that the equation of state features a change of curvature with density. This behavior is related to the change of the structure of confined squares: while for small packing fractions the system behaves as one-dimensional hard segments, when density increases two highly localized layers of squares are formed near the walls. However, this does not imply the existence of a phase transition, as can be seen from the inset of panel (d): the heat capacity shows no divergence or discontinuity at the packing fraction where most structural changes take place inside the channel –around the maximum–. We can see that the FMT underestimates the position of the peak ($\eta_{FMT} \sim 0.5$, while $\eta_{TMM} \sim 0.6$) and also overestimates its height.

For the other two cases, $W = 1.5$ and $W = 1.92$, the results exhibit the generally good performance of FMT in describing highly-confined fluid structures –panels (b) and (c) respectively– and the equations of state –panels (e) and (f) respectively– for wider channels. This adequacy is due to the dimensional reduction property fulfilled by the present functional. Note that now, because confinement is not so high, the layers adsorbed to the wall are less localized as compared to the $W = 1.08$ case.

Let us move now to the study of particle correlations in our confined system. To this aim we have calculated the pair correlation function of a particle located at $z = \tilde{z}$, denoted as $g(0, \tilde{z}, x, z)$. It is obtained as the ratio $\rho(x, z; \tilde{z})/\rho(z)$ where $\rho(z)$ is the one-dimensional density profile of the confined fluid used up to now. The profile $\rho(x, z; \tilde{z})$ is the two-dimensional –(x, z)– density of the confined fluid subject also to an external potential created by a fixed square located at $(0, \tilde{z})$. Basically we fix a particle at a particular position and obtain the density profile in its surroundings.

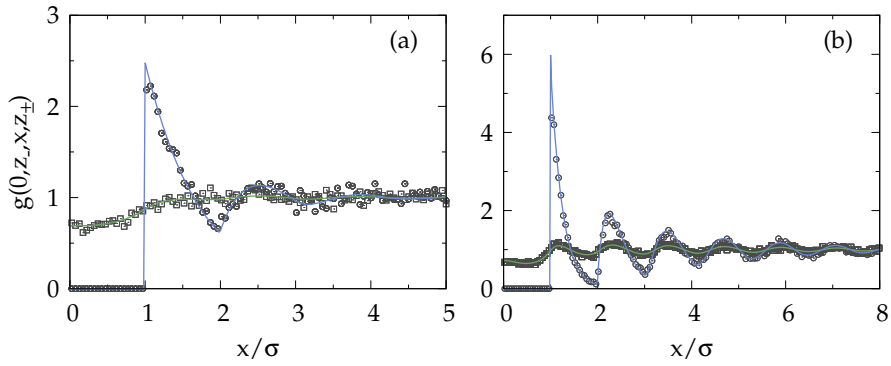

Figure 3.9: Pair correlation functions $g(0, z_-, x, z_-)$ (blue curves and circles) and $g(0, z_-, x, z_+)$ (green curves and squares) for channels with $W = 1.92$ and packing fractions $\eta = 0.4$ (a) and 0.55 (b). Symbols represent MC results.

In figure 3.8 the functions $g(0, z_-, x, z_\pm)$ are plotted for the channel $W = 1.08$ and in comparison with MC results (symbols). We have defined $z_\pm \equiv \pm(H - \sigma)/2$ as the coordinates of the upper (+) and lower (-) wall contact. Therefore $g(0, z_-, x, z_\pm)$ measures the pair correlation function with a reference square located at the lower wall along the x direction and at fixed $z = z_\pm$. Of course, at $(x < 1, z_-)$ there cannot be any particle because the reference particle is located at $(0, z_-)$, and this is the reason why $g(0, z_-, x < 1, z_-) = 0$ (blue curves). On the other hand, it is possible to place a particle at (x, z_+); in fact, $g(0, z_-, 0, z_+)$ presents a maximum representing a strongly correlated dimer (green lines). In panel (a) we plot $g(0, z_-, 0, z_\pm)$ for packing fraction $\eta = 0.4$ and in panel (b) the same functions for $\eta = 0.6$. From these results we can conclude that for thin channels and high enough packing fractions the particles belonging to the same or different layers are strongly correlated and the results from FMT reproduce very well those obtained by MC simulations. Note that the MC data exhibit a large scatter because these data are extracted from a three-dimensional histogram in $(\tilde{z}, x, z)$ by fixing the bin indexes in two of the dimensions, $(\tilde{z}, z)$.

When the channel is wide enough ($W = 1.92$, figure 3.9) the correlations between particles belonging to different layers (green curves) exhibit a dramatic decrease. We again study the behaviour for two different packing fractions, $\eta = 0.4$ in panel (a) and $\eta = 0.55$ in panel (b). While in the thinner channel the pair correlation functions corresponding to the two different layers practically coincide, here the correlation with the opposite layer is rapidly damped and hardly follows the correlation function $g(0, z_-, 0, z_-)$. Correlations of particles in the same layer (blue lines) show a similar behaviour for both channel widths. In any case all the correlations have an exponential decay, showing the absence of phase transitions.

The good description of highly confined PHS fluids made by FMT is a consequence of its compliance with dimensional crossover. However, we expect that

as the channel becomes wider, the high degree of accuracy shown here will be lost. To illustrate this, we have looked for possible phase transitions in wider channels ($H > 3\sigma$) between confined columnar phases (Col_n) with different number of layers n. A Col_2–Col_3 layering transition is found at $H/\sigma = 3.05$ and bulk chemical potential $\beta\mu \sim 18$, with coexisting Col_2 and Col_3 phases having packing fractions $\eta = 0.615$ and 0.907, respectively. Since it is well known that confined hard-core interacting particles in dimension $D = 1 + \epsilon$ (with $\epsilon < 1$) do not exhibit any phase transitions (*79*), this is a spurious prediction of FMT that stems from its mean-field nature.

Finally we consider the oblique channel, i.e. a channel with walls forming an angle of 45° with respect to the edge-lengths of squares. Note that the original reference system –that with axes parallel to the two squares edge-lengths– is not very adequate to present the results. For this reason it is more convenient to show them in a rotated reference system with coordinates (x', z') rotated 45°, x' being parallel and z' perpendicular to the walls. Note also that now the relation between channel section and space available for centers of mass is $H = W + \sigma\sqrt{2}$.

Figure 3.10(b) shows the functions $g(0, z'_-, x', z'_\pm)$ for the case $W = 1.13$ and $\eta = 0.43$ for which two rhombuses in contact with opposite walls cannot overtake along the channel. It is clear that the peaks in $g(0, z'_-, x', z'_-)$ (blue line) and $g(0, z'_-, x', z'_+)$ (green line) are out of phase, reflecting the fact that particles are located in a zigzag configuration –see figure 3.10(a)–, which facilitates high-packing configurations in the fluid phase. This structure was already observed in (*66*), where the TMM was used to study hard squares confined in oblique channels and confined hard disks. In the inset of figure 3.10(b) the density profile of FMT (red line) is represented in comparison with MC results (symbols). It shows that despite their high packing fraction, rhombuses are distributed over the whole channel, not just close to the walls, as can be seen from the relatively high value of the density in the middle of the pore. Note that, despite the perfect agreement between the FMT and MC density profiles, correlations are grossly overestimated by FMT.

In contrast to the profiles shown for the parallel channel, here we only have compared the FMT results with MC simulations, but not with TMM. This is because analytic results for the density profile and nonuniform pair distribution function can only be obtained from TMM when the channel width is such that particles only interact with nearest neighbours, i.e. with two neighbours. Including next-nearest neighbours, which is necessary for wider channels, is possible in principle but a formidable task in practice.

In figure 3.10(c) the same functions are plotted for the case $W = 1.53$ and $\eta = 0.44$. Now rhombuses in contact with opposite walls can overtake along the channel –this can be seen in the correlation function, which is nonzero and has a maximum at $x = 0$ for $z' = z'_+$–. In this case the peaks of the correlation functions are also out of phase but not as pronounced as in the previous case.

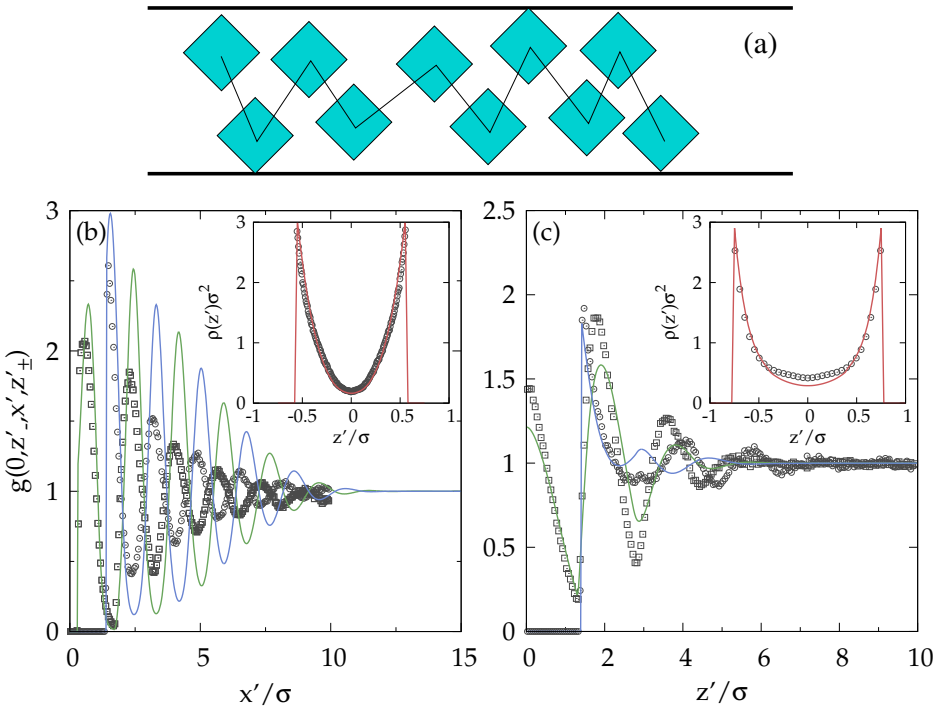

Figure 3.10: (a) Sketch of confined rhombuses in the most likely configuration. (b) Correlation functions $g(0, z_-, x, z_-)$ (blue curves) and $g(0, z_-, x, z_+)$ (green curves) for the oblique channel with $W = 1.13$ and packing fraction $\eta = 0.43$. Symbols are MC results –circles for $g(0, z_-, x, z_-)$ and squares for $g(0, z_-, x, z_+)$–. Inset: Density profile of rhombuses for same W and η of FMT (red line) and MC (circles). (c) Same functions as in (b), but for $W = 1.53$ and packing fraction $\eta = 0.44$.

We can see that comparison with MC simulations is reasonable, both for density profile and correlations.

To end this section we compare in figure 3.11 the density profiles as obtained from FMT (green dashed curves) and from TMM (blue solid curves) for channels with $W = 0.354$ –panel (a)– and $W = 0.707$ –panel (b)–. These channels are sufficiently narrow that the use of the TMM to compute the density profiles is possible. As we can see, the FMT compares perfectly with the exact calculations. In (a) the density profile is practically constant because we are close to the 1D limit. In (b) the relatively high value of the density profile at the centre of the pore reflects the lower particle adsorption at the walls, as compared to the parallel channel.

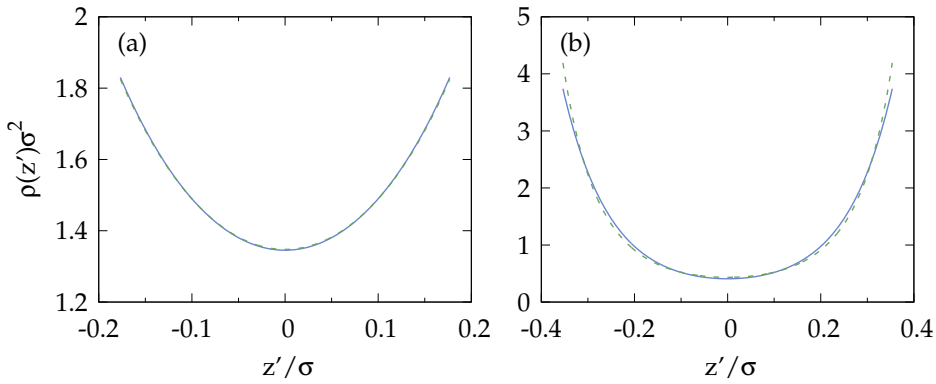

Figure 3.11: Density profiles of rhombuses confined in channels with $W = 0.354$, $\eta = 0.3$ (a), and $W = 0.707$, $\eta = 0.4$ (b). Blue solid and green dashed lines represent the TMM and FMT results respectively.

3.6 REMARKS AND COMMENTS

The principal motivation of the present chapter was to check the performance of the functional that will be used in the following chapters of the thesis. Firstly to give validity to the choice of density functional, and secondly to explore its limits and find a frame to discuss the future results from a rigorous perspective.

With respect to the bulk system, FMT performs better for high packing fractions. In the regime of the crystal phase, and up to the close packing limit, the results agree extremely well with simulations. However, for lower densities FMT predicts a spurious columnar phase –also reported in (*76*, *80*)– from $\eta > 0.538$ up to the appearance of the crystal as the more stable phase at $\eta \sim 0.75$. The equation of state is very good compared with simulations, except in the region around the spurious transition. There the virial-route PY equation of state compares very well with simulations but fails at higher packings. Another feature that points to the good performance of FMT is the prediction of a high percentage of vacancies which is in agreement with recent simulations (*78*, *81*). Bulk correlations are a bit overemphasized by FMT in both OZ and test particle route. In this aspect the PY approximation describes better the pair correlation function when compared to simulations.

In terms of confinement, the results presented here confirm the expectation that the FMT functional accurately describes highly confined fluids. It compares very well with TMM results for density profiles, equations of state and heat capacities in the different channels. The structure of the fluid is very well accounted for in all cases, and only small differences are found in the shape, which is more Gaussian-like than that from exact results. With respect to equations of state and heat capacity, the comparison is again very similar, but performance is obtained better for wider channels.

Also pair correlations obtained from FMT, using the test-particle route, agree in general quite well with simulation results. However, the agreement changes with the system of study. While in the parallel channel the correlation functions from FMT follow extremely well those of simulations, correlations in the oblique channel are not so well accounted for. Both FMT and simulations predict a zigzag configuration but the amplitude and frequency of the pair correlation function do not agree as nicely as in the parallel channel.

Finally we must mention that there is an unwanted feature of the FMT functional as the channel thickness becomes larger. We have shown that, when the system approaches the two-dimensional limit, FMT predicts phase transitions involving two and three layers of squares. However, it is well known that this behaviour should not appear for narrow channels. This feature is a spurious prediction of FMT that reflects the mean-field nature of the density functional.

4 CONFINEMENT OF RODS IN SQUARE CAVITIES

4.1 EFFECT OF CONFINEMENT

Since the seminal study of Onsager on the isotropic to nematic transition for hard thin rods (*7*) the labour in the field has been intense. Nowadays the behaviour of hard anisotropic particles at bulk is well understood. Bolhuis and Frenkel (*82*), in a great computational work, calculated the complete phase diagram in the density-aspect ratio plane. Later Graf and Löwen (*83*) also faced that study but using a DFT and obtaining a reasonable agreement with the previous work on a broad range of the phase diagram.

However, the study of liquid crystals under confinement is still an open field because there exist a wide variety of phenomenology that affects the behaviour: the presence of confined external potentials can dramatically change the symmetries of phases and the order of phase transitions. As a consequence of this, the results are usually counter-intuitive due to this added complexity. Moreover from a mathematical point of view confined situations tend to be more complicated and, consequently, there are less studies of this kind.

In this chapter we analyze the effect of confinement of two-dimensional hard rods in square nanocavities. With nanocavities we just mean that their size is comparable to the particles characteristic lengths, so not only the regions close to walls are affected but all the cavity.

4.1.1 Confinement in a square cavity

At the end the physics of hard particle systems are governed by entropy. However, the phase behaviour shows up under different effects which are better understood when they are isolated that when looking at the whole picture. This is because some effects may compete in a different way and, as a result, some of them can be hidden by the others or new phenomena could appear from the combination of them. So in order to understand the physics behind the obtained results that we will see, it can be useful to describe the main entropic effects taking part in the confinement of rods in a square cavity.

It is well known that first-order transitions at bulk have their correspondence when the fluid is confined. Nevertheless, this transition is shifted by ΔT in temperature or by $\Delta\mu$ in chemical potential with respect to the bulk transition. This effect is called *capillary ordering* and is analogous to the phenomenon of capillary condensation in ordinary fluids governed by the Kelvin equation (*84*).

Here the shift is predicted to be proportional to the inverse of the cavity size $\Delta\mu \sim h^{-1}$ when $h \to \infty$ with its precise value and sign being dependent on the surface interactions. Higher order corrections are needed to be included for not-so-large systems.

Another phenomena arising from confinement are the so-called *commensuration effects*. When phases with partial or full spatial order are present –such as smectic, columnar or crystal– the cavity size can enhance or suppress their stability depending on the relation between h and the natural periodicity, a, of the lattice or layered structure. In situations when cavity size is very different to an integer number of liquid crystal periods ($h \neq na$) the spatially ordered phases may be frustrated and in cases when $h \sim na$ they may be stabilized. Commensuration effects have been observed in crystals (*85*–*87*) and in liquid crystals in three (*88*–*92*) and two (*93*) dimensions. When the size of the cavity is changed commensuration transitions are found between structures with different number of layers.

Anchoring or surface induced ordering also affects the complex behaviour under confinement. This comes from the known fact that surfaces are able to orient the main axes of particles close to them due to specific interactions or just because of excluded volume effects. An example of the first case are molecular systems where the interactions with surfaces depend on some chemical properties and on the relative particle orientation. The second case is always present but it is more important for hard anisotropic particles. Excluded volume of particles close to surfaces is reduced when particles are aligned parallel to the surface. This in turn can induce a phenomenon called *wetting*: a macroscopic layer of orientationally ordered phase with the director being parallel to the surface is stabilized due to the gain in the free-volume per particle and, consequently, the configurational entropy is increased. This constitutes the physical interpretation of anchoring and of course it will be relevant only at high densities.

In confined systems surface induced ordering may compete with itself when different surfaces tend to orient particles in different directions. In figure 4.1 some of these situations are depicted. The first example represents two parallel and infinite walls that favour two perpendicular directions. The left wall favours homeotropic orientation, i.e. the local free energy is minimized when the particles axes are parallel to the surface normal. Instead the right wall induces a planar orientation and tends to orient particles with their axes parallel to the wall. When a nematic phase is stable two orientations compete and in order to minimize total surface free energy one of the following situations may appear: either the nematic director smoothly rotates from one surface to the other –figure 4.1(a)–, or the nematic director dramatically change in a step-like fashion –figure 4.1(b)–. In the first case the deformation of the director field implies an increase in the elastic free energy (*94*) and in the second a line defect (dashed line) appears separating regions with different orientations. However, the creation of an interface separating two regions with different orientations

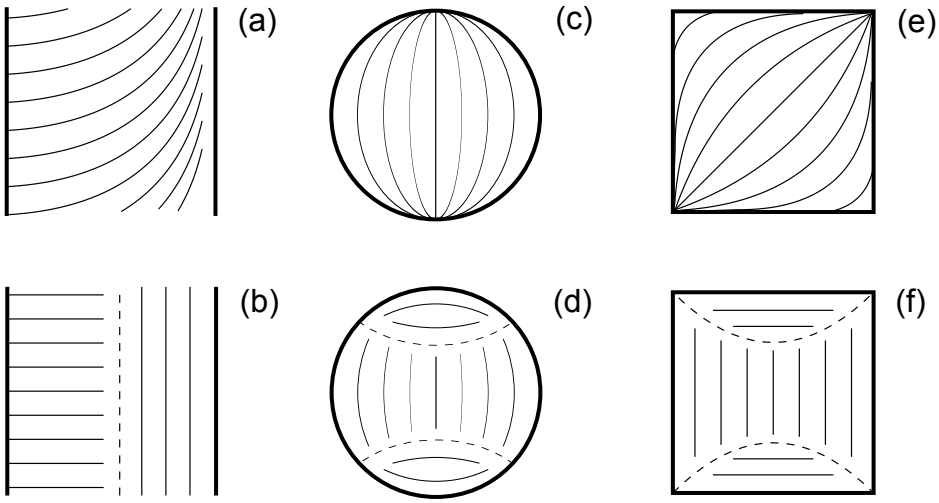

Figure 4.1: Sketch of two-dimensional systems with surface induced order competition: (a) and (b) correspond to two parallel infinite walls with different surface orientation; in (c) and (d) a circular cavity with planar surface orientation; in (e) and (f) a square cavity with the same planar ordering.

has associated an energy cost. At the end the more stable structure will depend on the distance between walls and on the thermodynamics conditions. Generally small cavities and high densities favour the step-like structure since a drastic distortion of the director field occurs the and packing of particles is more efficient than in the distorted configuration. In contrast, large separations or low densities could present the configuration of panel (a) with a smooth change in the director field. This phenomenology was firstly predicted in the region around a line defect (*95*) and then studied in a slit pore using Landau-de Gennes theory (*96*–*98*), DFT (*99*, *100*) and simulations (*101*–*103*).

In closed cavities the phenomenology is similar. Figures 4.1(c) and 4.1(d) correspond to a circular cavity and figures 4.1(e) and 4.1(f) to a square cavity. In these cases all the surfaces promote planar ordering but the fact that their normal vector varies spatially result in different induced orientation which provoke a competition between different nematic director alignment. For the distorted configurations –situations (c) and (e)– the induced order by all surfaces implies the formation of point defects, where the director field has a singularity. In the circular cavity two opposite defects are formed while in the square one four point defects appear at the corners. Under certain conditions these structures destabilize with respect to the step-like configurations –situations (d) and (f)–. Here a central nematic region, with the director following the surface curvature, separates two other domains with the opposite director orientation, satisfying the local planar ordering. Recent Monte Carlo simulations on circular (*104*) and square (*105*, *106*) cavities together with experiments on quasi-monolayers

of granular cylinders (28) have confirmed the presence of these nematic-director structures.

It is worthwhile to take into account that spatially ordered phases (smectic, columnar or crystal) can only appear in the undistorted configuration, as they are shown in panels (b), (d) and (f). Because these phases appear at higher densities the confined system will generally follow this sequence: at low density the isotropic phase is stable; then a nematic order appears in a distorted configuration; and when its elastic energy is high enough a transition to the step-like structure takes place. Finally at higher densities particles organize in partial spatially ordered phases –smectic or columnar– and eventually total order –crystal–.

4.2 FMT FOR THE SQUARE CAVITY

In order to study the system of hard rectangles confined in a square cavity we have used the FMT presented in section 2.4. The system is depicted in figure 4.2 with rods of length L and width σ in a square cavity of side H. We use the Zwanzig approximation: only two orientations are allowed, those with their main axis parallel to x or y Cartesian axes. We have already discussed the validity of the restricted orientation approximation for high density configurations. In the square cavity it is even more justified because the surfaces induce ordering in two mutually perpendicular directions.

The confinement in the square cavity is accounted by an external potential defined as

$$V^{\nu}_{ext}(\mathbf{r}) = \begin{cases} 0 & \frac{\sigma^{\nu}_x}{2} \leqslant x \leqslant H - \frac{\sigma^{\nu}_x}{2}\,,\ \frac{\sigma^{\nu}_y}{2} \leqslant y \leqslant H - \frac{\sigma^{\nu}_y}{2} \\ \infty & \text{otherwise} \end{cases} \tag{4.1}$$

where σ^{ν}_{μ} are the particle edge-lengths as defined for equation 2.36. This potential constitutes the condition for particles being inside the cavity. Note that it depends on the species $\nu = \{x, y\}$ because it acts over the particle centers of mass and the condition to be inside the cavity depends on the position and orientation of the rod.

To ensure the non-overlapping between particles and walls we can just fix $\rho_{\nu}(\mathbf{r}) = 0$ in the spatial region where the external potential is infinite and

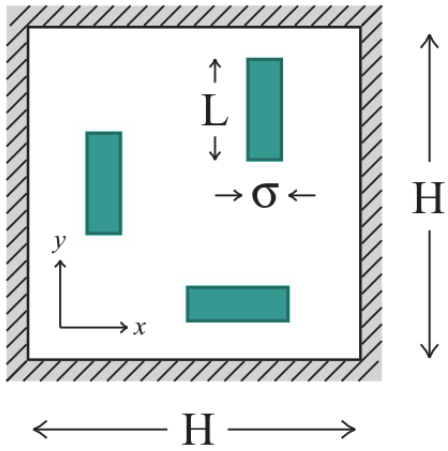

Figure 4.2: Sketch of hard rectangles of length L and width σ confined in a square cavity of side H. Only two particle orientations are allowed.

remove the part of the free energy functional related with $V_{ext}^{\nu}(\mathbf{r})$. Therefore, following equation 2.38, the weighted densities have the explicit form

$$\begin{aligned} n_0(\mathbf{r}) = \frac{1}{4}\Bigg[&\rho_x\left(x-\frac{L}{2},y-\frac{\sigma}{2}\right)+\rho_x\left(x-\frac{L}{2},y+\frac{\sigma}{2}\right)\\ &+\rho_x\left(x+\frac{L}{2},y-\frac{\sigma}{2}\right)+\rho_x\left(x+\frac{L}{2},y+\frac{\sigma}{2}\right)+\rho_y\left(x-\frac{\sigma}{2},y-\frac{L}{2}\right)\\ &+\rho_y\left(x-\frac{\sigma}{2},y+\frac{L}{2}\right)+\rho_y\left(x+\frac{\sigma}{2},y-\frac{L}{2}\right)+\rho_y\left(x+\frac{\sigma}{2},y+\frac{L}{2}\right)\Bigg] \end{aligned} \tag{4.2}$$

$$\begin{aligned} n_{1x}(\mathbf{r}) = \frac{1}{2}\Bigg\{&\int_{x-L/2}^{x+L/2}dx'\left[\rho_x\left(x',y-\frac{\sigma}{2}\right)+\rho_x\left(x',y+\frac{\sigma}{2}\right)\right]\\ &+\int_{x-\sigma/2}^{x+\sigma/2}dx'\left[\rho_y\left(x',y-\frac{L}{2}\right)+\rho_y\left(x',y+\frac{L}{2}\right)\right]\Bigg\} \end{aligned} \tag{4.3}$$

$$\begin{aligned} n_{1y}(\mathbf{r}) = \frac{1}{2}\Bigg\{&\int_{y-\sigma/2}^{y+\sigma/2}dy'\left[\rho_x\left(x-\frac{L}{2},y'\right)+\rho_x\left(x+\frac{L}{2},y'\right)\right]\\ &+\int_{y-L/2}^{y+L/2}dy'\left[\rho_y\left(x-\frac{\sigma}{2},y'\right)+\rho_y\left(x+\frac{\sigma}{2},y'\right)\right]\Bigg\} \end{aligned} \tag{4.4}$$

$$\begin{aligned} n_2(\mathbf{r}) = &\int_{x-L/2}^{x+L/2}dx'\int_{y-\sigma/2}^{y+\sigma/2}dy'\rho_x(x',y')\\ &+\int_{x-\sigma/2}^{x+\sigma/2}dx'\int_{y-L/2}^{y+L/2}dy'\rho_y(x',y') \end{aligned} \tag{4.5}$$

and the derivatives of the excess part of the free energy density with respect to the weighted densities (as defined in equation 2.57) have the following expressions

$$\phi_0^\nu(\mathbf{r}) = -\frac{1}{4}\ln\left\{\left[1-n_2\left(x-\frac{\sigma_x^\nu}{2},y-\frac{\sigma_y^\nu}{2}\right)\right]\times\left[1-n_2\left(x-\frac{\sigma_x^\nu}{2},y+\frac{\sigma_y^\nu}{2}\right)\right]\times\left[1-n_2\left(x+\frac{\sigma_x^\nu}{2},y-\frac{\sigma_y^\nu}{2}\right)\right]\times\left[1-n_2\left(x+\frac{\sigma_x^\nu}{2},y+\frac{\sigma_y^\nu}{2}\right)\right]\right\} \tag{4.6}$$

$$\phi_{1x}^\nu(\mathbf{r}) = \frac{1}{2}\int_{x-\sigma_x^\nu/2}^{x+\sigma_x^\nu/2} dx'\left[\frac{n_{1y}(x',y-\sigma_y^\nu/2)}{1-n_2(x',y-\sigma_y^\nu/2)}+\frac{n_{1y}(x',y+\sigma_y^\nu/2)}{1-n_2(x',y+\sigma_y^\nu/2)}\right] \tag{4.7}$$

$$\phi_{1y}^\nu(\mathbf{r}) = \frac{1}{2}\int_{y-\sigma_y^\nu/2}^{y+\sigma_y^\nu/2} dy'\left[\frac{n_{1x}(x-\sigma_x^\nu/2,y')}{1-n_2(x-\sigma_x^\nu/2,y')}+\frac{n_{1x}(x+\sigma_x^\nu/2,y')}{1-n_2(x+\sigma_x^\nu/2,y')}\right] \tag{4.8}$$

$$\phi_2^\nu(\mathbf{r}) = \int_{x-\sigma_x^\nu/2}^{x+\sigma_x^\nu/2} dx'\int_{y-\sigma_y^\nu/2}^{y+\sigma_\nu^y/2} dy'\left[\frac{n_0(x',y')}{1-n_2(x',y')}+\frac{n_{1x}(x',y')n_{1y}(x',y')}{[1-n_2(x',y')]^2}\right]. \tag{4.9}$$

These functions in turn define analytically the gradient of the grand potential with respect to the density profile. However, as the square cavity is spatially discretized, the numerical and analytical gradient are not exactly the same which is related to the fact of approximating the integrals by sums. Depending on the quadrature method used the grid points are not equally weighted, for example an integral computed numerically through the trapezoidal rule weights all points with $\omega = 1$ except for the end points that are weighted half $\omega = 0.5$. Taking this issue into account the the gradients are almost the same but some points of the mesh are affected with different integral weights. See appendix B for exact expressions.

Once we obtain the explicit expressions of the grand potential and its gradient, the model was solved numerically with the following parameters: the space was discretize in a square grid with 20 per particle width σ or grid step $\Delta x = \Delta y = 0.05\sigma$. As an exception for the particular case of hard squares, the mesh was selected finer with $\Delta x = \Delta y = \sigma/60$. For instance, a grid of $\sim 10^6$ points result in the case $H = 8L$ and $\kappa = 6$.

The two density profiles ρ_x, ρ_y at each grid point were taken as independent variables and using the conjugate gradient method a minimization of the grand potential was performed. However, the minimization variables used were not the local densities but $\xi_\nu(\mathbf{r}) \equiv \sqrt{\rho_\nu(\mathbf{r})}$ since the latter show better convergence properties due to their larger variation close to the regions where the density is very small. After the change of variables we obtain the new gradient as

$$\frac{\partial\Omega}{\partial\xi_\nu} = \frac{\partial\Omega}{\partial\rho_\nu}\frac{\partial\rho_\nu}{\partial\xi_\nu} = 2\xi_\nu^{-1}\frac{\partial\Omega}{\partial\rho_\nu}. \tag{4.10}$$

The iterative process is very efficient and the convergence is such that the norm of the gradient vector per mesh point achieved is typically 10^{-12}. We

select initial guesses corresponding to isotropic configurations ($\rho_x = \rho_y \neq f(\mathbf{r})$) or other already equilibrated density profiles with slightly different conditions –chemical potential or cavity size–. This latter method was used to reach metastable configurations in order to determine the transition point between different density structures. It will be explained in more detail in section 4.5.

4.3 BULK PHASE TRANSITIONS

Our aim is to study the effect of confinement in the system of rods, so firstly we need to know the phase behaviour of the hard rectangles at bulk. We have calculated the bulk phase diagram to later compare with the results of the confined system.

In order to study spatially ordered phases at bulk we can take advantage of their symmetries. We expose below two methods used to determine the phase transitions between uniform or non-uniform phases.

4.3.1 Isotropic–nematic spinodal

In section 2.4.1 we showed that the molar fraction of species can be uniquely expressed through a nematic order parameter and the equilibrium state condition is given by equation 2.50. For the isotropic state we have $Q = 0$ and when the nematic order appears above a certain packing fraction η^* we have $Q > 0$. Because the transition is of second order, in the neighbourhood of the transition point the order parameter is negligible small so we can expand equation 2.50 up to first order in Q with the result

$$\left[1 - \frac{y}{2}(\kappa + \kappa^{-1} - 2)\right] Q = 0 \tag{4.11}$$

which has a non-trivial solution ($Q \neq 0$) only when $1/y^* = (\kappa + \kappa^{-1} - 2)/2$. Taking into account that $\eta = 1/(1 + y^{-1})$ we find that the packing fraction corresponding to the isotropic-nematic transition is

$$\eta^* = 2/(\kappa + \kappa^{-1}). \tag{4.12}$$

Then for a system with $\eta > \eta^*$ the nematic phase become more stable than the isotropic one. However, it does not mean that the nematic constitutes the equilibrium state. Transitions from isotropic to non-uniform phases might occur before η^*, as we will see in section 4.5.2, with the nematic phase becoming metastable.

4.3.2 Inhomogeneous phases

Non-uniform configurations have periodic structures so a suitable way of characterizing them is through a Fourier series of the density profiles

$$\rho_\nu(\mathbf{r}) = \rho_0 \gamma_\nu \sum_{\vec{k}} \alpha^\nu_{k_1,k_2} \cos(q_x k_1 x) \cos(q_y k_2 y) \tag{4.13}$$

where $\rho_0 = (d_x d_y)^{-1} \int_0^{d_x} dx \int_0^{d_y} dy \rho(x,y)$ is the average density over the unit cell with $\rho(x,y) = \sum_\nu \rho_\nu(x,y)$; γ_ν is the molar fraction of species ν fulfilling $\gamma_x + \gamma_y = 1$; $\vec{k} = (k_1, k_2)$ with $k_i \in \mathbb{N}$; $\alpha^\nu_{k_1,k_2}$ are the Fourier coefficients with the constraint $\alpha^\nu_{0,0} = 1$; $q_i \equiv 2\pi/d_i$ with d_i the lattice parameter in the real space along the i direction.

The weighted densities then take the form

$$n_\alpha(\mathbf{r}) = \rho_0 \sum_{\nu,\vec{k}} \gamma_\nu \alpha^\nu_{k_1,k_2} \hat{\omega}^{(\alpha)}_\nu(\vec{k}) \cos(q_x k_1 x) \cos(q_y k_2 y) \tag{4.14}$$

where the Fourier transforms of the weighting functions are explicitly

$$\hat{\omega}^{(0)}_\nu(\vec{k}) = \chi_0\left(\frac{q_x k_1 \sigma^\nu_x}{2}\right) \chi_0\left(\frac{q_y k_2 \sigma^\nu_y}{2}\right) \tag{4.15}$$

$$\hat{\omega}^{(1x)}_\nu(\vec{k}) = \sigma^\nu_x \chi_1\left(\frac{q_x k_1 \sigma^\nu_x}{2}\right) \chi_0\left(\frac{q_y k_2 \sigma^\nu_y}{2}\right) \tag{4.16}$$

$$\hat{\omega}^{(1y)}_\nu(\vec{k}) = \sigma^\nu_y \chi_0\left(\frac{q_x k_1 \sigma^\nu_x}{2}\right) \chi_1\left(\frac{q_y k_2 \sigma^\nu_y}{2}\right) \tag{4.17}$$

$$\hat{\omega}^{(2)}_\nu(\vec{k}) = a \chi_1\left(\frac{q_x k_1 \sigma^\nu_x}{2}\right) \chi_1\left(\frac{q_y k_2 \sigma^\nu_y}{2}\right) \tag{4.18}$$

being $a = \sigma L$ the particle area, $\chi_0(x) \equiv \cos(x)$ and $\chi_1(x) \equiv \sin(x)/x$.

The free energy per unit area is

$$\mathcal{F} \equiv \frac{\beta(\mathcal{F}_{id}[\{\rho_\nu\}] + \mathcal{F}_{exc}[\{\rho_\nu\}])a}{A} = \frac{a}{d_x d_y} \int_0^{d_x} dx \int_0^{d_y} dy \Phi(x,y) \tag{4.19}$$

where $\Phi = \Phi_{id} + \Phi_{exc}$ and

$$\Phi_{exc}(x,y) = -n_0(x,y) \log[1 - n_2(x,y)] + \frac{n_{1x}(x,y) n_{1y}(x,y)}{1 - n_2(x,y)} \tag{4.20}$$

$$\Phi_{id}(x,y) = \sum_\nu \rho_\nu(x,y)[\log \rho_\nu(x,y) - 1]. \tag{4.21}$$

In order to obtain the equilibrium profiles we need to minimize the free energy with respect to the set of parameters $z \equiv [\gamma_x, q_x, q_y, \{\alpha^\nu_{k_1,k_2}\}]$ (note that we can choose γ_x or γ_y since they are related through $\gamma_x = 1 - \gamma_y$). Thus the gradients of $\mathcal{F}^*$ can be calculated as

$$\frac{\partial \mathcal{F}^*}{\partial z} = \frac{\partial \mathcal{F}^*_{id}}{\partial z} + a \int_0^1 d\tilde{x} \int_0^1 d\tilde{y} \sum_\alpha \frac{\partial \Phi}{\partial n_\alpha}(\tilde{x},\tilde{y}) \frac{\partial n_\alpha}{\partial z}(\tilde{x},\tilde{y}) \tag{4.22}$$

where we have defined the reduced units $\tilde{x} \equiv 2x/d_x$ and $\tilde{y} \equiv 2y/d_y$ and $\mathcal{F}^*_{id} \equiv \beta\mathcal{F}_{id}\,a/A$ is the ideal part of the free energy per unit area. The derivatives of the ideal part of the free energy are just

$$\frac{\partial \mathcal{F}^*_{id}}{\partial \gamma_x} = \eta_0 \left\{ \log\left(\frac{\gamma_x}{\gamma_y}\right) + \int_0^1 d\tilde{x} \int_0^1 d\tilde{y}\, [\Psi_x(\tilde{x},\tilde{y}) \log \Psi_x(\tilde{x},\tilde{y}) - \Psi_y(\tilde{x},\tilde{y}) \log \Psi_y(\tilde{x},\tilde{y})] \right\} \tag{4.23}$$

$$\frac{\partial \mathcal{F}^*_{id}}{\partial \alpha^{\nu}_{k_1,k_2}} = \eta_0 \gamma_\nu \int_0^1 d\tilde{x} \int_0^1 d\tilde{y} \cos(\pi k_1 \tilde{x}) \cos(\pi k_2 \tilde{y}) \log \Psi_\nu(\tilde{x},\tilde{y}) \tag{4.24}$$

and the derivatives of the weighted densities with respect to each parameter appear as

$$\frac{\partial n_\alpha}{\partial \gamma_x} = \rho_0 \left[\sum_{\vec{k}} \left(\alpha^x_{k_1,k_2} \hat{\omega}^{(\alpha)}_x(\vec{k}) - \alpha^y_{k_1,k_2} \hat{\omega}^{(\alpha)}_y(\vec{k}) \right) \cos(\pi k_1 \tilde{x}) \cos(\pi k_2 \tilde{y}) \right] \tag{4.25}$$

$$\frac{\partial n_\alpha}{\partial q_\mu} = \rho_0 \sum_{\nu,\vec{k}} \gamma_\nu \alpha^\nu_{k_1,k_2} \frac{\partial \hat{\omega}^{(\alpha)}_\nu(\vec{k})}{\partial q_\mu} \cos(\pi k_1 \tilde{x}) \cos(\pi k_2 \tilde{y}) \tag{4.26}$$

$$\frac{\partial n_\alpha}{\partial \alpha^{\nu}_{k_1,k_2}} = \rho_0 \gamma_\nu \hat{\omega}^{(\alpha)}_\nu(\vec{k}) \cos(\pi k_1 \tilde{x}) \cos(\pi k_2 \tilde{y}) \tag{4.27}$$

At this point, with all the gradients of the free energy calculated, the equilibrium profiles are obtained, as usually, via the conjugate gradients method. Note that the Fourier expansion of equation 4.13 takes into account all the possible symmetries: for the crystal phase we have $\alpha^\nu_{k_1,k_2} \neq 0\ \forall\, k_i$ while the columnar and smectic configurations fulfils $\alpha^\nu_{0,k_2} = 0$ and $\alpha^\nu_{k_1,0} = 0$ respectively. In order to carry out the calculations we also need to truncate the Fourier series up to a certain number of coefficients. The sum is truncated when $\alpha^\nu_{\vec{k}}$ are small enough. In practice we have used coefficients up to the tenth order, i.e. a total of 100 for each profile. This threshold has been checked to be sufficient by solving the same system with a larger set of coefficient and obtaining the same results.

4.4 SYSTEM PROPERTIES

Before showing and discussing the results let us firstly define the physical magnitudes we use to quantify the structural and thermodynamics properties.

4.4.1 Local order parameter

In the description of confined liquid crystals the local orientational order is a key point. For this reason, we need to define the order tensor $\hat{Q}(\mathbf{r})$ with components

$$\hat{Q}_{ij} = \langle 2\hat{u}_i\hat{u}_j - \delta_{ij} \rangle \qquad i,j = \{1,2\}. \tag{4.28}$$

Here $\langle \cdots \rangle$ represents a particle average and $\hat{\mathbf{u}}$ is the unit vector pointing along the particle axis. A rod with arbitrary orientation φ has $\hat{\mathbf{u}} = (\cos\varphi, \sin\varphi)$. However, in our restricted-orientation model there exists only two allowed directions –or four possible angle orientations– and, consequently, the local angular distribution function $h(\varphi, \mathbf{r})$ can be written as

$$h(\varphi,\mathbf{r}) = \frac{\rho_x(\mathbf{r})}{\rho(\mathbf{r})}\left[\frac{\delta(\varphi)+\delta(\varphi-\pi)}{2}\right] + \frac{\rho_y(\mathbf{r})}{\rho(\mathbf{r})}\left[\frac{\delta\left(\varphi-\frac{\pi}{2}\right)+\delta\left(\varphi-\frac{3\pi}{2}\right)}{2}\right] \tag{4.29}$$

which is normalized $\int_0^{2\pi}\int_{\mathcal{S}} d\varphi d\mathbf{r} h(\varphi,\mathbf{r}) = 1 \quad \forall \mathcal{S}$. Then within the present approach the components of the local ordering tensor can be calculated as

$$\hat{Q}_{ij}(\mathbf{r}) = \int_0^{2\pi} d\varphi h(\varphi,\mathbf{r}) \begin{pmatrix} \cos 2\varphi & \sin 2\varphi \\ \sin 2\varphi & -\cos 2\varphi \end{pmatrix} = Q(\mathbf{r}) \begin{pmatrix} 1 & 0 \\ 0 & -1 \end{pmatrix} \tag{4.30}$$

where we have used that $\langle \sin 2\varphi \rangle_h = 0$. Consequently, the local order parameter comes as

$$Q(\mathbf{r}) = \int_0^{2\pi} d\varphi h(\varphi,\mathbf{r}) \cos 2\varphi = \frac{\rho_x(\mathbf{r}) - \rho_y(\mathbf{r})}{\rho(\mathbf{r})}. \tag{4.31}$$

From this definition it is clear that $-1 \leqslant Q \leqslant 1$. Since the order tensor is always diagonal in the reference frame defined by the two possible perpendicular orientations, the director can only point along x axis ($Q > 0$) or y axis ($Q < 0$). Intermediate situations with the director pointing at an angle φ different from 0, $\pi/2$, π or $3\pi/2$ cannot be described.

4.4.2 Pressure

In a first order transition there is a discontinuity in density. As usual, the coexisting densities of the transition are calculated by equating the chemical potentials and pressures at each coexisting phases. Using the thermodynamic definition of pressure

$$\beta p = A^{-1}\left[\int_{\mathcal{A}} d\mathbf{r}\beta \sum_\nu \mu_\nu \rho_\nu(\mathbf{r}) - \int_{\mathcal{A}} d\mathbf{r}\Phi(\mathbf{r})\right] \tag{4.32}$$

and taking into account that $\mu_\nu = \delta\mathcal{F}/\delta\rho_\nu^{eq}(\mathbf{r})$ and substituting the expression for the free energy density one obtains

$$\beta p = A^{-1}\int_{\mathcal{A}} d\mathbf{r}\left(\frac{n_0(\mathbf{r})}{1-n_2(\mathbf{r})} + \frac{n_{1x}(\mathbf{r})n_{1y}(\mathbf{r})}{(1-n_2(\mathbf{r}))^2}\right). \tag{4.33}$$

4.5 RESULTS

This section is devoted to present the results and discuss the phase behaviour. Because our aim is to study the effect of the confinement on the liquid crystal structures we need firstly to obtain the phase behaviour at bulk. Further we will study the system confined in a squared cavity. We have studied the influence of particle aspect ratio, cavity size and density. The results are presented as follows: in separate sections we present the bulk and surface phase diagrams of hard rectangles with $\kappa = 1$, 3 and 6. Whereas the phase diagrams at bulk depends only on the density and aspect ratio of rods, phase diagrams of confined systems depends also on the cavity size. Commensuration transitions will be shown when varying the latter.

The fact that we are in two dimensions makes the columnar and smectic phases to be indistinguishable because partial positional order can only appear in 1D. However, in analogy to 3D systems we will call columnar phase to that in which particle axes is parallel to the liquid crystal layer and smectic phase to that with particles perpendicular to the layers –see figure 1.1–.

4.5.1 $\kappa = 1$

For this aspect ratio particles are squares and there exists only one component due to the symmetry $\rho_x \equiv \rho_y$. For the same reason the smectic and columnar phases are identical so we will refer only to columnar when required. Only three phases are possible in this system: isotropic (I), columnar (Col) and crystal (Cry). We have minimized the free energy at bulk for all the possible phases and the results are shown in figure 4.3.

The bulk phase diagram exhibits the following sequence of phase transitions when increasing the density

$$\mathrm{I} \rightarrow \mathrm{Col} \rightarrow \mathrm{Cry}.$$

At low densities the only stable phase is the isotropic one. At an intermediate packing fraction we find an I→Col transition located at $\eta = 0.538$ which within the accuracy of our calculations is continuous (however, we should take into account that the Col phase was not found stable in MD simulations of hard parallel squares (*107*) which exhibits a fluid-crystal transition at $\eta \sim 0.8$). The FMT predicts that from the same bifurcation point also appears a metastable crystal phase with free energy very close to that of the Col phase. First these two branches separates slightly but then they become closer until a first order Col→Cry transition takes place. The packing fractions of the two coexisting phases are $\eta_{\mathrm{Col}} = 0.726$ and $\eta_{\mathrm{Cry}} = 0.730$. These two points in the phase diagram correspond to the states with the same chemical potential and pressure. In practice we have calculated them by the common tangent construction.

Let us move now to the confined system. In this case we have implemented a free minimization in the real space discretized as explained in section 4.2.

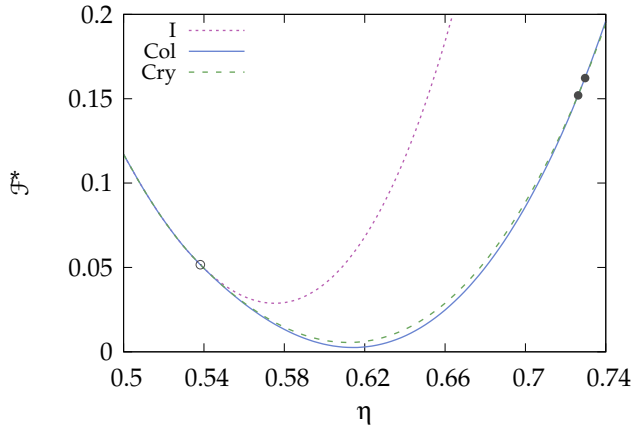

Figure 4.3: Free energy density branches in reduced units $\mathcal{F}^* \equiv \beta\mathcal{F}L\sigma/A - f$ of the I, Col and Cry phases with respect to packing fraction for squares. The straight line $f = a\eta + b$, with $a = 6.20$ and $b = -3.22$, has been subtracted from the free energies in order to better visualise the curves. The open circle represents the second order I→Col transition and the two solid circles are the coexisting packing fractions of the first order Col→Cry transition.

We have explored the phase diagram for different cavity sizes H and chemical potentials μ. Once two different structures (one of them metastable) were found we varied the μ or H used as initial guesses those obtain from the previous minimization steps. In this way we were able to calculate the grand potentials for both structures as a function of μ or H and found the crossing between both branches which is just constitutes the transition point.

The system of confined squares behaves differently from the bulk one. At low densities –or chemical potentials– the isotropic phase is the stable one but in contrast to the bulk the density profile is, by confinement, locally anisotropic near the walls. However, when the chemical potential is increased a crystal phase, instead of the columnar, appears. The near energy degeneracy of columnar and crystal phases at bulk is broken and the crystal phase becomes much more stable now: since the cavity has a square shape and particles are completely symmetric –same length and width–, the system cannot break the symmetry along a single direction. Even though the walls could in principle favor columnar ordering, this situation obviously generates frustration as two perpendicular Col structures are promoted by orthogonal walls and particles could not easily diffuse within each layer. Thus the localization of particles on a square lattice minimizes the free energy when the density is increased.

The sequence in the confined system is then

$$\mathrm{I} \rightarrow \mathrm{Cry}.$$

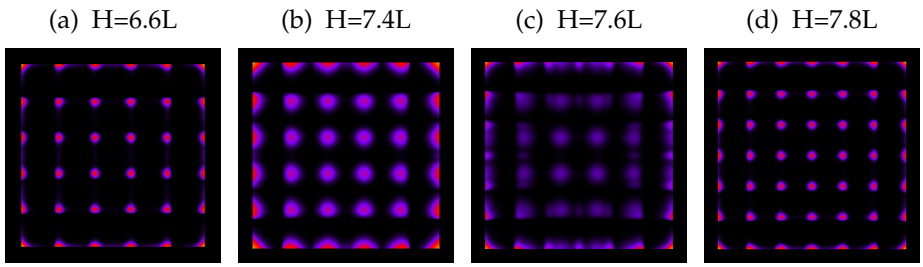

Figure 4.4: Density contour plots of confined structures for $\kappa = 1$ and chemical potential $\beta\mu = 8.376$ corresponding to the commensuration transition $Cry_6 \to Cry_7$. Equilibrated density profiles when increasing the cavity size from $H = 6.6L$ to $H = 7.8L$ are shown. Brightness saturation has been adjusted differently in each panel to optimize contrast.

Additionally, we also observe commensuration transitions between crystal structures with different number of layers when varying H. The number and configuration of the crystal peaks depend very much on the cavity side H . We proceed now to describe commensuration transitions. Suppose we obtain a bulk crystal lattice parameter of $a \sim 1.18L$ for a given chemical potential. Then when the system is confined for the same μ a square lattice with n^2 peaks will fit into the cavity when $H = H_n$, with $H_n = (n-1)a + L$ or $H_n/L \simeq 1.18n - 0.18$. Therefore, we expect a transition between a structure with n^2 peaks, labeled Cry_n, and another one with $(n+1)^2$ peaks, Cry_{n+1}, at roughly $H/L \simeq (H_n + H_{n+1})/2L = 1.18n + 0.41$, i.e. at $H/L = 1.59, 2.77, 3.95, 5.13, 6.31, 7.49, 8.67, \ldots$.

This effect can be observed in figure 4.4 where equilibrium density profiles are depicted for different cavity sizes. The transition is located somewhere between panels (b) and (c). At each transition point the two coexisting structures are slightly distorted: the one with n^2 peaks is slightly expanded, whereas that with $(n+1)^2$ peaks is slightly compressed. Note that when the cavity size well commensurates with the bulk lattice parameter then the peaks are highly localized. In contrast, for poorly commensurating cavities these peaks are spatially smeared out. The elastic free energy cost associated with having a lattice parameter different from that of bulk is the driving mechanism of commensuration transitions.

In order to present the commensuration transitions we have compared the energy branches of each structure near the transition. In its vicinity two crystal structures with n^2 and $(n+1)^2$ peaks are possible, one of them as a metastable state. In figure 4.5(a) we schematically depict the energy branches as a function of H for two different structures for a fixed chemical potential. From the crossing point we obtain the cavity size at which the first order commensuration transition between these structures appears. Then proceeding in the same way for other values of μ we get the transition lines in the $\mu - H$ plane, see our results in figure 4.5(b). The crossing between energy branches become less clear

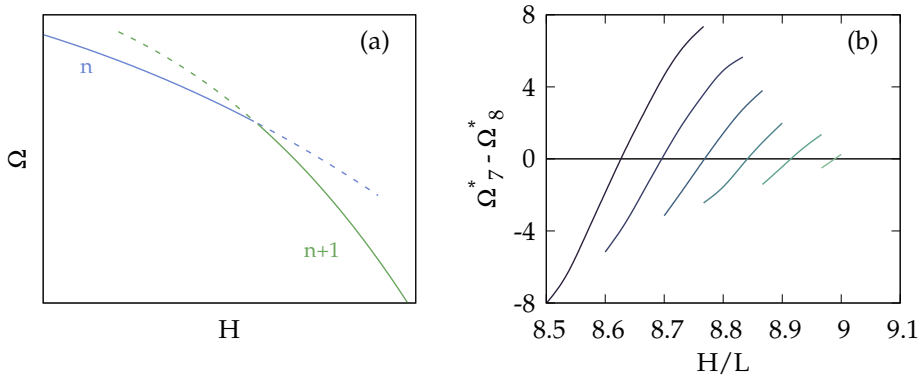

Figure 4.5: (a) Sketch of the crossing of energy curves for two different Cry structures with n^2 and $(n+1)^2$ peaks. Dashed lines represent metastable regions. (b) Dimensionless energy difference between Cry_7 and Cry_8 structures for different chemical potentials from $\beta\mu = 9.562$ (darker color) to $\beta\mu = 6.059$ (lighter color).

for low chemical potential until the point where these branches do not cross but are tangent. Under these conditions a critical point appears separating the isotropic phase and the two different crystal structures.

The whole phase diagram is presented in figure 4.6. The location of critical points tend asymptotically as $H \to \infty$ to the chemical potential corresponding to the bulk I–Col transition (dotted line). The solid lines departing from these points represent the $Cry_n \to Cry_{n+1}$ commensuration transitions. Note that the crystal structures inside the cavity emerge continuously from isotropic-like configurations as μ increases up to the points where commensuration transitions take place. Thus the continuous I–(Col,Cry) transitions at bulk are suppressed by confinement.

4.5.2 $\kappa = 3$

We now proceed to describe the phase behaviour of rectangular particles with aspect ratio $\kappa = 3$, so two different species are present: $\rho_x(\mathbf{r})$ and $\rho_y(\mathbf{r})$. Unlike the system of hard squares now stable or metastable nematic (N) and smectic (Sm) phases exist. The free energy minimization at bulk gives us the phase diagram shown in figure 4.7 with all stable and metastable energy branches corresponding to different phases. When density is increased we find the following sequence of equilibrium phases

$$I \to \text{Col}.$$

Like in the previous case the system exhibits a transition from isotropic to columnar phase. However, this transition is now of first order with coexisting

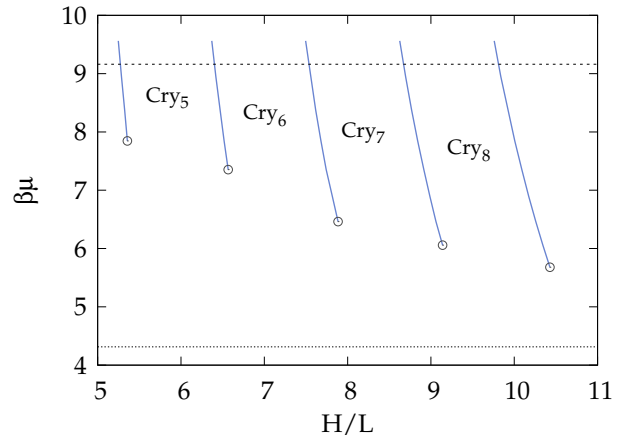

Figure 4.6: Phase diagram of the confined fluid with rods of aspect ratio $\kappa = 1$ in the $\mu - H$ plane. Solid lines represent first order commensuration transitions with open circles indicating the terminal critical points. Horizontal lines show the bulk chemical potential of the I→Col (dotted) and Col→Cry (dashed) transitions.

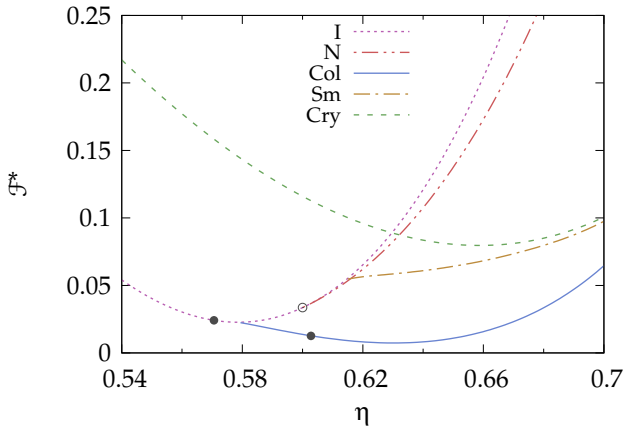

Figure 4.7: Free energy density branches in reduced units $\mathcal{F}^* \equiv \beta\mathcal{F}L\sigma/A - f$ of the I, N, Col, Sm and Cry phases as a function of packing fraction of rods with $\kappa = 3$. The straight line $f = a\eta + b$, with $a = 7.17$ and $b = -3.91$, has been subtracted from the free energies in order to better visualise the curves. The two solid circles are the coexisting packing fractions of the first order I→Col transition and the open circle represents the I→N bifurcation point.

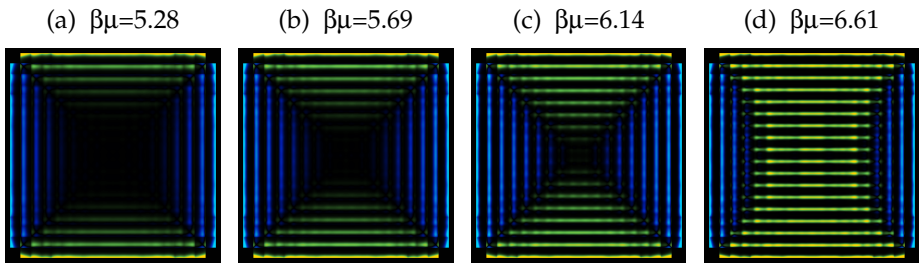

Figure 4.8: Density false-color plots of $Q(\mathbf{r})\rho(\mathbf{r})$ for $\kappa = 3$ and fixed cavity size $H = 7L$. Cases with different chemical potential values in the range $\beta\mu = 5.28$–6.61 are shown. Note that the situations corresponding to $\rho_y > \rho_x$ are represented in blue and $\rho_y < \rho_x$ in yellow-green.

packing fractions $\eta_I = 0.570$ and $\eta_{Col} = 0.603$. Note that the bifurcation to the nematic phase, as predicted by equation 4.12, is metastable and located at $\eta = 0.6$, above the I–Col transition.

The energy branch of the solid phase is that of the one-component system of parallel rods, i.e. that with $\gamma_x = 1, \gamma_y = 0$ or $\gamma_x = 0, \gamma_y = 1$. This crystal phase is equivalent to the one of the previous section ($\kappa = 1$) after rescaling the system along the particle axis. A crystal configuration with $0 < \gamma_x, \gamma_y < 1$ has not been found, however, another work (93), using the same model, obtained a plastic solid with $\gamma_x = \gamma_y$ as a metastable phase. This energy branch is less favoured than the Sm and Cry when increasing the density so it is not expected to play any role at very high packing fractions. Nevertheless, the crystal configuration may stabilize with respect to the columnar at higher densities because the energy branches become closer when increasing the density. Up to the maximum explored packing fraction $\eta \sim 0.73$ we have not found a stable Cry phase. From the tendency of the energy branches it seems that this transition, in case of existing, occurs near the close packing.

When the system is confined the excluded volume effects tend to align rods parallel to wall. As a consequence of this, columnar-like configurations are favoured near surfaces. In (93) surface properties of this fluid has been studied with the same theoretical model. That work studied the fluid of hard rectangles with $\kappa = 3$ in the presence of an infinite hard wall and showed that columnar layers wet the wall. When increasing the density this film of columnar phase adsorbed between the wall and the isotropic phase grows in thickness until it diverges at the bulk transition.

In the square cavity the behaviour is similar. The bulk I→Col transition remains first order for not too small cavities when the system is confined. In the confined isotropic phase the presence of the four walls promote columnar ordering in their neighbourhood but with two pairs promoting orthogonal orientations. The energy cost resulting from this frustration is relaxed at higher densities when the system exhibits a a strong symmetry breaking creating a

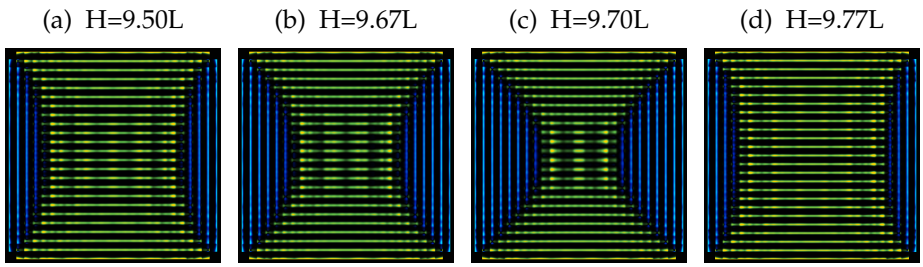

Figure 4.9: Density contour plots of confined structures for $\kappa = 3$ and $\beta\mu = 7.901$ indicating structural changes across one commensuration transition. Different cavity sizes from $H = 9.50L$ to $H = 9.77L$ are shown. These structures correspond to the $Col_{24} \rightarrow Col_{25}$ transition. Color code is the same as in figure 4.8.

large region of Col ordering. In figure 4.8 we can see a representation of these structures. A sequence of equilibrated density profiles belonging to the I→Col transition is shown in increasing order of chemical potential. The actual function plotted is $\rho(\mathbf{r})Q(\mathbf{r})$ in order to be able to visualize the two species ρ_ν at the same time. Horizontal rods have positive order parameter which is represented in yellow-green whereas vertical rods correspond to negative values of the order parameter, represented in bluish colors.

We call confined isotropic phase to a structure which is symmetric but with considerable Col-like oscillations propagating from the four walls, like those in (a)-(c) panels of figure 4.8. At the transition the symmetry is broken and a well-developed columnar structure, parallel to two of the surfaces, appears in the central region of the cavity, while two small islands of columns in the perpendicular direction are adsorbed on the other two surfaces. The confined columnar phase has a complicated structure that results from the inability to satisfy the parallel alignment of particles with respect to the four walls in a single uniform columnar phase. Only two such conditions can be verified and the result is the formation of two smaller regions at two opposing walls where surface orientation is parallel but opposite to that of the central wider columnar region.

Apart from I→Col transition we get again first order commensuration transitions, this time between columnar structures with different number of layers Col_n. A typical commensuration transition is shown in figure 4.9 where equilibrated profiles for fixed chemical potential and different cavity sizes are depicted. At the transition the system develops an additional layer in the central region. Because the orientational order is very high, the transition mainly involves translational degrees of freedom in the direction perpendicular to the columns and it is the wall distance along this direction that is relevant. In the sequence shown, the thermodynamic transition occurs at $H = 9.44L$ so the (a)-(c) panels correspond to metastable configurations of the Col_{24} phase. We have

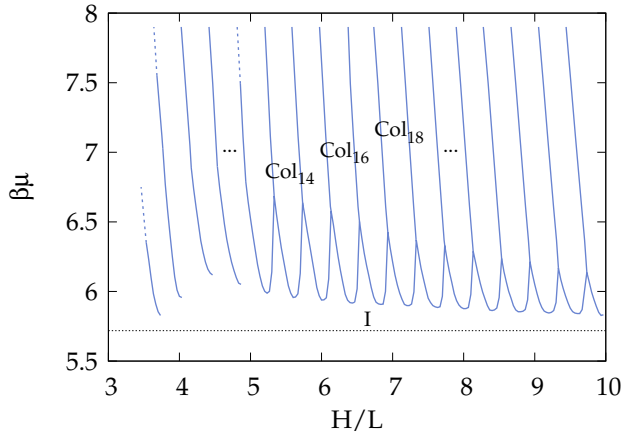

Figure 4.10: Phase diagram of the confined fluid with rods of aspect ratio $\kappa = 3$ in the $\mu - H$ plane. Dotted horizontal line corresponds to the bulk chemical potential of the I→Col transition. Dashed lines continuing commensuration transition at small cavity size are extrapolated from other results because of difficulties in numerical convergence.

selected these in order to show a possible way in which the nucleation of the new phase could take place when cavity size is changed smoothly. Of course this need not to be the kinetic behaviour of the transition but could give an insight of the process. A more careful method to study the dynamics within DFT will be studied in chapter 6.

Said this, the mentioned commensuration transitions present the following features. When increasing H the two columnar regions perpendicular to the main one grow in size at the expense of the central structure. This strong confined central region develops highly localized peaks which resemble locally more a crystal phase than a columnar one. When cavity size is larger this structure destabilizes and the peaks in the central region rearrange into a new columnar layer –with the surface structure largely unaffected– and the size of the regions with perpendicular orientation reduces to its usual value.

The whole phase diagram for the confined system in the $\mu - H$ plane is shown in figure 4.10. There are some important aspects to comment in that graphic. Note first that the confined I→Col transition (dotted horizontal line) is a highly non-monotonic function of cavity size and it is connected to commensuration transitions $\mathrm{Col}_n \rightarrow \mathrm{Col}_{n+1}$ (solid lines) between columnar structures with different number of layers. It is first order except for very small cavities $H \lesssim 5L$ where isotropic phase is continuously transformed into a columnar-like phase. Another important characteristic to notice is that the confined I→Col transition is always above the bulk one and tend to it when increasing cavity size. In the wetting situation where the fluid is confined between two walls one would expect the transition to occur below the bulk one. However, here we are also

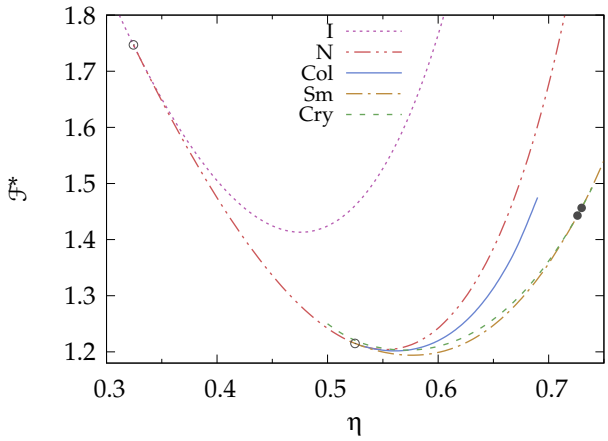

Figure 4.11: Free energy density branches in reduced units $\mathcal{F}^* \equiv \beta\mathcal{F}L\sigma/A - f$ of the I, N, Col, Sm and Cry phases as function of the packing fraction for rods with $\kappa = 6$. The straight line $f = a\eta + b$, with $a = 5.5$ and $b = -4$, has been subtracted from the free energies in order to better visualise the curves. The open circles represent the I→N and N→Sm transitions. The two solid circles correspond to the coexisting packing fractions of the first order Sm→Cry transition.

dealing with frustration effects. There are two pairs of perpendicular walls where wetting layers grow in different orientations, competing with each other and delaying the transition.

4.5.3 $\kappa = 6$

For $\kappa = 6$ the phase sequence at bulk is quite different from the previous cases. Now the Col phase is no longer stable and it is replaced by the Sm one. Furthermore rods are elongated enough so that nematic configuration becomes stable before non-uniform phases show up. The sequence that arises from the bulk phase diagram of figure 4.11 is

$$\mathrm{I} \to \mathrm{N} \to \mathrm{Sm} \to \mathrm{Cry}.$$

At low densities a second order I→N transition appears for $\eta = 0.324$. The nematic phase remains stable up to $\eta = 0.525$ where a continuous N→Sm transition takes place. In the region of smectic phase stability other inhomogeneous phases also exist although they are metastable. However, while the columnar energy branch strongly separates from the stable smectic branch, the crystal one remains close to the latter and finally becomes more stable. A first order Sm→Cry transition takes place with coexisting packing fractions of $\eta_{\mathrm{Sm}} = 0.726$ and $\eta_{\mathrm{Cry}} = 0.730$. This crystal phase is the same as the one discussed in the sys-

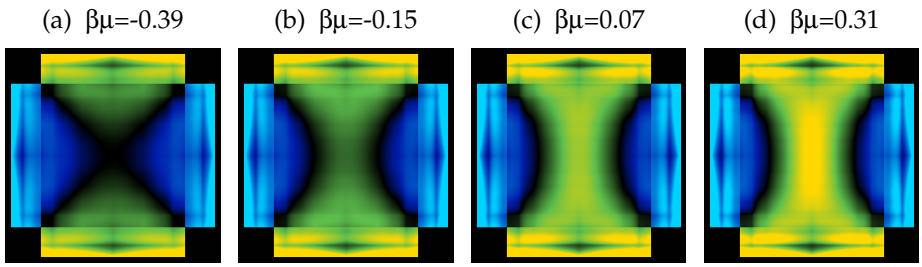

Figure 4.12: $Q(\mathbf{r})\rho(\mathbf{r})$ false-color plots of confined structures for rods with $\kappa = 6$ and $H = 3L$. $Q(\mathbf{r}) > 0$ ($\rho_x > \rho_y$) is represented in yellow-green and $Q(\mathbf{r}) < 0$ ($\rho_y > \rho_x$) in bluish colors. Structures for different values of chemical potential (indicated on top of each panel) are shown. (a) Symmetric configuration (confined I phase). (b)–(d) Symmetry-breaking configurations.

tem of $\kappa = 3$ but scaled properly, i.e. the one-component composed of parallel rods.

In the confined system the behaviour is more complex than previous cases due to larger number of stable phases present at bulk. We will see that in the confined system two regions with different phase behavior can be identified which constitute the confined counterpart of the bulk nematic and bulk smectic. They are separately covered in the following sections.

I→N transition under confinement

In principle one would not expect an I→N transition when confining since at bulk it is of second order. However, we do find it and it is due to a symmetry breaking of the nematic director inside the square cavity. In figure 4.12 we present the field $Q(\mathbf{r})\rho(\mathbf{r})$ for a given cavity when increasing the density. At low chemical potential –panel (a)– the confined structure is an isotropic phase with the density profile presenting near the walls some adsorption and local induced ordering parallel to them. In the center of the system the density is of course non-zero but order parameter is vanishingly small. This configuration is fully symmetric since it has the fourfold symmetry of the square cavity. Above a certain chemical potential one of the two competing particle orientations wins and breaks the symmetry in the central region of the cavity –(b)-(d) panels–. This symmetry breaking from fourfold to twofold has an associated continuous transition. The second order nature of this transition can be observed from the evolution of the order parameter in the square cavity. In figure 4.13 it is shown the average value of order parameter and the average of its absolute value defined as

$$\langle Q \rangle = \frac{1}{A}\int_{\mathcal{A}} d\mathbf{r} Q(\mathbf{r}), \quad \langle |Q| \rangle = \frac{1}{A}\int_{\mathcal{A}} d\mathbf{r} |Q(\mathbf{r})|. \tag{4.34}$$

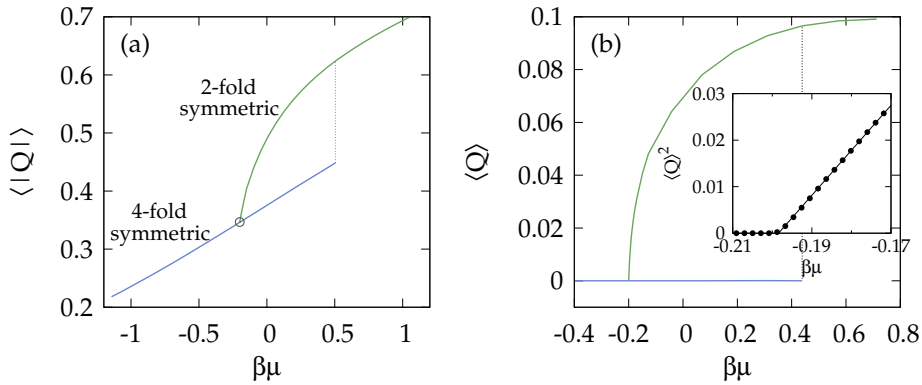

Figure 4.13: (a) Average of the absolute value of order parameter as a function of chemical potential around the surface I→N transition for $\kappa = 6$. Green line corresponds to the twofold nematic phase while the blue line corresponds to the fourfold isotropic phase with dotted line representing the jump to the stable configuration. (b) Mean order parameter. The inset corresponds to the square of the mean order parameter (points) around the transition with a linear fit (dashed line).

$\langle Q \rangle$ grows continuously from zero above the transition point along the stable twofold symmetric branch. However, if one use as initial guess a fourfold symmetric state one remains in the metastable branch until a given μ when it jumps to the twofold symmetric phase. In the inset of panel (b) it is shown the linear tendency of $\langle Q \rangle^2$ as a function of μ close and above the transition as expected from Landau theory.

This transition is of purely symmetry breaking and it is present only in squared cavities. We have also studied quasi-squared confined systems, i.e. cavities with one of the directions slightly longer than the other. The result is that there is no I→N transition indeed. The longest side breaks the symmetry and the orientation promoted by the longer walls makes one of the species to be favoured with respect to the other at any density. Consequently, the order parameter keeps always nonzero.

The surface I→N transition for different cavity sizes is presented in the phase diagram of figure 4.14. Notice that it has a non-monotonic behaviour and can occur above or below the value of the chemical potential corresponding to the bulk I→N transition, $\mu^*_{\text{I-N}}$. The chemical potential of the surface transition tend to $\mu^*_{\text{I-N}}$ as $H \to \infty$ and approaches to it from above. It can be understood from the surface properties of the fluid in contact with a single hard wall: we know that, as the continuous bulk transition is approached from below, there is a critical wetting in the wall-isotropic phase preceding the nematic phase. In the cavity, close to but below $\mu^*_{\text{I-N}}$, a film of the almost-critical wetting on each of the four walls should develop, causing orientational frustration in the central

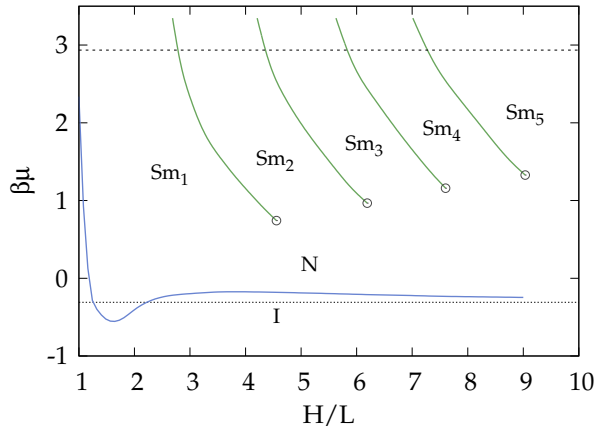

Figure 4.14: Phase diagram of the confined fluid of rods with aspect ratio $\kappa = 6$ in the $\mu - H$ plane. Solid green lines show the commensuration transitions and the solid blue line is the confined I→N transition. Horizontal lines correspond to the bulk I→N transition (dotted) and bulk N→Sm transition (dashed). Open circles are the terminal critical points of the commensurate transitions.

region of the cavity. This effect makes the symmetry-breaking mechanism to be postponed and the transition to occur above the bulk value.

The complex and oscillating behaviour of the surface I→N transition for very small cavities can be understood as follows: for cavity size $H \simeq 1.6L$ there is a minimum in the transition curve, followed by a maximum at larger $H \simeq 4.0L$. This feature is a consequence of particle size commensurating effects in the cavity. For $H \simeq 2.3L$ (where $\mu(H) \simeq \mu^*_{I\text{-}N}$) the density profile unusually presents its maxima in contact with the centers of the four walls, but no longer near the cavity corners as usually, since not more than one particle can now be accommodated parallel and close to the walls. When $H \simeq 1.2L$ (where again $\mu(H) \simeq \mu^*_{I\text{-}N}$) the unique density maximum is displaced to the center of the cavity. Now it is more difficult for particles to break the symmetry and be oriented along a single direction, thus the transition line increases to very high chemical potentials.

Smectic commensurate transitions under confinement

At higher densities we find a confined smectic phase, with no transition from the nematic. In the same way as the appearance of a crystal structure for $\kappa = 1$, we find here a continuous transformation from a nematic configuration to the smectic one when the density is increased. In contrast to bulk phases, confined ones are not purely nematic or smectic and, consequently, there is no way to trace out a clear separation between both confined phases in the phase diagram.

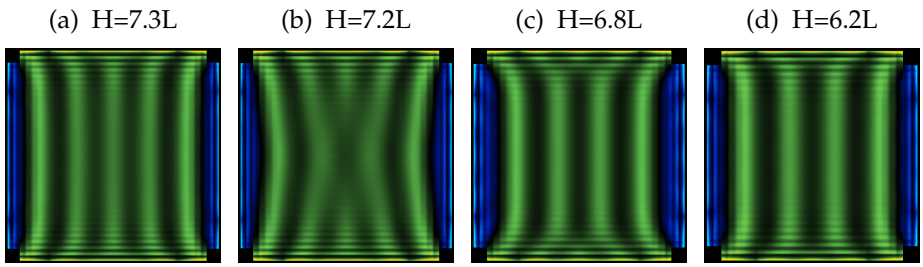

Figure 4.15: Density contour plots of confined structures for $\kappa = 6$ and $\beta\mu = 2.336$ indicating structural changes across one commensurate transition. Equilibrated profiles when decreasing cavity size from $H = 9.50L$ to $H = 9.77L$ are shown. These structures correspond to the $Sm_5 \rightarrow Sm_4$ transition. Color code is the same of figure 4.8.

When the nematic at the center of the cavity gets structured in different layers that resemble the smectic phase at bulk we obtain again first order commensuration transitions between smectic structures with different number of layers $Sm_n \rightarrow Sm_{n+1}$ when H or μ is changed. These transitions are analogous to their columnar and crystal counterparts seen in previous sections. For instance, in figure 4.15 we show a sequence of equilibrated profiles for a fixed chemical potential when the size of the cavity is decreased. In the same way as in $Col_n \rightarrow Col_{n-1}$ transitions for $\kappa = 3$, here the translational degrees of freedom are only important since the orientational order parameter is almost saturated. The commensuration mechanism is effective along the direction perpendicular to the layers and involves the distance between the walls parallel to the layers –vertical walls in the figure–. The other two walls –perpendicular to the layers– induce local ordering in their neighbourhood. In contrast to $\kappa = 3$, where the new column was nucleated in the central region and the surface structure remained unaltered, in this case the layer-growth mechanism involves defects that begin or end at the walls perpendicular to the layers. In the case of layer growth two defects are created at the two walls, which then propagate to the center of the cavity and give rise to a new smectic layer. In the case where one layer disappears the defects are formed at the center and then migrate to the walls. This is the case represented in figure 4.15, which corresponds to the $Sm_5 \rightarrow Sm_4$ transition as H is decreased. Note that the structures next to the vertical walls grow a bit as the transition takes place, squeezing the central region and bending the smectic layers. Again this behavior may be representative of the nucleation processes involving a change of one smectic layer. (a) and (b) panels correspond to the metastable part of Sm_5 phase while in (c) and (d) the system is already in the stable free energy branch of the Sm_4 phase.

Finally notice that in the phase diagram depicted in figure 4.14 the commensuration transitions occur below the bulk N→Sm but approaching to it when the size of the cavity is increased. This is a consequence of a capillary effect:

unlike the columnar case here there is not a competition between two smectics induced by walls because the existence of the nematic has already broken that symmetry. Then smectic layers are easily stabilized since the order parameter rapidly saturates and, consequently, particles begin to gain translational order.

4.6 REMARKS AND COMMENTS

In this last section we are going to remark the more important aspects shown by the results of our model. Let us begin saying that the weaker point of it is related to the restricted order approximation used. As previously mentioned, it probably does not well capture the behaviour at low densities because particles tend to cover a wide range of orientations. However, the main objective of this chapter was the study of highly ordered liquid crystal phases at high packing fractions and these structures are mainly populated with particles having parallel or mutually perpendicular orientations, even more in the squared confinement. In terms of the obtained results we can say that the spatially ordered phases (such as columnar, smectic or crystal) and the transitions between them transitions are very well captured. On the other hand, the description of cavities with isotropic and nematic ordering will be only qualitatively captured.

Let us begin discussing the latter cases. The prediction that the nematic phase is suppressed below some aspect ratio both in bulk and under confinement is correct but the exact value at which it takes place may not be very accurate, as well as the location at which the I→N transition occurs. The behaviour of the transition line depicted in figure 4.14 is probably correct for small cavities where, due to the square symmetry of it, parallel and perpendicular orientations will be much more likely and, consequently, the theory should be more accurate. Another important point is that our model can only predict a transition to a nematic with its main director parallel to one of the walls. However, we have already discussed in section 4.1.1 that a nematic phase with the director pointing in one of the diagonals may take place before, moving the transition to a lower density. An extension of our model to study the transition through these two different nematics configurations I→ N_1 → N_2 could be done by including two more species with orientations 45º (or 225º) and 135º (or 335º). In this way particles could be aligned parallel to walls and also in the diagonal direction. However, this would also require a great effort in constructing the model since the derivation of a fundamental-measure density functional with four species of hard rods would require severe approximations that would certainly affect the accurate description of particle correlations.

With respect to nonuniform phases, the model predicts the columnar structure to be stabilized for particles with short aspect ratio while the smectic phase becomes more stable for more elongated rods. At bulk both columnar and smectic phases are stable up to very high packing fractions. It is important to note that even though we know that the columnar phase at bulk for $\kappa = 1$ is a

spurious result –see chapter 3– its presence in systems of short rods for $\kappa > 1$ is correct (*108*). In the confined system the columnar phase for $\kappa = 1$ destabilizes with respect to the Cry phase and for $\kappa = 3$ and $\kappa = 6$ the Col and Sm configurations present two secondary small structures perpendicular to the main one in order to satisfy the wall induced order. This prediction has been later observed in experiments of confined colloidal particles which exhibit a phase behaviour in agreement with our theoretical results (*109*).

In summary the general scenario that emerges from the present work is the following: in a severely restricted geometry such as the square cavity, a liquid-crystal fluid is subject to several competing mechanisms: surface interactions, elasticity due to director deformation, surfaces with different normal orientation causing frustration... the competition of which causes a complex behavior in the confined system. This problem has been studied before concerning the confined nematic phase. Since our model can predict the stability of nonuniform bulk phases –smectic, columnar and crystal–, we have been able to extend these studies to incorporate the effect of spatial periodicity of nonuniform phases and the commensurate effects associated with their confinements. Capillarity, surface-generated frustration, and commensurating effects all work together to create complex phase behavior in the confined fluid.

5 BIAXIAL PARTICLES IN MONOLAYERS

5.1 INTRODUCTION

In this chapter we study the phase behaviour of three-dimensional particles with their centers of mass restricted to a flat surface. This system is equivalent to a mixture of two-dimensional particles, being these the projections of 3D particles in the monolayer. However, they are able to rotate and, consequently, the molar fractions of the different 2D projections can change. In particular we focus on the effect of particle biaxiality in its phase behaviour.

The interest on the orientational ordering generated by a system of biaxial particles (without axial symmetry) dates back to the first theoretical work by Freiser predicting a biaxial phase (*110*). The biaxial nematic phase is present when the main and secondary axes of particles are globally oriented along two different nematic directors, instead of the unique director present in the uniaxial nematic seen up to now. In figure 5.1 we show a sketch representation of board-like particles in uniaxial and biaxial nematic configurations. In the left panel –uniaxial nematic– the main axes of particles are vertically oriented but the secondary axes have arbitrary orientation. However, in the right panel –biaxial nematic– not only the main axes are oriented but also the secondary axes do, pointing perpendicular to the former.

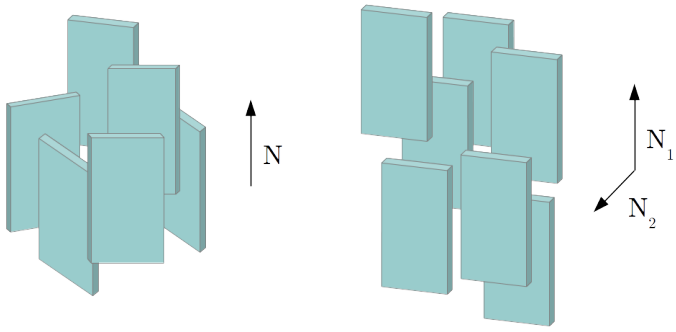

Figure 5.1: Left: board-like particles in uniaxial nematic configuration. Long edge length of particles are all oriented vertically. Right: particles in biaxial nematic phase with secondary axes also oriented.

The interest of nematic biaxial phases is due to the interesting novel properties and their possible applications. Among them one of the most promising

comes from its potential use in fast electro-optical devices. They may provide a much faster response to the change of external (usually electromagnetic) potentials as compared with uniaxial nematic based devices (*111*, *112*). As a consequence of this, a lot of research has been done in the searching of molecules exhibiting this phase (*113*–*117*).

In the theoretical framework the study of biaxial ordering has been based on hard-body and Gay–Berne-type interaction models for biaxial particles. Examples of particle shapes used in theoretical models are: sphero-platelets (*118*, *119*), biaxial ellipsoids (*120*, *121*) and bent-core particles (*122*–*125*). However, particle biaxiality is not a necessary condition in order to obtain a biaxial phase. The latter has also been found in binary mixtures of uniaxial plate-like and rod-like particles (*126*–*131*). Nevertheless, from an experimental point of view the realization of this exotic phase has proved to be rather complicated. The first observation dates back to the study of Yu and Saupe (*132*) in a lyotropic liquid crystal mixture forming cylindrical micelles. particles in the low density region. Later many experimental studies have observed the biaxial phase in a wide range of situations involving different particles shape (*133*).

The present study is based on board-like particles. Much of the interest in these particles comes from recent experimental observations of biaxial phase in suspensions of board-like goethite nanorods (*134*–*136*). These experiments have given rise to several theoretical studies in order to determine the global phase behavior of hard board-shaped particles (*119*, *137*) and also to identify those processes which promote the formation of the biaxial nematic phase (*138*, *139*). In a further step there has also been studied the effect of dimensional reduction on the stability of biaxial liquid-crystal phases by inserting goethite nanorods into a soft lamellar matrix of non-ionic surfactant (*140*–*142*).

The motivation of the work described in the present chapter lie in a better understanding of the ordering properties of board-shaped particles in confined geometries from a theoretical point of view. In particular we have studied the effect of particle biaxiality on the phase diagram emerging from a system of board-like particles constrained to a monolayer. Particles are three-dimensional but the fact that their centers of mass are constrained to 2D makes the problem similar to a system of two-dimensional particles –the projections of particles on the monolayer–. Consequently, we can adapt the FMT developed in chapter 2 in order to study the present system.

The chapter is organized as follows: firstly we present the model of the system in section 5.2. Then we develop the DFT for our system with uniform (section 5.3) and nonuniform (section 5.4) phases. The main results obtained from the theory are presented in section 5.5. Finally we conclude in section 5.6 with some comments and remarks.

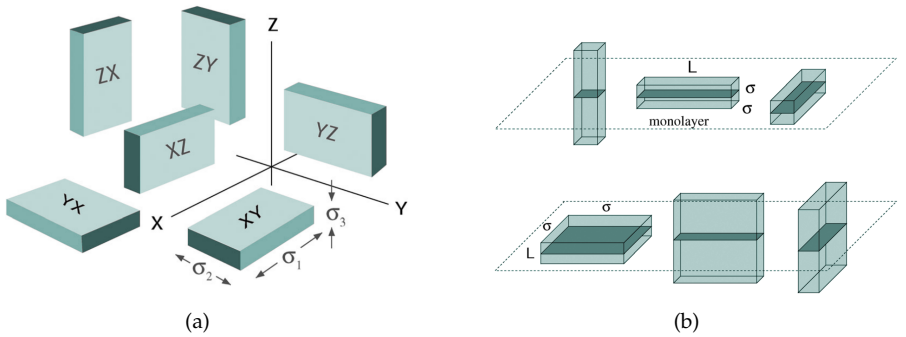

(a) (b)

Figure 5.2: Left: Board particles of edge-lengths $\sigma_1 \geqslant \sigma_2 \geqslant \sigma_3$. Six Zwanzig species are possible labelled by $\mu\nu$ representing the orientation of the main and intermediate particle length. Right: Particles and their projections (shadow areas) for uniaxial boards. In the upper panel is a prolate particle ($\sigma_1 = L$ and $\sigma_2 = \sigma_3 = \sigma$) with its three independent orientations and in the lower panel is an uniaxial oblate particle ($\sigma_1 = \sigma_2 = \sigma$ and $\sigma_3 = L$).

5.2 MODEL FOR BOARD-LIKE PARTICLES IN A MONOLAYER

In our model particles are hard boards defined by their three edge-lengths $\sigma_1 \geqslant \sigma_2 \geqslant \sigma_3$ and with their centers of mass resting in the monolayer plane. They are free to move within the flat surface and free to rotate in the full 3D solid angle. However, here we make use again of the Zwanzig approximation and only three orientations along the Cartesian axes are allowed. Regarding the particle symmetry this result in six possible orientations, sketched in left panel of figure 5.2. Then the system can be studied as a six-component mixture and the species can be identified by the labels $\mu\nu$. These two indices indicate the orientation of the longest $-\sigma_1-$ and intermediate $-\sigma_2-$ particle length, with $\mu, \nu = \{x, y, z\}$ and $\mu \neq \nu$.

Although particles are able to rotate in 3D, the system can be studied as effective 2D. Because particles are constrained to the monolayer the six-component mixture system is analogous to the system of their two-dimensional projections, as depicted in right panel of figure 5.2. And because their projections are squares and rectangles we can face the problem adapting the FMT used in previous chapters to the six-species mixture. In the next section the theoretical description will be shown.

In order to characterize the particle geometry it is more appropriate to use the two main particle aspect ratios defined as $\kappa_1 \equiv \sigma_1/\sigma_3$ and $\kappa_2 \equiv \sigma_2/\sigma_3$. These aspect ratios fulfill the relation $1 \leqslant \kappa_2 \leqslant \kappa_1$. In practice we fix $\sigma_3 = 1$ and choose the other edge lengths to define different particle shapes.

Another important particle property to be measured is the biaxiality. We define it via the following relation involving the two aspect ratios

$$\theta \equiv (\kappa_1 - 1)^{-1} \left(\frac{\kappa_1}{\kappa_2} - \kappa_2 \right). \tag{5.1}$$

It fulfills $\theta \in [-1, 1]$. Let us show that it accomplish the features of a biaxial geometric parameter: for fixed κ_1, θ varies from -1 (when $\kappa_2 = \kappa_1$, corresponding to uniaxial plate-like geometry) to 1 (when $\kappa_2 = 1$, pertaining to uniaxial rod-like geometry). The value $\theta = 0$ corresponds to perfect biaxiality, i.e. $\kappa_2 = \sqrt{\kappa_1}$. When $\kappa_2 > \sqrt{\kappa_1}$ particles are considered to be oblate whereas when $\kappa_2 < \sqrt{\kappa_1}$ particles are considered to be prolate.

5.3 FMT FOR NEMATIC PHASES

In the case of uniform phases, density profiles do not depend on spatial variables and the density of each species is given by $\rho_{\mu\nu} = \rho\gamma_{\mu\nu}$. Here ρ is the total 2D density and $\gamma_{\mu\nu}$ is the molar fraction of the species $\mu\nu$ and all of them fulfill the constraint $\sum_{\mu,\nu} \gamma_{\mu\nu} = 1$. The weighted functions within FMT extended to the six component mixture of hard rectangles with edge-lengths $\sigma^{\tau}_{\mu\nu} = \sigma_3 + (\sigma_1 - \sigma_3)\delta_{\tau\mu} + (\sigma_2 - \sigma_3)\delta_{\tau\nu}$ are

$$\omega^{(0)}_{\mu\nu}(\mathbf{r}) = \frac{1}{4}\delta\left(\frac{\sigma^x_{\mu\nu}}{2} - |x|\right)\delta\left(\frac{\sigma^y_{\mu\nu}}{2} - |y|\right) \tag{5.2}$$

$$\omega^{(1x)}_{\mu\nu}(\mathbf{r}) = \frac{1}{2}\Theta\left(\frac{\sigma^x_{\mu\nu}}{2} - |x|\right)\delta\left(\frac{\sigma^y_{\mu\nu}}{2} - |y|\right) \tag{5.3}$$

$$\omega^{(1y)}_{\mu\nu}(\mathbf{r}) = \frac{1}{2}\delta\left(\frac{\sigma^x_{\mu\nu}}{2} - |x|\right)\Theta\left(\frac{\sigma^y_{\mu\nu}}{2} - |y|\right) \tag{5.4}$$

$$\omega^{(2)}_{\mu\nu}(\mathbf{r}) = \Theta\left(\frac{\sigma^x_{\mu\nu}}{2} - |x|\right)\Theta\left(\frac{\sigma^y_{\mu\nu}}{2} - |y|\right) \tag{5.5}$$

and then the weighted densities, $n_\alpha(\mathbf{r}) = \sum_{\mu\nu}\left[\rho_{\mu\nu} * \omega^{(\alpha)}_{\mu\nu}\right](\mathbf{r})$, have the explicit expressions

$$n_0 = \frac{\rho^*}{\sigma_3^2} \quad n_{1x} = \frac{\rho^*}{\sigma_3}\Psi_{1x} \quad n_{1y} = \frac{\rho^*}{\sigma_3}\Psi_{1y} \quad n_2 = \rho^*\Psi_2 \tag{5.6}$$

where $\rho^* \equiv \rho\sigma_3^2$ is the density in reduced units and per unit area, and

$$\Psi_{1x} = (\gamma_{xy} + \gamma_{xz})\kappa_1 + (\gamma_{yx} + \gamma_{zx})\kappa_2 + \gamma_{zy} + \gamma_{yz} \tag{5.7}$$

$$\Psi_{1y} = (\gamma_{yx} + \gamma_{yz})\kappa_1 + (\gamma_{xy} + \gamma_{zy})\kappa_2 + \gamma_{zx} + \gamma_{xz} \tag{5.8}$$

$$\Psi_2 = (\gamma_{xy} + \gamma_{yx})\kappa_1\kappa_2 + (\gamma_{xz} + \gamma_{yz})\kappa_1 + (\gamma_{zx} + \gamma_{zy})\kappa_2. \tag{5.9}$$

The ideal part of the free energy in reduced units is

$$\Phi^*_{id} \equiv \Phi_{id}\sigma_3^2 = \beta\mathcal{F}_{id}\sigma_3^2/A = \rho^* \left[\ln \rho^* - 1 + \sum_{\mu,\nu} \gamma_{\mu\nu} \ln \gamma_{\mu\nu}\right] \tag{5.10}$$

and the excess part comes as

$$\Phi^*_{exc} \equiv \Phi_{exc}\sigma_3^2 = \beta\mathcal{F}_{exc}\sigma_3^2/A = \sigma_3^2 \left[-n_0 \ln(1-n_2) + \frac{n_{1x}n_{1y}}{1-n_2}\right] = \\ = \rho^* \left[-\ln(1-\eta) + y\Psi_{1x}\Psi_{1y}\right] \tag{5.11}$$

where the packing fraction η is just the value of n_2 function –for uniform systems– and we have also defined $y \equiv \rho^*/(1-\eta)$.

To obtain the equilibrium molar fractions we need to minimize the total free energy density $\Phi^* = \Phi^*_{id} + \Phi^*_{exc}$ with respect to $\gamma_{\mu\nu}$, obtaining

$$\gamma_{\mu\nu} = \frac{e^{-\chi_{\mu\nu}}}{\sum_{\alpha\beta} e^{-\chi_{\alpha,\beta}}} \tag{5.12}$$

with

$$\chi_{\mu\nu} = y\left[\Psi_{1x}\kappa^y_{\mu\nu} + \Psi_{1y}\kappa^x_{\mu\nu} + \left(1 + y\Psi_{1x}\Psi_{1y}\right)\kappa^x_{\mu\nu}\kappa^y_{\mu\nu}\right] \tag{5.13}$$

being $\kappa^\tau_{\mu\nu} = 1 + (\kappa_1 - 1)\delta_{\tau\mu} + (\kappa_2 - 1)\delta_{\tau\nu}$ ($\tau = \{x, y\}$ and $\delta_{\tau\mu}$ is the Kronecker delta).

The system of equations 5.12 cannot be solved analytically, we solved it through an iterative fixed point method.

Finally, the chemical potentials of the species at equilibrium have the same value and read

$$\beta\mu_{\tau\nu} = \beta\mu_0 = \ln\left(\frac{y}{\sum_{\alpha,\beta} e^{-\chi_{\alpha\beta}}}\right), \quad \forall\, \tau, \nu \tag{5.14}$$

and the pressure in reduced units is

$$p^* \equiv \sigma_3^2\left(\frac{n_0}{1-n_2} + \frac{n_{1x}n_{1y}}{(1-n_2)^2}\right) = y + y^2\Psi_{1x}\Psi_{1y} \tag{5.15}$$

which are required to calculate the coexistence densities in the case of first order phase transitions.

5.3.1 Uniform phases and order parameters

Depending on the relative molar fractions of species we can distinguish different uniform phases:

ISOTROPIC (I): all species are equally represented.

$$\gamma_{\mu\nu} = 1/6 \quad \forall\, \mu, \nu.$$

UNIAXIAL NEMATIC (N_u): the molar fractions are equal in pairs

$$\gamma_{zx} = \gamma_{zy} \neq \gamma_{xz} = \gamma_{yz} \neq \gamma_{xy} = \gamma_{yx}.$$

BIAXIAL NEMATICS (N_b): in general they are all different:

$$\gamma_{zx} \neq \gamma_{zy} \neq \gamma_{xz} \neq \gamma_{yz} \neq \gamma_{xy} \neq \gamma_{yx}.$$

In order to determine the degree of order in each phase it is very useful to define order parameters for the uniaxial and biaxial configurations. In the case of biaxial particles two order tensors can be defined

$$\hat{Q}_{ij} = \frac{1}{2}\left\langle 3u_i u_j - \delta_{ij} \right\rangle \qquad \hat{B}_{ij} = \frac{1}{2}\left(\langle n_i n_j \rangle - \langle m_i m_j \rangle \right) \tag{5.16}$$

with $i, j = \{1, 2, 3\}$ and where u_k, n_k and m_k are the k-components of the unit vectors **u**, **n** and **m** along the longest, intermediate and smallest particle lengths respectively. $\hat{Q}_{ij}$ is the usual nematic ordering tensor and $\hat{B}_{ij}$ accounts for the biaxial ordering. Following the Zwanzig model these tensors are diagonal and have the explicit form

$$\hat{Q} = \begin{pmatrix} -\dfrac{Q - \Delta_Q}{2} & 0 & 0 \\ 0 & -\dfrac{Q + \Delta_Q}{2} & 0 \\ 0 & 0 & Q \end{pmatrix} \tag{5.17}$$

$$\hat{B} = \begin{pmatrix} -\dfrac{B - \Delta_B}{2} & 0 & 0 \\ 0 & -\dfrac{B + \Delta_B}{2} & 0 \\ 0 & 0 & B \end{pmatrix} \tag{5.18}$$

with Q and B are uniaxial nematic order parameters defined as

$$Q \equiv Q_{zz} = \frac{1}{2}\left(3 \sum_{\nu \neq z} \gamma_{z\nu} - 1 \right) \tag{5.19}$$

$$B \equiv B_{zz} = \frac{1}{2}\left(\sum_{\mu \neq z} \gamma_{\mu z} - \sum_{\mu,\nu \neq z} \gamma_{\mu\nu} \right). \tag{5.20}$$

where, without loose of generality, we have taken the main director of prolate particles pointing along the z axis. The case of oblate particles is discussed

below. Q is the usual uniaxial order parameter and note that $B \neq 0$ for both uniaxial and biaxial symmetries. The biaxial order parameters can be obtained as

$$\Delta_Q \equiv Q_{xx} - Q_{yy} = \frac{3}{2}\left(\sum_{\nu\neq x}\gamma_{x\nu} - \sum_{\nu\neq y}\gamma_{y\nu}\right) \tag{5.21}$$

$$\Delta_B \equiv B_{xx} - B_{yy} = \frac{1}{2}\left(\sum_{\mu\neq x}\gamma_{\mu x} - \sum_{\mu\neq y}\gamma_{\mu y} + \sum_{\mu,\nu\neq y}\gamma_{\mu\nu} - \sum_{\mu,\nu\neq x}\gamma_{\mu\nu}\right) \tag{5.22}$$

which are different from zero only in biaxial configurations.

Note that for uniaxial rods ($\theta = 1$), the vector **u** points along the main symmetry axis –longest particle length–, the other two being equivalent. Thus, the above definitions for $\{Q, B, \Delta_Q, \Delta_B\}$ are correct in the limit $\theta \to 1$, and they will be used for any $\theta > 0$. However, for uniaxial oblate particles ($\theta = -1$), the main particle axis should be taken to lie along the shortest particle length **m**, the other two being equivalent: **u** and **m** should be interchanged for $\theta < 0$, and all four order parameters can be obtained from the same formulas as before but replacing $\gamma_{\mu\nu}$ by $\gamma_{\tau\nu}$ (with $\tau \neq \mu, \nu$). In this way we obtain, for example, that $Q \to -1/2$ for perfect planar nematic ordering, as it should be.

As a consequence of this, the parameter $\Delta_Q^* \equiv 2\Delta_Q/3$ will be used to measure the degree of biaxiality for uniaxial plate-like and rod-like particles ($\theta = \pm 1$), while in the case of biaxial particles ($-1 < \theta < 1$) the parameter Δ_B will be the one used. It can be shown that, for perfect biaxial order, $|\Delta_B| \to 1$ and 0.5 for rods and plates respectively, while $|\Delta_Q^*| \to 1$ for both particles. In any case, we will always use absolute values of biaxial order parameters in the results.

5.3.2 Bifurcation to biaxial phase

This section is devoted to the calculation of the uniaxial-biaxial second order transition line in the phase diagram. To do so let us define the new variables $x_\pm = (\gamma_{zx} \pm \gamma_{zy})/2$, $y_\pm = (\gamma_{xz} \pm \gamma_{yz})/2$, and $z_\pm = \left(\gamma_{xy} \pm \gamma_{yx}\right)/2$. Note that for the uniaxial nematic phase these variables are just $x_+ = \gamma_{zx}$, $y_+ = \gamma_{xz}$, $z_+ = \gamma_{xy}$ and $x_- = y_- = z_- = 0$. Let us also define the quantities

$$s_\pm = x_\pm(\kappa_2 \pm 1) + y_\pm(\kappa_1 \pm 1) + z_\pm(\kappa_1 \pm \kappa_2). \tag{5.23}$$

In this new variables we find that

$$\Psi_{1x}\Psi_{1y} = s_+^2 - s_-^2, \quad \Psi_2 = 2\left(x_+\kappa_2 + y_+\kappa_1 + z_+\kappa_1\kappa_2\right). \tag{5.24}$$

Then the ideal part of the free energy density becomes

$$\Phi^*_{id} = \rho^* \left\{ \ln \rho^* - 1 + \sum_{\nu=\pm 1} [(x_+ + \nu x_-) \ln (x_+ + \nu x_-) + \right.$$
$$\left. + (y_+ + \nu y_-) \ln (y_+ + \nu y_-) + (z_+ + \nu z_-) \ln (z_+ + \nu z_-)] \right\} \quad (5.25)$$

while the excess part has the same expression as in equation 5.11. We minimize the total free energy with respect to $x_\pm$, $y_\pm$ and $z_\pm$ and obtain the following set of equations

$$\ln \left(x_+^2 - x_-^2\right) + 2\lambda \left[1 + \lambda(s_+^2 - s_-^2)\right] \kappa_2 + 2\lambda(\kappa_2 + 1)s_+ + 2\Lambda = 0 \quad (5.26)$$
$$\ln \left(y_+^2 - y_-^2\right) + 2\lambda \left[1 + \lambda(s_+^2 - s_-^2)\right] \kappa_1 + 2\lambda s_+(\kappa_1 + 1) + 2\Lambda = 0 \quad (5.27)$$
$$\ln \left(z_+^2 - z_-^2\right) + 2\lambda \left[1 + \lambda(s_+^2 - s_-^2)\right] \kappa_1\kappa_2 + 2\lambda(\kappa_1 + \kappa_2)s_+ + 2\Lambda = 0 \quad (5.28)$$
$$\ln \left(\frac{x_+ + x_-}{x_+ - x_-}\right) - 2\lambda(\kappa_2 - 1)s_- = 0 \quad (5.29)$$
$$\ln \left(\frac{y_+ + y_-}{y_+ - y_-}\right) - 2\lambda(\kappa_1 - 1)s_- = 0 \quad (5.30)$$
$$\ln \left(\frac{z_+ + z_-}{z_+ - z_-}\right) - 2\lambda(\kappa_1 - \kappa_2)s_- = 0 \quad (5.31)$$

with Λ being a Lagrange multiplier which guarantees the constraint $2(x_+ + y_+ + z_+) = 1$ and where

$$\lambda = \frac{\rho^*}{1 - \rho^* \Psi_2}. \quad (5.32)$$

In the neighbourhood of the transition line, in the region of biaxial phase stability, we have that x_-, y_-, $z_- \approx 0$ so we can expand equations 5.29, 5.30 and 5.29 up to first order in these variables. The result can be written in a matrix form $A \cdot \mathbf{v} = \mathbf{0}$, with $\mathbf{v} = (x_-, y_-, z_-)^t$ and A being

$$\begin{pmatrix} 1 - \lambda(\kappa_2 - 1)^2 x_+ & -\lambda(\kappa_1 - 1)(\kappa_2 - 1)x_+ & -\lambda(\kappa_1 - \kappa_2)(\kappa_2 - 1)x_+ \\ -\lambda(\kappa_1 - 1)(\kappa_2 - 1)y_+ & 1 - \lambda(\kappa_1 - 1)^2 y_+ & -\lambda(\kappa_1 - \kappa_2)(\kappa_1 - 1)y_+ \\ -\lambda(\kappa_1 - \kappa_2)(\kappa_2 - 1)z_+ & -\lambda(\kappa_1 - \kappa_2)(\kappa_1 - 1)z_+ & 1 - \lambda(\kappa_1 - \kappa_2)^2 z_+. \end{pmatrix} \quad (5.33)$$

This matrix should be evaluated at $x_+ = \gamma_{zx}$, $y_+ = \gamma_{xz}$ and $z_+ = \gamma_{xy}$ which are the correct limits at the transition. The nontrivial solution of $A \cdot \mathbf{v} = \mathbf{0}$ is reached when $|A| = 0$ which is equivalent to the condition

$$\begin{aligned}\lambda^{-1} &= x_+(\kappa_2 - 1)^2 + y_+(\kappa_1 - 1)^2 + z_+(\kappa_1 - \kappa_2)^2 \\ &= \frac{(\kappa_1 - \kappa_2)^2}{2} - (\kappa_1 - 1)(\kappa_1 + 1 - 2\kappa_2)x_+ - (\kappa_2 - 1)(\kappa_2 + 1 - 2\kappa_1)y_+.\end{aligned} \tag{5.34}$$

The values of x_+, y_+ and z_+ are those obtained from equations 5.26, 5.27 and 5.28 considering $x_- = y_- = z_- = 0$. Note that, as they are not independent variables, we can solve the equations for x_+ and y_+ and substitute $z_+ = 1/2 - x_+ - y_+$ in all the parameters depending on z_+. This results in

$$x_+ = C^{-1} e^{-\lambda\left[\kappa_2(1+\lambda s_+^2) + (\kappa_2+1)s_+\right]} \tag{5.35}$$

$$y_+ = C^{-1} e^{-\lambda\left[\kappa_1(1+\lambda s_+^2) + (\kappa_1+1)s_+\right]} \tag{5.36}$$

$$\begin{aligned}C = 2\Bigg\{ & e^{-\lambda\left[\kappa_2(1+\lambda s_+^2) + (\kappa_2+1)s_+\right]} \\ & + e^{-\lambda\left[\kappa_1(1+\lambda s_+^2) + (\kappa_1+1)s_+\right]} \\ & + e^{-\lambda\left[\kappa_1\kappa_2(1+\lambda s_+^2) + (\kappa_1+\kappa_2)s_+\right]}\Bigg\}\end{aligned} \tag{5.37}$$

where, considering that $x_+ + y_+ + z_+ = 1/2$, s_+ can be rewritten as

$$s_+ = \frac{\kappa_1 + \kappa_2}{2} - (\kappa_1 - 1)x_+ - (\kappa_2 - 1)y_+. \tag{5.38}$$

Once these values are found the packing fraction at which the bifurcation occurs can be calculated from

$$\eta = \frac{\lambda\Psi_2}{1 + \lambda\Psi_2}, \quad \Psi_2 = \kappa_1\kappa_2 - 2\kappa_2(\kappa_1 - 1)x_+ - 2\kappa_1(\kappa_2 - 1)y_+. \tag{5.39}$$

Finally it is important to note that for some values of particle biaxiality, θ, there might exist more than one value of packing fraction at which bifurcations occur. In order to obtain all of them we have started the minimization with different initial guesses.

5.3.3 Critical end-point of the N-B transition

As we will see in section 5.5, the uniaxial-biaxial transition does not exist for any pair of particle aspect ratios κ_1 and κ_2. Here we obtain the terminal points that

separate the phase diagram in regions with different number of uniaxial-biaxial phase transitions. These points are those where the spinodal, $\rho'(\theta) \to \infty$, has an infinite derivative.

The transition line defined by equations 5.35 and 5.36 can be rewritten as

$$f_1(x_+, y_+) \equiv x_+ - \frac{e^{-\xi_1(x_+,y_+)}}{2\sum_{i=0}^{3} e^{-\xi_i(x_+,y_+)}} \tag{5.40}$$

$$f_2(x_+, y_+) = y_+ - \frac{e^{-\xi_2(x_+,y_+)}}{2\sum_{i=0}^{3} e^{-\xi_i(x_+,y_+)}} \tag{5.41}$$

where the functions $\xi_i(x_+, y_+)$ are

$$\xi_1(x_+, y_+) = -\lambda\left[\kappa_2(1+\lambda s_+^2) + (\kappa_2+1)s_+\right] \tag{5.42}$$

$$\xi_2(x_+, y_+) = -\lambda\left[\kappa_1(1+\lambda s_+^2) + (\kappa_1+1)s_+\right] \tag{5.43}$$

$$\xi_3(x_+, y_+) = -\lambda\left[\kappa_1\kappa_2(1+\lambda s_+^2) + (\kappa_1+\kappa_2)s_+\right]. \tag{5.44}$$

Then the critical end-points of the transition line come by setting the Jacobian to zero

$$J(x_+, y_+) \equiv \begin{vmatrix} \frac{\partial f_1}{\partial x_+} & \frac{\partial f_1}{\partial y_+} \\ \frac{\partial f_2}{\partial x_+} & \frac{\partial f_2}{\partial y_+} \end{vmatrix} = 0 \tag{5.45}$$

after some algebra it results in

$$\begin{aligned} J(x_+, y_+) = {} & 1 + 3x_+y_+(1-2x_+-2y_+)\lambda^3(\kappa_1-1)^2(\kappa_2-1)^2(\kappa_2-\kappa_1)^2 \\ & + x_+(1-2x_+)\frac{\partial \xi_{13}}{\partial x_+} + y_+(1-2y_+)\frac{\partial \xi_{23}}{\partial y_+} - 2x_+y_+\left(\frac{\partial \xi_{23}}{\partial x_+} + \frac{\partial \xi_{13}}{\partial y_+}\right) \end{aligned} \tag{5.46}$$

where we have defined $\xi_{i3} \equiv \xi_i - \xi_3$ which have the following explicit expressions for their derivatives

$$\frac{\partial \xi_{13}}{\partial x_+} = -\left[\lambda\left(\kappa_2 + (1 + 2\lambda\kappa_2 s_+)s_+\right)(\kappa_1 + 1 - 2\kappa_2) - 1 - 2\lambda\kappa_2 s_+\right]\lambda(\kappa_1 - 1)^2 \tag{5.47}$$

$$\frac{\partial \xi_{13}}{\partial y_+} = -\left[\lambda\left(\kappa_2 + (1 + 2\lambda\kappa_2 s_+)s_+\right)(\kappa_2 + 1 - 2\kappa_1) - 1 - 2\lambda\kappa_2 s_+\right]\lambda(\kappa_1 - 1)(\kappa_2 - 1) \tag{5.48}$$

$$\frac{\partial \xi_{23}}{\partial x_+} = -\left[\lambda\left(\kappa_1 + (1 + 2\lambda\kappa_1 s_+)s_+\right)(\kappa_1 + 1 - 2\kappa_2) - 1 - 2\lambda\kappa_1 s_+\right]\lambda(\kappa_1 - 1)(\kappa_2 - 1) \tag{5.49}$$

$$\frac{\partial \xi_{23}}{\partial y_+} = -\left[\lambda\left(\kappa_1 + (1 + 2\lambda\kappa_1 s_+)s_+\right)(\kappa_2 + 1 - 2\kappa_1) - 1 - 2\lambda\kappa_1 s_+\right]\lambda(\kappa_2 - 1)^2. \tag{5.50}$$

Thus the critical end points can be calculated by solving equations 5.35, 5.36 and 5.45 with the previous explicit expressions.

5.4 FMT FOR NONUNIFORM PHASES

The nematic phases obtained in the preceding section will be stable as long as nonuniform phases are unstable. For high enough densities inhomogeneous configurations –such as columnar, smectic or crystal– may appear. In order to obtain the transition to nonuniform phases we calculate the spinodal instability of a uniform phase with respect to density modulations of a given symmetry. As explained in section 4.3.2, the natural way of dealing with nonuniform phases is in the Fourier space. Then the spinodal instability can be obtained by searching the singularities of the inverse of the structure factor matrix, whose elements in the Fourier space and in reduced units are

$$T_{\mu\nu,\tau\iota}(\mathbf{q}^*, \rho^*) = \delta_{\mu\nu,\tau\iota} - \rho\sqrt{\gamma_{\mu\nu}\gamma_{\tau\iota}}\hat{c}_{\mu\nu,\tau\iota}(\mathbf{q}^*, \rho^*) \tag{5.51}$$

with $\hat{c}_{\mu\nu,\tau\iota}(\mathbf{q}^*, \rho^*)$ being the Fourier transforms of the direct correlation functions, calculated from the second functional derivatives of $\mathcal{F}_{exc}[\{\rho_{\mu\nu}\}]$

$$-\hat{c}_{\mu\nu,\tau\iota}(\mathbf{q}^*, \rho^*) = \sum_{\alpha,\beta} \frac{\partial^2 \Phi_{exc}}{\partial n_\alpha \partial n_\beta} \hat{\omega}^{(\alpha)}_{\mu\nu}(\mathbf{q}^*)\hat{\omega}^{(\beta)}_{\tau\iota}(\mathbf{q}^*) \tag{5.52}$$

with $\alpha, \beta \in \{0, 1x, 1y, 2\}$, and where we have also denoted

$$\delta_{\mu\nu,\tau\iota} = \begin{cases} 1 & \text{if} \quad \mu = \tau, \quad \text{and} \quad \nu = \iota \\ 0 & \text{otherwise.} \end{cases} \tag{5.53}$$

The Fourier transforms of the weighting functions have the explicit forms

$$\hat{\omega}^{(0)}_{\mu\nu}(\mathbf{q}^*) \equiv \hat{w}^{(0)}_{\mu\nu}(\mathbf{q}^*) = \prod_{\tau=x,y} \chi_0\left(\frac{q^*_\tau \kappa^\tau_{\mu\nu}}{2}\right) \tag{5.54}$$

$$\hat{\omega}^{(1x)}_{\mu\nu}(\mathbf{q}^*) \equiv \sigma_3 \hat{w}^{(1x)}_{\mu\nu}(\mathbf{q}^*) = \sigma_3 \kappa^x_{\mu\nu} \chi_1\left(\frac{q^*_x \kappa^x_{\mu\nu}}{2}\right) \chi_0\left(\frac{q^*_y \kappa^y_{\mu\nu}}{2}\right) \tag{5.55}$$

$$\hat{\omega}^{(1y)}_{\mu\nu}(\mathbf{q}^*) \equiv \sigma_3 \hat{w}^{(1y)}_{\mu\nu}(\mathbf{q}^*) = \sigma_3 \kappa^y_{\mu\nu} \chi_0\left(\frac{q^*_x \kappa^x_{\mu\nu}}{2}\right) \chi_1\left(\frac{q^*_y \kappa^y_{\mu\nu}}{2}\right) \tag{5.56}$$

$$\hat{\omega}^{(2)}_{\mu\nu}(\mathbf{q}^*) \equiv \sigma_3^2 \hat{w}^{(2)}_{\mu\nu}(\mathbf{q}^*) = \sigma_3^2 \prod_{\tau=x,y} \kappa^\tau_{\mu\nu} \chi_1\left(\frac{q^*_\tau \kappa^\tau_{\mu\nu}}{2}\right) \tag{5.57}$$

where we have introduced the functions $\hat{w}^{(\alpha)}_{\mu\nu}(\mathbf{q}^*)$ and also we have defined $\chi_0(x) \equiv \cos(x)$, $\chi_1(x) \equiv \sin(x)/x$ for $x \neq 0$ while $\chi_1(0) \equiv 1$. The derivatives of the excess free energy with respect to the weighted densities are

$$\frac{\partial^2 \Phi_{exc}}{\partial n_0 \partial n_2} = \frac{\partial^2 \Phi_{exc}}{\partial n_{1x} \partial n_{1y}} = \frac{1}{1-n_2} = \frac{y}{\rho^*} \tag{5.58}$$

$$\frac{\partial^2 \Phi_{exc}}{\partial n_{1x} \partial n_2} = \frac{n_{1y}}{(1-n_2)^2} = \frac{y^2 \Psi_{1y}}{\rho^* \sigma_3} \tag{5.59}$$

$$\frac{\partial^2 \Phi_{exc}}{\partial n_{1y} \partial n_2} = \frac{n_{1x}}{(1-n_2)^2} = \frac{y^2 \Psi_{1x}}{\rho^* \sigma_3} \tag{5.60}$$

$$\frac{\partial^2 \Phi_{exc}}{\partial n_2^2} = \frac{n_0}{(1-n_2)^2} + \frac{2 n_{1x} n_{1y}}{(1-n_2)^3} = \frac{y^2 + 2y^3 \Psi_{1x} \Psi_{1y}}{\rho^* \sigma_3^2}. \tag{5.61}$$

Then the elements of the inverse of the structure factor matrix can be written as

$$\begin{aligned} T_{\mu\nu,\tau\iota}(\mathbf{q}^*, \rho^*) = \delta_{\mu\nu,\tau\iota} + y\sqrt{\gamma_{\mu\nu}\gamma_{\tau\iota}} \Big\{ & \langle \hat{w}^{(0)}_{\mu\nu}(\mathbf{q}^*) \hat{w}^{(2)}_{\tau\iota}(\mathbf{q}^*) \rangle \\ & + \langle \hat{w}^{(1x)}_{\mu\nu}(\mathbf{q}^*) \hat{w}^{(1y)}_{\tau\iota}(\mathbf{q}^*) \rangle + y \Big[\Psi_{1y} \langle \hat{w}^{(1x)}_{\mu\nu}(\mathbf{q}^*) \hat{w}^{(2)}_{\tau\iota}(\mathbf{q}^*) \rangle \\ & + \Psi_{1x} \langle \hat{w}^{(1y)}_{\mu\nu}(\mathbf{q}^*) \hat{w}^{(2)}_{\tau\iota}(\mathbf{q}^*) \rangle + \left(1 + 2y \Psi_{1x} \Psi_{1y}\right) \hat{w}^{(2)}_{\mu\nu}(\mathbf{q}^*) \hat{w}^{(2)}_{\tau\iota}(\mathbf{q}^*) \Big] \Big\} \end{aligned} \tag{5.62}$$

where it has been defined

$$\langle \hat{w}^{(\alpha)}_{\mu\nu}(\mathbf{q}^*) \hat{w}^{(\beta)}_{\tau\iota}(\mathbf{q}^*) \rangle \equiv \hat{w}^{(\alpha)}_{\mu\nu}(\mathbf{q}^*) \hat{w}^{(\beta)}_{\tau\iota}(\mathbf{q}^*) + \hat{w}^{(\beta)}_{\mu\nu}(\mathbf{q}^*) \hat{w}^{(\alpha)}_{\tau\iota}(\mathbf{q}^*). \tag{5.63}$$

Therefore the spinodal instability of a uniform phase with respect to density modulations can be found from the conditions that the determinant of the matrix and its gradient are zero

$$|T(\mathbf{q}^*, \rho^*)| = 0, \quad \boldsymbol{\nabla}_{\mathbf{q}^*} |T(\mathbf{q}^*, \rho^*)| = 0. \tag{5.64}$$

With this procedure we find the values ρ^*_b and $\mathbf{q}^*_b$ at bifurcation, i.e. the first value of ρ^*_b for which $|T(\mathbf{q}^*, \rho^*_b)| = 0$ for some $\mathbf{q}^*$. In practice we select $\mathbf{q}^* =$

$(q_x^*, 0)$ or $\mathbf{q}^* = (0, q_y^*)$ with $q_{x,y}^* = 2\pi\sigma_3/d_{x,y}$ where d_x and d_y are the periods of nonuniform phases along x and y respectively. Thus the gradient in equation 5.64 should be replaced by the partial derivatives $\partial/\partial q_x^*$ or $\partial/\partial q_y^*$ respectively. The values $\gamma_{\mu\nu}$ at each step of the numerical procedure used to solve equations 5.64 are found from the solution of equation 5.12.

5.5 RESULTS

Let us study now the phase behaviour of the system as obtained from the developed theory. In order to present it in a clear way we will first study the phase diagram for particles with low κ_1 as a function of particle biaxiality. In a further step we will study how the topology of the phase diagram changes when increasing the largest aspect ratio of particles, κ_1.

The phase diagrams have been obtained as follows: for each pair κ_1, θ the bifurcation analysis developed in section 5.3.2 gives the uniaxial-biaxial bifurcation point. In addition we have always checked the nature of the transition –continuous *vs.* first order–. Finally, the spinodal instabilities of uniform nematic phases, N_u and N_b, with respect to density modulations of crystal, columnar or smectic symmetries are also obtained from the appropriate bifurcation theory presented in section 5.4.

5.5.1 Effect of particle biaxiality

We begin studying the phase behaviour of particles with low aspect ratio κ_1 as a function of particle biaxiality. In figure 5.3 results for $\kappa_1 = 5$ and $\kappa_1 = 10$ are plotted. In the first case –panel (a)– there exists a small shaded region, close to $\theta = -1$, in which biaxial phase is stable. The N_u–N_b bifurcation line (solid) crosses the curve associated with the spinodal instability to the nonuniform phases (dashed) at $\theta \approx -0.5$. The figure also shows the lack of biaxial ordering in the rod-like ($\theta > 0$) part of the phase diagram, since the N_b bifurcation point is located at a density higher than that of the nonuniform spinodal. For $\kappa_1 = 10$ –panel (b)– the region of stability of N_b is considerably enlarged, spanning the interval from $\theta = -1$ up to $\theta \approx 0$. This behaviour can be explained as follows: for $\theta = -1$ there are only three species corresponding to the projections of plates on the surface, an square of dimensions $\sigma_1 \times \sigma_1$ and two rectangles with mutual perpendicular orientations of dimensions $\sigma_1 \times \sigma_3$ (remember that for this case $\sigma_1 = \sigma_2 > \sigma_3$). As $\kappa_1 \equiv \sigma_1/\sigma_3$ increases, the density at which a I–N transition of hard rectangles takes place becomes lower due to excluded volume interactions. This mechanism is the same for biaxial particles, where the large squares (with low molar fraction) are replaced by rectangles of projected area $\sigma_1 \times \sigma_2$ and the small rectangles are replaced by two different species with projected areas $\sigma_1 \times \sigma_3$ and $\sigma_2 \times \sigma_3$, both of them pointing their main axes to x

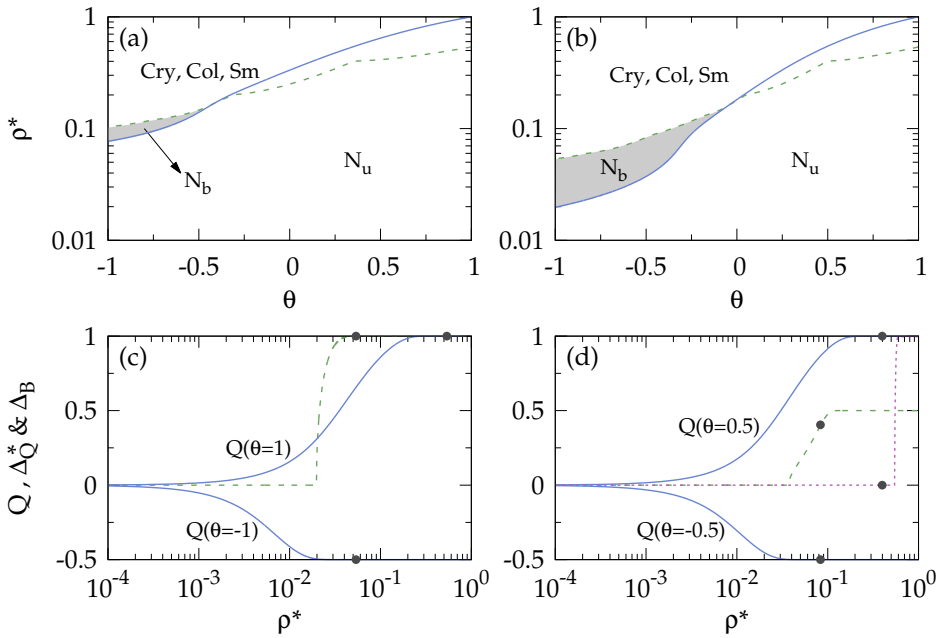

Figure 5.3: (a) Phase diagram in the scaled density plane ρ^* *vs.* particle biaxiality parameter θ for $\kappa_1 = 5$. Solid curve represents the continuous N_u–N_b transition. Dashed curve is the spinodal instability from the uniform to the nonuniform phases. Regions of biaxial stability are shaded. (b) Same as (a), but for $\kappa_1 = 10$. (c) Uniaxial Q –blue solid curve– and biaxial Δ^*_Q –green dashed curve– order parameters as a function of scaled density ρ^* for uniaxial plates ($\theta = -1$) and rods ($\theta = 1$) with $\kappa_1 = 10$. Filled circles on the curves indicate the instabilities to nonuniform phases. (d) Same as (c), but Δ^*_Q for plate-like ($\theta = -0.5$) and Δ_B for rod-like ($\theta = 0.5$, purple dotted curve) biaxial particles.

or y. This excluded volume effect constitutes the main reason why the biaxial phase stability increases with κ_1.

The degree of order in each region of the phase diagram is shown in panels (c) and (d) of figure 5.3. Both uniaxial (Q, blue lines) and biaxial (Δ^*_Q,green lines and Δ_B, purple line) order parameters are shown for some values of θ and $\kappa_1 = 10$. In panel (c) the ordering properties for uniaxial ($\theta = \pm 1$) particles is presented. These results are the same of a previous study only centered in uniaxial particles (*143*). For rod particles ($\theta = 1$) the only uniform phase is the uniaxial nematic, with the director perpendicular to the surface. Its order parameter Q continuously rises from zero (at $\rho^* = 0$) to 1. Once the order parameter is saturated a transition to a nonuniform phase takes place. The scenario from the particles point of view is the following: the species with biggest projected area –rectangles– continuously decreases in population with respect to the species with smallest projected area –squares–. At high densities

only small squares are present in the monolayer. Meanwhile the symmetry of the rectangles is not broken since both species are equally populated for any density.

The case of plates ($\theta = -1$), still panel (c), is different. The uniaxial order parameter continuously decreases from zero and saturates at $Q = -0.5$, its minimum value, for high densities. This behaviour appear because the total projected area is minimized with species with smallest cross-section areas (rectangles) being favoured with respect to the biggest ones (squares). However, the biaxial order parameter Δ_Q^* is zero up to some density when it rapidly rises and saturates at $\Delta_Q^* = 1$. Here the biaxial phase appears as a consequence of the symmetry breaking of projected rectangles. Then for high densities only one species survives, that with projected rectangles in one of the directions. At higher densities the biaxial phase loses its stability against nonuniform phases.

For biaxial particles the picture is similar to the uniaxial case. The order parameters are shown in panel (d). For rod-like particles ($\theta = 0.5$) the uniaxial order parameter increases continuously from zero favouring species with small projected area. Now the biaxial phase is also present at high densities but being metastable with respect to nonuniform phases. Plate-like particles ($\theta = -0.5$) exhibit uniaxial order at low densities and when Q saturates a transition to the biaxial phase takes place. The biaxial order parameter increases with density but before reaching its maximum value nonuniform phases become more stable. This is due to the fact that the N_u–N_b transition appears at higher densities when increasing the particle biaxiality. Consequently, the region of biaxial stability shrinks and Δ_B is not able to saturate before the appearance of nonuniform phases.

The orientational ordering of plate-like biaxial particles can be better visualized by drawing some particle configurations to show how the system evolves as density increases. To this purpose we sketch three projected area configurations of biaxial boards with $\kappa_1 = 10$ and $\kappa_2 = 6$ ($\theta = -0.481$) for three different values of the scaled density: $\rho^* = 0.025$, 0.04 and 0.055, corresponding to panels (a), (b) and (c) of figure 5.4 respectively. The sketches are done so that the molar fractions of different species, $\gamma_{\mu\nu}$, coincides with those obtained from the free energy minimization. For $\rho^* = 0.025$ [panel (a)] the equilibrium configuration corresponds to the N_u phase. At low densities the system always presents this uniaxial phase which is characterized by a favouring of small projected areas while species with the biggest cross-sectional areas are practically absent. Those with intermediate cross-sectional area are in between the other two. The molar fractions of particles with the smallest cross-sections, $\sigma_2 \times \sigma_3$ shown in black, are oriented along x and y axis with equal probability. Thus $\gamma_{zx} = \gamma_{zy}$. The same occurs with the other projected areas: the intermediate ones, $\sigma_1 \times \sigma_3$ shown in red, corresponding to molar fractions $\gamma_{xz} = \gamma_{yz}$, and the biggest one, $\sigma_1 \times \sigma_2$ shown in gray, corresponding to molar fractions $\gamma_{xy} = \gamma_{yx}$. Thus we have that $\gamma_{zy} = \gamma_{zx} > \gamma_{yz} = \gamma_{xz} > \gamma_{xy} = \gamma_{yx}$.

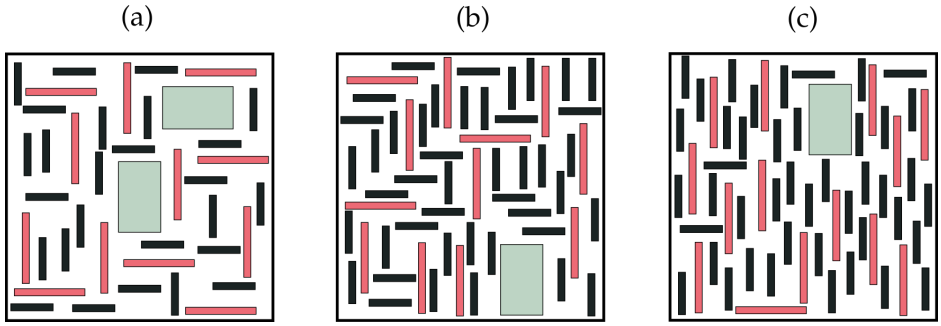

Figure 5.4: Sketch of projected area configurations of biaxial boards with $\kappa_1 = 10$ and $\theta = -0.481$ corresponding to $\rho^* = 0.025$ [N_u (a)], 0.04 [N_b (b)] and 0.055 [N_b (c)]. The three different projections are shown in black, red and gray colors corresponding to the smallest, intermediate and biggest projected areas respectively.

When the density is increased a transition to biaxial phase takes place and the orientational symmetry of projected particles is broken. In panel (b) of the sketch, corresponding to $\rho^* = 0.04$, the orientational symmetry is broken along the y-axes and, consequently, the number of projected rectangles with their longest axes pointing to y increases at the expense of those pointing to x-axis. Now the molar fractions fulfil $\gamma_{zy} > \gamma_{zx} > \gamma_{yz} > \gamma_{xz} > \gamma_{yx} > \gamma_{xy}$. Finally in panel (c), for density $\rho^* = 0.055$, the majority of rectangles point to y-axis and thus the biaxial ordering is almost perfect.

From these results we can conclude that, contrary to intuition, the main effect of particle biaxiality is the destabilization of the N_b phase. Note how the shaded regions of N_b stability in the phase diagrams of figure 5.3, bounded by the two spinodal curves, shrinks as θ increases from the uniaxial case $\theta = -1$. There is a clear physical interpretation of this behavior. For uniaxial plates, with dimensions $\sigma_1 \times \sigma_1 \times \sigma_3$, there are two identical rectangular and mutually perpendicular projections with dimensions $\sigma_1 \times \sigma_3$, which have different molar fractions for a given density and, consequently, N_b stabilizes. The larger projection, of dimensions $\sigma_1 \times \sigma_1$, has a vanishingly small molar fraction. When particle biaxiality increases keeping fixed the largest aspect ratio ($\kappa_1 = 10$), decreasing σ_2 from σ_1, the original projected rectangular species of equal areas become now different, with dimensions $\sigma_1 \times \sigma_3$ (intermediate species) and $\sigma_2 \times \sigma_3$ (smallest species). Note that the biggest species, that with dimensions $\sigma_1 \times \sigma_2$, will continue to have a vanishingly small molar fraction. In order to minimize the excluded volume interactions between particles, the fraction of $\sigma_2 \times \sigma_3$ species should be favoured with respect to the other, and the total density has to increase in order to stabilize the N_b phase (remind that a larger aspect ratio favours the N_u–N_b symmetry breaking).

5.5.2 Effect of particle aspect ratio κ_1

Once we have studied the phase behaviour of boards with low aspect ratio let us move now to study how the topology of the phase diagram changes with κ_1. The main results are presented in figure 5.5 where phase diagrams for $\kappa_1 = 20$, 55 and 70 are shown in the $\rho^* - \theta$ and $\eta - \theta$ planes. Increasing κ_1, the biaxial region in the oblate part of the phase diagram ($\theta < 0$) is widen. In addition, above $\kappa_1 = 21.34$, an island of biaxial ordering appears surrounded by a reentrant N_u phase. This peculiar behaviour has been already observed for uniaxial rods in (*143*) and here it persist for biaxial rods. This region also gets larger and spans to $\theta \sim 0$ when increasing κ_1. Above $\kappa_1 \simeq 60$ the two biaxial regions coalesce into a single one from which there exists biaxial stability for any value of θ.

Let us now study in detail each situation because several interesting features emerge from the phase diagrams. In panels (a) and (d) of figure 5.5 we present the case of $\kappa_1 = 20$. The phase diagram is similar to that of $\kappa_1 = 10$ shown in figure 5.3, however, now the biaxial region is enlarged, being stable from $\theta = -1$ to 0 approximately. For higher values of κ_1 a new region of biaxial stability appears in the prolate region with a reentrant uniaxial phase. When κ_1 is increased it spans a wider region. Just at $\kappa_1 = 21.34$ it appears as a single point at $\theta = 1$ and then a new region emerges and moves to lower values of θ for larger κ_1, up to $\kappa_1^* = 59.5$ when it reaches $\theta \approx 0$ and coalesces with the biaxial oblate region. Panels (b), (e) for $\kappa = 55$ and (c), (f) for $\kappa = 70$ correspond respectively to situations below and above κ_1^* when the two biaxial regions coalesce. For the former case the N_b region in the oblate and prolate parts of the phase diagrams shrinks as we approach to $\theta \approx 0$, disappearing completely at the critical-end point shown with an open circle. In panels (c) and (f) there is only one critical-end point because the two disconnected N_b regions coalesce into a single one.

The presence of a biaxial phase in monolayers of uniaxial rods is easy to understand. For high enough aspect ratios, by increasing the density, the total packing fraction of the projected rectangular species $\sigma_1 \times \sigma_3$ reaches the value η_{2D}^* (that of the I–N transition of hard rectangles in 2D), and an orientational symmetry breaking at the surface of the monolayer takes places. Of course the presence of the squared species, $\sigma_3 \times \sigma_3$, should be taken into account. However, at low densities and high aspect ratios the packing fraction of squares is small compared to that of rectangles. When the total density is further increased, the packing fraction of squares also gets larger because of projected area minimization, while the packing fraction of rectangles decreases down to the value η_{2D}^* and, consequently, N_b looses its stability with respect to the N_u.

In the case of biaxial rod-like particles the stability of N_b can be explained as follows. When particle biaxiality is increased (θ decreases from 1), rectangular species become inequivalent and the largest one, of dimensions $\sigma_1 \times \sigma_2$, rapidly decreases in molar fraction with respect to the intermediate one, of di-

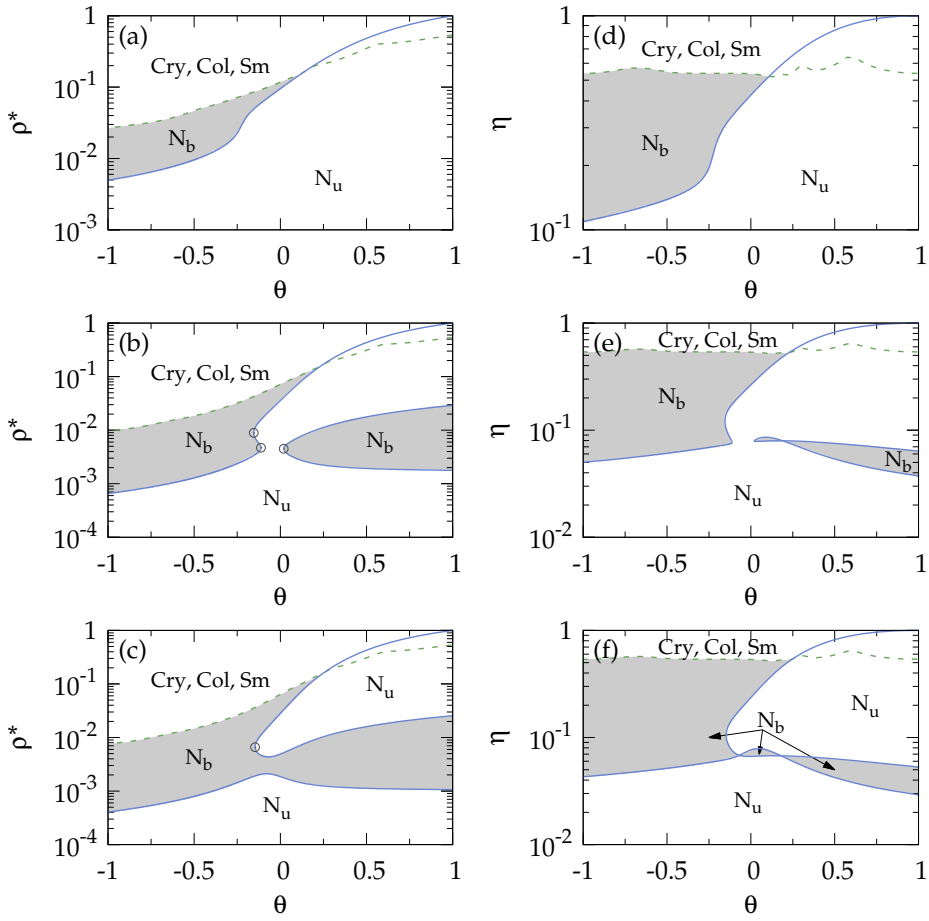

Figure 5.5: Phase diagrams in the $\rho^* - \theta$ [(a), (b), and (c)] and $\eta - \theta$ [(d), (e), and (f)] planes for $\kappa_1 = 20$ [(a) and (d)], 55 [(b) and (e)] and 70 [(c) and (f)]. The regions of stability of different phases are correspondingly labelled with N_b phase shaded. Curves have the same meanings as in figure 5.3. Open circles over the curves represent the positions of critical end-points.

mensions $\sigma_1 \times \sigma_3$. Therefore the total density should increase so that the total area fraction of the projected rectangles becomes of the order of η^*_{2D}, and the N_u–N_b transition density increases. On the other hand, the alignment of particles along the normal direction of the monolayer is enhanced when biaxiality increases and the packing fraction of the smallest species grows at the expense of the other two. Consequently, the N_b–N_u transition curve moves to lower densities.

Notice that the central region, i.e. where particle biaxiality is close to be perfect ($\theta \sim 0$), presents a lower tendency to form biaxial phase. We need larger

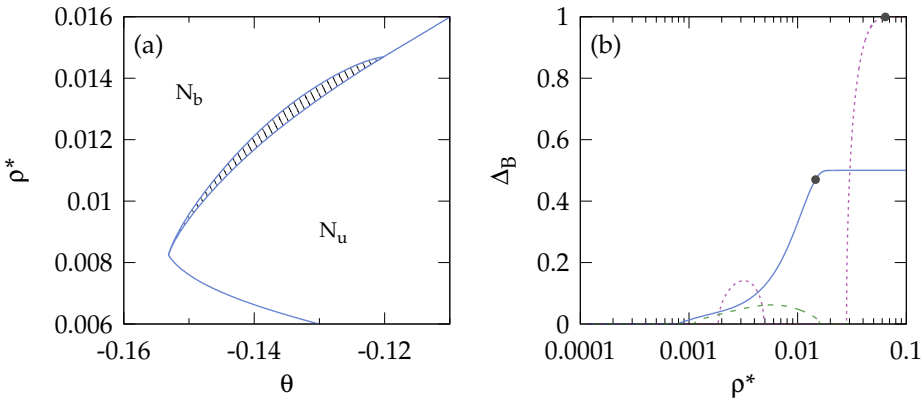

Figure 5.6: (a) Detail of figure 5.5(b) in which a region of first-order N_u–N_b transitions (hatched area) is observed. (b) Biaxial order parameter Δ_B *vs.* ρ^* for $\theta = -0.5$ (blue solid), 0 (purple dotted) and 0.5 (green dashed) for $\kappa_1 = 70$. Filled circles on the curves indicate the instabilities to non-uniform phases.

values of κ_1 to make N_b stable, and when it does, the range of ρ^* with biaxial order is rather small.

In the oblate region of the phase diagram another interesting feature is apparent: a small region of reentrant N_u appears around the critical-end points. When κ_1 is increased the N_u–N_b spinodal deforms and develops a loop near $\theta \sim 0$, see panel (b) of figure 5.5. Notice also that the oblate biaxial region is fully developed at $\kappa_1 \sim 50$ and barely change when increasing κ_1. See panels (b) and (c) for $\kappa_1 = 55$ and $\kappa_1 = 70$ respectively where this part of the phase diagram is unaltered except for the fact that the prolate biaxial region has coalesced with the oblate one.

With respect to the nature of the N_u–N_b transition, it is important to say that it is always continuous, except for $\kappa_1 \gtrsim 40$ in a very small range of particle biaxiality corresponding to the density loop mentioned before. This is shown in figure 5.6(a) where a detail of the phase diagram for $\kappa_1 = 55$ is shown. The hatched area represents the N_u–N_b coexistence region.

In order to see the degree of biaxial order in each region, Δ_B is plotted for $\kappa_1 = 70$ as a function of ρ^* for some characteristic cases in figure 5.6(b). There are important differences between the three different θ presented. For plate-like particles ($\theta = -0.5$, blue solid curve) the biaxial order increases from the bifurcation point and finally saturates at its maximum value. Notice that the transition to nonuniform phases takes place when Δ_B is almost saturated. In the case of rod-like particles ($\theta = 0.5$, green dashed curve) the biaxial order in the region in which N_b is stable exhibits a non-monotonic and rather small change, going to zero as we approach to N_u–N_b and N_b–N_u transitions. The prolate N_b island is then a weak biaxial phase. Finally, for perfectly biaxial particles ($\theta = 0$, purple dotted curve) firstly we find a small region of N_b

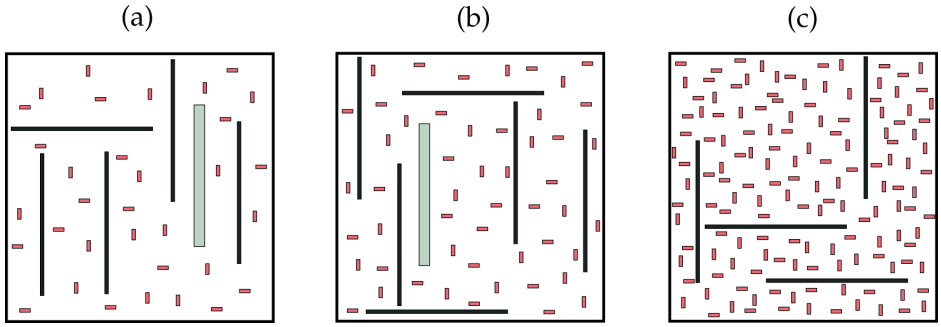

Figure 5.7: Sketch of projected areas configurations of biaxial prolate boards with $\kappa_1 = 40$ and $\theta = 0.265$ corresponding to $\rho^* = 0.007$ [N_b (a)], 0.01 [N_b (b)] and 0.025 [N_u (c)]. The three different projections are shown in red, black and gray colors corresponding to the smallest, intermediate and biggest projected areas respectively.

presenting low values of Δ_B. At a higher density another N_u–N_b transition takes place with Δ_B growing up to its maximum value. When it saturates, a transition to a nonuniform phase takes place.

To better visualize the ordering properties we show in figure 5.7 some projected area configurations of biaxial prolate boards with $\kappa_1 = 40$ and $\kappa_2 = 3$ ($\theta = 0.265$) for three densities: $\rho^* = 0.007$ [N_b (a)], 0.01 [N_b (b)] and 0.025 [N_u (c)]. The relation between cross-sectional areas and the molar fractions of different species are the same as those corresponding to the already discussed oblate case: the fluid is rich in smallest projected-area species and thus the majority of boards have their long axis pointing perpendicular to the monolayer. However, now the orientational symmetry-breaking is promoted by the presence of intermediate species (shown in black) corresponding to boards with their longest axis laying on the surface while its second, intermediate axis, is perpendicular to it. Note that although the number of intermediate species is much smaller than those with the smallest projected areas (in red), their packing fractions exhibit the opposite relation. Also notice that, when the density is increased from 0.007 to 0.01, the degree of biaxial ordering has a negligible increment –compare panels (a) and (b)– and it could even decrease up to disappear completely –compare panels (b) and (c)–. This is a direct consequence of the phase diagram topology in which the N_b is sandwiched between two N_u phases.

Finally it is fruitful to mention two more interesting features of the phase diagrams depicted in figure 5.5. It is clear that depending on κ_1 and θ the number of transitions between uniform phases –N_u and N_b– can be one or three. The curve in the $\kappa_1 - \theta$ plane separating regions of one and three solutions is just the continuous boundary of critical end-points. It is represented in figure 5.8(a) where both regions are correspondingly labelled. The zone having three phase transitions is associated to the presence of the reentrant N_u and, as we have discussed before, it appears in the prolate region ($\theta \gtrsim 0$) for $\kappa_1 > 21.34$. It

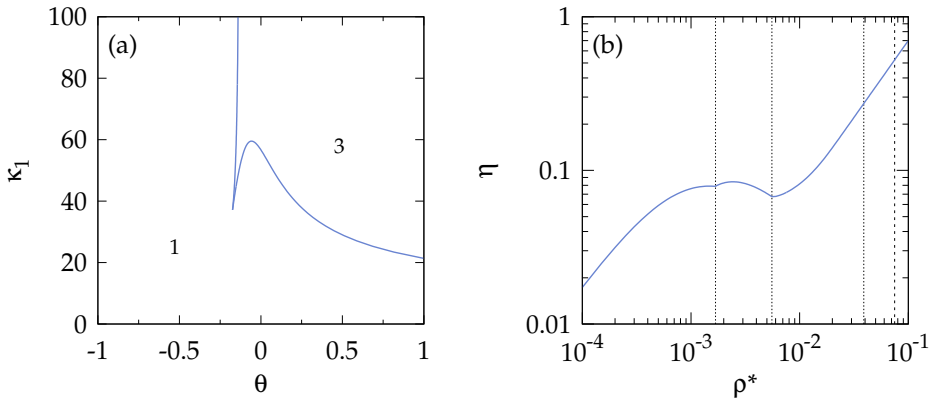

Figure 5.8: (a) Location of critical end-points in the $\kappa_1 - \theta$ plane. The curve separates regions where one or three phase transitions between uniform phases take place. (b) η vs. ρ^* for $\kappa_1 = 70$ and $\theta = 0.04$ [see figure 5.5(c)] showing the packing fraction inversion. Vertical lines show the values of ρ^* corresponding to phase transitions between different phases.

firstly appear for uniaxial rods and as particles become more biaxial the biaxial stability is delayed to higher κ_1.

The last peculiar behaviour that we study is the packing-fraction inversion appearing in the phase diagram for particles with high enough κ_1 and $\theta \simeq 0$. This is shown in figure 5.5(e) and (f) for $\kappa_1 = 55$ and 70 respectively. In this region the lower $N_u \to N_b$ and upper $N_b \to N_u$ transition curves in the $\rho^* - \theta$ plane cross and change their relative locations when plotted in the $\eta - \theta$ plane. This peculiar phenomenon can be clearly visualized in figure 5.8(b), where the packing fraction η is plotted against ρ^*. When the density is increased we find the following behaviour: once the first N_u–N_b transition takes place, the packing fraction exhibits a maximum and then decreases until reaching the N_b–N_u transition. For larger ρ^* the packing fraction exhibits the usual monotonic behaviour. This effect can be explained by expressing the packing fraction as a function of ρ^* and the order parameters Q and B

$$\eta = \frac{\rho^*}{3}\{\kappa_1(\kappa_2+1)+\kappa_2-[\kappa_1(\kappa_2+1)-2\kappa_2]\,Q-3\kappa_1(\kappa_2-1)B\}. \qquad (5.65)$$

From here we can see that it is possible for the packing fraction to decrease with ρ^* when the order parameters are positive and increase sufficiently with ρ^*. In this situation the uniaxial ordering is strongly promoted so that the number of particles of the species with smallest projected area increases rapidly enough, thus compensating the total density increase.

Just to finish the present study we briefly discuss the behaviour of the system in more complex (and realistic) situations. In particular, we have studied in (*144*) the effect of adsorption on rod-plate mixtures confined to a monolayer, where the interaction with the surface was modeled proportional to the pro-

jected area of particles. Here we find a complex and rich phase behaviour and, in comparison with the present study, some analogies can be made: (i) there exists a N_b–N_u spinodal which is very similar to the one shown in the present chapter when we replace the biaxial order parameter, θ, by the molar fraction of the mixture; (ii) when the adsorption strength is increased, the phase diagram presents an island of biaxial stability analogous to the one found here when increasing the aspect ratio of particles. In the same way, this region also coalesces with the main N_b–N_u spinodal above a critical value of adsorption strength.

5.6 REMARKS AND COMMENTS

The main result of the present study consist, contrary to expectations, that particle biaxiality destabilizes the N_b phase in the cases where the latter is present. This phenomenon is directly related with the competition between the biaxiality promoted by the two-dimensional spatial constraint on particle centers of mass and the biaxial ordering promoted by particle biaxiality for high enough densities. For biaxial particles the rectangular projected areas are inequivalent and the mixing entropy stabilizes the 2D isotropic phase, mainly for plate-like geometry.

A rich variety of interesting features also emerge in the phase diagrams which have been studied in detail. With respect to the island of biaxial phase in the prolate region, we should be careful because it could be a direct consequence of the restriction on particle orientations. The fact that it presents a small degree of biaxial order could make the phase to be no longer stable when particles are freely-rotating. In fact, Monte Carlo simulations and Parsons-Lee DFT point in this direction for uniaxial ellipsoidal particles without orientational restrictions (*145*). While plate-like particles exhibit a N_b phase like in the present study, their rod-like counterparts do not. However, it would be necessary to explore a larger variety of particle geometries, without imposing orientational constraints, to finally discard the presence of a biaxial nematic phase for rod-like particles.

In section 5.1 we mentioned the connection of the present study with recent experiments of goethite nanorods confined between the bilayers of a lamellar phase made from nonionic surfactant (*140*–*142*). It is fruitful to compare –at least qualitatively– our results with those of the experiments. Their particles orient perpendicular to an applied magnetic field along the lamellae axis so that negative uniaxial order parameters can be obtained, resulting in stacked sheets of liquid-like quasi-two-dimensional rods. Particle sizes were estimated by optical and X-ray diffraction methods to be $315 \times 38 \times 18$ nm^3 resulting, in our notation, in aspect ratios $\kappa_1 = 17.5$ and $\kappa_2 = 2.1$ ($\theta = 0.37$), i.e. relatively biaxial particles. Particle interactions are approximately hard, but they interact with the lamellae in complex ways, probably resulting in effective attractions

between the rods in a sheet. Intersheet interactions also exist, although they are probably weak. The authors find an 'isotropic' phase –corresponding to the uniaxial nematic phase N_u in our study– and a 'nematic' phase –our biaxial N_b phase– and suggest a possible continuous phase transition between the two at a packing fraction which was not possible to estimate in the experiment. This particle geometry would correspond closely to the phase diagram of figures 5.5(a) and (d). In our diagram, the experimental value of θ is slightly larger than the predicted limiting point for the biaxial phase before uniaxial phase pass directly to a nonuniform phase. A number of factors could explain the difference: modified attractive interactions and size polydispersity in the experimental nanorod system, both of which could change the stability of the biaxial phase, and/or defects in the theoretical approach. Further experiments would be useful to explore different regions of the phase diagrams and in order to compare the general features emerging from theoretical studies. The present study could serve as a guide for future experiments of confined board-shaped colloidal systems.

6 DYNAMICS OF PATTERN FORMATION

6.1 INTRODUCTION

The present chapter –the last of the first part of the thesis– is devoted to study the dynamics of pattern formation, such as the growth of crystal and columnar ordering. Up to now we have seen the equilibrium properties of bulk and different confined fluids. This chapter is an introduction to study the dynamics of such systems and our goal is to shed some light on the dynamical properties of pattern formation. In particular we will deal only with squared particles. On the one hand we will study how the equilibrium patterns already studied (chapters 3 and 4) develop and change from different initial conditions. On the other hand, we will also study the formation of structured profiles in presence of obstacles and how its geometry affects the resulting patterns.

At this point we know that DFT works remarkably well for confined and highly spatially structured systems. However, it only provides the equilibrium properties but not how that configuration is reached. Some methods, such as the time dependent Ginzburg–Landau and the Cahn–Hilliard equations, have been used to extend the equilibrium theories in order to account for the dynamics. However, they are not appropriate for high density fluids with inhomogeneous profiles. In that context, with the aim to obtain relaxative dynamic theory for highly structured systems, Marconi and Tarazona derived the first dynamic version of the DFT, the so-called dynamic density functional theory (DDFT) (*146*). In its first description it was developed for isotropic particles –spheres– and later it was extended to uniaxial anisotropic particles (*147*) and to particles with arbitrary shape (*148*).

One of the main advantages of DFT is that all the structural and thermodynamical properties of the system can be obtain from the minimization of the density functional with respect to the density profile. In the study of the dynamics of the system we need to take into account velocity particle distributions and time correlations since they are very important for the hydrodynamic description. However, following the arguments of Marconi and Tarazona –which will be explained in the next section– one can obtain a DDFT where the hydrodynamic modes are irrelevant thus the dynamics being only dependent on the time dependent density distribution. This approximation is justified for systems following a relaxational dynamics, those in which velocity distributions do not play an important role. In the following section we briefly describe this

approximation and we discuss in more detail the conditions under which it is valid.

6.2 DDFT

The DDFT developed by Marconi and Tarazona (*146*) leads to a deterministic equation for the evolution of the time dependent density profile which has the form of a continuity equation

$$\frac{\partial \rho(\mathbf{r},t)}{\partial t} + \boldsymbol{\nabla}\cdot\mathbf{j}(\mathbf{r},t) = 0 \tag{6.1}$$

where the time is scaled with particle mobility and with the current of particles depending on the free energy functional as

$$\mathbf{j}(\mathbf{r},t) = -\rho(\mathbf{r},t)\boldsymbol{\nabla}\left.\frac{\delta\beta\mathcal{F}[\rho]}{\delta\rho(\mathbf{r})}\right|_{\rho(\mathbf{r},t)}. \tag{6.2}$$

Notice that the great advantages of this formulation are that (i) it constitutes is a closed equation for $\rho(\mathbf{r},t)$ and (ii) it exploits the powerful description that DFT makes on dense systems. To obtain equation 6.1 two approximations have been made. The first one is to consider that velocity correlations are irrelevant and thus only relaxational dynamics can be described. Although it could be seen as a severe approximation, at high densities particle collisions make the energy and momentum flows much more quickly than the density modulations (*149*). In this way the two dynamics are decoupled and one can study the evolution of density profiles without the information of particle velocities.

After this first approximation, the derivation of DDFT starts with the stochastic Langevin equation which after averaging over a Gauusian noise produces an equation for the density operator, $\hat{\rho}(\mathbf{r},t)$. After identifying some terms of the obtained equation with those obtained for the free energy functional, a second approximation is made in order to obtain the particle correlations $\rho^{(2)}(\mathbf{r},\mathbf{r}',t) \equiv \langle\hat{\rho}(\mathbf{r},t)\hat{\rho}(\mathbf{r}',t)\rangle$, which in the simplest mean field approximation is just $\rho^{(2)}(\mathbf{r},\mathbf{r}',t) = \rho(\mathbf{r},t)\rho(\mathbf{r}',t)$. This means that, if the density profile is $\rho_0(\mathbf{r}) \equiv \rho(\mathbf{r},t_0)$ at a certain time, the pair correlation function is obtained from the derivatives of the free energy functional $\mathcal{F}[\rho_0]$ –as seen in chapter 2[1].

Before adapting the DDFT to our functional for parallel hard squares, we should mention an interesting feature of the dynamics of equation 6.1. From it, we can show –see appendix C– that during the evolution the free energy always decrease, i.e.

$$\frac{d\mathcal{F}[\rho]}{dt} = -\int d\mathbf{r}\rho(\mathbf{r},t)\left(\nabla\frac{\delta\mathcal{F}}{\delta\rho}\right)^2 \leqslant 0. \tag{6.3}$$

1 In 2.1.1 we have seen the relation between the derivatives of the free energy functional with the direct correlation function $c^{(2)}(\mathbf{r},\mathbf{r}')$. And the direct correlation function is related to the functional inverse of the pair correlation function $\rho^{(2)}(\mathbf{r},\mathbf{r}')$.

The stationary solution is of course the equilibrium density profile given by the DFT, corresponding to the uniform value of the chemical potential $\mu = \delta\mathcal{F}/\delta\rho(\mathbf{r})$, but the trajectory from an initial density profile $\rho(\mathbf{r}, t = 0)$ to its equilibrium one $\rho(\mathbf{r}, t \to \infty)$ does not have to be along the steepest descent direction. For this reason the density profile evolutions during commensuration transitions studied in chapter 4 do not correspond to a real dynamics. Those trajectories would correspond to quasistatic evolutions in which the cavity size is changed slowly so that the system is equilibrated during the change.

6.3 SYSTEMS OF STUDY AND NUMERICAL RESOLUTION

In the following sections we will study the relaxative dynamics of hard squares from different initial conditions and two different kind of external potentials: one that mimics the confinement of particles in square cavities and other that mimics the presence of obstacles with different geometries and using periodic boundary conditions. Both situations can be described through external potentials that are included in the free energy functional as

$$\mathcal{F}[\{\rho\}] = \int d\mathbf{r}\,[\Phi(\mathbf{r}, t) + \rho(\mathbf{r}, t)V_{ext}(\mathbf{r})] \tag{6.4}$$

where $\Phi(\mathbf{r}, t)$ is the free energy density defined in chapter 2 (with explicit expressions presented in chapter 3) and $V_{ext}(\mathbf{r})$ is the external potential.

The explicit form of the dynamic equation 6.1 for our density function is shown in appendix D. However, it cannot be solved analytically so we use a simple iteration method to solve it numerically. Both spatial and temporal variables are discretized and the continuity equation reads

$$\rho(x_i, y_j, t_{n+1}) = \rho(x_i, y_j, t_n) - \Delta t \boldsymbol{\nabla} \cdot \mathbf{j}(x_i, y_j, t_n) \tag{6.5}$$

where (x_i, y_j) is the grid point obtained after discretizing the space with spatial steps of $\Delta x = \Delta y = \sigma/40$ (σ being the particle length). The time step is changed during the evolution in order to optimize the convergence of the iterative process. For the first stages the structural changes are stronger so we set $\Delta t = 5 \cdot 10^{-4}$, but when the dynamics becomes more smooth we are able to increase the time step up to $\Delta t = 10^{-1}$. Finally, the spatial derivatives of the flux are computed using the central finite-difference method.

For each case we define an external potential which will be shown in the corresponding section. These are soft potentials, i.e. they are not step-like but with strong decays in order to resemble hard ones. The reason for not choosing hard potentials is that, due to their intrinsic singularities, they do not conserve the number of particles, see appendix E for details.

Before describing the main features of each system it is useful to remember the bulk phase diagram of hard squares (studied in chapter 4 and shown in

figure 4.3). The isotropic phase is stable for packing fractions up to $\eta = 0.538$ where a second order transition to columnar phase takes place. For intermediate η the columnar structure is stable, but the energy of the crystal phase is very close to that of the columnar. Finally, from $\eta = 0.726$ the crystal phase becomes stable through a first order transition. However, the small energy difference between columnar and crystal phases at intermediate packing fractions makes the system quite critical when the symmetry of the external potential is varied. For instance we saw in chapter 4 that the behaviour of hard squares confined into square cavities dramatically change with respect to bulk behaviour: from isotropic phase we go directly to a crystal one. It is important to keep in mind this feature of the system in order to understand the results when we confine or perturb the system with obstacles.

6.4 CRYSTALLIZATION INDUCED BY CONFINEMENT

The first system under study is a confining potential with square symmetry. We use a periodic potential defined as

$$\beta V_{ext}(\mathbf{r}) = -\epsilon \log\left([1 - \Psi(x)]\,[1 - \Psi(y)]\right) \tag{6.6}$$

with

$$\Psi(z) = \frac{1}{2} \sum_{k=-N}^{N} \left\{ \operatorname{erf}\left[\sqrt{\alpha}\left(z + \frac{\sigma}{2} + kh\right)\right] - \operatorname{erf}\left[\sqrt{\alpha}\left(z - \frac{\sigma}{2} + kh\right)\right] \right\} \tag{6.7}$$

where $\operatorname{erf}(x)$ represents the standard error function, h is the periodicity (i.e. the side length of the cavity), α controls the decay of the potential and ϵ defines its height. The number of terms in the sum is selected large enough so that the convergence of the sum is guaranteed, in practice we set $N = 20$. A representative graphic of the external potential with the parameter values used is shown in figure 6.1.

In the present section we will study the dynamical evolution of hard squares density profile confined in the square cavity defined above. In analogy with the results of chapter 4 for hard walls, the equilibrium profiles for soft potentials correspond to confined crystal structures. Future subsections are devoted to study the dynamics from different initial conditions: in section 6.4.2 we start from constant density profiles, in section 6.4.3 from columnar configurations and in section 6.4.4 the initial profiles are crystal structures in order to study commensuration transitions.

6.4.1 Magnitudes to quantify the dynamics

In order to better understand the dynamical evolution we define here the main magnitudes that will be used in the following sections.

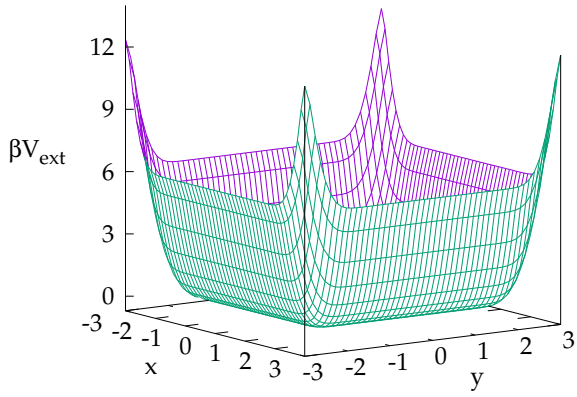

Figure 6.1: Form of the confining external potential for a square cavity of size $h = 6\sigma$.

LAYERS $\mathcal{A}_i$: the crystalline layers are defined as the concentric square-like chains formed by density peaks. And the boundaries of each layer are defined by the local minima of the density profile in between two neighbouring chains. Two examples of those frontiers are represented in figure 6.2, notice that the most interior layer can be formed by one or four peaks, depending on the parity of the number of layers.

INTERLAYER FLUX $\mathcal{J}_i^{(\text{inter})}$: it is the total flux of particles crossing the boundaries of $\mathcal{A}_i$. It is equal to the exchange rate of particles $[N_i(t)]$ inside $\mathcal{A}_i$ with its neighbouring layers, obtained by integrating the equation 6.1

$$\mathcal{J}_i^{(\text{inter})}(t) \equiv -\frac{dN_i(t)}{dt} = -\frac{d}{dt}\int_{\mathcal{A}_i} d\mathbf{r}\rho(\mathbf{r},t) = \\ = \int_{\mathcal{A}_i} d\mathbf{r}\boldsymbol{\nabla}\cdot\mathbf{j}(\mathbf{r},t) = \int_{\mathcal{L}_i} dl\mathbf{j}(\mathbf{r},t)\cdot\mathbf{n}_i \quad (6.8)$$

where we have used the Gauss theorem in the last term which is a line integral over the boundary $\mathcal{L}_i$ of $\mathcal{A}_i$, with external normal $\mathbf{n}_i$. Using the squared symmetry of our system it is straightforward to show that

$$\mathcal{J}_i^{(\text{inter})}(t) = 8\left[\int_0^{l_{i-1}/2} dy j_x\left(\frac{l_{i-1}}{2}, y, t\right) - \int_0^{l_i/2} dy j_x\left(\frac{l_i}{2}, y, t\right)\right] \quad (6.9)$$

with $j_x(\mathbf{r},t)$ being the x-component of vector $\mathbf{j}(\mathbf{r},t)$, and where the boundaries $\mathcal{L}_i$ are located at

$$\mathcal{L}_i : \begin{cases} |x| = \frac{l_k}{2},\ |y| \leqslant \frac{l_k}{2} \\ |x| \leqslant \frac{l_k}{2},\ |y| = \frac{l_k}{2} \end{cases}, \quad k = \{i-1, i\}. \quad (6.10)$$

Notice that we have set the origin of coordinates at the center of the system and that the layers are ordered from the walls ($i = 1$) to the center of the cavity ($i = \mathcal{N}_{\text{layers}}$), with $\mathcal{N}_{\text{layers}}$ the total number of layers. Finally note also that because the total number of particles is conserved we have $\sum_i \mathcal{J}_i^{(\text{inter})}(t) = 0$.

SATURATION TIME t_{sat}: in order to determine when the dynamics has reached already the equilibrium state (or close enough) we define t_{sat} as the first time in which the interlayer fluxes satisfy

$$t_{sat} \equiv t : \sum_i \left| \mathcal{J}_i^{(\text{inter})}(t) \right| < 10^{-5}. \tag{6.11}$$

The value of the saturation time depends of course on the threshold and on the magnitude selected; however, the global behaviour does not change qualitatively using other criteria, such as the total flux in the cavity, or the difference in energy between two consecutive time steps.

TOTAL INTERLAYER FLUX $\mathcal{J}^{(\text{inter})}$: this magnitude computes the total interchange of particles between layers during all the evolution

$$\mathcal{J}^{(\text{inter})} \equiv \sqrt{\sum_i \int_0^{t_{sat}} dt \left[\mathcal{J}_i^{(\text{inter})}(t) \right]^2}. \tag{6.12}$$

MAXIMUM INTERLAYER FLUX $\mathcal{M}^{(\text{inter})}$: it is the maximum value of the interlayer fluxes computed over all layers and over all the time

$$\mathcal{M}^{(\text{inter})} \equiv \max_{i,t} \left(\left| \mathcal{J}_i^{(\text{inter})}(t) \right| \right). \tag{6.13}$$

NUMBER OF FLUX OSCILLATIONS $\mathcal{E}^{(\text{inter})}$: in order to obtain information about the non-monotonicity of the interlayer fluxes over time $\mathcal{E}^{(\text{inter})}$ is defined as the number of extrema of all curves $\mathcal{J}_i^{(\text{inter})}(t)$

$$\mathcal{E}^{(\text{inter})} \equiv \sum_i \#\text{extrema} \left[\mathcal{J}_i^{(\text{inter})}(t) \right]. \tag{6.14}$$

TOTAL FLUX $\mathcal{J}^{(\text{total})}$: with the idea of getting information about the total flux within the whole cavity (not only between layers) we define $\mathcal{J}^{(\text{total})}$

$$\mathcal{J}^{(\text{total})} \equiv \int_0^{t_{sat}} dt \int_{\mathcal{A}} d\mathbf{r} \left[|j_x(\mathbf{r}, t)| + |j_y(\mathbf{r}, t)| \right] \tag{6.15}$$

where $\mathcal{A} \equiv \cup_i \mathcal{A}_i$ defines the entire cavity.

DENSITY PEAKS ρ_{max}: this magnitude characterize the maximum value of the density profile. It is related with the structure of the profile since, generally, highly localized peaks have higher values of ρ_{max}

$$\rho_{max} \equiv \max_{\mathcal{A}}[\rho_{eq}(\mathbf{r})]. \tag{6.16}$$

LAYER PACKING FRACTION $\eta_i(t)$: mean packing fraction of the layer $\mathcal{A}_i$

$$\eta_i(t) \equiv \mathcal{A}_i^{-1} \int_{\mathcal{A}_i} d\mathbf{r}\rho(\mathbf{r},t)\sigma^2. \tag{6.17}$$

Note that the width of layers are in general different so we usually have that

$$\mathcal{N}_{layers}^{-1} \sum_{i=1}^{\mathcal{N}_{layers}} \eta_i(t) \neq \eta_0 \equiv A^{-1} \int_{\mathcal{A}} d\mathbf{r}\rho(\mathbf{r},t)\sigma^2 \tag{6.18}$$

i.e. the average of the mean packing fractions per layer is not a conserved magnitude and it is different from the total mean packing fraction η_0 which is indeed conserved.

6.4.2 Dynamic evolution from constant density profiles

Firstly we begin to study of the crystallization process from initial constant profiles with $\eta_0 = 0.6$. The initial structure is different from bulk equilibrium since for this packing fraction we know that the columnar phase is stable. However, it is also interesting to study this case since the behaviour is qualitatively the same for $\eta_0 = 0.5$ (in which the bulk profile is indeed constant), but $\eta_0 = 0.6$ is more interesting due to stronger structuring processes. It is also adequate in order to compare with result of section 6.4.3 with initial columnar profiles.

The final structure will depend on the relation between the metastable crystal lattice parameter at bulk a_{Cry} and cavity side h. We expect that changing h we get structures commensurating better or worse, i.e. $h/a_{Cry} \approx k \in \mathbb{N}$ or not. In figure 6.2 we compare two of these equilibrated profiles: for $h = 5.1\sigma$ –panel (a)– the bulk crystal period does not commensurate well with cavity size and, consequently, the peaks appear diffuse; on the other hand, we have for $h = 5.8\sigma$ –panel (b)– very localized peaks due to the good commensuration between h and a_{Cry}. Notice that in the latter case the height of the peaks is higher but the structure also develops bridges between neighbouring peaks belonging to the same layer. This means that particles are able to fluctuate along these directions (but with high probability of being localized) and, consequently, the crystal phase can support a large fraction of vacancies. This idea is also consistent with the ratio between the number of particles in each configuration (N) and the number of density peaks (N_{peaks}). While the occupation parameter $\zeta \equiv N/N_{peaks}$ in panel (a) is close to 1 for $h = 5.1\sigma$, in the transition to the

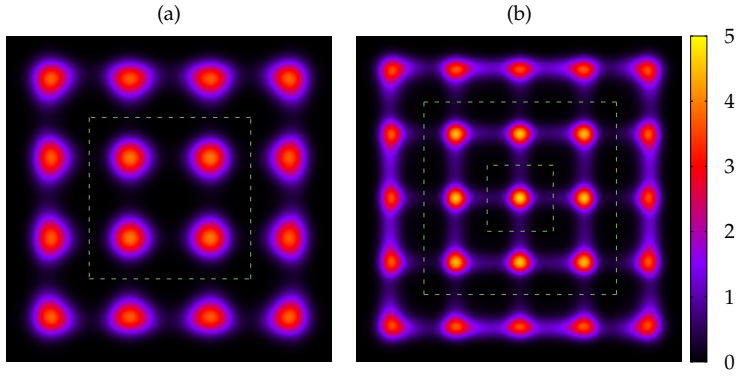

Figure 6.2: Final density profiles inside squared cavities of sides (a) $h = 5.1\sigma$ and (b) $h = 5.8\sigma$ from initial constant profiles with $\eta_0 = 0.6$. Dashed green lines represent the boundaries between layers.

configuration shown in panel (b) for $h = 5.8\sigma$ a whole new layer of peaks have been created, so in this case ζ needs to decrease significantly.

Let us now study the evolution from a constant profile. In figure 6.3 we show the layer packing fractions $\eta_i(t)$ for each case. For $h = 5.1\sigma$ –panel (a)– the first stages of the dynamics show a small decrease of $\eta_1(t)$ (blue curve), after that the layer packing fraction reaches a minimum and is followed by a smaller increase to its stationary value $\eta_1(\infty) < 0.6$ reached at $t \sim 300$. In this case the repulsive potential expel the excess of particles in contact with the soft wall creating a first layer with a lower mean packing fraction. In contrast, the inner layer (green curve), formed at the end by four peaks, increases its packing fraction, reaches a maximum, and tends to its stationary value $\eta_2(\infty) > 0.6$.

The dynamic evolution for $h = 5.8\sigma$ –panel (b)– is quite different. The packing fraction of the layer next to the wall (blue curve) is again lower at long times when compared to its initial value: $\eta_1(\infty) < 0.6$. However, unlike the former case, at short times the packing fraction in that layer increases, reaches a maximum and has a further decrease. The second layer (green curve) has the opposite behaviour than the first one and the third layer (purple curve), at the end enclosing a single peak, exhibits a dramatic decrease at short times followed by a sustained increase with $\eta_3(\infty) < 0.6$. But the main difference with respect to the dynamics corresponding to $h = 5.1\sigma$ consist on a saturation time of $t_{sat} \sim 3000$, one order of magnitude above. The reason for such difference comes, as we will study later, from the different type of particle fluxes dominating each situation: for well commensurated cavities –like in panel (b)– the interlayer are dominant over the intralayer ones, while the picture in poorly commensurated cavities –panel (a)– is the opposite. Thus, the main effect of the external potential on the layers in (b) consists firstly on the movement of particles inside each layer up to their final, highly localized, positions and further expelling or extracting particles from the neighbouring layers in order to

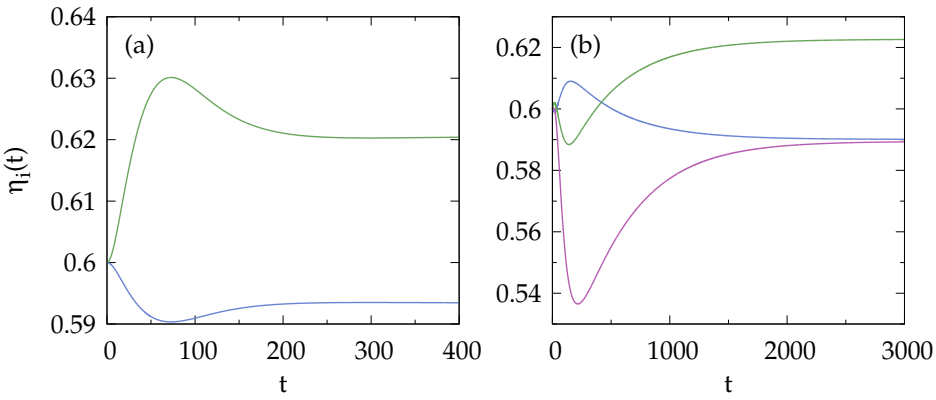

Figure 6.3: Mean layer packing fractions as a function of time for the evolution from constant profiles with $\eta_0 = 0.6$ in cavities of (a) $h = 5.1\sigma$ and (b) $h = 5.8\sigma$. Blue, green and purple lines represent $\eta_1(t)$, $\eta_2(t)$ and $\eta_3(t)$ respectively.

conform a regular square lattice. In contrast, for cavities with final delocalized peaks due to worse commensuration –panel (a)–, the interlayer fluxes are more important so the dominant effect of the external potential on the first layer is to expel the excess of particles to the interior of the cavity and then the other layers are restructured interchanging particles with their neighbouring layers. The more complex dynamics of well commensurated cavities makes their saturation times to be higher.

In order to support the previous argument we show in figure 6.4 the interlayer fluxes for each layer. In panel (a), $h = 5.1\sigma$, the first layer looses particles so it becomes a source of them with a positive flux over its boundaries. This flux reaches a maximum, has a lower decay and then gets to a minimum followed by a monotonic relaxation to zero. Obviously, the interlayer flux in the second layer is the specular reflection of $\mathcal{J}_1^{(\text{inter})}(t)$ since the conservation of particles implies that $\sum_i \mathcal{J}_i^{(\text{inter})}(t) = 0$. On the other hand, panel (b) shows the interlayer fluxes for $h = 5.8\sigma$. For $t \gtrsim 20$ the behavior is the opposite to the previous case: the boundaries of the first layer are crossed by particles entering to it from the second layer, so $\mathcal{J}_1^{(\text{inter})}(t)$ is a negative decreasing function up to its minimum value; after that it has a further increase, changes its sign becoming a source of particles; finally $\mathcal{J}_1^{(\text{inter})}(t)$ reaches a maximum and relaxes to zero at long times. The interlayer flux of the second layer is roughly the opposite and the one for the central layer is very similar to the second but of much less magnitude. For very short times ($t \lesssim 20$) the dynamics of the first two layers are the opposite to their previous described behaviour –see inset of panel (b)– : source-like layers become sink-like layers and vice versa. The fact that the central layer is barely affected in this first stages confirms how the effect of the external potential spreads with finite velocity from the walls to the inner layers.

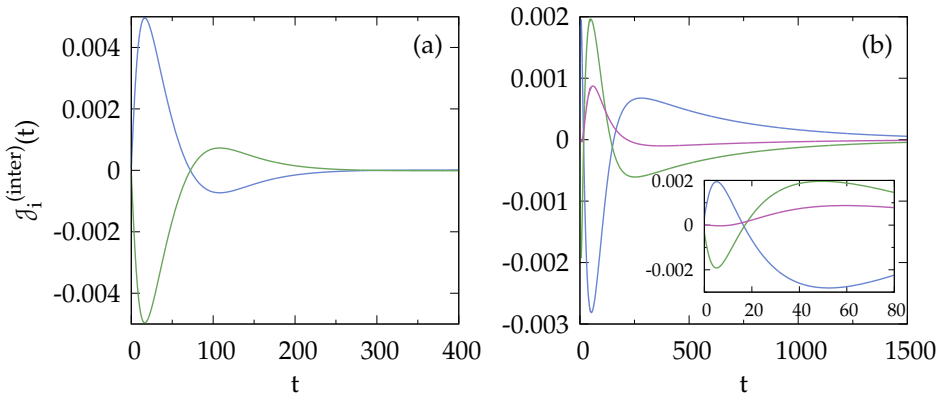

Figure 6.4: Interlayer fluxes as a function of time during the evolution from constant profiles with $\eta_0 = 0.6$ in cavities of (a) $h = 5.1\sigma$ and (b) $h = 5.8\sigma$. Blue, green and purple lines represent $\mathcal{J}_1^{(inter)}(t)$, $\mathcal{J}_2^{(inter)}(t)$ and $\mathcal{J}_3^{(inter)}(t)$ respectively. Inset in (b) shows a zoom of the first stages of the evolution.

Notice also that the flux for $t \lesssim 20$ has no effect in the layer packing fractions (figure 6.3) even when the maxima of $\mathcal{J}_i^{(inter)}(t \lesssim 20)$ are similar to those of $\mathcal{J}_i^{(inter)}(t \gtrsim 20)$ because the involved time scales are very different. Finally another interesting difference between well and poorly commensurated cavities is the higher non-monotonic dynamics of the former case. In both panels (b) of figures 6.3 and 6.4 we can observe that the evolutions are more non-monotonic presenting a higher number of extrema than those of panels (a). One might think that this difference could be a consequence of the larger number of layers for the case (b) and, consequently, a more complex competition. However, we will show below that it has nothing to do with the number of layers but with the commensuration between cavity size and the bulk metastable crystal lattice parameter.

After comparing two characteristic situations in which h and a_{Cry} do and do not commensurate well, now we study in detail how it depends with the cavity size. With these results we will try to generalize the picture already found for $h = 5.1\sigma$ and $h = 5.8\sigma$ to a whole range of h. In figure 6.5(a) we compare the value of the highest density peaks (ρ_{max}, blue circles), the saturation time (t_{sat}, green squares) and the maximum interlayer flux ($\mathcal{M}^{(inter)}$, purple triangles) as a function of h. We see that saturation times are larger for well commensurated structures, i.e. when density peaks are more localized and $\rho_{max}(h)$ reaches its maxima. On the other hand, the interlayer flux behaviour is the opposite: the minima of $\mathcal{M}^{(inter)}(h)$ are perfectly correlated to the maxima of $\rho_{max}(h)$. Obviously it is necessary more time to reach final configurations with highly structured density profiles. Also the dynamics of particle localization in this case is dominated by intralayer, instead of interlayer, fluxes, as we see in panel (b): here we can see that the total interlayer flux $\mathcal{J}^{(inter)}(h)$ (purple triangles) is

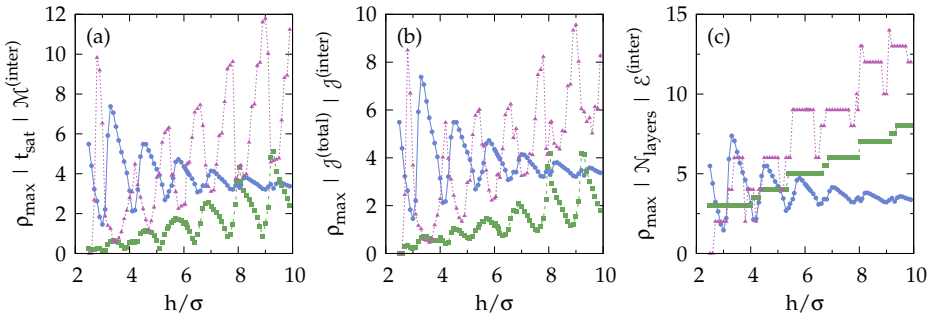

Figure 6.5: Comparison between different magnitudes as a function of cavity size h: maximum value of density peaks ρ_{max} (blue circles), scaled saturation time $t_{sat} \times 10^{-3}$ [green squares in (a)], scaled maximum interlayer flux $\mathcal{M}^{(inter)} \times 800$ [purple triangles in (a)], scaled total flux $\mathcal{J}^{(total)} \times 0.025$ [green squares in (b)]], scaled total interlayer flux $\mathcal{J}^{(inter)} \times 80$ [purple triangles in (b)], number of layers $\mathcal{N}_{layers}$ [green squares in (c)] and number of flux oscillations $\mathcal{E}^{(inter)}$ [purple triangles in (c)].

maximum for poorly commensurated cavities so equilibrium density profiles with delocalized peaks are obtained through a more intense interlayer flux by exchanging particles with its neighbouring layers. On the other hand, well commensurated cavities reach their final states with lower values of $\mathcal{J}^{(inter)}(h)$. In contrast, the total flux $\mathcal{J}^{(total)}(h)$ (green squares) presents its maxima for well commensurated cavities, i.e. when the interlayer ones are less important. So we can extract the important conclusion that the intralayer fluxes are the dominant ones during the relaxation dynamic to well structured density profiles and it is the cause for the larger saturation times.

In panel (c) we study the non-monotonicity of interlayer fluxes via the number of flux oscillations $\mathcal{E}^{(inter)}$ (purple triangles). As shown in the figure, it is higher for well commensurated cavities, as we have already seen before. The migration of particles to highly localized positions inside each layer with their further restructuring through interlayer fluxes result in a complex and highly non-monotonic relaxation dynamics. Finally we have also represented the number of layers as a function of h, $\mathcal{N}_{layers}(h)$ shown with green squares. It is interesting to note that the abrupt changes in $\mathcal{N}_{layers}(h)$ occurs in a small interval of h corresponding to poorly commensurating cavities. These changes are related to the first-order commensuration transitions of confined Cry structures inside hard walls (chapter 4). Nevertheless, although the density profiles are radically changed, they are not true phase transitions. When the hard external potential is replaced by a soft one, these phase transitions are suppressed.

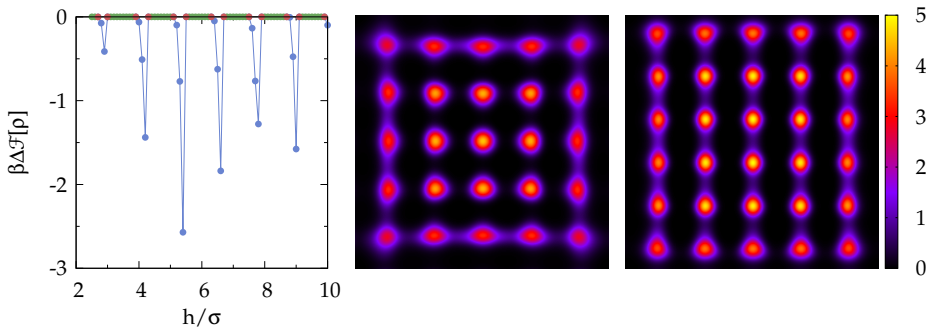

Figure 6.6: Left: free energy difference between equilibrated profiles with initial columnar and constant profiles, $\Delta\mathcal{F}[\rho] \equiv \mathcal{F}^{(\mathrm{Col})}[\rho] - \mathcal{F}^{(\mathrm{o})}[\rho]$, as a function of cavity size. The colour maps are final density profiles from initial constant (center) and columnar (right) profiles for $h = 6.6\sigma$ and $\eta_0 = 0.57$.

6.4.3 Dynamic evolution from Col profiles

Let us now study what happens when the initial density profile is taken with columnar symmetry. In fact, for a mean packing fraction $\eta_{\mathrm{Col}} = 0.6$ this constitutes the equilibrium phase at bulk so the dynamics can be seen as that of bulk system which is suddenly confined by a squared repulsive potential. We choose the position of the external potential so that the columnar layers of the initial profile are symmetrically confined inside the cavity. Notice that even though $\eta_{\mathrm{Col}} = 0.6$, depending on the cavity size the mean packing fraction in the confined system, η_0, may be different since h need not to contain an integer number of columnar periods.

The first result that we have observed is that the final structures obtained are generally the same as those with initial constant profiles for same η_0, i.e. crystal structures. However, we found that for some specific values of h the equilibrated profiles from constant and columnar initial conditions are different, as they are shown in figure 6.6 for $h = 6.6\sigma$. As we can see, the equilibrated profile starting from Col phase consist of an asymmetric crystal structure with different number of layers along x and y directions. Additionally this asymmetric structure has lower free energy so it is stable with respect to the symmetric crystal obtained from flat profiles, as it is shown in the left panel of the figure, where we plot the free energy difference between final configuration. In this graphic we can also observe that asymmetric structures only appear for small windows of h (blue symbols) while outside them the general trend consist on the final dynamic convergence to symmetric crystalline configurations independent of the selected initial conditions (green and red symbols). We have observed that the values of h for which asymmetric structures appear correspond to those well commensurated with the bulk columnar period a_{Col}, i.e. $h/a_{\mathrm{Col}} \approx k \in \mathbb{N}$. At this packing fraction the Col phase is stable at bulk, so if h is such that an integer number of layers can be accommodated, then the

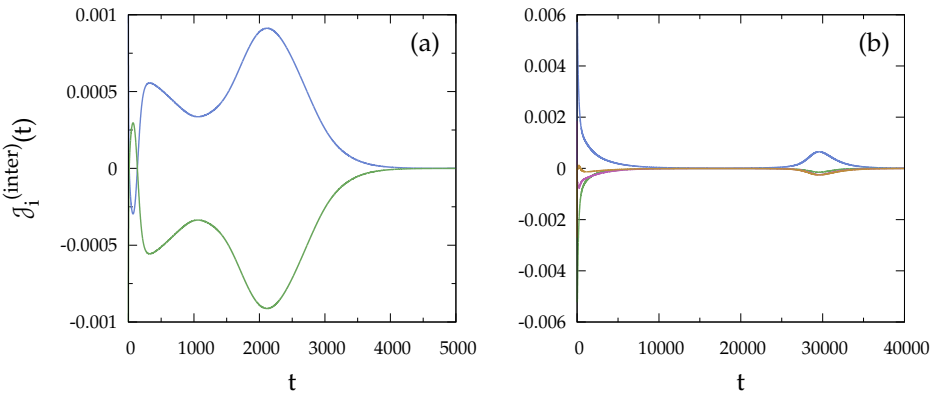

Figure 6.7: Interlayer energy fluxes for cavities with (a) $h = 4.3\sigma$ and (b) $h = 9.1\sigma$ with initial columnar profiles. Blue, green, purple and brown lines correspond to interlayer fluxes of first to fourth layer respectively.

total free energy results lower than the one of the symmetric profile. However, the main effect of the external potential, as we have pointed out before, consists on a localization of particles around the nodes of a regular lattice. Thus the combined commensuration and particle localization mechanisms make the system dynamics to conserve the same number of columnar layers as the initial profile (spreading in the y direction) with a further localization of particles within each layer. This localization along y-direction inside each layer is such that the distance between neighbouring peaks are similar to $a_{Cry} \neq a_{Col}$. Also notice that the asymmetric phase presents a higher number of density peaks so it has more vacancies. However, the layers are more fluidized since there exist bridges between peaks and in this way particles are able to move more easily between their positions in their the layer. In other words, the structure is in between a columnar and a crystal phase.

With respect to the fluxes, the conclusions reached in the preceding section are still valid here; however, in the present case the situation is a bit more complicated since we are imposing some structure at the beginning that may be quite different to the final one. We have seen that for h commensurating well with a_{Col} the initial columnar structure help to reach the final asymmetric configuration. However, this is not always the case. When the final structure is symmetric, depending on the value of h two possibilities arise: the number of vertical layers of the initial Col profiles could be different or the same to the number of density peaks in the x-direction for the final crystal configuration. The first situation have been already explained and consist of: (i) from an initial profile with N columnar layers (along vertical direction), particles within each layer localizes around N nodes of a square lattice ($N \times N$), and (ii) the bridges joining peaks along the vertical direction further symmetrize also along the x-direction creating a fully symmetric Cry profile. This situation

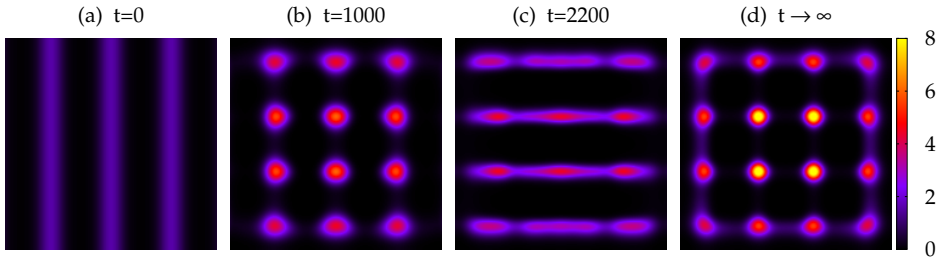

Figure 6.8: Density profiles of the evolution of a columnar phase confined in a cavity of $h = 4.3\sigma$ at times $t = 0$, $t = 1000$, $t = 2200$ and $t = t_{sat}$.

corresponds to the values of h shown in blue in the left panel of figure 6.6. On the other hand, there are also some values of h in which the number of initial columnar layers are different to the number of peaks along x-direction in the final symmetric crystal (shown with red symbols). In these situations the system needs to carry out important restructuring since one layer must be created. This is usually translated in longer flux evolutions. In addition to this, those are generally values of h with a similar commensuration with a_{Col} and a_{Cry}. Consequently, two different dynamic routes, symmetric and asymmetric, compete creating a dynamical frustration and dramatically enlarging saturation times. In figure 6.7 we show interlayer fluxes evolutions for $h = 4.2\sigma$ and $h = 9.1\sigma$. In the first situation –panel (a)– we see a rectification in the flux dynamics that can be understood looking at the evolution of density profiles (figure 6.8): at the beginning the profile consist of three columnar layers [panel (a)]; for $t \in [0, \sim 1000]$ each column begins to structure in four different peaks forming an asymmetric 3×4 configuration [three density peaks in the x-direction and four in y, panel (b)]; the decrement of $\mathcal{J}_1(t)$ just before $t \sim 1000$ is associated with the sharpening of already localized peaks; however, the system in this asymmetric configuration is frustrated and the flux is further reactivated for $t \in [\sim 1000, \sim 2000]$ in which particles delocalize in the horizontal direction, creating columnar layers in the x direction [panel (c)]. Finally, from $t \gtrsim 2000$, these layers structurate in 4 peaks creating a final symmetric 4×4 crystal [panel (d)]. In the second case –panel (b)– the situation is similar but the system gets trapped in a metastable configuration much more time: the initial profile is a columnar structure with seven columnar layers; they crystallize in an asymmetric 7×8 configuration and seem to reach an stationary profile, however, after a long period with almost no dynamics the peaks along x-direction columnarize in order to later crystallize again with an additional peak, i.e. reaching an 8×8 symmetric structure.

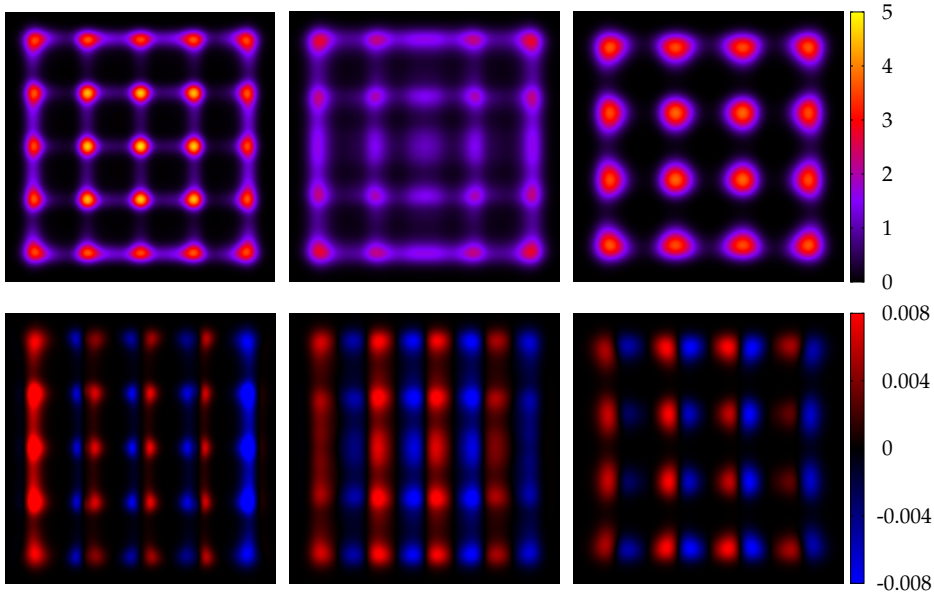

Figure 6.9: Top panels: density profiles at times $t = 0$, $t = 40$ and $t = 300$ (from left to right) for a cavity with $h = 5.1\sigma$. Bottom panels: fluxes $j_x(\mathbf{r})$ for the same times as top panels. In order to show a single color scale the fluxes have been multiplied by 3 and 40 in the central and right panels respectively.

6.4.4 Commensuration transition between Cry structures

To end the study of the dynamics in the square cavity this final section is devoted to the study of the evolution of initial crystal profiles that do not commensurate well with h. In order to prepare such initial structure we begin with an equilibrated profile (as obtained in section 6.4.2) for a slightly different h and scale it to fit to the new cell. This evolution is similar to the process of changing the cavity size of an equilibrated system and its following reorganization. In chapter 4 we gave some insights on a possible path that commensuration transitions could follow between crystal structures when changing h. All intermediate states were equilibrium ones, so the evolution had only sense for quasistatic processes. Here the problem is studied through a real dynamics.

We begin with the case of a square cavity with $h = 5.1\sigma$ in which the initial profile is a symmetric crystal structure with three layers corresponding to the scaled equilibrium profile of $h = 5.8\sigma$. In figure 6.9 we show the density profiles and fluxes in x direction $j_x(\mathbf{r})$ (since $j_y(x, y) = j_x(y, x)$) for the initial 5×5 configuration, an intermediate one and the last close to the final 4×4 profile. From this figure we find the following evolution: the fluxes at $t = 0$ are higher at the walls, pushing the layers to the center. At the same time the flux around each density peak tends to delocalize them, especially those at the center of

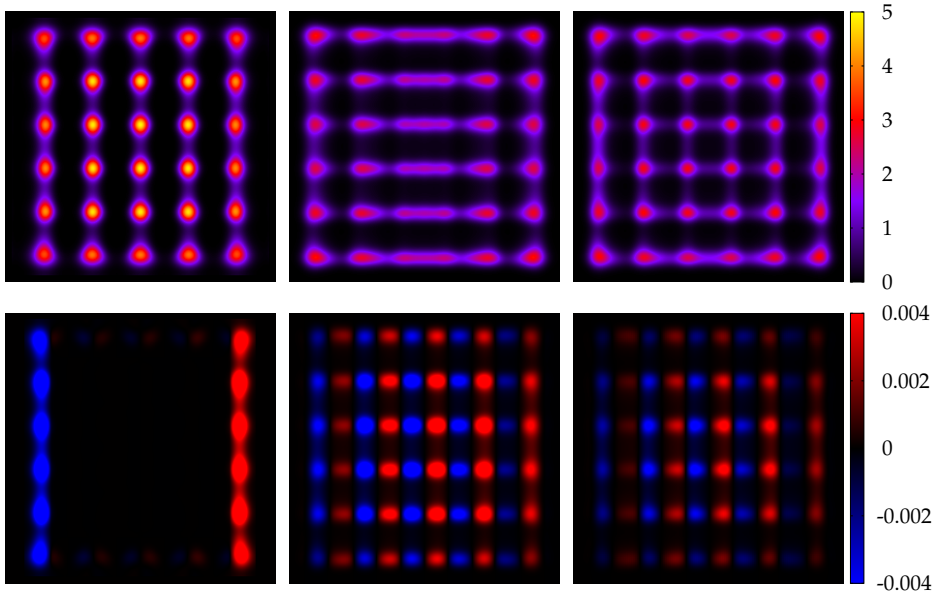

Figure 6.10: Top panels: density profiles at times $t = 0$, $t = 800$ and $t = 3000$ (from left to right) for a cavity with $h = 7.0\sigma$. Bottom panels: fluxes $j_x(\mathbf{r})$ for the same times as top panels. In order to show a single color scale the fluxes have been multiplied by 20 and 200 in the central and right panels respectively.

each layer. This dynamics takes the system to the configuration shown in the central panels with a very diffuse density profile, in particular the central horizontal and vertical chains of peaks which are in process of disappearing. At this point the flux activity is higher in these central chains (the flux j_x is more important for the central vertical chain and j_y, not shown, is the important one for the central horizontal chain) making their peaks to migrate to neighbouring layers. In the right panels we see that the central chains have already disappeared, the peaks are smeared out and the layers have migrated to their final equilibrium position.

To complete the section let us study another evolution but now involving the opposite process, i.e. starting from an equilibrated profile and enlarging the cavity size. In addition we choose an asymmetric initial profile in order to analyze the dynamics between asymmetric and symmetric crystal structures. So in this case we start with an equilibrated profile with $h = 6.6\sigma$ and rescaling to fit it in a cavity with $h = 7.0\sigma$. Three representative profiles of the evolution and their corresponding flux fields are shown in figure 6.10 for $t = 0$, $t = 800$ and $t = 3000$. Like in the previous case the leading dynamics comes from the region next to the walls; however, now the effect is the opposite: the layers have more space and there exists a strong flux in the outer region pushing the peaks against the walls. In the process of layer migration to the outside the

central layers follow the outer ones and the period of the structure gets larger. In particular the period in the x direction becomes less commensurated since there are only 5 chains in contrast to the stable configuration with 6 horizontal chains. As a consequence of this, we can see in the central panels how the profile restructures to later gain a new vertical chain in order to commensurate better the crystal period with the cavity size. This is done through a fluidization of the central peaks in the x direction. After that, we show in the right panels how the particles in emerging columns are again localized with the appearance of a new vertical chain of peaks.

6.5 GROWTH OF NONUNIFORM PHASES AROUND OBSTACLES

Once we better understand the dynamics of pattern formation through its flux evolution we are going now to study qualitatively the effect that the presence of obstacles with different geometries have on the dynamics of crystallization/-columnarization. We impose periodic boundary conditions outside the box to numerically solve the dynamics equation from a constant density profile.

In practice we cannot solve the equations for infinite systems so in order to model them we solve square lattices with periodic boundary conditions and sizes large enough: we reach a compromise between large h, to get reasonable results, and realistic times of convergence. Typically we set $h \sim 25\sigma$ but we have also explored $h \sim 50\sigma$ finding no significant differences. For each situation we have solved the system with slightly different values of h since periodic boundary conditions can play an important role when h does not commensurate well with the equilibrium structure. Then we choose the case with lower free energy per unit area. In practice we obtain results for a window of h spanning a whole period of the crystal or columnar phase to ensure that we find the global minimum of $\mathcal{F}[\rho]/h^2$.

6.5.1 Square and circular obstacles

Let us begin with circular and square obstacles which present a similar behaviour. The initial packing fraction was set to $\eta_0 = 0.6$. Here, like for the confined system, the dynamics begins in the neighbourhoods of the external potential which mimics the presence of repulsive objects, and is the responsible of taking the profile out of a metastable configuration. However, in contrast to the square confinement, the evolution now starts from the center of the system

and spreads out. The external potential for the circular and square obstacles are respectively defined as

$$V_{ext}^{(circ)}(\mathbf{r}) = \epsilon \log\left[1 + \Psi\left(\sqrt{x^2 + y^2}\right)\right] \tag{6.19}$$

$$V_{ext}^{(sq)}(\mathbf{r}) = \epsilon \log\left[1 + \Psi(x)\,\Psi(y)\right] \tag{6.20}$$

with

$$\Psi(z) = \frac{1}{2}\left\{\mathrm{erf}\left[\sqrt{\alpha}(z + d_{obs})\right] - \mathrm{erf}\left[\sqrt{\alpha}(z - d_{obs})\right]\right\} \tag{6.21}$$

ϵ and α are related, as usual, with the height and decay of the potential and d_{circ} is the effective size of the obstacle, i.e. the diameter of the circle or the side of the square.

In figure 6.11 we show the density profiles for the system with a circular obstacle with radius $r = d_{obs}/2 = 0.5\sigma$ (top panels) and for a square obstacle of side $d_{obs} = 0.75\sigma$ (bottom panels) at three different times. At the beginnings the main effect that obstacles have on the profile evolution is to expel particles from them, creating a perturbation in the density profile which propagates moving away from the obstacle. In this way two mutual perpendicular waves structure the density behind the wave front in two columnar configurations, one parallel to the x direction and the other parallel to the y direction. As the columnar ordering can only exists along a single direction, the presence of two mutual perpendicular fronts generates a strong frustration. In particular the particles located at the intersections of these fronts begin to localize to avoid this frustration. This localization is further propagated along the columnar layers, previously formed from the front. Finally a final crystal phase without defected regions stabilizes in the whole system.

The dynamics of the circular and square obstacles are very similar, the only noticeable difference comes from the crystal structure around the obstacles; nevertheless, it depends only on the size of the obstacle but not on its geometry. The size of the circular obstacle fits in between one period of the crystal structure and thus four peaks are developed around it, being the vertexes of a square with edge lengths parallel to the lattice directions, therefore the distance between neighbouring peaks at contact with the obstacle preserves the bulk lattice parameter. On the other hand, the square obstacle is bigger and fill two periods of the crystal lattice. Consequently, a vacancy appears at the center and four peaks are now the vertexes of a square rotated 45° with respect to lattice directions. Notice that the peaks in contact with the obstacles are always higher, meaning that at these positions the particles are anchored to them. For larger obstacle sizes, independent of its geometry, the final configuration is similar: a crystal structure with higher number of vacancies and with peaks at contact spatially distributed in such way to approximately preserve the bulk crystal structure. Of course always exists a small deformation of the lattice around the obstacle: the distance between particles are not exactly the same as we get closer to the obstacle.

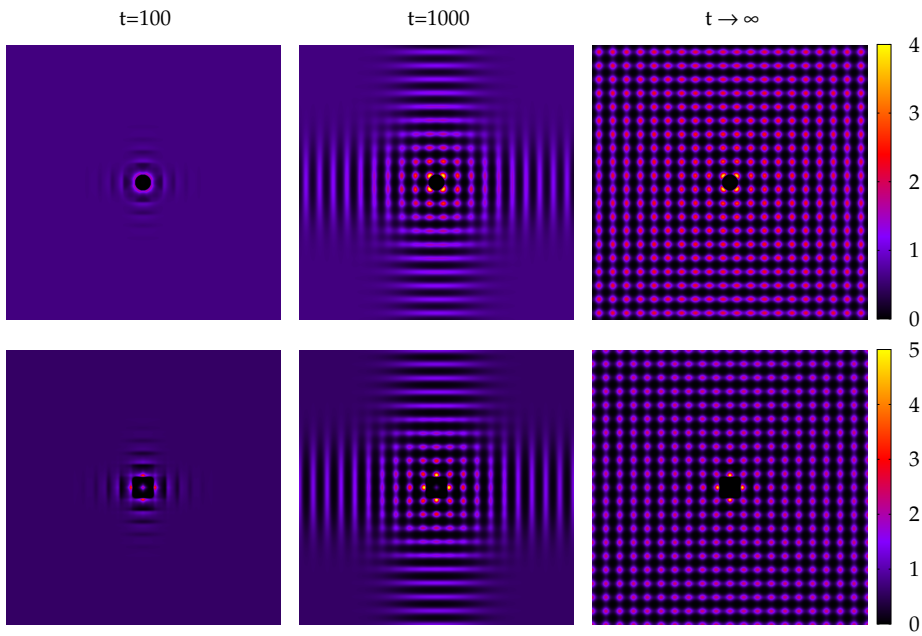

Figure 6.11: Density profiles for the evolution of constant profiles in systems with a circular obstacle of $r = d_{obs}/2 = 0.5\sigma$ (top panels) and a square obstacle of $d_{obs} = 0.75\sigma$ (bottom panels) at times $t = 100$ (left), $t = 1000$ (center) and $t \to \infty$ (right).

Notice that the effect of a fourfold symmetric obstacle (invariant under rotations of 90°) is similar to the symmetric confinement studied in square cavities: even though the bulk stable phase for $\eta_0 = 0.6$ is the columnar, the two competing columnar structures induced by the external potential make the crystal phase to be the equilibrium one in these cases.

6.5.2 Bar obstacles

¿What happens when the obstacle is asymmetric?¿Does one of the induced columnar fronts win over the other? In this section we study the evolution from a constant density profiles in presence of rectangular obstacles. We model them through the following external potential

$$V_{ext}^{(bar)}(\mathbf{r}) = \epsilon \log\left[1 + \Psi_x(x)\,\Psi_y(y)\right] \tag{6.22}$$

with

$$\Psi_k(z) = \frac{1}{2}\left\{\mathrm{erf}\left[\sqrt{\alpha}(z + d_{obs}^{(k)})\right] - \mathrm{erf}\left[\sqrt{\alpha}(z - d_{obs}^{(k)})\right]\right\} \tag{6.23}$$

and the external potential parameters are same as for the previous studies. The geometry of the bar obstacle is defined by $d_{obs}^{(x)} < d_{obs}^{(y)}$ which determine its

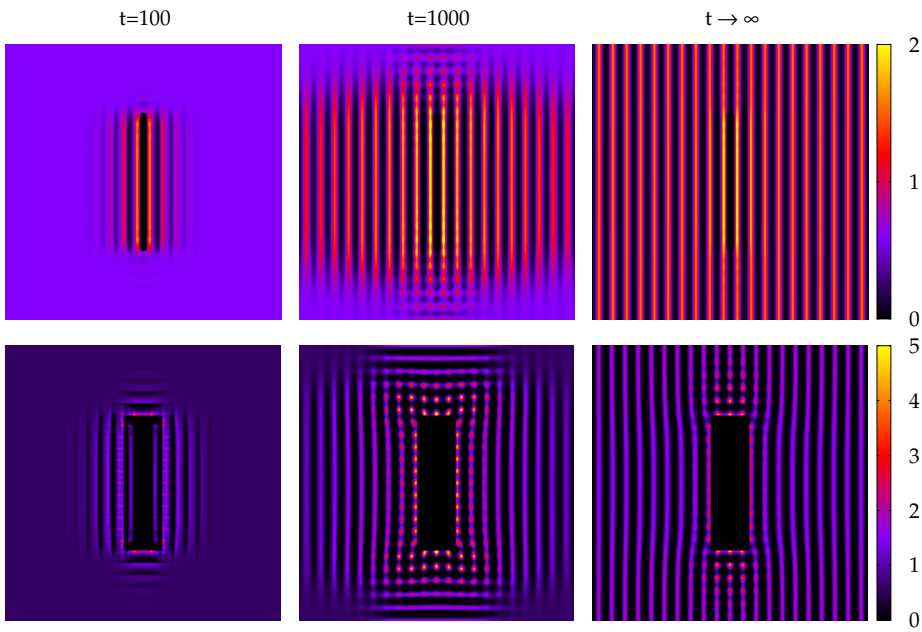

Figure 6.12: Density profiles for the evolution of constant profiles in systems with rectangular obstacles of $d_{obs}^{(y)} = 12\sigma$. Top panels correspond to $d_{obs}^{(x)} = 0.2\sigma$ and bottom panels to $d_{obs}^{(x)} = 3.15\sigma$. Profiles for times $t = 100$ (left), $t = 1000$ (center) and $t \to \infty$ (right).

width and length respectively along x and y directions. We have test different sizes and packing fractions and here we show three cases that well represent the general trend. In figure 6.12 we have plotted the evolution of the density profiles for two rectangular obstacles with different width and initial constant profile of $\eta_0 = 0.6$. Top panels correspond to the case of $d_{obs}^{(x)} = 0.2\sigma$ and $d_{obs}^{(y)} = 12\sigma$. In the first case we can see that, firstly, the density in the obstacle region is quickly expelled out and a wetting layer is developed next to the rectangle along its longest sides. This later creates a front wave in the x direction that develops a columnar phase in the system parallel to the obstacle. The short perpendicular walls also induce a small perturbation in the y direction and at intermediate times the competition with the main columnar structure result in a region with a rather small peak localization. But the further developing of the columnar phase with layers parallel to the obstacle impose a global columnar ordering in the whole system. Notice that the final structure consist of a perfect columnar phase where the obstacle fits perfectly between two layers. In contrast to this situation, we show in the bottom panels another evolution for the same initial profile but with a rectangle width that does not commensurate well with the periodicity of the bulk columnar phase, $d_{obs}^{(x)} = 3.15\sigma$. Here the initial

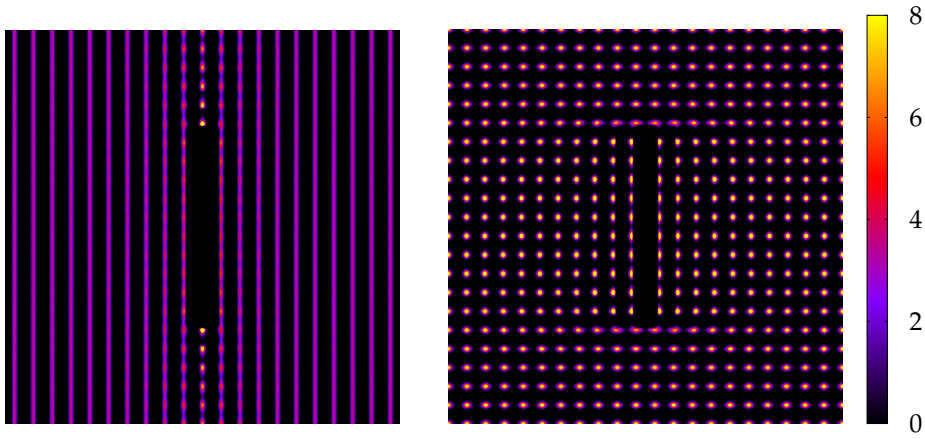

Figure 6.13: Equilibrated density profiles for rectangular obstacles with $d_{obs}^{(x)} = 1.65\sigma$ (left) and $d_{obs}^{(x)} = 1.14\sigma$ (right), both having $d_{obs}^{(y)} = 12\sigma$. The initial configurations were constant profiles with $\eta_0 = 0.75$.

stages are similar to the previous case with the expelling of particles inside the obstacle and creating two perpendicular columnar waves. However, now the obstacle width does not fit well with the natural periodicity of the columnar phase and, consequently, a crystal structure is preferred in the vicinity of the bar. At intermediate times $3-4$ layers are highly localized in both x and y directions, but finally the global columnar phase develops completely far from the obstacle and confines the crystal structure to a small region above and below the rectangle in the neighbourhood of the small length. Furthermore the equilibrated columnar structure is deformed near the obstacle in order to adapt the bulk columnar periodicity to the shape of the bar.

Up to now we have seen that circular and square obstacles induce crystal structures even when the bulk stable phase is columnar and that bar obstacles stabilize the columnar under the same conditions (sometimes with deformations around the obstacle). So now we could wonder what happens when the bulk stable configuration is a crystal phase and we place a rectangular obstacle. In order to explore that situation we have studied systems with different bar obstacles and initial flat profiles of $\eta_0 = 0.75$. The dynamics is analogous to the previous case and we just show in figure 6.13 the final states for two different geometries: $d_{obs}^{(x)} = 1.14\sigma$ and $d_{obs}^{(x)} = 1.65\sigma$, both with $d_{obs}^{(y)} = 12\sigma$. As we can see, now the commensuration between bulk periodicity and the width of the obstacle is crucial for the final configuration. Obstacles which adapt well to the columnar structure can induce columnar phases for systems with mean packing fractions somewhat greater than that of the bulk crystal stability (left panel). Here the wetting promoted by the longer walls propagates a strong columnar perturbation. Notice that in the neighbourhood of the shorter walls

the layers ending at the obstacle present a crystal structure. This is due to a wetting effect: the density at the contact is higher and the particles within the layer are correlated with the one at the wall. But as the correlation decays with distance the layer gets its columnar structure when it moves away from the bar.

On the other hand, we also study an obstacle that does not commensurate well with the bulk columnar period (right panel of figure 6.13). As seen before, when the obstacle does not fit well with the columnar structure there is a larger region of crystallization and in the present case, where the bulk stable phase is the crystal, it finally propagates ending in a global crystal configuration, which is more favourable than bending the columnar structure.

6.5.3 Other geometries

Finally we have also explored obstacles with their main axis different to x and y directions. In figure 6.14 we present two equilibrated configurations of initial constant profiles with $\eta_0 = 0.6$ in presence of a 45° rotated square obstacle and a triangular one. Notice that in the first case the final profile must be the same as the one obtained for the square obstacle, with the lattice directions parallel to the square. However, we force parallel hard squares rotated with respect to the obstacle with the idea to study how the crystal structure is deformed around it. We obtain an equilibrated structure similar to that corresponding to the non-rotated square. The only difference consists on the particle distribution close to the obstacle, which is slightly fluidized and deformed to connect the x and y lattice directions. The other case studied, an equilateral triangle, presents a final columnar structure oriented along the x direction. Apart from the global columnar order induced, like in rectangular obstacles, the layers ending at the walls present some crystal structure in its surrounding due to the localization of the density profile in contact with the obstacle.

6.6 REMARKS AND COMMENTS

The study of the dynamics of columnar and crystal growth in systems with square particles shows very interesting features. Here we have explored crystallization processes in confined systems and the effect of obstacles in bulk dynamics. One of the main conclusions that can extract is that, contrary to intuition, profiles which commensurate well with cavity size tend to present longer dynamics. We have seen that the responsible of this effect is the complex competition between interlayer and intralayer fluxes in the system. When the initial profile is flat the final structure is always a symmetric crystal due to the unbroken symmetry of the constant profile and the square symmetry of the external potential. However, when we start from well commensurated columnar profiles, we may obtain asymmetric crystals with lower free energy.

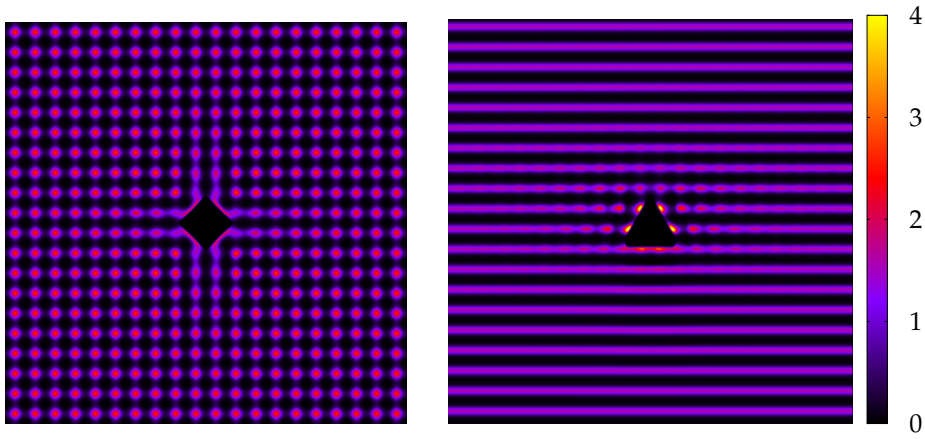

Figure 6.14: Equilibrated density profiles for rhomboid (left) and triangle (right) obstacles. Initial states consisted of constant density profiles with $\eta_0 = 0.6$.

To complete the study of the square confinement we have also presented some commensuration transition between crystal structures with different number of layers. These represent real dynamics in contrast to the sequences presented in chapter 4, which constitutes a series of equilibrated density profiles for different cavity sizes, i.e. only valid for quasistatic processes. But it is important to note that in that case there existed real commensuration transitions (crossing of free energy branches) due to the hard-like nature of the external potential; on the other hand, the structural changes seen in the present chapter are not true phase transitions because of the soft character of the confining potential.

In addition to the confinement dynamics we have also studied the structuring of constant profiles around obstacles with different geometries. The main result comes from the fact that the shape of obstacles may determine the growth of the spatially ordered phases: columnar or crystal, independent of their relative stability at bulk. In this way we have seen how fourfold symmetric obstacles, such as squares and circles, tend to stabilize crystal structures while those without fourfold symmetry, such as rectangles, tend to columnarize the density profiles.

We leave as a future work the study of the dynamics of hard rectangular particles. However, the implementation of DDFT for such systems are not straightforward. In the restricted orientation approximation we deal with two species but the continuity equation 6.1 would imply the conservation in the number of particles for each species. But the number of particles of each species is not constant (only the sum of them) as particles are able to rotate. As a consequence, one have to make some approximations for studying the system with the present formalism. A possibility is to decouple the dynamics of particle rotation and diffusion. If this statement is reasonable for some system (because the time scales of both dynamics are very different) one could study the

evolution of the slower degree of freedom and equilibrate the other variable instantaneously at each step.

7 EXPERIMENTS ON VIBRATED MONOLAYERS OF RODS

7.1 INTRODUCTION

In the second part of the thesis we will move to the study of granular media. Our interest in granular media comes from the interesting connections they share with equilibrium liquid crystals, despite the fact that they belong to very different disciplines.

Granular matter can be defined as a collection of athermal grains interacting via contact forces. The term athermal comes from the size of the particles, typically above the micrometer scale, which is large enough so that thermal energy is negligible. A consequence of the macroscopic size of the grains is that collisions are inelastic and friction is present so the system is very dissipative and particles come to rest easily. Therefore the system does not explore configurational space unless it is excited with external energy. Metastable states are frequent and, in the presence of external energy input, far from equilibrium dynamics are present. That situation makes this kind of systems very difficult to study from a physical description. The number of particles is very high so Newtonian dynamics is not feasible, and the fact that granular media are far from equilibrium does not allow us in general to use typical averaging methods developed for equilibrium systems, such as thermodynamics or statistical mechanics. On the other hand, the number and size of components are orders of magnitude different from liquids and approximations made for them (like the ones leading to Navier-Stokes equations) do not work.

An astoundingly diverse set of peculiar and counter-intuitive behaviours take place in granular matter and that makes them complex systems. Those phenomena emerge even from very simple interactions, similar to what happens in equilibrium liquid crystals, as we have seen in previous chapters.

Our interest in granular media comes from the observation that, under some conditions, their behaviour resemble that of thermal systems. Patterning (*26*, *28*, *150*), defects (*151*), crystallization (*27*) and many other properties have been seen to be very similar to those of equilibrium systems. However, this analogy must be taken carefully because the physics behind them is totally different. On the one hand thermal systems are composed of microscopic particles driven by temperature, which is responsible for the system to explore phase space and reach equilibrium. On the other hand, granular media are composed of particles so large that temperature does not play a role. As pointed out above, these systems are highly dissipative and we need some external energy to make the

system explore different configurations –the temperature counterpart–. Consequently, granular matter is often far from equilibrium and the dynamics need not evolve to configurations with maximum entropy or minimum free energy. Non-equilibrium behaviour has been reported in the literature, to cite some examples: violation of equipartition (*152*), density inhomogeneities (*35*, *153*) and non-Maxwellian velocity distributions (*31*, *154*).

However, the similarities between both worlds exist even from the fundamental point of view. Interactions in granular matter are hard-like: particles do not see each other until they get in contact. Therefore the dynamics exploring the configurational space may not reach the maximum entropy configuration, but packing effects are very important. In fact one expects that, as non non-equilibrium dynamics become less important, packing effects will be more relevant –and probably the system will become more equilibrium-like–. There is an ideal situation when an energy balance in the system is reached: the external energy is injected homogeneously and it is totally dissipated in the collisions between particles. If this energy balance is not fulfilled the energy surplus is responsible for other non-equilibrium dynamics, such as collective motions (*26*, *155*). On the other hand, if the energy injected is not distributed homogeneously it can lead to segregation or density fluctuations (*156*, *157*). Thus there seem to exist some regimes where mean-field theories and computer simulations for equilibrium thermal hard particles –i.e. methods based on entropy maximization– may be useful in discussing results from granular systems.

The motivation to study granular media has therefore exceeded its natural area. The interest for granular matter itself is still very active (*25*). But, in addition, increasing attention is now being paid to the relation to other systems, in particular to active matter (*155*) and the aforementioned connection with thermal liquid crystals. These similarities have led some authors to point out the possibility of exploring some aspects of microscopic systems from the point of view of granular matter (*28*, *154*). The advantage of this approximation is that granular media are easily tractable so one can generate desirable conditions and study the experiments from the particle point of view, whereas in the microscopic system it is usually more complicated.

Our experiments consist of cylindrical particles confined in a quasi-2D circular container, which is vibrated by an electromagnetic shaker. The vertical space is less than two particle diameters so that particles are able to vibrate but in practice they live in a 2D space in the sense that only one monolayer can be formed. Because of this spatial constraint the system can be seen approximately as a set of hard rectangles, the 2D projection of rods (for exact geometry specifications see next section). Our choice for a two-dimensional system has two motivations. Firstly, the comparison with entropic phenomenology of equilibrium liquid crystals that we studied via DFT. Since our theories are made for 2D, we are in a key position to compare the phenomenology of both systems. Secondly, a two-dimensional experiment has several advantages with respect to 3D ones, namely: the system can be studied from the particle point of view

because positions, orientations and velocities of all particles can be recorded from above using a camera. This allows us to study the dynamics in detail. A further advantage is that gravity, perpendicular to the plane, plays no role so we can compare directly with microscopic hard systems not subject to any external potential.

7.2 SETUP AND IMAGE PROCESSING

Our experimental setup is similar to others previously reported in the literature (*26*–*28*, *150*, *155*, *156*, *158*). It consists of a quasi-2D circular container, where particles are placed in, coupled to a vertical shaker. Rods are in the space between two methacrylate disks which allow image acquisition from above. Distance between these two disks is set in the range $\sigma < d < 2\sigma$, with σ the rod diameter, so that particles are able to vibrate but they cannot overlap. Between the two disks there is an aluminum ring that confines the particles within a circular geometry. The electromagnetic shaker is connected to a signal generator and to a power amplifier with which we can control the frequency and amplitude of the oscillation. Peak accelerations are measured by a three-axis accelerometer controlled by an Arduino microprocessor; these data are used to define dimensionless effective acceleration.

Particles were provided by Opac (*159*) and are made of free-cutting steel (9SMnPb28K) which is a non magnetic material. This is very important because the electromagnet inside the shaker creates a magnetic field. Cylinders are 1mm in diameter with two slightly rounded caps that project around 0.13mm.

In order to get optimal pictures of the system during the experiment we have built an illumination setup consisting of six lamps of white light placed around the system, a light diffuser, a DSRL camera and an automatic interval shutter for the camera. During the experiment we take several bursts of 5 images. The time interval between two frames of a burst is around a third of a second and the time interval between bursts can vary in each experiment, typically between 1 and 5 minutes. The different images from a single burst are used to study the dynamical properties (temperatures, velocities, rotations...) because we can identify particles in different frames and detect particle tracks. To study static properties (such as order parameters, clusters, density profiles...) we do not need particles trajectories, a single frame is necessary. However, the five images of each burst give us more statistics.

The images were analyzed using a home-made script for ImageJ. We are able to track, on average, around 99% of particles and obtain its center of mass and orientation. With this data we connect particles of consecutive frames of a burst and make trajectories of particles using a home-made program in C. Our algorithm works better than others found in the literature, maybe because of the high density packing fraction of particles involved and the special feature of particles being anisotropic. In the experiments with $\kappa \geqslant 8$, over 98% of particle

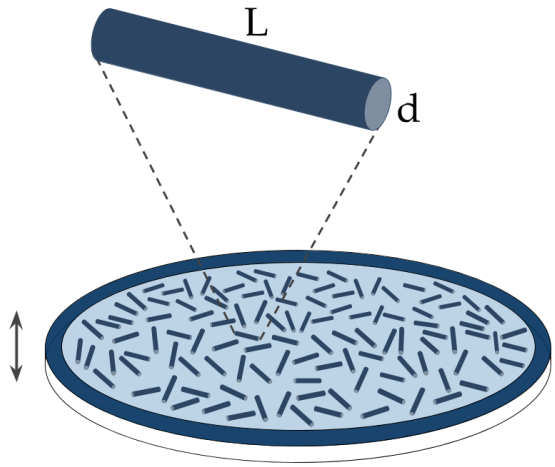

Figure 7.1: Sketch of the experimental setup.

trajectories are well described. However, for $\kappa = 6$ and $\kappa = 4$ the accuracy decreases because of the higher number of particles and its smaller size. In the worst case (very high packing fractions) we get around 93% of trajectories for $\kappa = 6$ and 85% for $\kappa = 4$. But in this case the statistics is better because the number of particles (and hence the number of trajectories) is higher.

7.3 ONE-COMPONENT SYSTEM

We will study a one-component system of rods, i.e. all particles are identical. Our main motivation to study this system was to make a close exploration of the tetratic phase. This configuration corresponds to a biaxial nematic with two perpendicular directors –left panel of figure 7.2–. In thermal systems the tetratic phase is stable for rods with low aspect ratio (*160*–*162*), and the stability of this configuration can be explained from entropic arguments. Remember the chapter 1 where we discussed the appearance of nematic phase from a competition between different kinds of entropy (section 1.2.1). We saw that the nematic stabilizes because the excluded area has a minimum when rectangles point in the same direction even though the ideal part of the entropy is low. Tetratic configurations posses clearly a higher ideal entropy than nematic one (the number of particle orientations is larger), but any configuration different from nematic has a lower interaction entropy since the excluded area is minimum for it. The point is that the excluded area presents a local minimum at $\pi/2$ and the smaller the aspect ratio is the more pronounced this minimum is –see right panel of figure 7.2–. This feature makes the tetratic phase stable for low aspect ratio particles in which the local minimum is close to the global one.

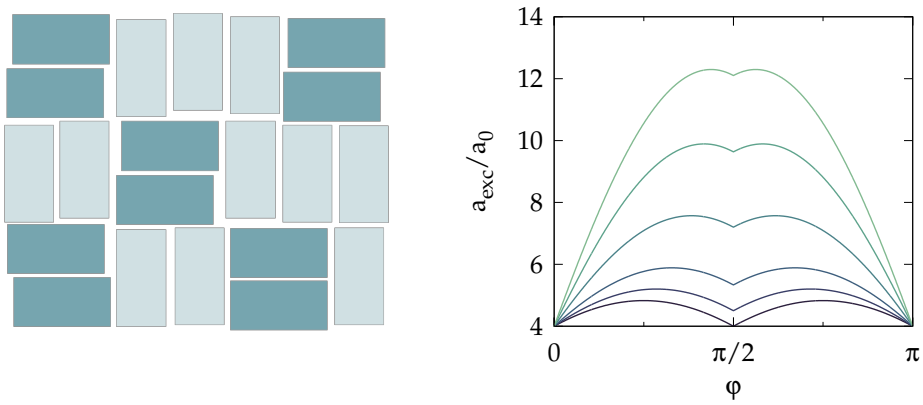

Figure 7.2: Left: sketch of a tetratic configuration. Right: Excluded area for two rectangles with relative angle φ. Curves for aspect ratios $\kappa = 1$, 2, 3, 5, 7.5 and 10 are represented in decreasing order of darkness.

Our interest in the tetratic phase comes from the observation that experiments on granular rods (*26*, *150*) and Monte Carlo simulations (*150*) give a wider range of tetratic stability with respect to mean field predictions (*161*, *162*). While the latter predict the tetratic to be stable for rectangles with aspect ratio up to $\kappa_t = 2.2$ or $\kappa_t = 3.2$ (depending on whether two- or three-particle correlations are considered), experiments and equilibrium simulations result in $\kappa_t \sim 7.3$. We think that this discrepancy can be resolved regarding clustering effects and for this reason we made a detailed study of the experiment which will be developed in the present section. Additionally to the comparison with equilibrium systems in terms of order, we report on a diverse set of unique non-equilibrium behaviours characteristic of dissipative systems.

In order to study the tetratic phase experimentally we have performed several experiments exploring the behaviour as a function of the particles aspect ratio and density. In particular aspect ratios of $\kappa = 4$, 6, 8, 10 and 12 were studied. Since we are interested in the tetratic phase we have explored the regime of intermediate and high packing fractions: $\eta \gtrsim 0.5$. With respect to the vibrating conditions, we tried to avoid non-equilibrium dynamics as much as possible, in particular huge density fluctuations. For some frequency windows particles tend to migrate to certain places creating two coexisting phases: a highly packed region and a hole consisting of gas-like or even no particles at all. This phenomenon has been previously observed in other works (*154*). For all experiments we set the frequency to $\nu = 39$Hz and an amplitude a corresponding to dimensionless peak accelerations of $\Gamma = a\nu^2/g \sim 3-4$.

7.3.1 Order measurements

To study quantitatively the orientational and translational order in the system we calculate the corresponding order parameters. The order parameters are obtained locally because walls will affect order in the cavity and they may distort a global order. Then we make an average of local order to obtain a global value. The nematic and tetratic order parameters at position $\mathbf{r}$ can in general be obtained in two ways: either through the local angular distribution function $h(\varphi, \mathbf{r})$ or through the local nematic and tetratic order tensors $Q_{\alpha\beta}(\mathbf{r})$ and $T_{\alpha\beta\gamma\delta}(\mathbf{r})$.

In the first route the local order parameters are calculated as

$$q_k(\mathbf{r}) = \langle \cos k\varphi \rangle = \int_0^{2\pi} d\varphi h(\varphi, \mathbf{r}) \cos\left(k[\varphi - \varphi_0(\mathbf{r})]\right) \tag{7.1}$$

where $k = 2$ correspond to nematic, $k = 4$ to tetratic and φ_0 is the orientation of the local director.

The order tensors have the explicit expressions

$$Q_{\alpha\beta}(\mathbf{r}) = \left\langle 2\hat{u}_\alpha \hat{u}_\beta - \delta_{\alpha\beta} \right\rangle \tag{7.2}$$

$$T_{\alpha\beta\gamma\delta}(\mathbf{r}) = 4\langle \hat{u}_\alpha \hat{u}_\beta \hat{u}_\gamma \hat{u}_\delta \rangle - \frac{1}{2}(\delta_{\alpha\beta}\delta_{\gamma\delta} + \delta_{\alpha\gamma}\delta_{\beta\delta} + \delta_{\alpha\delta}\delta_{\beta\gamma}) \tag{7.3}$$

with $\hat{\mathbf{u}} \equiv (\hat{u}_x, \hat{u}_y) = (\cos\varphi, \sin\varphi)$ being the unit vector of a particle. In this route the nematic and tetratic order parameters are associated to the highest eigenvalues and the director comes from their associated eigenvectors.

Both routes give results slightly different but qualitatively consistent. In what follows results from the local angular histogram will be shown. The global nematic and tetratic order parameters are obtained from the global orientational distribution function defined as $h(\varphi) = \langle h(\varphi - \varphi_0(\mathbf{r})) \rangle_{\mathbf{r}}$. Because surfaces often induce strong order next to them we exclude from our calculations a shell of $\sim 1-3$ particle lengths close to the walls, depending on density and aspect ratio of particles, in order to eliminate surface effects as much as possible.

Together with nematic and tetratic configurations, we find smectic order in the experiments. In order to account for this type of order we also measure the standard smectic order parameter, defined as

$$\sigma_S(\mathbf{r}) = \left| \frac{1}{n} \sum_{i=1}^{n} e^{i\mathbf{w}\cdot\mathbf{r}_i} \right| \tag{7.4}$$

where $|\cdots|$ denotes the modulus of the complex argument, n is the number of particles in the local region, $\mathbf{r}_i$ is the position of the i-th rod and $\mathbf{w}$ is the wave-vector of the smectic structure. Its direction is set to the local director and the wavelength is tuned to the smectic structure, being typically $\lambda_S \sim 1.1L$. A global smectic order parameter can be defined by averaging over all local regions (excluding again the shell next to the surface)

$$\sigma_S = \langle \sigma_S(\mathbf{r}) \rangle_{\mathbf{r}}. \tag{7.5}$$

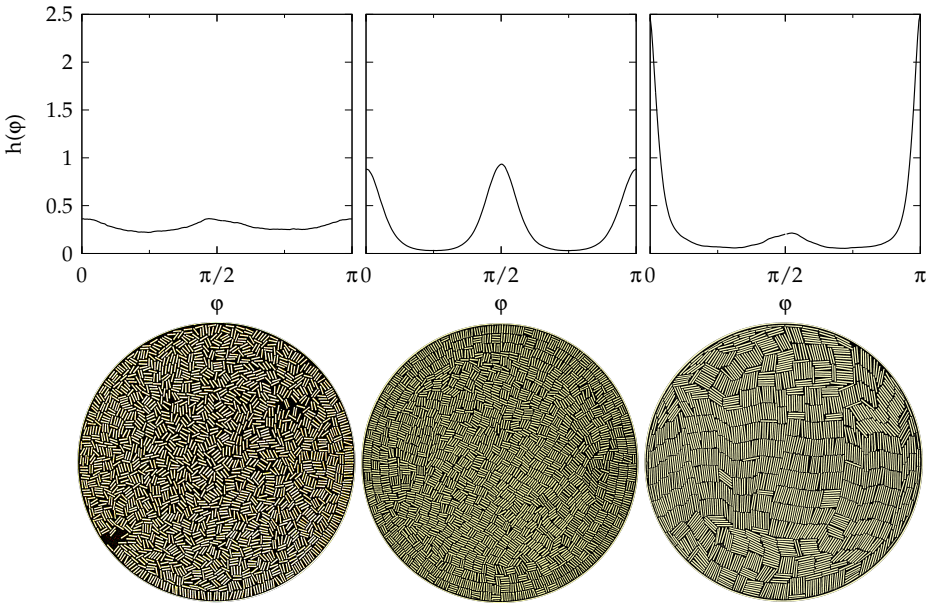

Figure 7.3: Averaged angular distributions (top) and representative particle configurations (bottom). From left to right isotropic phase for $\kappa = 4$ and $\eta = 0.52$; tetratic for $\kappa = 4$ and $\eta = 0.70$; smectic for $\kappa = 8$ and $\eta = 0.81$.

7.3.2 Ordered phases

In order to easily connect order parameters with experimental particle configurations we show in figure 7.3 the angular distributions for the three main phases observed in our system. For low densities we always find isotropic configurations with flat distribution functions –left panel–. These distributions give low values of order parameters. At higher packing fractions we get, for low aspect ratio, a tetratic phase –central panel–. Its angular distribution has two peaks of similar heights and displaced by $\pi/2$ radians, corresponding to the two perpendicular directors. The order parameter q_4 is high as compared to q_2 since the distribution has a periodicity of $\pi/2$. Finally we also find smectic configurations which are composed of particles with similar orientations and structured in layers –right panel–. For this reason, the angular distribution has only one main peak (periodicity π) and both q_2 and q_4 are high. The secondary central peak represents small regions with tetratic correlations coexisting with the smectic phase. Note that from the angular distribution the smectic phase is identical to a nematic (not found in the experiments). In order to differentiate both we need to look at the smectic order parameter (defined in equation 7.4), which will be studied in future sections.

Two features may be noticed from the particle configurations of figure 7.3. First it is clear that the isotropic distribution is not completely flat or random

but it has a small undulation. This can be explained as a consequence of the finite number of particles contained in the local regions used to compute the local order parameter: even in a globally disordered configuration, a small region with a few particles will always exhibit a weak orientational order with an associated director. Since all distribution functions from different regions are shifted to locate the origin at the local director before averaging, angles of 0 and $\pi/2$ are biased and accumulate small values that add up to give a non-flat angular distribution. Furthermore at these intermediate packing fractions small tetratic correlations may be present. The second interesting feature from figure 7.3 is that the tetratic configuration presents layering induced by the walls in the surface normal direction. This is interesting because for equilibrium systems the induced order is usually parallel to the walls (*93*, *160*).

7.3.3 Time evolution of order parameters

In section 7.3.1 we have seen how to measure the order of a given configuration. However, we are interested in studying the steady state of the experiments, provided it exists. For this reason, we need to look at the evolution of order parameters. Note that the initial configuration is set carefully by hand in order to achieve the most random state possible. As a consequence, the initial order parameters are always small. Also, in order to check that the initial conditions do not influence the final configuration, we have repeated some experiments several times without finding any significant differences.

We have found two types of evolutions, represented in figure 7.4. In both we observe a very quick process of ordering associated to rod clusterization. For intermediate packing fractions there exists a transient of about 10^3s after which the order parameters reach a stationary state –figure 7.4(a)–. The particular case represented corresponds to a tetratic state where q_2 is close to zero and q_4 is clearly higher. In a pure tetratic the order parameters would be $q_2 = 0$ and $q_4 \neq 0$; however, due to the finite number of particles one expects q_2 to be non-zero, as explained in the previous section. On the other hand, we also have experiments where a stationary state cannot be defined, at least in the time windows explored –figure 7.4(b)–. This evolution is typical of very high packing fractions where smectic fluctuations and hydrodynamic effects are important. In later sections we speculate that fluctuations of order parameters, smectic structures and vorticity are related in our experiment. The tetratic phase, by contrast, is not affected by the hydrodynamics and, as a consequence, the order parameters are very stable with time.

From the results we can say that in most experiments a steady state is reached and order parameters associated to them can be obtained by averaging in the steady regime. However, in some experiments with very high packing fraction the behaviour is quite fluctuating and mean order parameters have no sense by themselves. For these cases we will calculate the order parameters by averaging in the whole experiment (removing the first quick organization where clusters

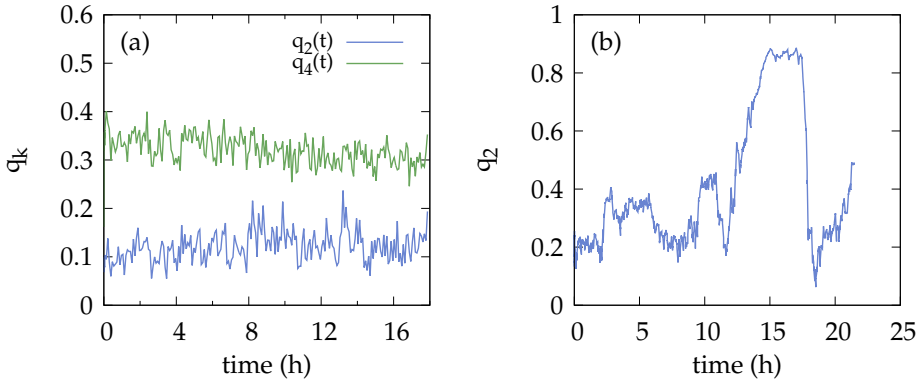

Figure 7.4: Time evolution of order parameters for two different experiments: (a) $\kappa = 4$, $\eta = 0.64$ and (b) $\kappa = 8$, $\eta = 0.81$.

are formed) but we have to keep in mind that those values do not correspond to steady state configurations.

7.3.4 Dependence with radius of local averaging region

There is another key point in the study of order parameters which is the definition of the local region in which we measure. In our study we compute q_k in a circular region of radius ξ. Of course the value of the order parameters will depend on the position, time and size of the local region: $q_k(\mathbf{r}, t, \xi)$. At bulk the order parameters do not depend on the local region, but confinement may distort a globally structured phase and promote local order instead. One would expect that order parameters will decrease with ξ because particles close to each other are more correlated. However, this decrease may not be uniform since a plateau should appear at radii of the order of the domain size.

In figure 7.5 we show the dependence of order parameters with local radius for all experiments. This result is very interesting and we can obtain a lot of information from it. For example we see that for low aspect ratio the tetratic order parameter clearly increases with packing fraction and saturates at some ξ, indicating that the directors of the tetratic phase do not change in the cavity. However, the nematic order parameter does not saturate, it only presents a plateau in some range of ξ corresponding to the typical sizes of smectic domains. For larger aspect ratios the picture is less clear due to the lower degree of order. Another feature that comes out from the graphs is that, in order to compare different experiments, a radius of $\xi = 4L$ is a good choice since order parameters are close to saturation or near the plateau. So from now on results of order parameters will be calculated with this local radius.

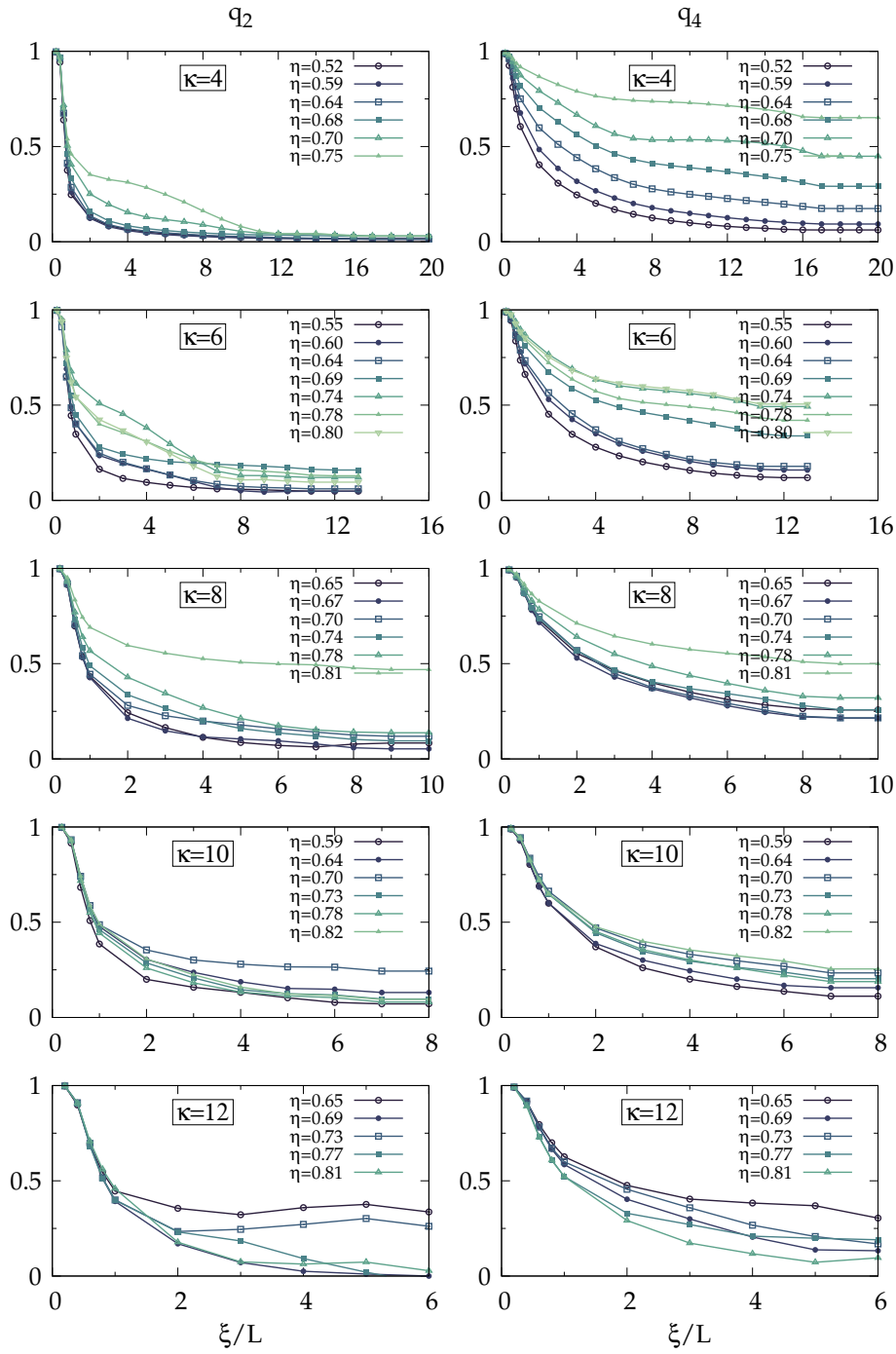

Figure 7.5: Dependence of nematic (left panels) and tetratic (right panels) order parameters with local radius ξ. Each graph corresponds to a particular κ and contains all η explored.

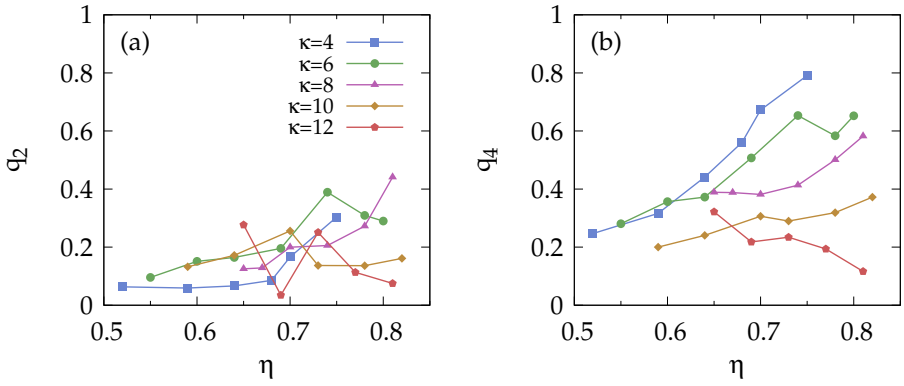

Figure 7.6: Nematic (a) and tetratic (b) order parameters as a function of packing fraction for different aspect ratios. Lines and points have the same meaning in both graphics.

7.3.5 Phase diagram of monomers

Once the procedure for computing the order parameters has been defined, we can gather all values of different experiments in their steady state (if possible). Figure 7.6 summarizes these results for all packing fractions and aspect ratios explored. From it we can conclude several things. First q_2 remains low for most of the cases except those with smectic fluctuations, where the nematic order parameter raises a bit. For low aspect ratio ($\kappa \leqslant 8$) q_2 grows with density and smectic fluctuations become more important for high packing fractions. However, for higher aspect ratios, the behaviour with η is more noisy and no clear connection is apparent. With respect to the tetratic order parameter q_4, the picture is clearer and two different behaviours seem to appear. Rods with low aspect ratio present a clear increase of q_4 with packing fraction, reaching considerably high values –the lower the value of κ the higher the tetratic order–. On the other hand, particles with large aspect ratio exhibit small changes with density as a consequence of the absence of order.

From our results we can think of a phase diagram where rods with $\kappa \lesssim 8$ show a region of tetratic stability for high packing fractions. This result is consistent with previous experiments, as said in the introduction, in particular with (*150*) which is the first work to study the system quantitatively in detail. However, in contrast with this work, we think that a quantitative phase diagram cannot be obtained since the transition from isotropic to ordered phases appears to be continuous and not sharp. Moreover smectic fluctuations coexist with the tetratic for high packing fractions. Another difference is that the authors of (*150*) claim to have obtained a nematic phase for large aspect ratios, while we do not observe nematic order for $\kappa = 10$ and $\kappa = 12$. Nevertheless, different protocols to quantify the order may lead to different conclusions on

the global ordering behaviour so we should take this disagreement carefully. Additionally, one must be cautious when comparing both experiments since some experimental conditions are different (rods material, free particle height, cavity size, etc.). For example they use plastic particles which present more inelastic collisions and tend to clusterize less. In the next section we will see that this feature could explain the difference observed with respect to the nematic phase.

7.3.6 Clustering

We have already mentioned that particles in the system form clusters easily and from the first stages of the experiment. For this reason it is interesting to study the properties of clustering. First of all we need to define what a cluster is. Given a particle configuration, one can intuitively identify clusters, see for example the left panel of figure 7.7. However, we need a criterion to define clusters in an unequivocal way. To us two neighbouring particles will belong to the same cluster if they satisfy at least one of the following conditions:

1. The distance between centers of mass is less than two particle diameters ($|\mathbf{r}_1^c - \mathbf{r}_2^c| < 2d$) and the maximum orientational difference is 15° ($|\varphi_1 - \varphi_2| < 15°$).

2. The distance between centers of mass is $|\mathbf{r}_1^c - \mathbf{r}_2^c| < 2.8d$ but the distance between particles fulfills the condition $\min(|\mathbf{r}_1 - \mathbf{r}_2|) < 2d$ and the maximum orientational difference is $|\varphi_1 - \varphi_2| < 7°$. The second condition is imposed to take into account particles at contact and almost parallel but displaced along the rod axis direction.

Nevertheless, the criterion parameters are not crucial in the sense that small changes in their values do not imply significant changes in the results. All the following results have been checked to be robust under reasonable changes in the parameters.

One could wonder how important clustering is with respect to thermal systems. In order to elucidate this we compare in the right panel of figure 7.7 the cluster distribution function $N_c(n)$ of an experiment and a Monte Carlo simulation of hard rectangles under the same conditions (particle aspect ratio, cavity size and density). The cluster distribution function is defined as the fraction of clusters with n monomers. We can see that in both cases the distributions are approximately exponential ($N_c(n) \propto e^{-\lambda n}$). However, the tendency of the granular system to clusterize is clearly higher. Between both distributions there is a factor of ~ 3 in the decay parameter.

We think that this difference comes from local inhomogeneities of the granular temperature, defined in the same way as in thermal systems as

$$T_g = \left\langle |\mathbf{v}_i - \mathbf{V}|^2 + \frac{L^2}{12}(\omega_i - \Omega)^2 \right\rangle \tag{7.6}$$

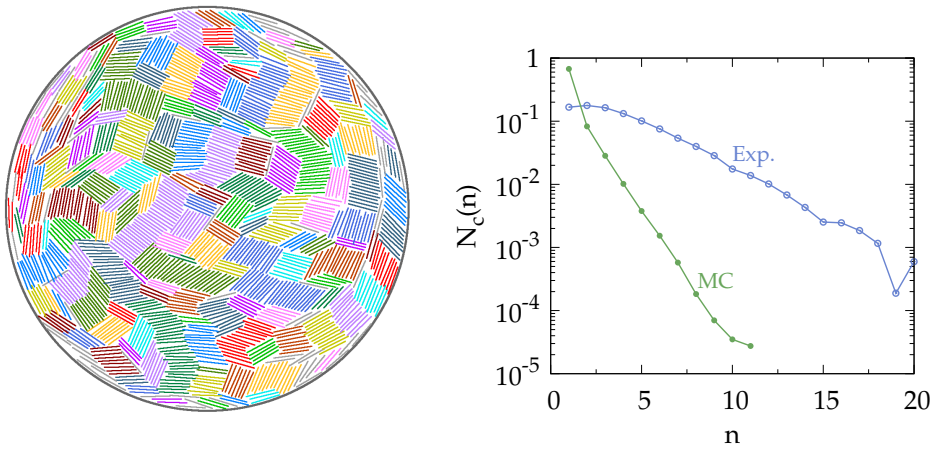

Figure 7.7: Left: particle configuration for the experiment $\kappa = 10$ and $\eta = 0.82$. Rods belonging to the same cluster are represented in the same color. Right: normalized cluster distributions for experiment (blue open circles) and Monte Carlo (green solid circles) at conditions $\kappa = 4$ and $\eta = 0.52$.

where $\mathbf{v}_i$ is the velocity of a given particle, $\mathbf{V}$ is the local velocity of the system around the given particle, ω_i and Ω are the corresponding angular velocities of the particle and its surroundings, and the prefactor $L^2/12$ is the moment of inertia of a rod of length L. The difference between granular and thermal temperatures is that dissipation in granular systems may be different depending on the particles and therefore an equipartition of energy does not necessarily apply. For example, the number of collisions to which a rod is subject is probably very different depending on whether it is part of a cluster or not. In the first situation the particle is inside a cluster in a packed configuration and, as a consequence, it experiences many collisions because of the proximity to its neighbours. This results in a locally cooling effect in which particles belonging to large clusters are 'colder'. In order to check this hypothesis we have calculated the average granular temperature for different cluster sizes $T_g(n)$, i.e. the average temperature of particles belonging to a cluster of size n. In general the results agree with our hypothesis since in $\sim 80\%$ of experiments the granular temperature decreases with n, as shown in figure 7.8(a). However, some experiments do not present this tendency and $T_g(n)$ barely changes with cluster size –figure 7.8(b)–.

A consequence of the clustering enhancement may be the absence of the nematic phase for long particles. It is well known that long thermal rods present nematic order at bulk, even when confined to circular cavities (*104*). But this phase has very low clustering because there are no positional correlations, only orientational ones, not compatible with the strong clustering found in the granular system. The nematic tendency besides clustering effect will probably result in a smectic phase, which is what we see at high densities. In the case of the

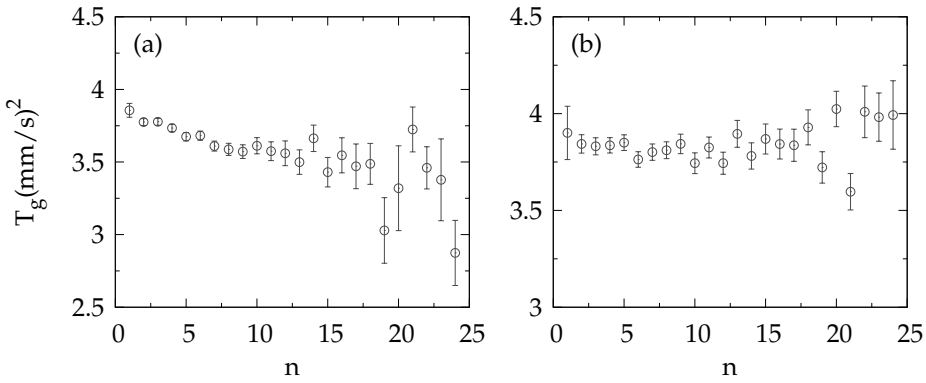

Figure 7.8: Average granular temperature as a function of cluster size for (a) $\kappa = 4$, $\eta = 0.68$ and (b) $\kappa = 6$, $\eta = 0.78$.

longest particles investigated, the confinement is much more important since the effective cavity size is smaller in terms of particle length and, consequently, a global uniaxial phase cannot be reached: no order exists, just clustering. Particles form a collection of disordered clusters which we call the *patchy* phase. The configuration of figure 7.7 is a good example.

Let us now study the clustering in the experiments in more detail. The left panels of figure 7.9 show the normalized cluster distributions $N_c(n)$ for all cases, i.e. the number of clusters with n monomers averaged in the steady state, provided it exists. The distributions are approximately exponential with a decay parameter λ depending on the particle aspect ratio and packing fraction. As expected, λ decreases with η because larger clusters are developed when the density increases. However, this effect is more pronounced for low κ while for $\kappa = 10$ and 12 all curves present a similar decay. The reason is twofold: for longer particles the physical size of a cluster with n rods is considerably larger than the corresponding one for shorter particles and it is more affected by confinement; moreover ordered phases appear for low aspect ratios and they promote the presence of large clusters, especially when the smectic is present.

The fact that cluster distributions are exponential-like has been already observed in Monte Carlo simulations for hard rectangles (*163*) and can be explained with a mechanism where the probability for a particle to join or leave a cluster is independent of the cluster size n (*164*).

From a closer inspection the cluster distributions present some deviations from a pure exponential behaviour. In the first part ($n \lesssim \kappa$) the distributions show a small positive curvature. After that the intermediate part is basically exponential and for high densities, when smectic fluctuations are present, the final part of the distributions exhibit nonexponential behaviours. In these cases fat-tail distributions fit better than pure exponential ones. The explanation for this effect could be that at high densities and when smectic fluctuations are

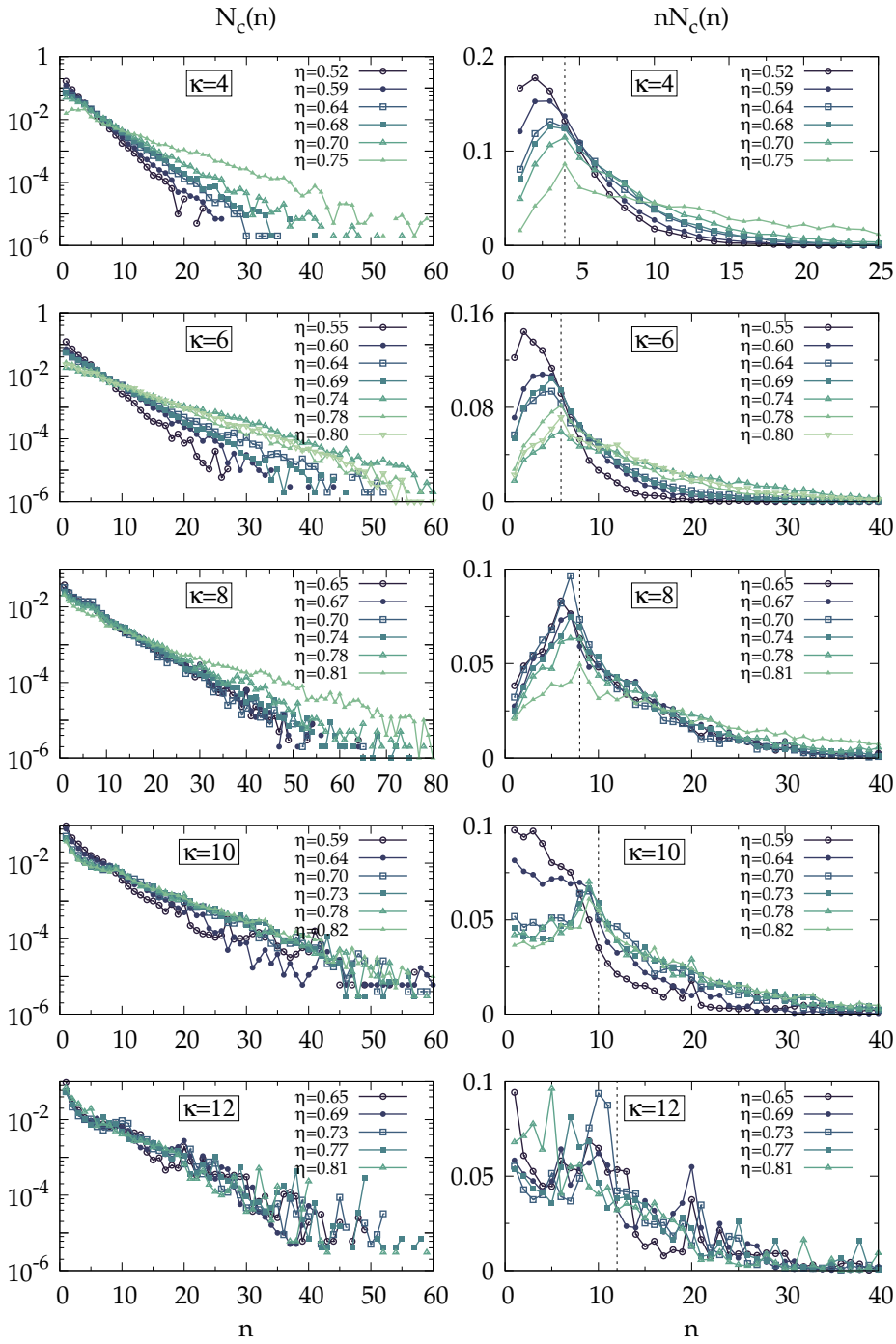

Figure 7.9: Normalized cluster distributions $N_c(n)$ (left panels) and fraction of particles in clusters of size n (right panels). Each panel corresponds to a particular κ and contains all η explored.

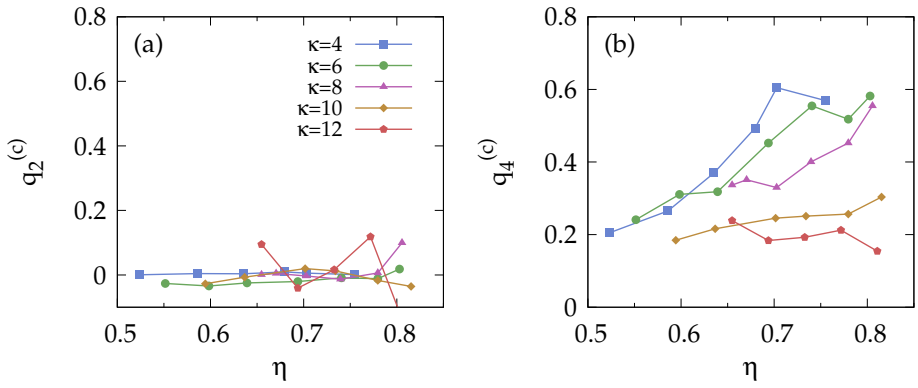

Figure 7.10: Nematic (a) and tetratic (b) order parameters for the mixture of clusters as a function of packing fraction for different aspect ratios. Lines and points have the same meaning in both panels.

present large clusters are formed not only by including new monomers but also by cluster aggregation.

The right panels of figure 7.9 show the cluster distributions multiplied by the size of clusters: $nN_c(n)$. These distributions give the number of particles belonging to a cluster of size n. An interesting result comes out here: the distributions present a peak at $n \sim \kappa$ which means that square-like clusters are particularly probable. This feature is consistent for $\kappa \lesssim 8$ while for larger aspect ratios the distributions are more noisy and diffuse (although a change in behaviour clearly exists around $n \approx \kappa$). Then, for particles with low aspect ratio, square-like clusters are particularly stable, a fact that favours the tetratic phase. A result very related and in agreement with our experimental observations is that a theory based on exponential distributions of clusters showed the enhancement of tetratic stability due to clustering effects (*163*).

7.3.7 New point of view: mixture of clusters

Because of the particular importance of clustering we are encouraged to look at the system from the point of view of clusters. Particles in a cluster are highly correlated and we could study the system as a polydisperse mixture of superparticles. From the set of rods that define a cluster we obtain the orientation, length and width of the superparticle by diagonalizing the gyration tensor. With that information we can obtain angular histograms and order parameters in exactly the same way as we did for monomers. Figure 7.10 shows the uniaxial and tetratic order parameters for the mixture of clusters in all experiments. The picture is qualitatively very similar to the results for monomers of figure 7.6. While the uniaxial order parameter $q_2^{(c)}$ is very small for all cases, the

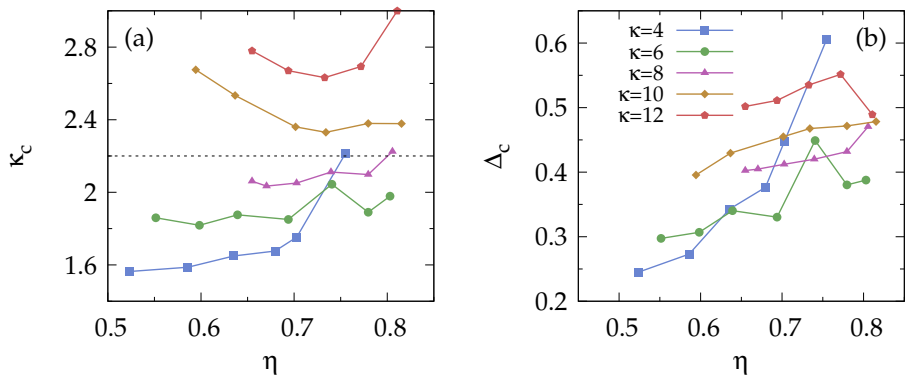

Figure 7.11: (a) Mean aspect ratio of clusters as a function of packing fraction for the different particle aspect ratios. The dashed horizontal line represents the critical value of aspect ratio for tetratic stability according to scaled-particle theory. (b) Polydispersity of clusters for the different experiments. Points and color have the same meaning in both graphs.

tetratic one $q_4^{(c)}$ clearly increases for $\kappa = 4$, 6 and 8 but remains practically constant for $\kappa = 10$ and 12. This result does not add any new information but reinforces the idea that looking the system as a mixture of superparticles makes sense.

In order to get a deeper understanding of the mixture of clusters we can study the mean aspect ratio of clusters and its dispersion (polydispersity), defined as

$$\kappa_c = \left\langle \frac{L_c}{d_c} \right\rangle \tag{7.7}$$

$$\Delta_c = \frac{1}{\kappa_c} \sqrt{\left\langle \left(\frac{L_c}{d_c} \right)^2 - \kappa_c^2 \right\rangle} \tag{7.8}$$

where L_c and d_c are the length and width of a cluster and the averages are defined for all clusters. A very interesting picture comes out from computing κ_c and Δ_c in all experiments, see figure 7.11. From a first inspection one observes that the mean aspect ratio of clusters for a given κ does not change much with η (except for some particular cases with large smectic fluctuations) but the mixture is quite polydisperse if we look at Δ_c. However, the most interesting feature comes from the values of κ_c. In figure 7.11(a) it is represented a horizontal dashed line at $\kappa^* = 2.18$ which is the critical aspect ratio for tetratic stability given by scaled-particle theory (*161*). Surprisingly the three particle aspect ratios exhibiting tetratic correlations ($\kappa = 4$, 6 and 8) lie in the stability region predicted by scaled-particle theory while the experiments with $\kappa = 10$ and 12 have $\kappa_c > 2.3$. It seems that the strong clustering in the vibrated system somehow renormalize the problem. Scaled-particle theory only accounts for

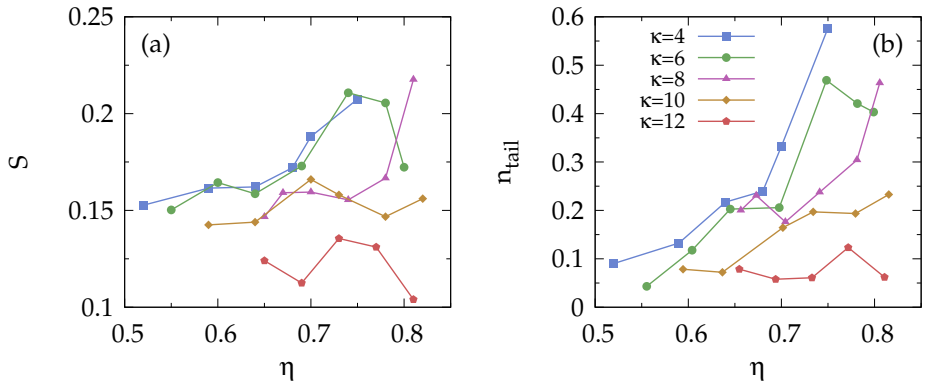

Figure 7.12: (a) Smectic order parameter as a function of packing fraction for all aspect ratios explored. (b) Fraction of particles in the tail of the cluster distribution, i.e. for $n > 2\kappa$.

two-body orientational correlations, but particles inside a cluster are all very correlated, so this feature cannot be captured by the theory. However, from the point of view of clusters all short-range correlations are hidden inside the superparticles and the remaining weak correlations between them can be treated as effective two-body correlations, which are well accounted for by mean-field theories.

7.3.8 Beyond the tetratic

The last section is devoted to explore other interesting aspects of the granular system which are not directly related to our first motivation, i.e. understanding the stability of tetratic phase for large κ.

We have already mentioned the smectic phase briefly but it deserves a deeper inspection here. In figure 7.12(a) it is shown the smectic order parameter, as defined in equation 7.4, for all cases. In general it grows with η but sometimes the behaviour is non-monotonic and quite noisy. This is due to the nature of the smectic phase which appears as fluctuations in space and time. For this reason, we need to characterize the smectic from a more detailed point of view. A possibility is to look at the tail of cluster distributions because smectic structures are composed of large clusters, in contrast with the tetratic phase. Furthermore this probe should be more robust than the smectic order parameter since long clusters should exist in an experiment with smectic fluctuations even when extended smectic structures are not present. In order for smectic regions to appear, a high number of large clusters is required, which will eventually aggregate and form smectic structures. Figure 7.12(b) shows the parameter n_s defined as the fraction of particles belonging to clusters with more than $n_c = 2\kappa$

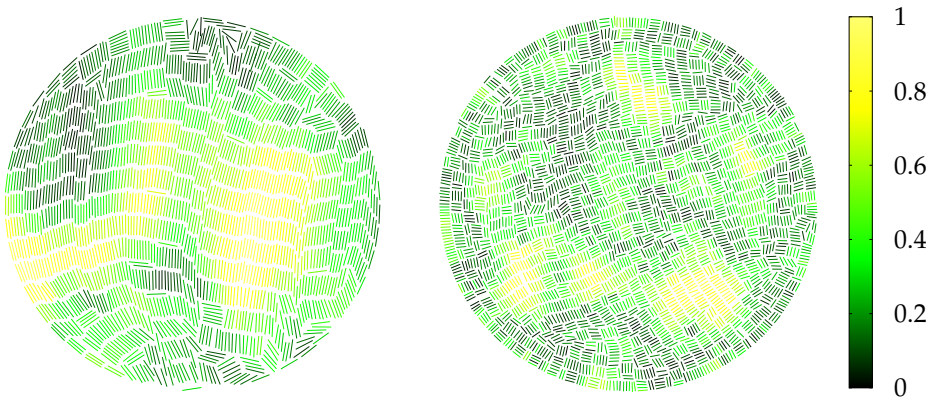

Figure 7.13: Particle configurations for two experiments with smectic fluctuations. Colours represent local smectic order parameter. Particles are slightly reduced in order to better visualize the structures. Holes correspond to particles not identified after image processing. Cases are $\kappa = 8$, $\eta = 0.81$ (left) and $\kappa = 4$, $\eta = 0.75$ (right).

particles, from which we consider the tail of the distribution. Notice that both S and n_s are correlated, but the picture provided by the latter is clearer.

To sum up, there exist no transition to a smectic phase, there are only fluctuations that appear at high densities and may coexist with other structures (tetratic or patchy). These fluctuations become more important at high packing fractions. In order to illustrate the spatial smectic fluctuations we show two configurations with the local smectic order parameter superimposed as a colour map in figure 7.13. The time evolution of these kind of images shows a very dynamic behaviour with smectic domains being created and destroyed continuously [a movie of the dynamic evolution is shown in (*165*)]. A signal of the time smectic fluctuations was given in figure 7.4(b) where the nematic order parameter is plotted as a function of time for a case with large smectic domains (of course q_2 does not measure smectic order but it is high when smectic structures are present).

One could wonder why the smectic phase is so fluctuating. The circular cavity clearly frustrates a global smectic structure but it could appear with defects –as we will see that happens in the tetratic– or different local smectic phases adapted to the surface. However, none of these cases occur but the fluctuating situation. We think that the reason for this has to do with the hydrodynamic flow and vorticity in the system, a property already studied in similar experiments (*155*). As a consequence, smecticity competes with vorticity, the second one favouring the breaking of smectic structures and creating these fluctuating events. On the other hand, we have tetratic order which is much more stable [a movie of the dynamic evolution is shown in (*165*)]. In fact, it even appears as a global phase percolating all the cavity, as shown in the left panel of figure

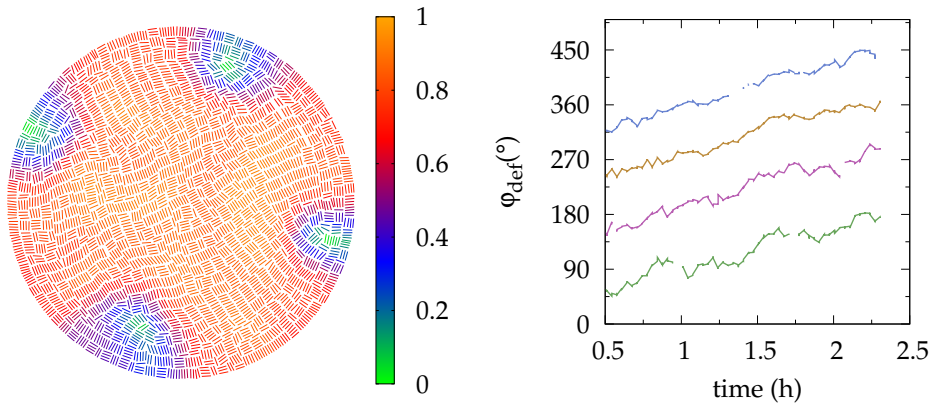

Figure 7.14: Left: particle configuration for $\kappa = 4$ and $\eta = 0.75$ with the local tetratic order parameter superimposed in colour. Right: polar angles of the four point defects as a function of time.

7.14, where a tetratic configuration is represented with the local tetratic parameter superimposed as a colour map. In order to satisfy the favoured orientation at the wall, the configuration needs to create four topological defects near the walls. From these results one can argue that, unlike the smectic case, tetratic order seems to be very stiff against vorticity and suppresses the velocity flow. The reason for such a difference could lie in the fact that the two orthogonal local directors are inconsistent with a rotational velocity field. Therefore tetratic states can exist for very long times in stable configurations.

When the vorticity is suppressed the granular monolayer behaves as a liquid-crystalline material in thermal equilibrium, whose properties can be understood from a competition between surface alignment, elasticity and defects that restore the symmetry (*151*). For example in the tetratic phase not only the order properties –already discussed– but also the point defects share many similarities with their thermal counterparts. Monte Carlo simulations under the same conditions also exhibit four point defects close to the boundaries and separated by a relative angle of approximately 90° in polar coordinates (*166*). In the right panel of figure 7.14 we represent the polar angles of the four point defects in the time evolution as obtained from the experiment. They appear close, but not in contact, to the wall and separated by the aforementioned 90°, as in the MC simulations. However, in the granular system there exists an additional effect which is a collective motion of particles all rotating as a solid body. This pure non-equilibrium phenomenon has been already reported (*26*, *155*) and observed in many of our experiments, regardless of the ordered phase of the particles. From figure 7.14 we can obtain an average angular velocity of around 70°/hour for that experiment, although this kind of collective motions are not always so constant but appearing, disappearing and even changing the direction of motion.

7.4 REMARKS AND COMMENTS

In the present chapter we have reported experimental results for a system of granular rods exhibiting different configurations depending on particle aspect ratio and packing fraction. In agreement with other works we have seen tetratic correlations in experiments with $\kappa \lesssim 8$ which is at variance with mean-field theories. Based on the strong tendency of these systems for clustering, we have studied the system from the point of view of clusters. From this perspective the system can be regarded as a mixture of superparticles, a kind of renormalization of the problem. Because square-like clusters are particularly stable, the mean aspect ratio of the superparticles is low and tetratic stability can be explained with scaled-particle theory. It is reasonable that this renormalization is at work since many-particle correlations are eliminated in the cluster view and only weak correlations between superparticles remain.

Additionally to the comparison with thermal systems, we have also reported on non-equilibrium effects genuine of granular media. For example fluctuations of smectic structures due to a competition with the hydrodynamic field. Also solid-body rotations have been seen as a consequence of the dissipative nature of the system.

Some other experiments related to our work are very interesting to be studied and remain as future work:

1. It would be interesting to compare carefully the results of the tetratic point defects with Monte Carlo simulations and also the possibility to fit the results of the fluctuations of defects with an elastic theory.

2. Related to the setup of the present chapter, it would be very valuable to perform a detailed study of the low density regime, where inhomogeneities and coexistence of different phases appear.

3. Modify the setup in order to make experiments with square cavities which will probably enhance the tetratic phase without frustrating globally. We could also look for particle structures with two wall domains like the ones obtained in chapter 4.

4. Another interesting modification of the experiment would be to include channels and obstacles in order to study particle correlations and compare with results of chapters 3 and 6.

5. Also interesting is the study of mixtures of rods with different aspect ratios. We have already begun to perform these experiments and we observe a fascinating behaviour: when particle aspect ratios are different enough, they segregate with different ordering properties (see figure 7.15).

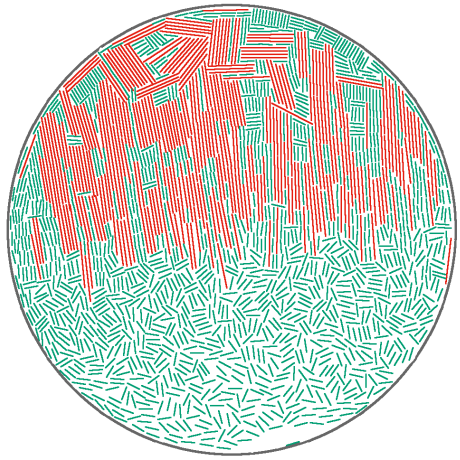

Figure 7.15: Particle configuration of a mixture of particles with aspect rations $\kappa_1 = 14$ (red) and $\kappa_2 = 4$ (green). Longest particles are highly packed and present nematic ordering, shorter ones exhibit a gas-like isotropic configuration.

CONCLUSIONES

This chapter is written in Spanish as required by the University regulations.

En esta sección final de la tesis vamos a remarcar los principales resultados obtenidos en los diferentes estudios presentados y las conclusiones a las que hemos llegado.

El objetivo principal del capítulo 3 era probar la validez de la teoría del funcional de la densidad (TFD) en condiciones de fuerte confinamiento y altas densidades. Para ello hemos comparado los resultados obtenidos mediante la TFD con resultados exactos y con simulaciones Monte Carlo (MC). En primer lugar hicimos un estudio de los sistemas de volumen en el que comprobamos que el régimen donde la TFD compara mejor con las simulaciones era el de altas densidades, para el cual la similitud es extraordinaria. Tanto la ecuación de estado en la zona de estabilidad de la fase cristalina como el número de vacantes coinciden en ambos casos. Con respecto a las correlaciones entre partículas vimos que la TFD las sobreestima un poco con respecto a los resultados del MC.

El estudio principal del capítulo 3 es la comparación de la TFD con los resultados exactos obtenidos mediante el método de la matriz de transferencia (MMT) en sistemas confinados, ya que son este tipo de sistemas en los que se centra la tesis. Para ello se han comparado perfiles de densidad, ecuaciones de estado y capacidades caloríficas de sistemas de partículas duras cuadradas confinadas en canales estrechos en los que no se pueden formar más de dos capas de partículas en la dirección transversal. La principal conclusión que obtenemos de los resultados es que la TFD funciona muy bien en este tipo de sistemas. Los perfiles de densidad son casi idénticos a los obtenidos mediante MMT y las ecuaciones de estado y capacidades caloríficas presentan también muy buen acuerdo. Con respecto a las correlaciones entre partículas, el MMT no puede obtenerlas, por lo que hemos hecho una comparación con simulaciones MC. Estas correlaciones coinciden bastante bien para el caso de un canal paralelo a uno de los lados de las partículas. Pero la comparación no es tan buena cuando el canal está inclinado 45° con respecto a los lados de las partículas. Esta discrepancia sin embargo no nos preocupa en relación a los próximos estudios ya que los mecanismos entrópicos favorecen orientaciones de las partículas que sean paralelas o perpendiculares con respecto a las paredes o a las partículas vecinas. Así se observa en los resultados obtenidos en el resto de capítulos.

En el capítulo 4 se ha estudiado el efecto del confinamiento en una cavidad cuadrada para un sistema de partículas rectangulares. Al comparar las fases de volumen con las que se obtienen en el sistema confinado para diferentes

tamaños de cavidad obtenemos varias conclusiones importantes. En primer lugar hemos observado que el efecto del confinamiento puede traer consigo la desestabilización de fases de equilibrio de volumen. Así ocurre, por ejemplo, para partículas con relación de aspecto $\kappa = 1$ en las que la fase columnar desaparece en el sistema confinado en favor del orden cristalino. También hemos estudiado la dependencia de los diagramas de fase de este sistema con la relación de aspecto de las partículas. De esta forma observamos fases nemáticas, columnares, esmécticas y cristalinas cuando la densidad es suficientemente alta. La periodicidad de las fases no uniformes hace que éstas se vean muy afectadas por la conmensuración con el tamaño de la cavidad. Como conclusión, estos tipos de sistemas están sujetos a una compleja mezcla de mecanismos que compiten entre sí para favorecer distintos tipos de orden: interacciones con la superficie, energía elástica debida a la deformación del director, frustración inducida por efectos de conmensuración y por el orden local favorecido por las superficies... En este estudio hemos presentado una explicación detallada de la interpretación física de dichos fenómenos que es extensible a muchos otros sistemas. Aunque la aproximación de orientaciones restringidas de las partículas (aproximación de Zwanzig) pueda parecer lejana a la realidad, hay que recordar que nuestro estudio está centrado en regímenes de alta densidad, en los cuales las fases líquido-cristalinas están compuestas principalmente por partículas con orientaciones paralelas o perpendiculares a la dirección de las inhomogeneidades, o mútuamente perpendiculares debido al confinamiento en cavidades cuadradas.. Además es importante señalar que en este tipo de casos la TFD se espera que aporte resultados cuantitativamente correctos, como estudiamos en el capítulo 3.

Otro sistema de partículas duras confinadas se estudia en el capítulo 5, donde éstas están restringidas a permanecer en una monocapa plana. En él nos hemos centrado en el efecto que tiene la biaxialidad de partículas (de tipo ortoédricas) en el diagrama de fases del sistema. Éste presenta una fenomenología muy rica que hemos estudiado en detalle en el capítulo. Pero la conclusión más importante que obtenemos es que la biaxialidad de las partículas desestabiliza la fase nemática biaxial, al contrario de lo que se podría esperar. La interpretación física a este fenómeno está detallada en el capítulo 5 y para ella nos ha resultado muy útil el estudio de partículas rectangulares del capítulo 4, ya que el sistema de la monocapa de partículas tridimensionales es equivalente al de sus proyecciones en la superficie (rectángulos).

Hasta este punto únicamente hemos estudiado las diferentes fases líquido-cristalinas de equilibrio, pero con el formalismo de la TFD no podemos obtener información acerca de la dinámica en este tipo de sistemas. Para ello hemos dedicado el capítulo 6 al estudio de la teoría dinámica del funcional de la densidad (TDFD), que da una descripción de la dinámica relajativa de formación de estructuras líquido-cristalinas. En particular nos hemos centrado en sistemas de partículas cuadradas. Por una parte, partiendo de perfiles iniciales de volumen con diferentes simetrías, hemos presentado un estudio detallado de cómo

se transforman al ser confinados en una cavidad cuadrada. De este primer estudio sacamos varias conclusiones importantes: (i) la dinámica es muy diferente en función de si los perfiles de equilibrio conmesuran bien con el tamaño de la cavidad o no, en particular las escalas de tiempo involucradas en los procesos de estructuración varían mucho dependiendo de dichas condiciones. (ii) La dinámica en cada uno de los casos anteriores está en gran medida determinada por el flujo entre diferentes capas de partículas o por el flujo interno de las capas. (iii) El perfil inicial es en algunos casos determinante en la estructura final estabilizada.

Por otra parte también se ha estudiado la dinámica de formación de patrones en sistemas de volumen cuando son perturbados por la presencia de un obstáculo. Los resultados de este estudio reflejan que la geometría del obstáculo tiene una influencia importante en la estructura del perfil de densidad final. Debido a que la dinámica se genera en las proximidades del obstáculo, su forma influye en la perturbación del perfil de densidad, que se propaga por todo el espacio. Como consecuencia hemos visto que diferentes obstáculos pueden inducir fases columnares o cristalinas en el sistema de cuadrados bajo las mismas condiciones.

El último capítulo de la tesis está dedicado al estudio experimental de medios granulares y a su fenomenología, en muchos casos similar a la de los correspondientes sistemas de equilibrio. El experimento consiste en un sistema de partículas cilíndricas que forman una monocapa y son vibradas verticalmente. Este aporte de energía externa hace que las partículas se muevan y eventualmente se ordenen de forma espontánea. Nuestro interés en este tipo de sistemas de no-equilibrio se debe a las similitudes en la formación de texturas líquido-cristalinas con los sistemas de equilibrio de partículas duras. En particular nos hemos centrado en la fase tetrática y nuestro objetivo era estudiar el porqué ésta se estabilizaba en los experimentos para partículas con relación de aspecto relativamente grande, en comparación con los sistemas de equilibrio que sólo presentan fase tetrática para relaciones de aspecto cortas. Después de un estudio detallado pudimos concluir que esa diferencia se debe a que las partículas en el sistema granular presentan una fuerte tendencia a clusterizar debido a mecanismos de disipación de energía. De hecho, estudiando el sistema granular desde la perspectiva de los clusters de partículas, la coincidencia de la estabilidad de la fase tetrática con los sistemas de equilibrio es casi perfecta. La fase tetrática encontrada en el sistema granular presenta una estabilidad robusta frente a los procesos dinámicos presentes en él, a diferencia de la fase esméctica también encontrada a altas densidades, que resulta ser muy fluctuante. Como trabajo adicional también hemos estudiado algunas propiedades de los procesos dinámicos presentes en el experimento. Algunos aspectos muestran unas equivalencias muy interesantes con los sistemas de equilibrio, en particular la formación de defectos en la fase tetrática. Pero un estudio detallado de esta fenomenología se deja para un futuro trabajo.

Appendices

A CONJUGATE GRADIENTS

The free energy functional has a closed expression but, in general, it is not possible to obtain analytically the density profile for which the grand potential presents a minimum. We need to do that numerically, so we firstly discretize the space and the density profiles in a grid of $N = n \times m$ points

$$\rho(\mathbf{r}) \longrightarrow \rho_{ij} \;\; i,j \in \mathbb{Z} \Longrightarrow \mathcal{F}[\rho(\mathbf{r})] \longrightarrow \mathcal{F}(\{\rho_{ij}\}) \tag{A.1}$$

and the same with the grand potential, which now will be a function of N variables instead of a functional.

In order to find numerically the minimum of a given function one can proceed in several ways. An intuitive way is start from a given point in the phase space, calculate its gradient and move in that direction until an energy minimum is found. The process is repeated as many times as necessary to reach the global or local minimum, where the gradient is zero –in practice small enough–. This process is called *steepest descent*. But there exist more efficient methods to reach the minimum faster like the *conjugate gradients*, which is the one we use.

The idea of the conjugate gradients method is the same as steepest descent but the directions along we move are not exactly the gradient at that point. The first step is the same, we compute the gradient direction given by

$$g_{ij}^{[0]} = \left.\frac{\partial F}{\partial \rho_{ij}}\right|_{\left\{\rho_{ij}^{[0]}\right\}} \tag{A.2}$$

where the superscript $^{[k]}$ means the iteration step number. Then we seek for the minimum of the free energy $\mathcal{F}$ along that direction

$$\mathcal{F}\left(\{\rho_{ij}^{[0]} + \alpha g_{ij}^{[0]}\}\right) \longrightarrow \alpha_{\min} \;:\; \left\{ \left.\frac{d\mathcal{F}}{d\alpha}\right|_{\alpha=\alpha_{\min}} = 0, \;\; \left.\frac{d^2\mathcal{F}}{d\alpha^2}\right|_{\alpha=\alpha_{\min}} > 0 \right\}. \tag{A.3}$$

In the following steps we proceed the same way but substituting the gradient with the conjugated vectors $pij^{[k]}$

$$\mathcal{F}\left(\{\rho_{ij}^{[k]} + \alpha p_{ij}^{[k]}\}\right) \longrightarrow \alpha_{\min} \longrightarrow \rho_{ij}^{[k+1]} = \rho_{ij}^{[k]} + \alpha_{\min} p_{ij}^{[k]} \tag{A.4}$$

where

$$p_{ij}^{[k]} = -g_{ij}^{[k]} + \beta p_{ij}^{[k-1]}, \quad p_{ij}^{[0]} = g_{ij}^{[0]} \tag{A.5}$$

$$\beta = \frac{\sum_{ij} g_{ij}^{[k]} g_{ij}^{[k]}}{\sum_{ij} g_{ij}^{[k-1]} g_{ij}^{[k-1]}} = \frac{\boldsymbol{g}^{[k]} \cdot \boldsymbol{g}^{[k]}}{\boldsymbol{g}^{[k-1]} \cdot \boldsymbol{g}^{[k-1]}} \tag{A.6}$$

There are some variations that work better in real cases where functions are not exactly quadratic. We have implemented the *Polak-Ribiere* one defined as

$$\beta = \frac{(\boldsymbol{g}^{[k]} - \boldsymbol{g}_j^{[k-1]}) \cdot \boldsymbol{g}^{[k]}}{\boldsymbol{g}^{[k-1]} \cdot \boldsymbol{g}^{[k-1]}}$$

For more detail about the method see (*167*).

A.1 1D MINIMIZATION

Optimize the minimization (A.4) is another important task in order to speed up the numerical convergence. Our algorithm works as follows for the 1D minimization: we begin at $\{\rho_{ij}^{[k]}\}$ and calculate two more points in the conjugate gradient direction $\{\rho_{ij}^{[k]} - \tau p_{ij}^{[k]}\}$ and $\{\rho_{ij}^{[k]} + \tau p_{ij}^{[k]}\}$, where τ is an arbitrary constant. Then we calculate the parabola defined by these three points and move to the minimum of the parabola. This process is repeated until the real minimum is reached –in practice only two or three steps are generally enough–.

B NUMERICAL GRADIENT

The grand potential is computed numerically once we have discretized the space, and its expression is not exactly the same as the analytical one. In particular the integrals, calculated through the trapezoidal rule, do not weight all points equally, those at the limits of the integrals are multiplied by 1/2. Consequently, the gradient of the grand potential must be calculated from the expression of the numerical gradient because there are little differences that become important when approaching to the minimum. Here we derive the analytic and numerical expressions of the grand potential in order to show these differences.

Equations 2.54 and 2.56 correspond to the analytic expressions of the grand potential and its gradient for a given density field $\rho_\nu(\mathbf{r})$. In order to compute it numerically we discretize the density field and convert the integrals into sums. The space is discretized within the square cavity of side H, defined by the mesh $\mathcal{S}$ with grid steps Δ

$$\rho_\nu(\mathbf{r}) \longrightarrow \rho_\nu(i,j) \qquad i,j \in \mathcal{S}. \tag{B.1}$$

Then the integrals are replaced by sums, which using the trapezoidal rule read

$$\int_a^b dx f(x) \longrightarrow \Delta \sum_{i=a/\Delta}^{b/\Delta} w_i f(i) \qquad w_i = \begin{cases} 1/2 & \text{if } i = a/\Delta,\ b/\Delta \\ 1 & \text{otherwise.} \end{cases} \tag{B.2}$$

B.1 ANALYTICAL GRADIENT

The analytical expression for the gradient of the grand potential within the cavity, where $v^\nu_{ext}(i,j) = 0$, is obtained from equation 2.56. In order to compute it numerically we could just discretize the space within the cavity and obtain

$$\beta \frac{\partial \Omega(\{\rho_\nu\})}{\partial \rho_\nu(i,j)} = \ln \rho_\nu(i,j) - \beta\mu_\nu + \sum_\alpha \phi^\nu_\alpha(i,j) \tag{B.3}$$

note that now the grand potential and free energy are not functionals but multivariable functions. The functions ϕ_α^ν being

$$\begin{aligned}\phi_0^\nu(i,j) = \frac{1}{4}\Bigg\{ & P_0\left(i-\frac{\sigma_x^\nu}{2\Delta}, j-\frac{\sigma_y^\nu}{2\Delta}\right) + P_0\left(i-\frac{\sigma_x^\nu}{2\Delta}, j+\frac{\sigma_y^\nu}{2\Delta}\right) \\ & + P_0\left(i+\frac{\sigma_x^\nu}{2\Delta}, j-\frac{\sigma_y^\nu}{2\Delta}\right) + P_0\left(i+\frac{\sigma_x^\nu}{2\Delta}, j+\frac{\sigma_y^\nu}{2\Delta}\right)\Bigg\}\end{aligned} \tag{B.4}$$

$$\phi_{1x}^\nu(i,j) = \frac{\Delta}{2}\sum_{i'=i-\sigma_x^\nu/2\Delta}^{i+\sigma_x^\nu/2\Delta} w_{i'}\left\{P_{1x}\left(i', j-\frac{\sigma_y^\nu}{2\Delta}\right) + P_{1x}\left(i', j+\frac{\sigma_y^\nu}{2\Delta}\right)\right\} \tag{B.5}$$

$$\phi_{1y}^\nu(i,j) = \frac{\Delta}{2}\sum_{j'=j-\sigma_y^\nu/2\Delta}^{j+\sigma_y^\nu/2\Delta} w_{j'}\left\{P_{1y}\left(i-\frac{\sigma_x^\nu}{2\Delta}, j'\right) + P_{1y}\left(i+\frac{\sigma_x^\nu}{2\Delta}, j'\right)\right\} \tag{B.6}$$

$$\phi_2^\nu(i,j) = \Delta^2 \sum_{i'=i-\sigma_x^\nu/2\Delta}^{i+\sigma_x^\nu/2\Delta}\ \sum_{j'=j-\sigma_y^\nu/2\Delta}^{j+\sigma_y^\nu/2\Delta} w_{i'}w_{j'}P_2(i',j') \tag{B.7}$$

where we have defined the following functions

$$P_0(i,j) \equiv -\ln[1-n_2(i,j)] \tag{B.8}$$

$$P_{1x}(i,j) \equiv \frac{n_{1y}(i,j)}{1-n_2(i,j)} \tag{B.9}$$

$$P_{1y}(i,j) \equiv \frac{n_{1x}(i,j)}{1-n_2(i,j)} \tag{B.10}$$

$$P_2(i,j) \equiv \frac{n_0(i,j)}{1-n_2(i,j)} + \frac{n_{1x}(i,j)n_{1y}(i,j)}{(1-n_2(i,j))^2} \tag{B.11}$$

B.2 NUMERICAL GRADIENT

As we have already pointed out before, the gradient should be calculated from the discretized grand potential:

$$\Omega(\{\rho_\nu\}) = \mathcal{F}(\{\rho_\nu\}) + \Delta^2 \sum_\nu \sum_{i,j\in\mathcal{S}} w_i w_j \rho_\nu(i,j)\left[v_{ext}^{(\nu)}(i,j) - \mu_\nu\right] \tag{B.12}$$

Note that the result will be certainly different than that obtained from the discretization of the analytical gradient (equation B.3). The free energy is calculated as

$$\begin{aligned}\beta\mathcal{F}(\{\rho_\nu\}) = \Delta^2 \sum_{i,j\in\mathcal{S}} w_i w_j \left(\frac{n_{1x}(i,j)n_{1y}(i,j)}{1-n_2(i,j)} - n_0(i,j)\ln[1-n_2(i,j)]\right) \\ + \Delta^2 \sum_\nu \sum_{i,j\in\mathcal{S}} w_i w_j \rho_\nu(i,j)\left[\ln\rho_\nu(i,j) - 1\right]\end{aligned} \tag{B.13}$$

where the weighted densities are

$$\begin{aligned} n_0(i,j) = \frac{1}{4}\Bigg[&\rho_x\left(i-\frac{L}{2\Delta},j-\frac{\sigma}{2\Delta}\right)+\rho_x\left(i-\frac{L}{2\Delta},j+\frac{\sigma}{2\Delta}\right)\\ &+\rho_x\left(i+\frac{L}{2\Delta},j-\frac{\sigma}{2\Delta}\right)+\rho_x\left(i+\frac{L}{2\Delta},j+\frac{\sigma}{2\Delta}\right)+\rho_y\left(i-\frac{\sigma}{2\Delta},j-\frac{L}{2\Delta}\right)\\ &+\rho_y\left(i-\frac{\sigma}{2\Delta},j+\frac{L}{2\Delta}\right)+\rho_y\left(i+\frac{\sigma}{2\Delta},j-\frac{L}{2\Delta}\right)+\rho_y\left(i+\frac{\sigma}{2\Delta},j+\frac{L}{2\Delta}\right)\Bigg] \end{aligned} \tag{B.14}$$

$$\begin{aligned} n_{1x}(i,j) = \frac{\Delta}{2}\Bigg\{&\sum_{i'=i-L/2\Delta}^{i+L/2\Delta} w_{i'}\left[\rho_x\left(i',j-\frac{\sigma}{2\Delta}\right)+\rho_x\left(i',j+\frac{\sigma}{2\Delta}\right)\right]\\ &+\sum_{i'=i-\sigma/2\Delta}^{i+\sigma/2\Delta} w_{i'}\left[\rho_y\left(i',j-\frac{L}{2\Delta}\right)+\rho_y\left(i',j+\frac{L}{2\Delta}\right)\right]\Bigg\} \end{aligned} \tag{B.15}$$

$$\begin{aligned} n_{1y}(i,j) = \frac{\Delta}{2}\Bigg\{&\sum_{j'=j-\sigma/2\Delta}^{j+\sigma/2\Delta} w_{j'}\left[\rho_x\left(i-\frac{L}{2\Delta},j'\right)+\rho_x\left(i+\frac{L}{2\Delta},j'\right)\right]\\ &+\sum_{j'=j-L/2\Delta}^{j+L/2\Delta} w_{j'}\left[\rho_y\left(i-\frac{\sigma}{2\Delta},j'\right)+\rho_y\left(i+\frac{\sigma}{2\Delta},j'\right)\right]\Bigg\} \end{aligned} \tag{B.16}$$

$$\begin{aligned} n_2(i,j) = \Delta^2 &\sum_{i'=i-L/2\Delta}^{i+L/2\Delta}\sum_{j'=j-\sigma/2\Delta}^{j+\sigma/2\Delta} w_{i'}w_{j'}\rho_x(i',j')\\ +\Delta^2 &\sum_{i'=i-\sigma/2\Delta}^{i+\sigma/2\Delta}\sum_{j'=j-L/2\Delta}^{j+L/2\Delta} w_{i'}w_{j'}\rho_y(i',j'). \end{aligned} \tag{B.17}$$

The grand potential defined in equation B.12 can be split in two terms: Ω_1 depending explicitly on the densities ρ_ν, and Ω_2 depending on these through the functions n_α, so

$$\frac{\partial\beta\Omega(\{\rho_\nu\})}{\partial\rho_\nu(i,j)} = \frac{\partial\beta\Omega_1}{\partial\rho_\nu(i,j)} + \sum_{i',j',\alpha}\frac{\partial\beta\Omega_2}{\partial n_\alpha(i',j')}\frac{\partial n_\alpha(i',j')}{\partial\rho_\nu(i,j)}. \tag{B.18}$$

The first term is just

$$\frac{\partial\beta\Omega_1}{\partial\rho_\nu(i,j)} = \Delta^2 w_i w_j\left[\ln\rho_\nu(i,j)-\beta\mu_\nu\right] \quad w_k = \begin{cases}1/2 & \text{if } k=\{0,\,H/\Delta\}\\ 1 & \text{otherwise.}\end{cases} \tag{B.19}$$

We can ignore the factor $w_i w_j$ because $w_i w_j = 1\ \forall\ \rho_\nu(i,j)\neq 0$. So if we compare with its analytical counterpart (the first two terms in equation B.3) the only difference is the global factor Δ^2.

Let us take a look at the second part of the gradient

$$\frac{\partial \beta\Omega_2[\{\rho_\nu\}]}{\partial \rho_\nu(i,j)} = \sum_{i',j',\alpha} \frac{\partial \beta\Omega_2}{\partial n_\alpha(i',j')} \frac{\partial n_\alpha(i',j')}{\partial \rho_\nu(i,j)} = \\ = \Delta^2 \sum_{i',j',\alpha} \tilde{P}_\alpha(i',j') \frac{\partial n_\alpha(i',j')}{\partial \rho_\nu(i,j)} = \Delta^2 \sum_\alpha \tilde{\phi}^\nu_\alpha \quad \text{(B.20)}$$

with the functions $\tilde{P}_\alpha(i,j)$ being

$$\tilde{P}_0(i,j) = -w_i w_j \log(1 - n2(i,j)) \quad \text{(B.21)}$$

$$\tilde{P}_{1x}(i,j) = w_i w_j \frac{n_{1y}(i,j)}{1 - n_2(i,j)} \quad \text{(B.22)}$$

$$\tilde{P}_{1y}(i,j) = w_i w_j \frac{n_{1x}(i,j)}{1 - n_2(i,j)} \quad \text{(B.23)}$$

$$\tilde{P}_2(i,j) = w_i w_j \left(\frac{n_0(i,j)}{1 - n_2(i,j)} + \frac{n_{1x}(i,j) n_{1y}(i,j)}{(1 - n_2(i,j))^2} \right) \quad \text{(B.24)}$$

and w_k as defined in equation B.19. The numerical differentiation of the weighted densities reads

$$\frac{\partial n_0(i',j')}{\partial \rho_\nu(i,j)} = \frac{1}{4} \delta\left(|i' - i| - \sigma^\nu_x/2\right) \delta\left(|j' - j| - \sigma^\nu_y/2\right) \quad \text{(B.25)}$$

$$\frac{\partial n_{1x}(i',j')}{\partial \rho_\nu(i,j)} = \frac{\Delta}{2} w_i^{(x)} \Theta\left(|i' - i| - \sigma^\nu_x/2\right) \delta\left(|j' - j| - \sigma^\nu_y/2\right) \quad \text{(B.26)}$$

$$\frac{\partial n_{1y}(i',j')}{\partial \rho_\nu(i,j)} = \frac{\Delta}{2} w_j^{(y)} \delta\left(|i' - i| - \sigma^\nu_x/2\right) \Theta\left(|j' - j| - \sigma^\nu_y/2\right) \quad \text{(B.27)}$$

$$\frac{\partial n_2(i',j')}{\partial \rho_\nu(i,j)} = \Delta^2 w_i^{(x)} w_j^{(y)} \Theta\left(|i' - i| - \sigma^\nu_x/2\right) \Theta\left(|j' - j| - \sigma^\nu_y/2\right). \quad \text{(B.28)}$$

Here the weights coming from the numerical integrations are

$$w_k^{(\mu)} = \begin{cases} 1/2 & \text{if } k = \pm\sigma^\nu_\mu/2 \\ 1 & \text{otherwise.} \end{cases} \quad \text{(B.29)}$$

Then the functions $\tilde{\phi}_\alpha$ that define the second part of the numerical gradient have the following expressions

$$\begin{aligned}\tilde{\phi}^\nu_0(i,j) = \frac{1}{4}\Bigg\{&\tilde{P}_0\left(i-\frac{\sigma^\nu_x}{2\Delta}, j-\frac{\sigma^\nu_y}{2\Delta}\right) + \tilde{P}_0\left(i-\frac{\sigma^\nu_x}{2\Delta}, j+\frac{\sigma^\nu_y}{2\Delta}\right)\\ &+\tilde{P}_0\left(i+\frac{\sigma^\nu_x}{2\Delta}, j-\frac{\sigma^\nu_y}{2\Delta}\right) + \tilde{P}_0\left(i+\frac{\sigma^\nu_x}{2\Delta}, j+\frac{\sigma^\nu_y}{2\Delta}\right)\Bigg\}\end{aligned} \tag{B.30}$$

$$\tilde{\phi}^\nu_{1x}(i,j) = \frac{\Delta}{2}\sum_{i'=i-\sigma^\nu_x/2\Delta}^{i+\sigma^\nu_x/2\Delta} w_{i'}\left\{\tilde{P}_{1x}\left(i', j-\frac{\sigma^\nu_y}{2\Delta}\right) + \tilde{P}_{1x}\left(i', j+\frac{\sigma^\nu_y}{2\Delta}\right)\right\} \tag{B.31}$$

$$\tilde{\phi}^\nu_{1y}(i,j) = \frac{\Delta}{2}\sum_{j'=j-\sigma^\nu_y/2\Delta}^{j+\sigma^\nu_y/2\Delta} w_{j'}\left\{\tilde{P}_{1y}\left(i-\frac{\sigma^\nu_x}{2\Delta}, j'\right) + \tilde{P}_{1y}\left(i+\frac{\sigma^\nu_x}{2\Delta}, j'\right)\right\} \tag{B.32}$$

$$\tilde{\phi}^\nu_2(i,j) = \Delta^2\sum_{i'=i-\sigma^\nu_x/2\Delta}^{i+\sigma^\nu_x/2\Delta}\sum_{j'=j-\sigma^\nu_y/2\Delta}^{j+\sigma^\nu_y/2\Delta} w_{i'}w_{j'}\tilde{P}_2(i',j'). \tag{B.33}$$

These expressions are almost equivalent to equations B.4-B.7, the only difference is in the functions $\tilde{P}_\alpha$ which are related to their analytic counterparts as: $\tilde{P}_\alpha(i,j) = w_i w_j P_\alpha(i,j)$. We can see that they are equal in all points except in a small set of them where $w_i w_j \neq 1$.

Now we are able to compare the analytical and numerical gradient

$$\text{Analytic:}\qquad \beta\frac{\partial\Omega[\{\rho_\nu\}]}{\partial\rho_\nu(i,j)} = \ln\rho_\nu(i,j) - \beta\mu_\nu + \sum_\alpha \phi^\nu_\alpha(i,j) \tag{B.34}$$

$$\text{Numeric:}\qquad \beta\frac{\partial\Omega[\{\rho_\nu\}]}{\partial\rho_\nu(i,j)} = \Delta^2\left(\ln\rho_\nu(i,j) - \beta\mu_\nu\sum_\alpha\tilde{\phi}_\alpha(i,j)\right) \tag{B.35}$$

In the numerical gradient there is an additional Δ^2 but it does not affect at all because it is a global factor. The only difference appears in the points where $\tilde{\phi}_\alpha(i,j) \neq \phi_\alpha(i,j)$, i.e. those in which the weights of the numerical integral defined in equation B.19 are different from 1. Even though this correspond to a tiny fraction of the mesh points it is crucial to have it into account in order to get numerical consistence to reach the minimum.

C PROOF OF THE MONOTONIC DECREASING OF FREE ENERGY

Here we prove that the dynamics, as obtained from the DDFT formalism, always follows a decreasing free energy path. The time derivative of the free energy can be written as

$$\frac{\partial \mathcal{F}}{\partial t} = \int d\boldsymbol{r} \frac{\delta \mathcal{F}}{\delta \rho}(\boldsymbol{r}, t) \frac{\partial \rho}{\partial t}(\boldsymbol{r}, t) \tag{C.1}$$

Using the evolution equation 6.1

$$\frac{\partial \mathcal{F}}{\partial t} = \int d\boldsymbol{r} \mu(\boldsymbol{r}, t) \boldsymbol{\nabla} \cdot [\rho(\boldsymbol{r}, t) \boldsymbol{\nabla} \mu(\boldsymbol{r}, t)] \tag{C.2}$$

where $\mu(\boldsymbol{r}, t)$ is the functional derivative of the free energy with respect to the density, i.e. the local chemical potential. Integrating by parts we get

$$\frac{\partial \mathcal{F}}{\partial t} = \frac{1}{2} \int_{\mathcal{C}} d\boldsymbol{l} \cdot \rho \boldsymbol{\nabla} \mu^2 - \int_{\mathcal{A}} d\boldsymbol{r} \rho \left[\boldsymbol{\nabla} \mu\right]^2 \tag{C.3}$$

The first term is a line integral over the perimeter of the cavity $\mathcal{C}$ and the second term a surface integral over the total area $\mathcal{A}$. For both confined systems and those with periodic boundary conditions the density profile will be symmetric with respect to the center and both Cartesian axes, so each point of the perimeter ($\boldsymbol{r}_0$) has an specular one ($\tilde{\boldsymbol{r}}_0$) with the same density but opposite derivative $\boldsymbol{\nabla} \mu^2$: $\rho(\boldsymbol{r}_0) \boldsymbol{\nabla} \mu^2(\boldsymbol{r}_0) = -\rho(\tilde{\boldsymbol{r}}_0) \boldsymbol{\nabla} \mu^2(\tilde{\boldsymbol{r}}_0)$. Consequently, the line integral becomes zero. Then we have that

$$\frac{\partial \mathcal{F}}{\partial t} = -\int_{\mathcal{A}} d\boldsymbol{r} \rho \left[\boldsymbol{\nabla} \mu\right]^2 \leqslant 0 \tag{C.4}$$

since $\rho(\boldsymbol{r}) \left[\boldsymbol{\nabla} \mu\right]^2 \geqslant 0$. As a consequence, the free energy always decreases in time.

D DDFT: EXPLICIT EXPRESSION OF THE EVOLUTION EQUATION

Within the DDFT the density profile $\rho(\mathbf{r},t)$ follows the differential equation

$$\begin{aligned}\frac{\partial\rho}{\partial t}(\mathbf{r},t) &= \boldsymbol{\nabla}\cdot\left(\rho(\mathbf{r},t)\boldsymbol{\nabla}\frac{\delta\mathcal{F}}{\delta\rho}(\mathbf{r},t)\right)\\ &= \sum_{i=1}^{2}\left\{\frac{\partial\rho}{\partial x_i}(\mathbf{r},t)\frac{\partial}{\partial x_i}\left[\frac{\delta\mathcal{F}}{\delta\rho}(\mathbf{r},t)\right]+\rho(\mathbf{r},t)\frac{\partial^2}{\partial x_i^2}\left[\frac{\delta\mathcal{F}}{\delta\rho}(\mathbf{r},t)\right]\right\}\end{aligned} \tag{D.1}$$

where we have defined $x_1\equiv x$ and $x_2\equiv y$ while $\mathbf{r}=(x_1,x_2)$. Let us now derive the expressions for the derivatives of $\delta\mathcal{F}/\delta\rho$ for hard squares in DDFT. Taking into account that $\delta\mathcal{F}_{id}/\delta\rho=\log\rho$ the ideal part becomes

$$\boldsymbol{\nabla}\cdot\left(\rho\boldsymbol{\nabla}\frac{\delta\mathcal{F}_{id}}{\delta\rho}\right)=\sum_{i=1}^{2}\frac{\partial}{\partial x_i}\left(\rho\frac{\partial\log\rho}{\partial x_i}\right)=\sum_i\frac{\partial^2\rho}{\partial x_i^2} \tag{D.2}$$

For the excess part we will compute the derivative, as usual, in terms of the ϕ_α functions: $\delta\mathcal{F}_{exc}/\delta\rho=\sum_\alpha\phi_\alpha$. The derivative in the x variable is then

$$\frac{\partial}{\partial x}\left[\frac{\delta\mathcal{F}_{exc}}{\delta\rho}\right](\mathbf{r})=\sum_\alpha\frac{\partial\phi_\alpha}{\partial x}(\mathbf{r})=S_1^{(1)}(\mathbf{r})+S_2^{(1)}(\mathbf{r}) \tag{D.3}$$

where we have split the sum in two terms, being $S_1^{(1)}(\mathbf{r})\equiv\partial\phi_0/\partial x+\partial\phi_{1x}/\partial x$ and $S_2^{(1)}(\mathbf{r})\equiv\partial\phi_{1y}/\partial x+\partial\phi_2/\partial x$, which explicit expressions

$$\begin{aligned}S_1^{(1)}(\mathbf{r})=\frac{1}{2}\Bigg\{&\frac{\int_{y-\sigma}^{y}dy'\rho(x+\sigma,y')}{1-n_2(x+\sigma/2,y-\sigma/2)}-\frac{\int_{y-\sigma}^{y}dy'\rho(x-\sigma,y')}{1-n_2(x-\sigma/2,y-\sigma/2)}\\ &+\frac{\int_{y}^{y+\sigma}dy'\rho(x+\sigma,y')}{1-n_2(x+\sigma/2,y+\sigma/2)}-\frac{\int_{y}^{y+\sigma}dy'\rho(x-\sigma,y')}{1-n_2(x-\sigma/2,y+\sigma/2)}\Bigg\}\end{aligned} \tag{D.4}$$

$$
\begin{aligned}
S_2^{(1)}(\mathbf{r}) = \frac{1}{2}\int_{y-\sigma/2}^{y+\sigma/2} dy' \Bigg\{ & \frac{\rho(x+\sigma, y'-\sigma/2)+\rho(x+\sigma, y'+\sigma/2)}{1-n_2(x+\sigma/2, y')} \\
& -\frac{\rho(x-\sigma, y'-\sigma/2)+\rho(x-\sigma, y'+\sigma/2)}{1-n_2(x-\sigma/2, y')} \\
& + 2n_{1x}(x+\sigma/2, y')\frac{\int_{y'-\sigma/2}^{y'+\sigma/2} dy''\rho(x+\sigma, y'')}{[1-n_2(x+\sigma/2, y')]^2} \\
& -2n_{1x}(x-\sigma/2, y')\frac{\int_{y'-\sigma/2}^{y'+\sigma/2} dy''\rho(x-\sigma, y'')}{[1-n_2(x-\sigma/2, y')]^2} \Bigg\}
\end{aligned}
\tag{D.5}
$$

To get the laplacian of $\delta\mathcal{F}_{exc}/\delta\rho$ we take the derivative of the previous expressions: $S_i^{(2)} \equiv \partial S_i^{(1)}/\partial x$, where

$$
\begin{aligned}
S_1^{(2)}(\mathbf{r}) = \frac{1}{2}\Bigg\{ & \frac{\int_{y-\sigma}^{y} dy' \frac{\partial\rho}{\partial x}(x+\sigma, y')}{1-n_2(x+\sigma/2, y-\sigma/2)} - \frac{\int_{y-\sigma}^{y} dy' \frac{\partial\rho}{\partial x}(x-\sigma, y')}{1-n_2(x-\sigma/2, y-\sigma/2)} \\
& + \frac{\int_{y}^{y+\sigma} dy' \frac{\partial\rho}{\partial x}(x+\sigma, y')}{1-n_2(x+\sigma/2, y+\sigma/2)} - \frac{\int_{y}^{y+\sigma} dy' \frac{\partial\rho}{\partial x}(x-\sigma, y')}{1-n_2(x-\sigma/2, y+\sigma/2)} \\
& + \frac{\int_{y-\sigma}^{y} dy'\rho(x+\sigma, y') \int_{y-\sigma}^{y} dy' \left[\rho(x+\sigma, y')-\rho(x, y')\right]}{[1-n_2(x+\sigma/2, y-\sigma/2)]^2} \\
& - \frac{\int_{y-\sigma}^{y} dy'\rho(x-\sigma, y') \int_{y-\sigma}^{y} dy' \left[\rho(x, y')-\rho(x-\sigma, y')\right]}{[1-n_2(x-\sigma/2, y-\sigma/2)]^2} \\
& + \frac{\int_{y}^{y+\sigma} dy'\rho(x+\sigma, y') \int_{y}^{y+\sigma} dy' \left[\rho(x+\sigma, y')-\rho(x, y')\right]}{[1-n_2(x+\sigma/2, y+\sigma/2)]^2} \\
& - \frac{\int_{y}^{y+\sigma} dy'\rho(x-\sigma, y') \int_{y}^{y+\sigma} dy' \left[\rho(x, y')-\rho(x-\sigma, y')\right]}{[1-n_2(x-\sigma/2, y+\sigma/2)]^2} \Bigg\}
\end{aligned}
\tag{D.6}
$$

and $S_2^{(2)} \equiv \sum_{i=1}^{4} S_{2,i}^{(2)}$, which are obtained separately from each term of $S_2^{(1)}$ as

$$S_{2,1}^{(2)}(\mathbf{r}) = \frac{1}{2}\int_{y-\sigma/2}^{y+\sigma/2} dy' \left\{ \frac{\frac{\partial \rho}{\partial x}(x+\sigma, y'-\sigma/2) + \frac{\partial \rho}{\partial x}(x+\sigma, y'+\sigma/2)}{1-n_2(x+\sigma/2, y')} + \frac{[\rho(x+\sigma, y'-\sigma/2) + \rho(x+\sigma, y'+\sigma/2)] \int_{y'-\sigma/2}^{y'+\sigma 2} dy'' \left[\rho(x+\sigma, y'') - \rho(x, y'')\right]}{[1-n_2(x+\sigma/2, y')]^2} \right\} \tag{D.7}$$

$$S_{2,2}^{(2)}(\mathbf{r}) = -\frac{1}{2}\int_{y-\sigma/2}^{y+\sigma/2} dy' \left\{ \frac{\frac{\partial \rho}{\partial x}(x-\sigma, y'-\sigma/2) + \frac{\partial \rho}{\partial x}(x-\sigma, y'+\sigma/2)}{1-n_2(x-\sigma/2, y')} + \frac{[\rho(x-\sigma, y'-\sigma/2) + \rho(x-\sigma, y'+\sigma/2)] \int_{y'-\sigma/2}^{y'+\sigma/2} dy'' \left[\rho(x, y'') - \rho(x-\sigma, y'')\right]}{[1-n_2(x-\sigma/2, y')]^2} \right\} \tag{D.8}$$

$$\begin{aligned} S_{2,3}^{(2)}(\mathbf{r}) = \int_{y-\sigma/2}^{y+\sigma/2} dy' \Bigg\{ & \frac{n_{1x}(x+\sigma/2, y') \int_{y'-\sigma/2}^{y'+\sigma/2} dy'' \frac{\partial \rho}{\partial x}(x+\sigma, y'')}{[1-n_2(x+\sigma/2, y')]^2} \\ & + \frac{1}{2}\frac{[\rho(x+\sigma, y'-\sigma/2) + \rho(x+\sigma, y'+\sigma/2)] \int_{y'-\sigma/2}^{y'+\sigma/2} dy'' \rho(x+\sigma, y'')}{[1-n_2(x+\sigma/2, y')]^2} \\ & - \frac{1}{2}\frac{[\rho(x, y'+\sigma/2) + \rho(x, y'-\sigma/2)] \int_{y'-\sigma/2}^{y'+\sigma/2} dy'' \rho(x+\sigma, y'')}{[1-n_2(x+\sigma/2, y')]^2} \\ & + \frac{2n_{1x}(x+\sigma/2, y') \int_{y'-\sigma/2}^{y'+\sigma/2} dy'' \rho(x+\sigma, y'') \int_{y'-\sigma/2}^{y'+\sigma/2} dy'' \left[\rho(x+\sigma, y'') - \rho(x, y'')\right]}{[1-n_2(x+\sigma/2, y')]^3} \Bigg\} \end{aligned} \tag{D.9}$$

$$
\begin{aligned}
S^{(2)}_{2,4}(\mathbf{r}) = -\int_{y-\sigma/2}^{y+\sigma/2} dy' \Bigg\{ & \frac{n_{1x}(x-\sigma/2,y') \int_{y'-\sigma/2}^{y'+\sigma/2} dy'' \frac{\partial \rho}{\partial x}(x-\sigma,y'')}{[1-n_2(x-\sigma/2,y')]^2} \\
& + \frac{1}{2} \frac{[\rho(x,y'-\sigma/2)+\rho(x,y'+\sigma/2)] \int_{y'-\sigma/2}^{y'+\sigma/2} dy'' \rho(x-\sigma,y'')}{[1-n_2(x-\sigma/2,y')]^2} \\
& - \frac{1}{2} \frac{[\rho(x-\sigma,y'-\sigma/2)+\rho(x-\sigma,y'+\sigma/2)] \int_{y'-\sigma/2}^{y'+\sigma/2} dy'' \rho(x-\sigma,y'')}{[1-n_2(x-\sigma/2,y')]^2} \\
& + \frac{2 n_{1x}(x-\sigma/2,y')}{[1-n_2(x-\sigma/2,y')]^3} \times \\
& \times \int_{y'-\sigma/2}^{y'+\sigma/2} dy'' \rho(x-\sigma,y'') \int_{y'-\sigma/2}^{y'+\sigma/2} dy'' \left[\rho(x,y'') - \rho(x-\sigma,y'')\right] \Bigg\}
\end{aligned}
\tag{D.10}
$$

From these expressions the second derivative with respect the x variable is

$$
\frac{\partial^2}{\partial x^2}\left[\frac{\delta \mathcal{F}}{\delta \rho}(\mathbf{r})\right] = \sum_i S^{(2)}_i(\mathbf{r}) \tag{D.11}
$$

The derivatives with respect to the y variable $\partial/\partial y\,[\delta\mathcal{F}/\delta\rho]$ and $\partial^2/\partial y^2\,[\delta\mathcal{F}/\delta\rho]$ can be found from the previous ones just by substituting $x \leftrightarrow y$ and then exchanging coordinates: for example $f(x+\sigma,y') \to f(y+\sigma,x') \to f(x',y+\sigma)$.

The time and spatial derivatives of the density profile expressions are numerically computed through finite difference approximations:

$$
\frac{\partial \rho}{\partial t}(\mathbf{r},t_{k+1}) = \frac{\rho_{k+1}(\mathbf{r}) - \rho_k(\mathbf{r})}{\Delta t} \tag{D.12}
$$

$$
\frac{\partial \rho}{\partial x}(\mathbf{r},t_k) = \frac{\rho_k(x+\Delta x,y) - \rho_k(x-\Delta x,y)}{2\Delta x} \tag{D.13}
$$

$$
\frac{\partial^2 \rho}{\partial x^2}(\mathbf{r},t_k) = \frac{\rho_k(x+\Delta x,y) + \rho_k(x-\Delta x,y) - 2\rho_k(x,y)}{(\Delta x)^2} \tag{D.14}
$$

E CONSERVATION OF PARTICLES IN DDFT

Here we are going to explain why continuity equation 6.1 does not conserve the number of particles for discontinuous external potentials. In order to make it easier let us deal with the one-dimensional problem

$$\frac{\partial \rho}{\partial t}(x,t) + \frac{\partial j}{\partial x}(x,t) = 0 \tag{E.1}$$

with $j(x,t) \equiv -\rho(x,t)\frac{\partial}{\partial x}\left(\frac{\delta \mathcal{F}}{\delta \rho(x,t)}\right)$. Let us study the variation of the total number of particles for two different kind of external potentials:

HARD POTENTIAL: if we have hard-like external walls located at $x = -H/2$ and $x = H/2$, the density is strictly zero outside the region $[-(H-\sigma)/2, (H-\sigma)/2]$. If we integrate the evolution equation over all space we get the total variation of particles in the system $N(t)$, which is equal to

$$\begin{aligned}\frac{dN(t)}{dt} = \int_{-(H-\sigma)/2}^{(H-\sigma)/2} dx \frac{\partial \rho}{\partial t}(x,t) = \int_{-(H-\sigma)/2}^{(H-\sigma)/2} dx \frac{\partial j(x,t)}{\partial x} = \\ = j\left(\frac{H-\sigma}{2}, t\right) - j\left(-\frac{H-\sigma}{2}, t\right) = 2j\left(\frac{H-\sigma}{2}, t\right)\end{aligned} \tag{E.2}$$

where we have taken into account the symmetry of the system $j(x,t) = -j(-x,t)$. The local chemical potential $\mu(x,t) \equiv \partial \mathcal{F}/\partial \rho = \ln[\rho(x)] + \sum_\alpha \phi_\alpha(x) + V_{ext}(x)$ is a functional of the density profile which departs from the wall with a derivative different from zero, so in general the chemical potential also has a non-zero derivative at contact resulting in a current at this point different from zero. Consequently, the number of particles in the system is not conserved.

SOFT POTENTIAL: let us now study the case when the walls are represented by a soft external potential with maxima at $x = -H/2$ and $x = H/2$. Here the integration of the continuity equation leads to

$$\frac{dN(t)}{dt} = \int_{-H/2}^{H/2} dx \frac{\partial \rho}{\partial t}(x,t) = 2j\left(\frac{H}{2}, t\right) \tag{E.3}$$

but the local chemical potential now depends on the external potential which exhibits a maximum at $x = H/2$. It is easy to show that the density

profile and the chemical potential both depart from the wall with zero derivative and then the current becomes zero: $j(H/2, t) = 0$. Thus the number of particles is conserved.

For this reason we use as confining cavity a soft potential in the study of dynamics of hard rectangles (chapter 6).

LIST OF PUBLICATIONS

Publications of the author related to the topics presented in the thesis:

1. **M. González-Pinto**, Y. Martínez-Ratón, E. Velasco, *Liquid-crystal patterns of rectangular particles in a square nanocavity*, Physical Review E **88**, 032506 (2013).

2. **M. González-Pinto**, Y. Martínez-Ratón, E. Velasco, S. Varga, *Effect of shape biaxiality on the phase behavior of colloidal liquid-crystal monolayers*, Physical Chemistry Chemical Physics **17**, 6389-6400 (2015).

3. **M. González-Pinto**, Y. Martínez-Ratón, S. Varga, P. Gurin, E. Velasco, *Phase behaviour and correlations of parallel hard squares: from highly confined to bulk systems*, Journal of Physics: Condensed Matter **28**, 244002 (2016).

4. Y. Martínez-Ratón, **M. González-Pinto**, E. Velasco, *Biaxial nematic phase stability and demixing behaviour in monolayers of rod-plate mixtures*, Physical Chemistry Chemical Physics **18**, 24569-24581 (2016).

5. P. Gurin, S. Varga, **M. González-Pinto**, Y. Martínez-Ratón, E. Velasco, *Ordering of hard rectangles in strong confinement*, Journal of Chemical Physics **146**, 134503 (2017).

6. **M. González-Pinto**, F. Borondo, Y. Martínez-Ratón, E. Velasco, *Clustering in vibrated monolayers of granular rods*, Soft Matter **13**, 2571-2582 (2017): Inside Front Cover.

7. **M. González-Pinto**, Y. Martínez-Ratón, E. Velasco, *Dynamical properties of heterogeneous crystallization of parallel hard squares*: in preparation.

BIBLIOGRAPHY

1. S. Hawking, *Does God Play Dice?* (Public Lectures, 1999).
2. P. G. de Gennes, J. Prost, *The Physics of Liquid Crystals* (Oxford University Press, 1993).
3. G. Friedel, *Annales de Physique* **18**, 273 (1922).
4. P. S. Pershan, *Structure of Liquid Crystal Phases* (World Scientific Lecture Notes in Physics, 1988).
5. H. Kelker, *Molecular Crystals and Liquid Crystals* **21**, 1–48 (1973).
6. D. Dunmur, T. Sluckin, *Soap, science and flat-screen TVs: a history of liquid crystals* (Oxford University Press, 2010).
7. L. Onsager, *Annals of the New York Academy of Sciences* **51**, 627–659 (1949).
8. W. G. Hoover, F. H. Ree, *Journal of Chemical Physics* **49**, 3609–3617 (1968).
9. J.-P. Hansen, I. R. McDonald, *Theory of simple liquids* (Elsevier, 1990).
10. D. Frenkel, *Nature Materials* **14**, 9–12 (2014).
11. W. Wood, J. D. Jacobson, *Journal of Chemical Physics* **27**, 1207–1208 (1957).
12. B. J. Alder, T. E. Wainwright, *Journal of Chemical Physics* **27**, 1207–1208 (1957).
13. J. L. Ericksen, *Transactions of The Society of Rheology* **5**, 23–34 (1961).
14. F. M. Leslie, *Advances in Liquid Crystals* **4**, 1–81 (1979).
15. J. L. Ericksen, *Res Mechanica* **4**, 381–392 (1987).
16. F. C. Frank, *Discussions of the Faraday Society* **25**, 19–28 (1958).
17. D. Andrienko, *Introduction to liquid crystals*, 2006.
18. P. G. de Gennes, *Molecular Crystals and Liquid Crystals* **12**, 193–214 (1971).
19. R. Zwanzig, *Journal of Chemical Physics* **39**, 1714 (1963).
20. W. Maier, A. Saupe, *Zeitschrift für Naturforschung A* **13**, 564–566 (1958).
21. W. Maier, A. Saupe, *Zeitschrift für Naturforschung A* **14**, 882–889 (1959).
22. W. Maier, A. Saupe, *Zeitschrift für Naturforschung A* **15**, 287–292 (1960).
23. N. Metropolis, S. Ulam, *Journal of the American Statistical Association* **44**, 335–341 (1949).
24. A. Fall *et al.*, *Physical Review Letters* **112**, 175502 (2014).
25. I. S. Aranson, L. S. Tsimring, *Review of Modern Physics* **78**, 641–692 (2006).

26. V. Narayan, N. Menon, S. Ramaswamy, *Journal of Statistical Mechanics: Theory and Experiment* **2006**, P01005 (2006).
27. P. M. Reis, R. A. Ingale, M. D. Shattuck, *Physical Review Letters* **96**, 258001 (2006).
28. J. Galanis, D. Harries, D. L. Sackett, W. Losert, R. Nossal, *Physical Review Letters* **96**, 028002 (2006).
29. S. Edwards, R. Oakeshott, *Physica A: Statistical Mechanics and its Applications* **157**, 1080–1090 (1989).
30. A. Baule, F. Morone, C. S. O'Hern, H. A. Makse, *arXiv*, 1602.04369 (2016).
31. I. Goldhirsch, *Annual Review of Fluid Mechanics* **35**, 267–293 (2003).
32. C. Scalliet, A. Gnoli, A. Puglisi, A. Vulpiani, *Physical Review Letters* **114**, 198001 (2015).
33. F. Paillusson, D. Frenkel, *Physical Review Letters* **109**, 208001 (2012).
34. D. L. Blair, T. Neicu, A. Kudrolli, *Physical Review E* **67**, 031303 (2003).
35. V. Narayan, S. Ramaswamy, N. Menon, *Science* **317**, 105–108 (2007).
36. R. Evans, *Fundamentals of inhomogeneous fluids*, ed. by D. Henderson (CRC Press, 1992).
37. J. F. Lutsko, *Advances in Chemical Physics* **144**, 1 (2010).
38. T. Morita, K. Hiroike, *Progress of Theoretical Physics* **25**, 537–578 (1961).
39. C. De Dominicis, *Journal of Mathematical Physics* **3**, 983–1002 (1962).
40. F. H. Stillinger, F. P. Buff, *Journal of Chemical Physics* **37**, 1–12 (1962).
41. J. L. Lebowitz, J. K. Percus, *Journal of Mathematical Physics* **4**, 116–123 (1963).
42. J. K. Percus, G. Stell, *The Equilibrium Theory of Classical Fluids*, ed. by H. L. Frisch, J. L. Lebowitz (W. A. Benjamin, New York, 1964).
43. P. Hohenberg, W. Kohn, *Physical Review* **136**, B864–B871 (1964).
44. C. Ebner, W. F. Saam, D. Stroud, *Physical Review A* **14**, 2264–2273 (1976).
45. J. K. Percus, *Journal of Statistical Physics* **15**, 505–511 (1976).
46. R. M. Gibbons, *Molecular Physics* **17**, 81–86 (1969).
47. P. Tarazona, *Physical Review A* **31**, 2672–2679 (1985).
48. Y. Rosenfeld, *Phys. Rev. Lett.* **63**, 980–983 (1989).
49. J. A. Cuesta, Y. Martínez-Ratón, *Journal of Chemical Physics* **107**, 6379–6389 (1997).
50. J. A. Cuesta, Y. Martínez-Ratón, *Physical Review Letters* **78**, 3681–3684 (1997).
51. A. González, J. A. White, F. L. Román, R. Evans, *Journal of Chemical Physics* **109**, 3637–3650 (1998).

52. A. González, J. A. White, F. L. Román, S. Velasco, *Journal of Chemical Physics* **125**, 064703 (2006).

53. Y.-X. Yu, J. Wu, *Journal of Chemical Physics* **119**, 2288–2295 (2003).

54. M. Kamalvand, T. Keshavarzi, G. A. Mansoori, *International Journal of Nanoscience* **7**, 245–253 (2008).

55. N. J. Mariani, C. Mocciaro, M. A. Campesi, G. F. Barreto, *Journal of Chemical Physics* **132**, 204104 (2010).

56. J. F. Lutsko, *Physical Review E* **74**, 021121 (2006).

57. A. Härtel *et al.*, *Physical Review Letters* **108**, 226101 (2012).

58. F. Turci, T. Schilling, M. H. Yamani, M. Oettel, *The European Physical Journal Special Topics* **223**, 421–438 (2014).

59. W. G. Hoover, C. G. Hoover, M. N. Bannerman, *Journal of Statistical Physics* **136**, 715–732 (2009).

60. L. Tonks, *Physical Review* **50**, 955–963 (1936).

61. D. A. Kofke, A. J. Post, *Journal of Chemical Physics* **98**, 4853–4861 (1993).

62. G. S. Joyce, *Physical Review Letters* **19**, 684–684 (1967).

63. J. M. Yeomans, *Statistical mechanics of phase transitions* (Clarendon Press, 1992).

64. L. M. Casey, L. K. Runnels, *Journal of Chemical Physics* **51**, 5070–5089 (1969).

65. P. Gurin, S. Varga, *Physical Review E* **83**, 061710 (2011).

66. S. Varga, G. Balló, P. Gurin, *Journal of Statistical Mechanics: Theory and Experiment* **2011**, P11006 (2011).

67. S. S. Ashwin, M. Z. Yamchi, R. K. Bowles, *Physical Review Letters* **110**, 145701 (2013).

68. M. J. Godfrey, M. A. Moore, *Physical Review E* **89**, 032111 (2014).

69. M. Z. Yamchi, S. S. Ashwin, R. K. Bowles, *Physical Review E* **91**, 022301 (2015).

70. I. E. Kamenetskiy, K. K. Mon, J. K. Percus, *Journal of Chemical Physics* **121**, 7355–7361 (2004).

71. P. Gurin, S. Varga, *Journal of Chemical Physics* **139**, 244708 (2013).

72. J. K. Percus, M. Q. Zhang, *Molecular Physics* **69**, 347–355 (1990).

73. M. J. Godfrey, M. A. Moore, *Physical Review E* **91**, 022120 (2015).

74. P. Gurin, S. Varga, *Journal of Chemical Physics* **142**, 224503 (2015).

75. M. González-Pinto, Y. Martínez-Ratón, S. Varga, P. Gurin, E. Velasco, *Journal of Physics: Condensed Matter* **28**, 244002 (2016).

76. S. Belli, M. Dijkstra, R. van Roij, *Journal of Chemical Physics* **137**, 124506 (2012).

77. M. Marechal, H. Löwen, *Physical Review Letters* **110**, 137801 (2013).

78. F. Smallenburg, L. Filion, M. Marechal, M. Dijkstra, *Proceedings of the National Academy of Sciences* **109**, 17886–17890 (2012).

79. J. A. Cuesta, A. Sánchez, *Journal of Physics A: Mathematical and General* **35**, 2373 (2002).

80. M. González-Pinto, Y. Martínez-Ratón, E. Velasco, *Physical Review E* **88**, 032506 (2013).

81. M. Marechal, U. Zimmermann, H. Löwen, *Journal of Chemical Physics* **136**, 144506 (2012).

82. P. Bolhuis, D. Frenkel, *Journal of Chemical Physics* **106**, 666–687 (1997).

83. H. Graf, H. Löwen, *Journal of Physics: Condensed Matter* **11**, 1435 (1999).

84. T. J. Sluckin, A. Poniewierski, *Molecular Crystals and Liquid Crystals Incorporating Nonlinear Optics* **179**, 349–364 (1990).

85. P. Pieranski, L. Strzelecki, B. Pansu, *Physical Review Letters* **50**, 900–903 (1983).

86. G. Navascués, P. Tarazona, *Molecular Physics* **62**, 497–507 (1987).

87. D. Chaudhuri, S. Sengupta, *Physical Review Letters* **93**, 115702 (2004).

88. D. de las Heras, E. Velasco, L. Mederos, *Physical Review Letters* **94**, 017801 (2005).

89. D. de las Heras, E. Velasco, L. Mederos, *Physical Review E* **74**, 011709 (2006).

90. V. Babin, A. Ciach, M. Tasinkevych, *Journal of Chemical Physics* **114**, 9585–9592 (2001).

91. M. Tasinkevych, A. Ciach, *Physical Review E* **72**, 061704 (2005).

92. T. Geisinger, M. Müller, K. Binder, *Journal of Chemical Physics* **111**, 5241–5250 (1999).

93. Y. Martínez-Ratón, *Physical Review E* **75**, 051708 (2007).

94. D. de las Heras, L. Mederos, E. Velasco, *Liquid Crystals* **37**, 45–56 (2009).

95. N. Schopohl, T. J. Sluckin, *Physical Review Letters* **59**, 2582–2584 (1987).

96. P. Palffy-muhoray, E. C. Gartland, J. R. Kelly, *Liquid Crystals* **16**, 713–718 (1994).

97. H. G. Galabova, N. Kothekar, D. W. Allender, *Liquid Crystals* **23**, 803–811 (1997).

98. A. Šarlah, S. Žumer, *Physical Review E* **60**, 1821–1830 (1999).

99. D. de las Heras, L. Mederos, E. Velasco, *Physical Review E* **79**, 011712 (2009).

100. P. I. C. Teixeira, F. Barmes, C. Anquetil-Deck, D. J. Cleaver, *Physical Review E* **79**, 011709 (2009).

101. C. Chiccoli, P. Pasini, A. Šarlah, C. Zannoni, S. Žumer, *Physical Review E* **67**, 050703 (2003).

102. C. Chiccoli *et al.*, *Molecular Crystals and Liquid Crystals* **500**, 118–131 (2009).

103. R. G. Marguta, Y. Martínez-Ratón, N. G. Almarza, E. Velasco, *Physical Review E* **83**, 041701 (2011).

104. D. de las Heras, E. Velasco, *Soft Matter* **10**, 1758–1766 (2014).

105. I. C. Gârlea, B. M. Mulder, *Soft Matter* **11**, 608–614 (2015).

106. T. Geigenfeind, S. Rosenzweig, M. Schmidt, D. de las Heras, *Journal of Chemical Physics* **142**, 174701 (2015).

107. W. G. Hoover, C. G. Hoover, M. N. Bannerman, *Journal of Statistical Physics* **136**, 715–732 (2009).

108. D. A. Triplett, K. A. Fichthorn, *Physical Review E* **77**, 011707 (2008).

109. L. B. G. Cortes, Y. Gao, R. P. A. Dullens, D. G. A. L. Aarts, *Journal of Physics: Condensed Matter* **29**, 064003 (2017).

110. M. J. Freiser, *Physical Review Letters* **24**, 1041–1043 (1970).

111. R. Berardi, L. Muccioli, C. Zannoni, *Journal of Chemical Physics* **128**, 024905 (2008).

112. S. Kumar, *Biaxial liquid crystal electro-optic devices*, US Patent 7,604,850, 2009.

113. D. W. Bruce, *The Chemical Record* **4**, 10–22 (2004).

114. K. Praefcke *et al.*, *Molecular Crystals and Liquid Crystals Science and Technology. Section A. Molecular Crystals and Liquid Crystals* **323**, 231–259 (1998).

115. K. Praefcke, *Molecular Crystals and Liquid Crystals Science and Technology. Section A. Molecular Crystals and Liquid Crystals* **364**, 15–24 (2001).

116. G. R. Luckhurst, *Thin Solid Films* **393**, 40–52 (2001).

117. G. R. Luckhurst, *Nature* **430**, 413–414 (2004).

118. M. P. Taylor, J. Herzfeld, *Physical Review A* **44**, 3742–3751 (1991).

119. S. D. Peroukidis, A. G. Vanakaras, *Soft Matter* **9**, 7419–7423 (2013).

120. P. J. Camp, M. P. Allen, *Journal of Chemical Physics* **106**, 6681–6688 (1997).

121. A. N. Zakhlevnykh, P. A. Sosnin, *Molecular Crystals and Liquid Crystals Science and Technology. Section A. Molecular Crystals and Liquid Crystals* **293**, 135–173 (1997).

122. P. I. C. Teixeira, A. J. Masters, B. M. Mulder, *Molecular Crystals and Liquid Crystals Science and Technology. Section A. Molecular Crystals and Liquid Crystals* **323**, 167–189 (1998).

123. M. A. Bates, G. R. Luckhurst, *Physical Review E* **72**, 051702 (2005).

124. S. Orlandi, R. Berardi, J. Steltzer, C. Zannoni, *Journal of Chemical Physics* **124** (2006).

125. P. Grzybowski, L. Longa, *Physical Review Letters* **107**, 027802 (2011).

126. R. Alben, *Journal of Chemical Physics* **59**, 4299–4304 (1973).

127. R. van Roij, B. Mulder, *Journal de Physique II* **4**, 1763–1769 (1994).

128. P. J. Camp, M. P. Allen, P. G. Bolhuis, D. Frenkel, *Journal of Chemical Physics* **106**, 9270–9275 (1997).

129. H. H. Wensink, G. J. Vroege, H. N. W. Lekkerkerker, *Journal of Chemical Physics* **115**, 7319–7329 (2001).

130. S. Varga, A. Galindo, G. Jackson, *Physical Review E* **66**, 011707 (2002).

131. R. Berardi, C. Zannoni, *Soft Matter* **8**, 2017–2025 (2012).

132. L. J. Yu, A. Saupe, *Physical Review Letters* **45**, 1000–1003 (1980).

133. C. Tschierske, D. J. Photinos, *Journal of Materials Chemistry* **20**, 4263–4294 (2010).

134. E. van den Pol, A. V. Petukhov, D. M. E. Thies-Weesie, D. V. Byelov, G. J. Vroege, *Physical Review Letters* **103**, 258301 (2009).

135. E. van den Pol, D. Thies–Weesie, A. Petukhov, D. Byelov, G. Vroege, *Liquid Crystals* **37**, 641–651 (2010).

136. G. J. Vroege, *Liquid Crystals* **41**, 342–352 (2014).

137. Y. Martinez-Raton, S. Varga, E. Velasco, *Physical Chemistry Chemical Physics* **13**, 13247–13254 (2011).

138. S. Belli, A. Patti, M. Dijkstra, R. van Roij, *Physical Review Letters* **107**, 148303 (2011).

139. S. Belli, M. Dijkstra, R. van Roij, *Journal of Physics: Condensed Matter* **24**, 284128 (2012).

140. K. Béneut, D. Constantin, P. Davidson, A. Dessombz, C. Chanéac, *Langmuir* **24**, 8205–8209 (2008).

141. D. Constantin, P. Davidson, C. Chanéac, *Langmuir* **26**, 4586–4589 (2010).

142. K. Slyusarenko, D. Constantin, P. Davidson, *Journal of Chemical Physics* **140**, 104904 (2014).

143. Y. Martínez-Ratón, S. Varga, E. Velasco, *Journal of Chemical Physics* **140**, 204906 (2014).

144. Y. Martinez-Raton, M. Gonzalez-Pinto, E. Velasco, *Physical Chemistry Chemical Physics* **18**, 24569–24581 (2016).

145. S. Varga, Y. Martinez-Raton, E. Velasco, G. Bautista-Carbajal, G. Odriozola, *Physical Chemistry Chemical Physics* **18**, 4547–4556 (6 2016).

146. U. M. B. Marconi, P. Tarazona, *Journal of Chemical Physics* **110**, 8032–8044 (1999).

147. M. Rex, H. H. Wensink, H. Löwen, *Physical Review E* **76**, 021403 (2007).

148. R. Wittkowski, H. Löwen, *Molecular Physics* **109**, 2935–2943 (2011).

149. I. M. de Schepper, E. G. D. Cohen, *Journal of Statistical Physics* **27**, 223–281 (1982).

150. T. Müller, D. de las Heras, I. Rehberg, K. Huang, *Physical Review E* **91**, 062207 (2015).

151. J. Galanis, R. Nossal, W. Losert, D. Harries, *Physical Review Letters* **105**, 168001 (2010).

152. K. Harth *et al.*, *Physical Review Letters* **110**, 144102 (2013).

153. M. G. Clerc *et al.*, *Nature Physics* **4**, 249–254 (2008).

154. J. S. Olafsen, J. S. Urbach, *Physical Review Letters* **81**, 4369–4372 (1998).

155. I. S. Aranson, D. Volfson, L. S. Tsimring, *Physical Review E* **75**, 051301 (2007).

156. Y. Komatsu, H. Tanaka, *Physical Review X* **5**, 031025 (2015).

157. G. M. Rodríguez-Liñán, Y. Nahmad-Molinari, G. Pérez-Ángel, *Plos One* **11**, 1–11 (2016).

158. L. Walsh, N. Menon, *Journal of Statistical Mechanics: Theory and Experiment*, 083302 (2016).

159. Pol. Ind. Arretxe-Ugalde, Ezurriki 16, 20305 IRUN (Guipúzcoa, Spain): Opac S.L. Elementos Normalizados, (www.opac.net).

160. H. Schlacken, H. J. Mogel, P. Schiller, *Molecular Physics* **93**, 777–787 (1998).

161. Y. Martínez-Ratón, E. Velasco, L. Mederos, *Journal of Chemical Physics* **122**, 064903 (2005).

162. Y. Martínez-Ratón, E. Velasco, L. Mederos, *Journal of Chemical Physics* **125**, 014501 (2006).

163. Y. Martínez-Ratón, E. Velasco, *Physical Review E* **79**, 011711 (2009).

164. J. A. Wattis, *Physica D: Nonlinear Phenomena* **222**, 1–20 (2006).

165. http://uam.es/personal_pdi/ciencias/evelasco/supp.html.

166. D. de las Heras, private communication.

167. W. H. Press, *Numerical recipes 3rd edition: The art of scientific computing*, see section 10.8 (Cambridge university press, 2007).